Design of Additively Manufactured Lattice Structures for Biomedical Applications

Lead Guest Editor: Massimo Martorelli

Guest Editors: Antonio Gloria, Cristina Bignardi, Michele Calì, and Saverio Maietta

Design of Additively Manufactured Lattice Structures for Biomedical Applications

Design of Additively Manufactured Lattice Structures for Biomedical Applications

Lead Guest Editor: Massimo Martorelli
Guest Editors: Antonio Gloria, Cristina Bignardi, Michele Calì, and Saverio Maietta

Chief Editor

Loredana Zollo, Italy

Editorial Board

Contents

Editorial

Design of Additively Manufactured Lattice Structures for Biomedical Applications

Massimo Martorelli [ID],[1] **Antonio Gloria** [ID],[2] **Cristina Bignardi** [ID],[3] **Michele Calì** [ID],[4] **and Sverio Maietta**[1]

[1]*Department of Industrial Engineering, Fraunhofer JL IDEAS—University of Naples Federico II, P.le Tecchio 80, Naples 80125, Italy*
[2]*Institute of Polymers, Composites and Biomaterials—National Research Council of Italy, V.le J.F. Kennedy 54—Mostra d'Oltremare Pad. 20, Naples 80125, Italy*
[3]*DIMEAS, Politecnico di Torino, Corso Duca degli Abruzzi, 24, Torino 10129, Italy*
[4]*Department of Electric, Electronics and Computer Engineering, University of Catania, V.le A. Doria, 6, Catania 95125, Italy*

Correspondence should be addressed to Massimo Martorelli; massimo.martorelli@unina.it

The special issue focuses on different features related to the design of additively manufactured lattice structures for biomedical applications. In many cases, the process-structure-property relationship and technical features are discussed from a morphological, mechanical, and functional point of view. In particular, an overview of the Additive Manufacturing processes, software methods, and design criteria, which allow the direct fabrication of 3D porous structures and lattices with tailored properties, are reported. Accordingly, the current special issue aims at providing new insights into the development of advanced devices and illustrates theoretical/experimental approaches used by researchers working in the field.

1. Introduction

The Additive Manufacturing (AM) techniques allow creation of objects with complex shape as they are based on the process of joining materials, layer upon layer, differently from subtractive manufacturing methods. These techniques were previously known as rapid prototyping techniques, thanks to the possibility of manufacturing objects avoiding the employment of molds or other forming tools, thus enabling to reduce considerably the designing time and costs of the objects [1]. Furthermore, AM techniques in

combination with reverse engineering [2–4] allow the development of customized devices.

The main application fields of these technologies are related to development of mold inserts, biomedical devices (i.e., prostheses and scaffolds), machine components, and other components for different engineering sectors. AM is considered an evolution of rapid prototyping and has benefited enormously from both materials and mechanical engineering [5–7]. The manufacturing process can take place in different ways, such as by sintering or by melting and subsequent solidification of the material.

In the case of a stratification process based on powder sintering, the consolidation is obtained using a laser beam (Selective Laser Sintering and Selective Laser Melting) or an electron beam (Electron Beam Melting).

The final properties of the fabricated device clearly depend on the kind of process and on the parameter optimization. If the consolidation process involves powder fusion and solidification, the main critical aspects are generally related to the development of residual stresses.

It is also frequently reported that in this case, the process can be compared to a localized welding, which provides a high level of energy in a small portion of material surrounded by a "cold" mass. Over the past few years, increasing attention has been paid to AM techniques as they

are able to overcome the limits of the traditional manufacturing methods.

However, with regard to the biomedical field, as reported in the literature, many problems still remain, especially in terms of biocompatibility of some materials and mechanical properties of the obtained devices which would not seem to be appropriate for load bearing applications in many cases (i.e., bone substitutes and prostheses).

The posttreatments can be complex, also involving thermal cycles which can modify the microcrystalline structure. Despite the fact that the literature contains a great number of articles which deal with problems related to the production of components and functional devices for biomedical applications [8–10], information on the microstructural features, deriving from the production process and posttreatments, is still lacking.

2. Structure of the Special Issue

The current Special Issue (SI) includes 11 articles concerning the application of the AM in the biomedical field, stressing the important role of this technology in the design and development of advanced devices. Specifically, the following topics have been discussed:

Overview of AM processes

Material and device characterization

Effect of process on microstructure and optimization

Software methods for the development of 3D models

Development of fixing systems for bone segments

Design of 3D porous structures with tailored properties

Manufacture of tools for research laboratories

Implementation of correction braces

Replicas of internal organs

Finally, the aim of the proposed SI was to invite contributions from researchers working in the field, providing a complete view of the current progresses.

3. The Proposed Articles

A synthesized description of the proposed papers is reported.

The paper "Design of Additively Manufactured Structures for Biomedical Applications: A Review of the Additive Manufacturing Processes Applied to the Biomedical Sector" by F. Calignano et al., illustrates an overview of the state of the art of the AM technology, used in the biomedical field, for the production of various components, prostheses, or replicas for doctors or surgeons training. A more detailed research is presented in "The Role of 3D Printing for Medical Applications: A State of Art" by A. Aimar et al., where both benefits and drawbacks of different AM technologies, the employed materials, and the type of application in the biomedical sector are analysed. The possibility to design

Ti6Al4V lattice structures with tailored architectural features, pore size, and geometry, without significantly affecting the mechanical performance of the device, is reported in the paper entitled "A Further Analysis on Ti6Al4V Lattice Structures Manufactured by Selective Laser Melting" by S. Maietta et al.

The paper "Robocasting of Bioactive SiO_2-P_2O_5-CaO-MgO-Na_2O-K_2O Glass Scaffolds" by F. Baino et al. proposes a study on the fabrication of bioactive silicate glass scaffolds with a gridlike 3D structure, using a robocasting process. Results from different kinds of analyses on the manufactured scaffolds are reported.

In the paper "Digital Design of Medical Replicas via Desktop Systems: Shape Evaluation of Colon Parts" by M. Bici et al., some results on the application of desktop systems for the prototyping of medical replicas involving complex shapes are discussed, in order to improve the preoperative planning or the surgery training.

In the paper "3D Printed Anatomy-Specific Fixture for Consistent Glenoid Cavity Position in Shoulder Simulator" by G. Venne et al., the study on a fixing system of bone structures for biomechanical testing is proposed. The proposed approach may be adapted for different anatomical structures and allows the preservation of the bony anatomy integrity, also providing a repeatable anatomical positioning with respect to the testing system.

In the paper "Application of 3D Printing Technology for Design and Manufacturing of a Mechanical Stretching Bioreactor" by G. Putame et al., AM technology is employed for the fabrication of customized components of a mechanical stretching bioreactor with potential application for mechanobiology studies and cardiac tissue engineering.

The study proposed in the paper "Mallet Finger Lattice Casts Using 3D Printing," by H. Choi et al., presents a lattice design of a device, which is first modelled and then printed according to patient-specific needs, also preventing necrosis or infection. Another important application is considered in the work "Additive manufacturing applications to flexible actuators for active orthoses and medical devices" by M. G. Antonelli et al. In particular, the results of the research are presented focusing on the application of AM for the fabrication of novel actuators (i.e., soft pneumatic actuators and pneumatic muscles), active orthoses, and a variable-stiffness grasper to be employed in natural orifice transluminal endoscopic surgery.

The paper "A new method for biostatistical miRNA pattern recognition with topological properties of visibility graphs in 3D space" by M. Babič et al., reports a new method for producing 3D graphs. Specifically, an intelligent neural network system for DNA pattern recognition is combined with the topological properties of visibility networks of a 3D space.

Conflicts of Interest

The editors declare that they have no conflicts of interest regarding the publication of this Special Issue.

Acknowledgments

Massimo Martorelli
Antonio Gloria
Cristina Bignardi
Michele Calì
Sverio Maietta

References

[1] N. Guo and M. C. Leu, "Additive manufacturing: technology, applications and research needs," *Frontiers of Mechanical Engineering*, vol. 8, no. 3, pp. 215–243, 2013.

[2] M. Martorelli, C. Pensa, and D. Speranza, "Digital photogrammetry for documentation of maritime heritage," *Journal of Maritime Archaeology*, vol. 9, no. 1, pp. 81–93, 2014.

[3] M. Calì, D. Speranza, and M. Martorelli, "Dynamic spinnaker performance through digital photogrammetry, numerical analysis and experimental tests," in *Lecture Notes in Mechanical Engineering*, B. Eynard, V. Nigrelli, S. Oliveri et al., Eds., Springer, Cham, Switzerland, pp. 585–595, 2017.

[4] V. Pagliarulo, F. Farroni, P. Ferraro et al., "Combining ESPI with laser scanning for 3D characterization of racing tyres sections," *Optics and Lasers in Engineering*, vol. 104, pp. 71–77, 2018.

[5] R. Ambu, A. Motta, and M. Calì, "Design of a customized neck orthosis for FDM manufacturing with a new sustainable biocomposite," in *Lecture Notes in Mechanical Engineering*, pp. 707–718, Springer, Cham, Switzerland, 2019.

[6] F. Trevisan, F. Calignano, A. Aversa et al., "Additive manufacturing of titanium alloys in the biomedical field: processes, properties and applications," *Journal of Applied Biomaterials & Functional Materials*, vol. 16, no. 2, pp. 57–67, 2018.

[7] S. Saska, L. C. Pires, M. A. Cominotte et al., "Three-dimensional printing and in vitro evaluation of poly(3-hydroxybutyrate) scaffolds functionalized with osteogenic growth peptide for tissue engineering," *Materials Science and Engineering: C*, vol. 89, pp. 265–273, 2018.

[8] N. Vitković, S. Mladenović, M. Trifunović et al., "Software framework for the creation and application of personalized bone and plate implant geometrical models," *Journal of Healthcare Engineering*, vol. 2018, Article ID 6025935, 11 pages, 2018.

[9] E. M. Zanetti, A. Aldieri, M. Terzini, M. Calì, G. Franceschini, and C. Bignardi, "Additively manufactured loadbearing implantable devices: grounds for caution," *Australasian Medical Journal*, vol. 10, no. 8, p. 700, 2017.

[10] D. Speranza, D. Citro, F. Padula et al., "Additive manufacturing techniques for the reconstruction of 3D fetal faces," *Applied Bionics and Biomechanics*, vol. 2017, Article ID 9701762, 10 pages, 2017.

Research Article

A Further Analysis on Ti6Al4V Lattice Structures Manufactured by Selective Laser Melting

Saverio Maietta,[1] **Antonio Gloria** ⓘ**,**[2] **Giovanni Improta,**[3] **Maria Richetta** ⓘ**,**[4]
Roberto De Santis ⓘ**,**[2] **and Massimo Martorelli** ⓘ[1]

[1]*Department of Industrial Engineering, Fraunhofer JL IDEAS—University of Naples Federico II, P.le Tecchio 80,
 80125 Naples, Italy*
[2]*Institute of Polymers, Composites and Biomaterials—National Research Council of Italy,
 V.le J.F. Kennedy 54—Mostra d'Oltremare Pad. 20, 80125 Naples, Italy*
[3]*Department of Public Health, University of Naples Federico II, via S. Pansini 5, 80131 Naples, Italy*
[4]*Department of Industrial Engineering, University of Rome Tor Vergata, 00133 Rome, Italy*

Correspondence should be addressed to Antonio Gloria; angloria@unina.it

Mechanical and architectural features play an important role in designing biomedical devices. The use of materials (i.e., Ti6Al4V) with Young's modulus higher than those of natural tissues generally cause stress shielding effects, bone atrophy, and implant loosening. However, porous devices may be designed to reduce the implant stiffness and, consequently, to improve its stability by promoting tissue ingrowth. If porosity increases, mass transport properties, which are crucial for cell behavior and tissue ingrowth, increase, whereas mechanical properties decrease. As reported in the literature, it is always possible to tailor mass transport and mechanical properties of additively manufactured structures by varying the architectural features, as well as pore shape and size. Even though many studies have already been made on different porous structures with controlled morphology, the aim of current study was to provide only a further analysis on Ti6Al4V lattice structures manufactured by selective laser melting. Experimental and theoretical analyses also demonstrated the possibility to vary the architectural features, pore size, and geometry, without dramatically altering the mechanical performance of the structure.

1. Introduction

With regard to metal manufacturing, the relationship among process parameters, microstructure, and mechanical properties is fundamental in different areas (i.e., sintering, welding, casting, and plastic forming) and generally involves innovative and traditional fabrication methods [1–3].

Structural and mechanical properties play a crucial role in the design of biomedical devices with tailored performances which should satisfy the desired requirements.

As an example, functional devices for tissue reconstruction should resemble the structure and properties of the natural tissue.

In this context, metals like titanium (Ti) and its alloys have been widely employed. Titanium alloys are usually considered to make orthopedic and dental implants, due to their excellent biocompatibility, good corrosion resistance, and high strength [4–6]. Total hip replacements, interbody fusion devices for spinal applications, bone screws and nails, and parts of artificial heart valves are currently developed using titanium alloys [4, 7]. Stress shielding effects as well as bone atrophy and implant loosening are related to implants developed using a material with Young's modulus (i.e., Ti6Al4V, 114 GPa) which is much higher than that of the cortical bone (i.e., 10–30 GPa) [4, 8, 9].

Today, there is a great need to increase and to optimize implant life as a consequence of population ageing, diffusion of extreme sports, costs of implant replacement, and revision surgery [4].

Long-lasting implants may be clearly designed if materials with mechanical properties close to those of human tissues are employed [4].

An interesting strategy to reduce the implant stiffness would be the design of 3D porous devices with controlled geometry and architecture. A further advantage in designing porous implants is the possibility of tissue ingrowth, which should stabilize the implant [4, 9].

Several studies on bone reconstruction have already reported a correlation between newly formed tissue and pore size, as porous devices may offer surface and space favoring cell adhesion and bone ingrowth [4, 10]. Furthermore, pore interconnection is another important feature allowing for cell migration and *in vivo* blood vessel formation [4, 10, 11].

In general, many technologies have been considered to fabricate porous metal devices (i.e., direct laser metal sintering, selective laser melting, chemical vapor deposition, and space holder method) [4, 12–14] and also employed for titanium [4, 9, 15, 16].

On the contrary, it is well known how traditional techniques such as metal injection molding present some advantages resulting in a fast fabrication of high amount of complex parts with decreased production costs and in the possibility to modulate the properties through a suitable selection of powder size and/or sintering temperature [4]. Metal injection molding was successfully used to fabricate porous Ti6Al4V devices and mechanical, morphological, and biological properties were also evaluated [4].

Over the past years, the relationship between design and manufacturing has been explored in several fields. Differently from conventional fabrication methods, additive manufacturing technologies allow the direct production of customized and lightweight structures with improved properties [17–19].

The applicability of porous structures and lattices has been widely reported especially focusing on the development of orthopedic implants and 3D scaffolds for tissue engineering. As for the tissue regeneration approach, lattice structures should be biocompatible, biodegradable, and bioresorbable. They should be suitably optimized for cell attachment and growth, ensuring adequate mass transport and mechanical properties [18, 19].

In designing 3D lattice structures, a "unit cell" may be selected and a volume based on it may be built up, even if different methods are generally used to design the 3D periodic structures, also involving topology optimization and issues related to the implementation of the homogenization theory [19].

Ti6Al4V lattice components were already fabricated by selective laser melting and then analyzed in terms of surface roughness, microhardness, compressive properties, and dimensional accuracy [17]. In particular, microlattice structures were designed using the pillar textile unit cell as base and further lattice topologies which included reinforcing vertical bars were also considered [17].

Furthermore, a wide range of porosity (i.e., 60–95%) and unit cells with different sizes have been proposed for developing different kinds of Ti6Al4V components [17, 20], as well as implants (i.e., macropores in the range of 400–1000 μm) which exhibited excellent osteointegration performance *in vivo* [21].

The aim of the current study was to provide a further theoretical-experimental analysis on Ti6Al4V lattice structures fabricated by SLM.

2. Materials and Methods

2.1. Design and Fabrication of 3D Lattice Structures. A computer-aided design- (CAD-) based approach was used to develop two kinds of morphologically controlled structures (Figure 1). Different cell units were designed, thus varying the pore size and using a strut diameter of 1 mm. Solid-Works® 2017 (Dassault Systemes, Paris, France) CAD system was used to carry the operations.

Two different kinds of additively manufactured structures were fabricated using an M2 Cusing SLM machine (Concept Laser, Lichtenfels, Germany) and Ti6Al4V powder (particle size: 45–105 μm):

Model A. Lattice structure (25 mm × 25 mm × 25 mm) with 5 mm × 5 mm × 5 mm cell units.

Model B. Lattice structure (30 mm × 24 mm × 30 mm) with 5 mm × 8 mm × 5 mm cell units.

Lattice structures were fabricated with a laser beam of 170 W power, and scanning speed was set to 1250 mm/s [17, 22].

Further processing parameters were the spot size (100 μm) and the oxygen content (<0.1%).

Additional heat treatment was performed at 650°C for 2 h in argon atmosphere, in order to avoid oxidation and to reduce internal stresses related to the high thermal gradients experienced during the fabrication process. Successively, the structures were subjected to sand blasting for partially removing molten particles [17].

2.2. Experimental and Theoretical Analyses. A stereomicroscope (Olympus SZX) and an image software were used to analyze the developed structures.

Experimental compression tests were carried out at a rate of 1 mm/min up to a load of 800 N, using an INSTRON 5566 testing system. Load-displacement curves were reported.

On the contrary, the IGES format was employed and the geometric models of the two morphologically controlled structures were imported into HyperMesh® (Hyper-Works®—14.0, Altair Engineering Inc., Troy, Michigan, USA), which is a typical finite element (FE) preprocessor used for the management and the generation of complex models, starting with the import of CAD geometry to exporting ready-to-run solver file.

FE analysis was performed on the developed models in order to simulate the experimental tests. Young's
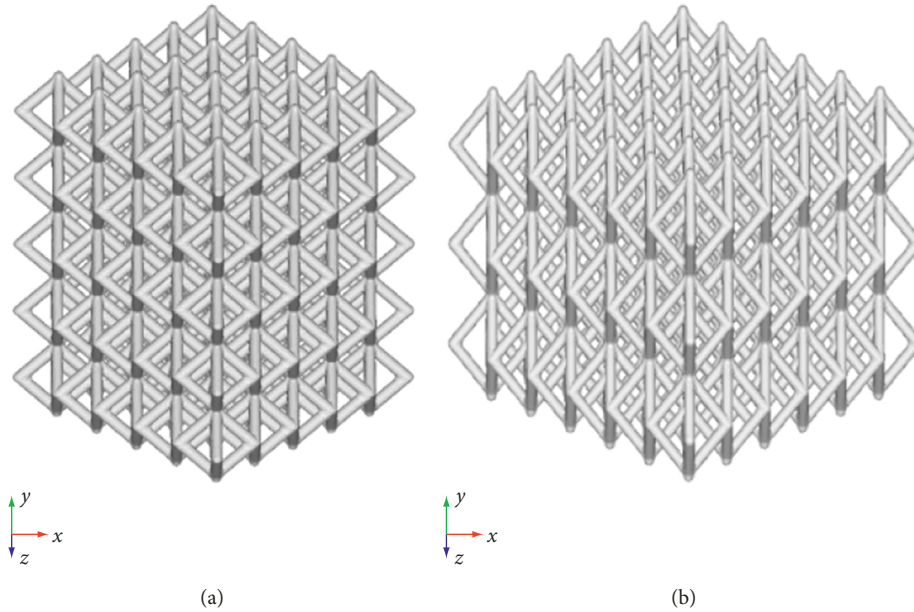
Figure 1: CAD models of lattice structures. (a) Model A. (b) Model B.

modulus and Poisson's ratio for Ti6Al4V are reported in Table 1.

The mesh was generated, and 3D solid CTETRA elements with four grid points were employed. Appropriate mesh size and refinement techniques were also used. Table 2 reports some technical features (i.e., total number of grids-structural, elements excluding contact, node-to-node surface contact elements, and degrees of freedom) for models A and B.

In addition, "freeze" type was used as contact conditions between the model and the compression plates. Constraints were applied for nodal displacements in all the directions. The external surface of the lower plate was constrained, whereas a compression load of 800 N acted on the external surface of the upper plate.

Linear static analyses were performed taking into account a nonfailure condition. Displacements, maximum principal stress, and von Mises stress distributions were evaluated.

3. Results and Discussion

In the biomedical field, it has been reported that the great mismatch between the stiffness of metal devices and surrounding tissues causes stress concentration and stress shielding effects, thus frequently leading to the implant loosening [4]. Anyway, it is also worth underlining that the implant stiffness, which determines stress distributions, depends not only on Young's modulus (an intrinsic mechanical property of the material) but also on the shape and size [4, 24, 25].

The properties of a device may be varied focusing on the material-shape combination and, hence, an appropriate combination of CAD-based approach and material selection. However, the important role of CAD and experimental and theoretical analyses has been frequently discussed for different kinds of biomedical applications [24–28].

Table 1: Young's modulus and Poisson's ratio employed for Ti6Al4V [4, 23].

Young's modulus (GPa)	Poisson's ratio
114	0.33

To overcome the drawbacks (i.e., stress shielding effects, bone atrophy, and implant loosening) related to the use of materials (i.e., Ti6Al4V) with Young's modulus higher than those of natural tissues, the design of porous devices may be considered for the reduction of the implant stiffness and, consequently, for the improvement of its stability by promoting tissue ingrowth [4].

Porosity and architecture may be taken into account to tailor mechanical and functional features of biomedical device. As an example, in the case of devices for tissue reconstruction and regeneration, if porosity increases, mass transport properties, which are crucial for cell behavior and tissue ingrowth, increase, whereas mechanical properties decrease [18].

Porous devices fabricated by additive manufacturing have the potential to be the next step in the development of up-to-date biomedical implants for several applications (i.e., bone reconstruction, dental implants, and interbody fusion devices).

Many attempts have been made to define architectural features, pore shape, and size, according to the mechanical and mass transport properties required for a specific application, also involving topology optimization, implementation of the homogenization theory, and well-defined algorithms and procedures. In the literature, many works report the potential to tailor mass transport and mechanical properties of additively manufactured structures by varying geometry, architectural features, as well as pore shape and size [18, 19].

The future looks bright for the additive manufacturing as it offers the possibility to design advanced and patient-specific

TABLE 2: Total number of grids (structural), elements excluding contact, node-to-node surface contact elements, and degrees of freedom.

Model	Total number of grids (structural)	Total number of elements excluding contact	Total number of node-to-surface contact elements	Total number of degrees of freedom
A	445,484	1,903,264	1,346	1,328,773
B	581,235	2,171,639	2,952	1,726,830

(a)   (b)

(c)   (d)
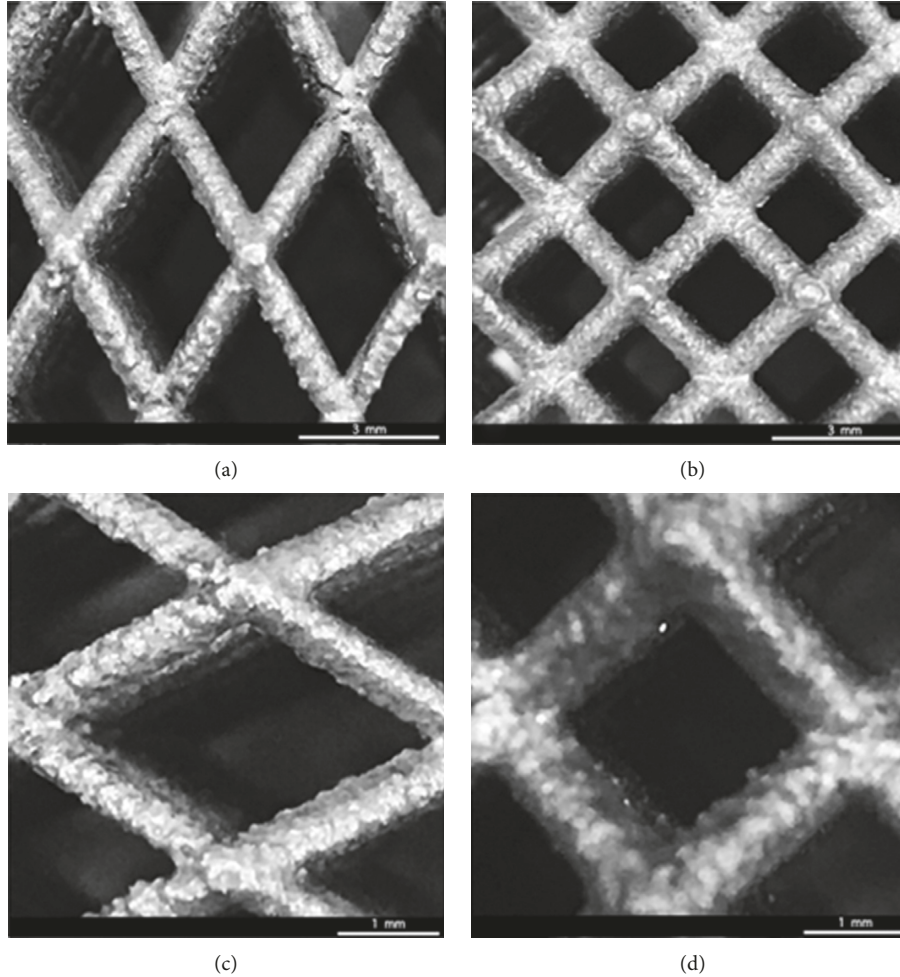
FIGURE 2: Results from morphological analysis performed on models B (a, c) and A (b, d) of Ti6Al4V lattice structures, using a stereomicroscope (Olympus SZX) and an image software.

implants in modern surgery. Accordingly, an individualized 3D printed Ti6Al4V cage for spinal cervical fusion was also proposed and developed integrating different approaches such as virtual reality simulation, CAD planning, and additive manufacturing [29]. In this case, a porous macro- and microcellular trabecular architecture was designed to improve osseointegration, and the porous cage was manufactured using SLM. Preliminary surgical implantations evidenced interesting results especially in terms of primary stability [29].

Furthermore, researchers already focused the attention on the design of Ti6Al4V implants by varying porosity in a wide range (i.e., up to 95%) and unit cells with different sizes (i.e., pores in the range of 400–1000 μm), which provided excellent osteointegration performance *in vivo* [21].

In this context, the present study would represent only a further step towards the analysis of Ti6Al4V lattice

structures designed using different architectural features and cell units, trying to improve the knowledge of the structure-property relationship through experimental and theoretical analyses.

Morphological analysis on the manufactured models allowed to study the structural features and the internal architecture of the devices and to confirm the consistency between theoretical values defined by the CAD-based approach and the experimental ones for the strut diameter and the cell unit sizes (Figure 2).

Results from experimental compression tests provided load-displacement curves which were linear up to a load level of 800 N (Figures 3 and 4).

In terms of mean value ± standard deviation, displacements of 0.023 ± 0.002 mm and 0.021 ± 0.002 mm were experimentally observed for models A and B, respectively.
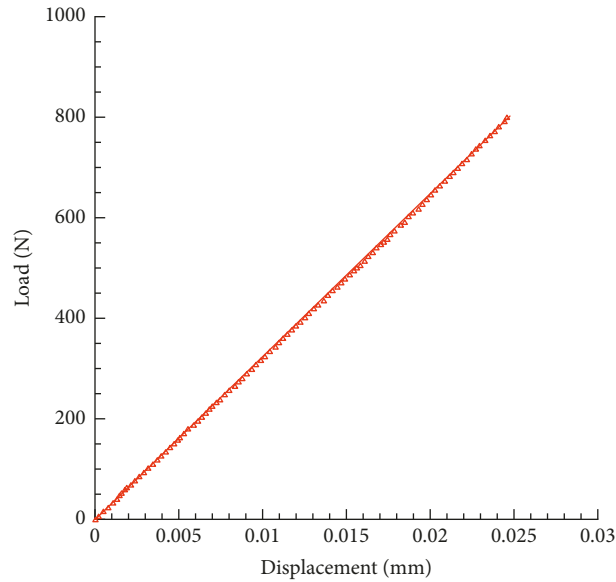
FIGURE 3: Results from experimental compression tests. Typical load-displacement curve obtained for model A of Ti6Al4V lattice.
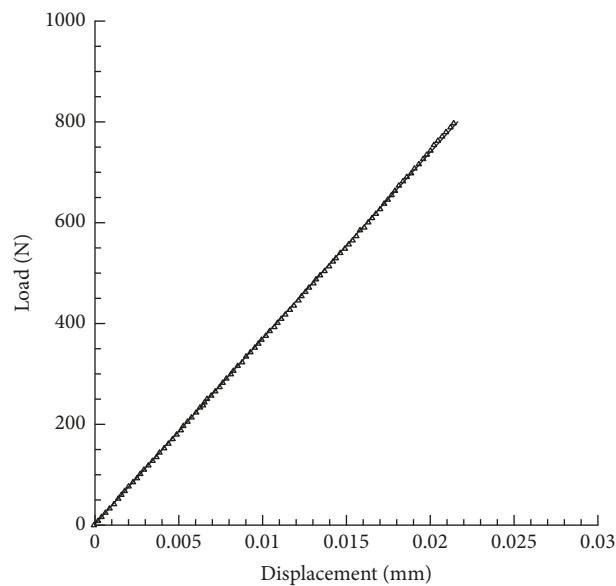
FIGURE 4: Results from experimental compression tests. Typical load-displacement curve obtained for model B of Ti6Al4V lattice.

On the contrary, FE analysis, which was carried out to simulate the experimental tests, allowed to obtain displacements, maximum principal stress, and von Mises stress distributions.

Specifically, Figure 5 reports the displacement contour plot for models A and B of Ti6Al4V lattice structures.

As expected on the basis of the results from the experimental tests, models A and B of Ti6Al4V lattice structures provided a maximum displacement value of about 0.024 mm and 0.020 mm, respectively. Thus, the results obtained from theoretical analyses were in agreement with the experimental ones.

The maximum principal stress and von Mises stress distributions were also evaluated and reported in Figures 6–9.

The linear load-displacement (and, hence, stress-strain) curves together with the maximum principal stress and von Mises stress distributions showed that plastic deformation was not present also at local levels.

Figures 6–9 evidence some differences in terms of stress distribution between the two proposed models according to the obtained values for the displacement (Figure 5), as a direct consequence of geometry, architectural features, and unit cell.

Even though in terms of stress distributions, some differences were found (Figures 6–9), as a greater number of regions with high local stress gradients were observed for model A in comparison to model B, and similar values of maximum stress were achieved for both models (i.e., von Mises stress of about 94–100 MPa) (Figures 6–10). In
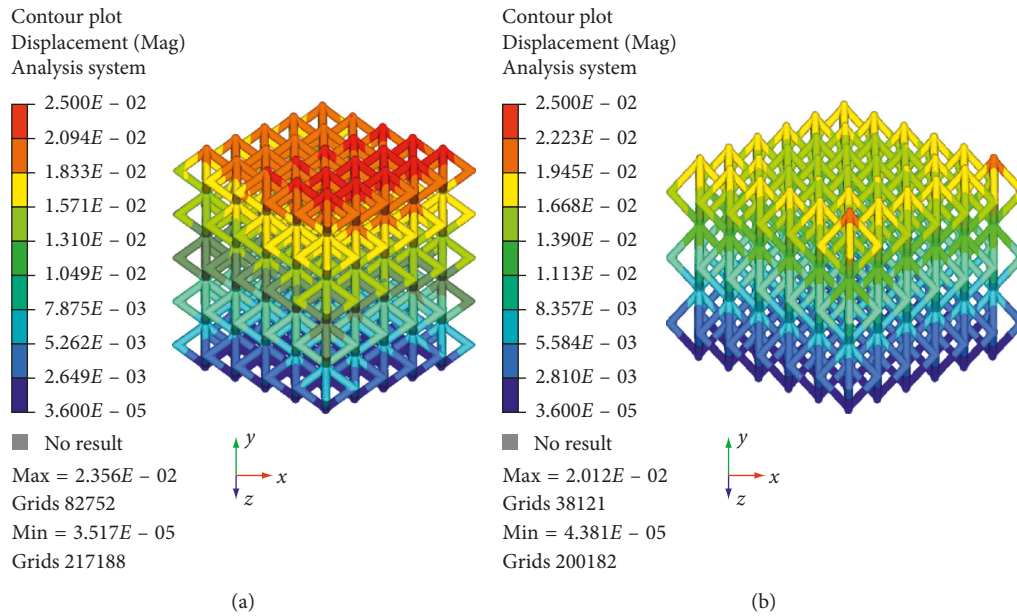
FIGURE 5: Results from FE analysis: displacement (mm) contour plot for model A (a) and model B (b) of Ti6Al4V lattice structures.
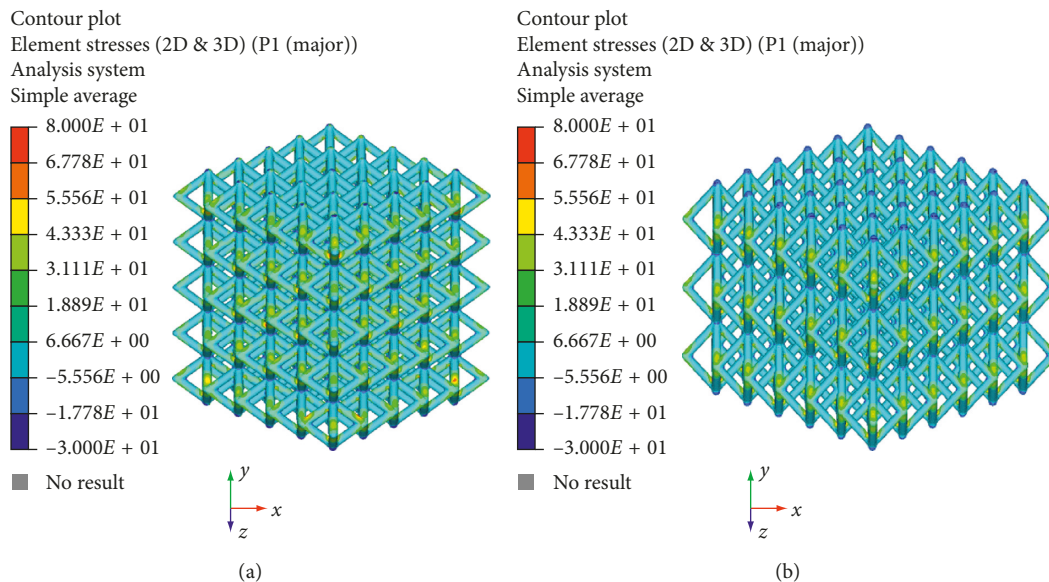
FIGURE 6: Results from FE analysis: maximum principal stress (MPa) distribution for model A (a) and model B (b) of Ti6Al4V lattice structures.

particular, although Figures 6–9 would evidence higher values of stress for model A in comparison to model B, Figure 10 reports an example of further section views for model B which better shows small local areas where the stress reached values similar to those found for model A. Thus, under the same loading condition, differences in geometrical and architectural features led to different stress distributions, however providing similar values of maximum stress, even if in model B they were achieved in smaller local areas.

Taking into account a methodology already reported for 3D porous structures with controlled architectural features [18],

the "apparent" stress (σ) and strain (ε) can be also evaluated ($\sigma = F/A_0$, $\varepsilon = \Delta H/H_0$), when the values of the force (F) measured by the load cell, the apparent initial cross-sectional area (A_0), the initial height (H_0), and the height variation (ΔH) of the structure are known.

Accordingly, starting from the above-reported considerations together with the obtained results, a compressive modulus of 1.4 ± 0.1 GPa and 1.1 ± 0.1 GPa can be determined for model A and model B, respectively.

However, it is worth noting that, even though in the case of porous structures, the compressive modulus does not represent the elastic modulus, which is an intrinsic property

Contour plot
Element stresses (2D & 3D) (P1 (major))
Analysis system
Simple average

| 8.000E + 01 |
| 6.778E + 01 |
| 5.556E + 01 |
| 4.333E + 01 |
| 3.111E + 01 |
| 1.889E + 01 |
| 6.667E + 00 |
| −5.556E + 00 |
| −1.778E + 01 |
| −3.000E + 01 |

No result

(a)

Contour plot
Element stresses (2D & 3D) (P1 (major))
Analysis system
Simple average

| 8.000E + 01 |
| 6.778E + 01 |
| 5.556E + 01 |
| 4.333E + 01 |
| 3.111E + 01 |
| 1.889E + 01 |
| 6.667E + 00 |
| −5.556E + 00 |
| −1.778E + 01 |
| −3.000E + 01 |

No result

(b)
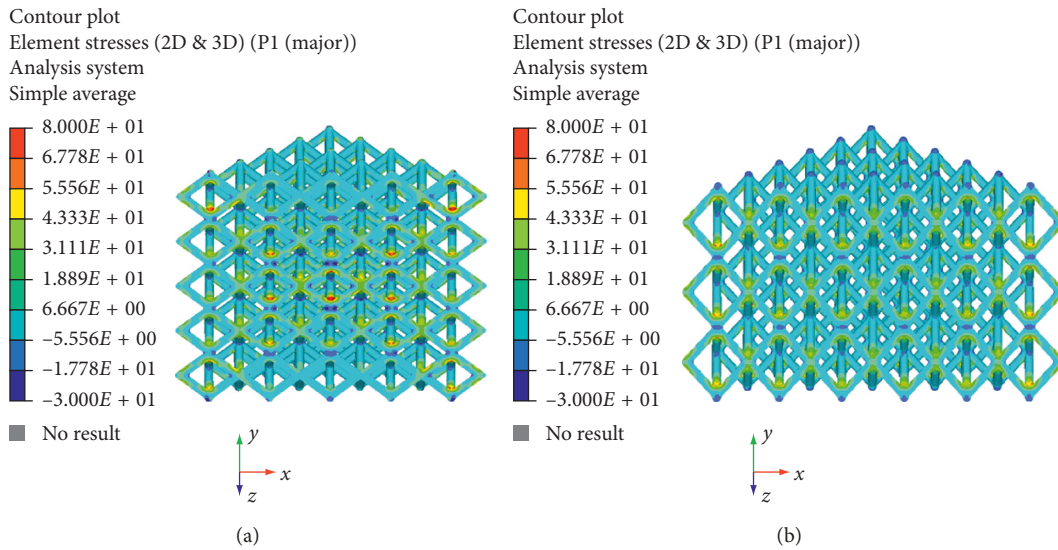
FIGURE 7: Results from FE analysis: maximum principal stress (MPa) distribution for model A (a) and model B (b) of Ti6Al4V lattice structures.

Contour plot
Element stresses (2D & 3D) (von Mises)
Analysis system
Simple average

| 1.000E + 02 |
| 8.894E + 01 |
| 7.789E + 01 |
| 6.683E + 01 |
| 5.578E + 01 |
| 4.472E + 01 |
| 3.367E + 01 |
| 2.261E + 01 |
| 1.156E + 01 |
| 5.000E − 01 |

No result

(a)

Contour plot
Element stresses (2D & 3D) (von Mises)
Analysis system
Simple average

| 1.000E + 02 |
| 8.894E + 01 |
| 7.789E + 01 |
| 6.683E + 01 |
| 5.578E + 01 |
| 4.472E + 01 |
| 3.367E + 01 |
| 2.261E + 01 |
| 1.156E + 01 |
| 5.000E − 01 |

No result

(b)
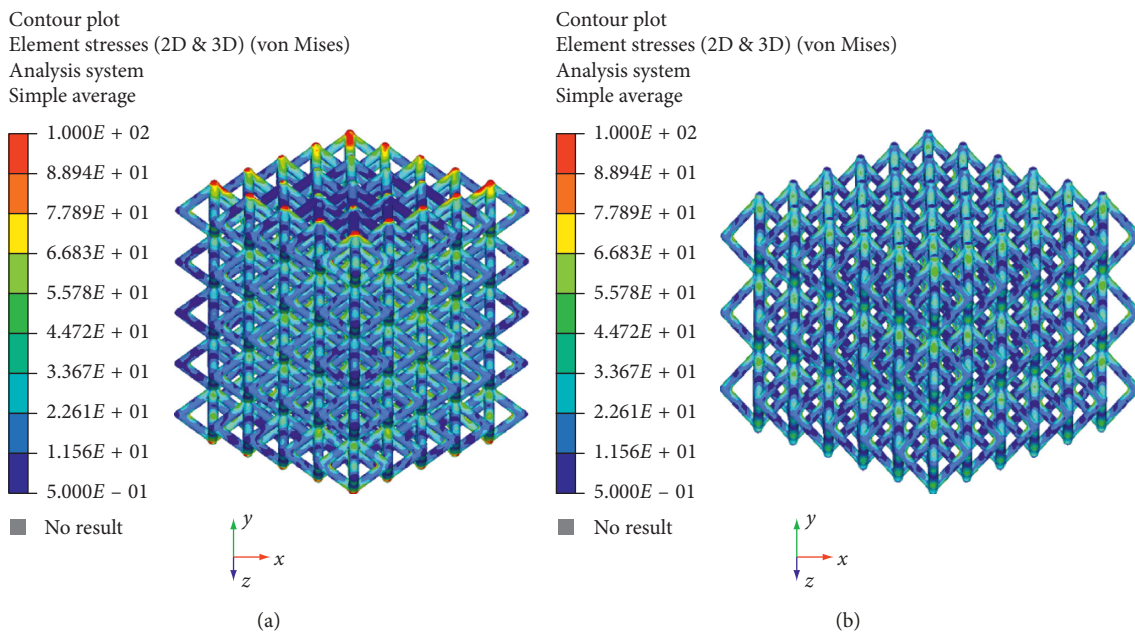
FIGURE 8: Results from FE analysis: von Mises stress (MPa) distribution for model A (a) and model B (b) of Ti6Al4V lattice structures.

of the material, and it clearly provides information on the stiffness of the designed structures.

Generally, structures for biomedical applications consist of materials like titanium and its alloys or other metals showing plastic deformation and yielding before fracture.

Devices must be designed so that they are loaded within the elastic limit and, clearly, do not yield.

Furthermore, it is well known how the heat treatment affects the behavior of the structures [17, 22].

For this reason, a static linear analysis was first performed using a nonfailure condition, and the present work would be a further study towards a future research with the aim of developing a complex model to describe the mechanical behavior and failure mechanisms of lattice structures manufactured by SLM, starting from the structure-property relationship.

For this reason, some potential limitations of the present research were as follows: (i) the linear static analysis carried out considering a nonfailure condition and the consequent lack of information on the strength and ductility of the manufactured structures, both at the theoretical and experimental levels and (ii) no evaluations of the effect of different heat treatments on the mechanical behavior.

(a)

(b)
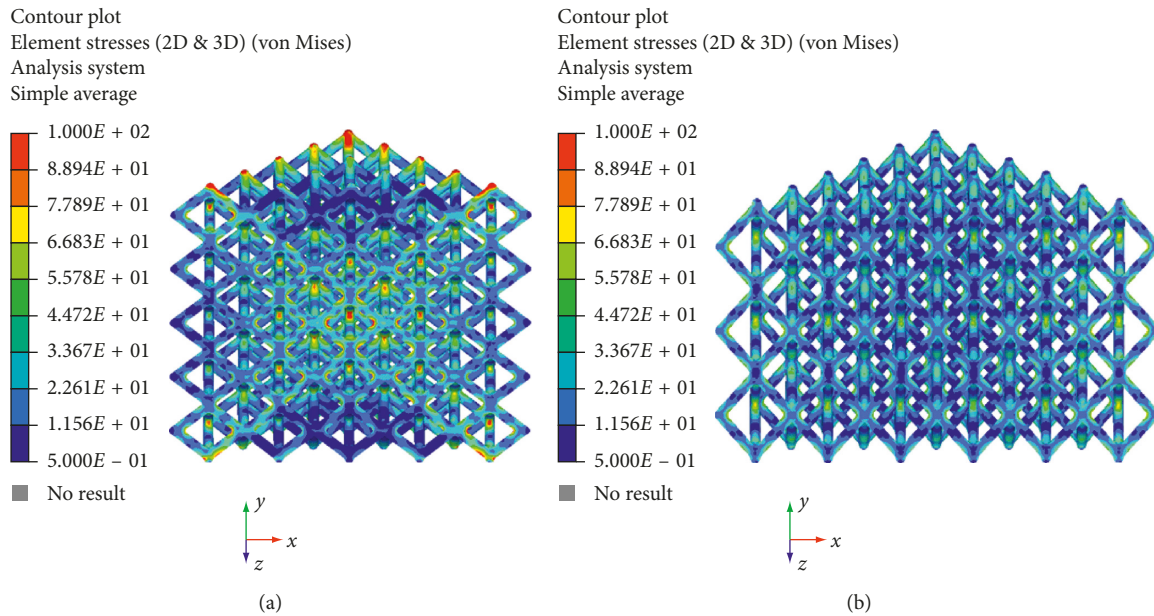
FIGURE 9: Results from FE analysis: von Mises stress (MPa) distribution for model A (a) and model B (b) of Ti6Al4V lattice structures.

(a)

(b)
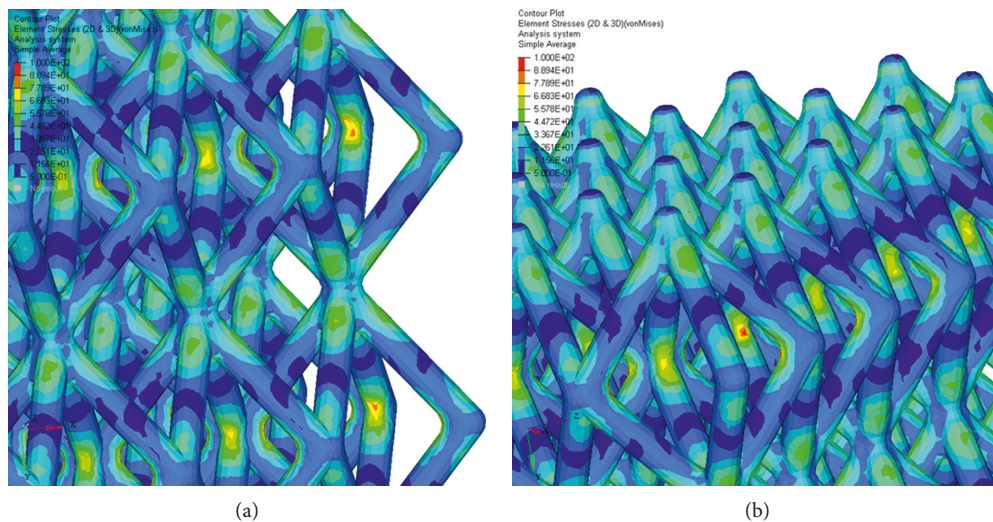
FIGURE 10: Results from FE analysis: von Mises stress (MPa) distribution for model B of Ti6Al4V lattice structures. Further section views (a) and (b). The color scale was chosen to allow comparisons.

4. Conclusions

Despite the limitations of the current analysis, the following conclusions were drawn:

(i) Structural features and internal architecture were visualized, and the consistency between theoretical values defined by the CAD-based approach and the experimental ones for the strut diameter and the cell unit sizes was verified.

(ii) The theoretical analyses performed on the two models were able to predict the experimental values for the displacement (0.023 ± 0.002 mm and 0.021 ± 0.002 mm) obtained from compression tests, also confirming the important role of CAD-FE modelling in the study of devices which could be predesigned to match the mechanical properties of natural tissues.

(iii) The possibility to tailor the architectural features, pore shape and size, and, eventually, mass transport properties, without dramatically altering the mechanical performance of the porous device, was confirmed.

Data Availability

All data generated or analyzed during this study are included in this article.

Conflicts of Interest

The authors declare that they have no conflicts of interest.

References

[1] M. Zhu, G. Xu, M. Zhou, Q. Yuan, J. Tian, and H. Hu, "Effects of tempering on the microstructure and properties of a high-strength bainite rail steel with good toughness," *Metals*, vol. 8, no. 7, p. 484, 2018.

[2] E. Fiorese, F. Bonollo, and E. Battaglia, "A tool for predicting the effect of the plunger motion profile on the static properties of aluminium high pressure die cast components," *Metals*, vol. 8, no. 10, p. 798, 2018.

[3] G. Jeon, K. Kim, J.-H. Moon, C. Lee, W.-J. Kim, and S. Kim, "Effect of Al 6061 alloy compositions on mechanical properties of the automotive steering knuckle made by novel casting process," *Metals*, vol. 8, no. 10, p. 857, 2018.

[4] A. Deing, B. Luthringer, D. Laipple, T. Ebel, and R. Willumeit, "A porous TiAl6V4 implant material for medical application," *International journal of biomaterials*, vol. 2014, Article ID 904230, 8 pages, 2014.

[5] M. Long and H. J. Rack, "Titanium alloys in total joint replacement-a materials science perspective," *Biomaterials*, vol. 19, no. 18, pp. 1621–1639, 1998.

[6] Y. Okazaki, S. Rao, Y. Ito, and T. Tateishi, "Corrosion resistance, mechanical properties, corrosion fatigue strength and cytocompatibility of new Ti alloys without Al and V," *Biomaterials*, vol. 19, no. 13, pp. 1197–1215, 1998.

[7] T. Ebel, "Titanium and titanium alloys for medical applications: opportunities and challenges," *PIM International*, vol. 2, pp. 21–30, 2008.

[8] A. Bandyopadhyay, F. Espana, V. K. Balla, S. Bose, Y. Ohgami, and N. M. Davies, "Influence of porosity on mechanical properties and in vivo response of Ti6Al4V implants," *Acta Biomaterialia*, vol. 6, no. 4, pp. 1640–1648, 2010.

[9] E. D. Spoerke, N. G. Murray, H. Li, L. C. Brinson, D. C. Dunand, and S. I. Stupp, "A bioactive titanium foam scaffold for bone repair," *Acta Biomaterialia*, vol. 1, no. 5, pp. 523–533, 2005.

[10] M. Mastrogiacomo, S. Scaglione, R. Martinetti et al., "Role of scaffold internal structure on in vivo bone formation in macroporous calcium phosphate bioceramics," *Biomaterials*, vol. 27, no. 17, pp. 3230–3237, 2006.

[11] Y. Kuboki, H. Takita, D. Kobayashi et al., "BMP-induced osteogenesis on the surface of hydroxyapatite with geometrically feasible and nonfeasible structures: topology of osteogenesis," *Journal of Biomedical Materials Research*, vol. 39, no. 2, pp. 190–199, 1998.

[12] G. Ryan, A. Pandit, and D. Apatsidis, "Fabrication methods of porous metals for use in orthopaedic applications," *Biomaterials*, vol. 27, no. 13, pp. 2651–2670, 2006.

[13] L. Mullen, R. C. Stamp, W. K. Brooks, E. Jones, and C. J. Sutcliffe, "Selective laser melting: a regular unit cell approach for the manufacture of porous, titanium, bone ingrowth constructs, suitable for orthopedic applications," *Journal of Biomedical Materials Research Part B: Applied Biomaterials*, vol. 89B, no. 2, pp. 325–334, 2009.

[14] T. Traini, C. Mangano, R. L. Sammons, F. Mangano, A. Macchi, and A. Piattelli, "Direct laser metal sintering as a new approach to fabrication of an isoelastic functionally graded material for manufacture of porous titanium dental implants," *Dental Materials*, vol. 24, no. 11, pp. 1525–1533, 2008.

[15] C. E. Wen, Y. Yamada, K. Shimojima, Y. Chino, H. Hosokawa, and M. Mabuchi, "Novel titanium foam for bone tissue engineering," *Journal of Materials Research*, vol. 17, no. 10, pp. 2633–2639, 2002.

[16] H. Shen and L. C. Brinson, "A numerical investigation of porous titanium as orthopedic implant material," *Mechanics of Materials*, vol. 43, no. 8, pp. 420–430, 2011.

[17] S. Campanelli, N. Contuzzi, A. Ludovico, F. Caiazzo, F. Cardaropoli, and V. Sergi, "Manufacturing and characterization of Ti6Al4V lattice components manufactured by selective laser melting," *Materials*, vol. 7, no. 6, pp. 4803–4822, 2014.

[18] M. Domingos, A. Gloria, J. Coelho, P. Bartolo, and J. Ciurana, "Three-dimensional printed bone scaffolds: the role of nano/micro-hydroxyapatite particles on the adhesion and differentiation of human mesenchymal stem cells," *Proceedings of the Institution of Mechanical Engineers, Part H: Journal of Engineering in Medicine*, vol. 231, no. 6, pp. 555–564, 2017.

[19] S. J. Hollister, "Porous scaffold design for tissue engineering," *Nature Materials*, vol. 4, no. 7, pp. 518–524, 2004.

[20] S. Merkt, C. Hinke, J. Bültmann, M. Brandt, and Y. M. Xie, "Mechanical response of TiAl6V4 lattice structures manufactured by selective laser melting in quasistatic and dynamic compression tests," *Journal of Laser Applications*, vol. 27, no. S1, Article ID S17006, 2014.

[21] Z. S. Bagheri, D. Melancon, L. Liu, R. B. Johnston, and D. Pasini, "Compensation strategy to reduce geometry and mechanics mismatches in porous biomaterials built with Selective laser melting," *Journal of the Mechanical Behavior of Biomedical Materials*, vol. 70, pp. 17–27, 2017.

[22] F. Cardaropoli, V. Alfieri, F. Caiazzo, and V. Sergi, "Manufacturing of porous biomaterials for dental implant applications through Selective laser melting," *Advanced Materials Research*, vol. 535–537, pp. 1222–1229, 2012.

[23] M. A. Saleh and A. E. Ragab, "Ti-6Al-4V helical spring manufacturing via SLM: effect of geometry on shear modulus," in *Proceedings of the International MultiConference of Engineers and Computer Scientists*, vol. 2, Hong Kong, China, March 2013.

[24] A. Gloria, S. Maietta, M. Martorelli, A. Lanzotti, D. C. Watts, and P. Ausiello, "FE analysis of conceptual hybrid composite endodontic post designs in anterior teeth," *Dental Materials*, vol. 34, no. 7, pp. 1063–1071, 2018.

[25] S. Maietta, R. De Santis, M. Catauro, M. Martorelli, and A. Gloria, "Theoretical design of multilayer dental posts using CAD-based approach and sol-gel chemistry," *Materials*, vol. 11, no. 5, p. 738, 2018.

[26] M. Giordano, P. Ausiello, M. Martorelli, and R. Sorrentino, "Accuracy evaluation of surgical guides in implant dentistry by non-contact reverse engineering techniques," *Dental Materials*, vol. 28, no. 9, pp. e178–e185, 2012.

[27] P. Ausiello, S. Ciaramella, F. Garcia-Godoy et al., "The effects of cavity-margin-angles and bolus stiffness on the mechanical behavior of indirect resin composite class II restorations," *Dental Materials*, vol. 33, no. 1, pp. e39–e47, 2017.

[28] P. Ausiello, S. Ciaramella, A. Fabianelli et al., "Mechanical behavior of bulk direct composite versus block composite and lithium disilicate indirect class II restorations by CAD-FEM modeling," *Dental Materials*, vol. 33, no. 6, pp. 690–701, 2017.

[29] U. Spetzger and A. Koenig, "Individualized three-dimensional printed cage for spinal cervical fusion," *Digital Medicine*, vol. 3, no. 1, p. 1, 2017.

Research Article
Mallet Finger Lattice Casts Using 3D Printing

Hyeunwoo Choi [ID],[1] Anna Seo [ID],[2] and Jongmin Lee [ID][1,3]

[1]*Department of Biomedical Engineering, Kyungpook National University, Daegu 41944, Republic of Korea*
[2]*Lee Gil Ya Cancer and Diabetes Institute, Gachon University of Medicine and Science, Yeonsu-gu, Incheon, Republic of Korea*
[3]*Department of Radiology, School of Medicine, Kyungpook National University, Daegu 41944, Republic of Korea*

Correspondence should be addressed to Anna Seo; csanseo@gmail.com and Jongmin Lee; jonglee@knu.ac.kr

Currently, research based on the technology and applications of 3D printing is being actively pursued. 3D printing technology, also called additive manufacturing, is widely and increasingly used in the medical field. This study produced custom casts for the treatment of mallet finger using plaster of Paris, which was traditionally used in clinical practice, and 3D printing technology, and evaluated their advantages and disadvantages for patients by conducting a wearability assessment. Mallet finger casts produced using plaster of Paris, when incorrectly made, can result in skin necrosis and other problems for patients. These problems can be mitigated, however, by creating casts using 3D printing technology. Additionally, plaster casts or ready-made alternatives can be inconvenient with respect to rapid treatment of patients. In contrast, 3D-printed casts appear to provide patients with appropriate treatment and increase their satisfaction because they are small in size, custom-made for each patient, and can be quickly made and immediately applied in clinical practice.

1. Introduction

Mallet finger refers to a deformity in which the finger cannot be extended due to severing of the extensor tendon at the distal phalanx or fracture of the bone to which it attaches. Mallet finger can be classified as tendinous, in which only the tendon is ruptured, or bony, in which it is accompanied by a broken phalanx. Surgical intervention is required in the case of bony mallet finger. However, tendinous mallet finger is treated conservatively, primarily by using a splint to extend the finger so that the tendon reattaches naturally. Traditional conservative treatments include fixation of plaster of Paris or metal casts, whereas surgical interventions include bone fragment fixation using steel wire, fixation with lag screws, tension band wire fixation, fixation using figure-eight tension band wire, intramedullary wire fixation, and dorsal suture.

Three-dimensional (3D) printing technology is widely used in industry, biology, and medicine [1]. Major applications of the technology include prosthetic fingers made using 3D scanners and printers [2], wrist protection devices [3], and synthetic bone implants made of calcium phosphate scaffolding using low-temperature 3D printing technology [4]. Custom-made orthopaedic wrist casts can be created using techniques such as fused deposition modelling with rapid prototyping (FDM-RP) and 3D printing [5–8]. 3D printing technology offers significant advantages in biomedical instrumentation and tissue engineering because of its ability to produce small quantities or single parts when needed based on patient-specific requirements [9] owing to its ability to produce recognizable 3D objects applied to surgery planning, orthoses, and related application programs [10], as well as the capability to produce single or small quantities of parts according to patient-specific needs.

Medical applications of 3D printing are rapidly expanding, and revolutions in medical services are expected [11]. The present study attempts to use a 3D printer to produce lattice casts that provide good ventilation, hygienic treatment, and clear X-ray images for treatment of mallet finger.

2. Materials and Methods

2.1. Subjects. Subjects of the study were selected randomly. Casts were designed for subjects' index fingers using either the traditional plaster of Paris method or MediACE 3D software (based on 3D scanning to measure the finger's dimensions).

2.2. Production of Plaster of Paris Casts. Plaster of Paris casts, which are traditionally used in clinical practice to treat mallet finger, were created as shown in Figure 1(a). Figure 1(b) shows a removed plaster of Paris cast.

2.3. Production of 3D-Printed Casts. First, the index finger was scanned repeatedly while maintaining posture of the extensor tendon (Figure 2) using a 3D scanner (3D Systems Sense scanner) to generate a stereolithography (STL) file of the finger. STL files, the end result of the 3D modelling process, are typically generated by computer-aided design (CAD) programs, which use this file type to store information about 3D models. The STL file shows the surface shape of a 3D object without representation of colour, texture, or other general characteristics of the model. Accordingly, STL files are widely used for rapid prototyping, 3D printing, and computer-aided manufacturing.

A 3D model of the mallet finger cast was then created based on the STL file (Figure 3) using the MediACE 3D software (Figure 4), and the final lattice design of the 3D-printed cast was completed (Figure 5).

The MediACE 3D software is expected to create beneficial business value in the medical industry and to contribute to implementation, distribution, and diffusion of customised medical services using 3D printing, the foundation of the 4th Industrial Revolution. It has been verified through clinical application and evaluation.

A mallet finger cast for 3D printing was designed using the mallet finger STL file and MediACE 3D and then converted into G-code. The cast, shown in Figure 6(a), was produced using polylactide (PLA) resin on a 3D Edison printer. For comparison, a plaster of Paris cast is shown in Figure 6(b).

2.4. Comparative Evaluation of Products. Application of the plaster of Paris and 3D-printed casts is shown in Figure 7. To evaluate the performance of and patients' satisfaction with each type of cast, a satisfaction evaluation (Quebec User Evaluation of Satisfaction; QUEST) [12] and a wearability evaluation (Product Performance Program; PPP) were conducted. The items of both measures were rated on a 5-point Likert scale from 1 (negative end of scale) to 5 (positive end of scale).

3. Results and Discussion

3D-printed lattice casts for treatment of mallet finger were produced based on STL files obtained through 3D scanning, the MediACE 3D software, and 3D printing technology. The advantages and disadvantages of the 3D-printed casts were

(a)

(b)

FIGURE 1: Plaster of Paris casts traditionally used to treat mallet finger in clinical practice. (a) Procedure for creating cast. (b) Removed plaster of Paris cast.

FIGURE 2: Finger maintaining posture of the extensor tendon.
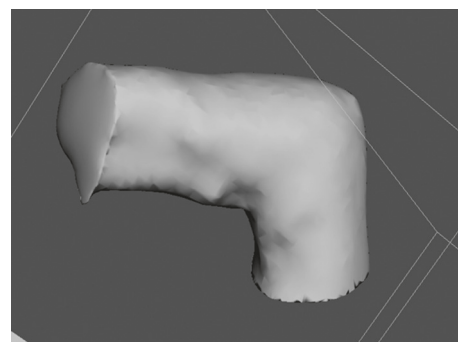
FIGURE 3: STL file of the mallet finger generated by the 3D systems sense scanner.
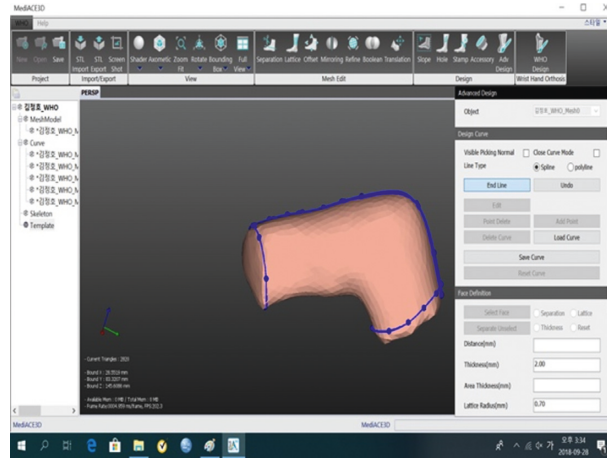
Figure 4: MediACE 3D masking model.
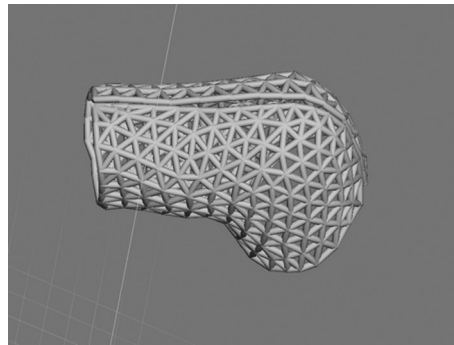
Figure 5: Final lattice design of 3D-printed mallet finger cast.

| (a) | (b) |
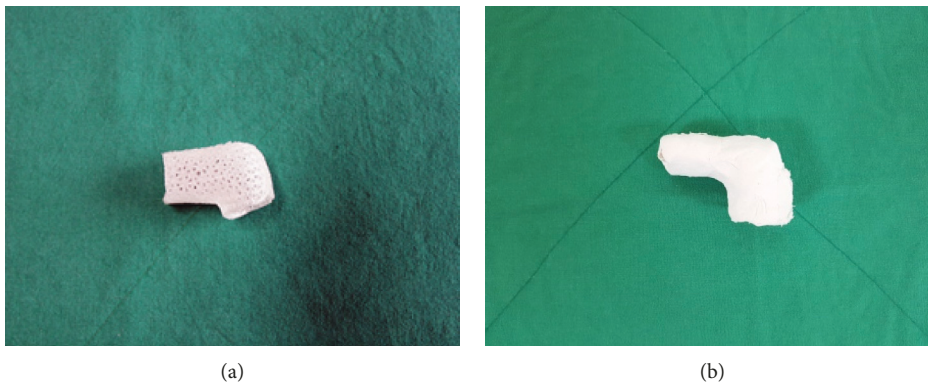
Figure 6: Comparison of removed mallet finger casts. (a) 3D-printed lattice cast. (b) Plaster of Paris cast.

then compared with those of plaster of Paris casts traditionally used in clinical practice.

The 3D-printed lattice casts showed results similar to those of the traditional plaster of Paris casts in the QUEST evaluation (Table 1). However, overall, subjects indicated that they were "very satisfied" or "satisfied" with the 3D-printed casts' dimensions, weight, adjustment, ease of use, and comfort. Subjects were more satisfied with the weight and ease of use of the 3D-printed casts than the plaster of

Paris casts (Table 1). Overall, the 3D-printed casts received a rating of "very satisfied" in the PPP wearability assessment (Table 2). In contrast, the plaster of Paris casts received many negative or "not applicable" ratings because they must be applied by medical staff.

The lattice design of the 3D-printed casts and their customised application can prevent necrosis or infection, offer a thickness and elasticity that guards against slipping off, and resolve other shortcomings of traditional plaster

(a)   (b)

FIGURE 7: Application of mallet finger casts. (a) Plaster of Paris cast. (b) 3D-printed lattice cast.

TABLE 1: User satisfaction evaluation of 3D-printed and plaster of Paris casts for mallet finger (QUEST).

| Item | 3D-printed lattice casts | | Plaster of Paris casts | |
	Score	Details	Score	Details
1. Dimensions	5		3	Determined by practitioner
2. Weight	5		3	Heavy
3. Adjustment	5		3	Difficult to adjust once hardened
4. Safety	5		3	Skin necrosis possible
5. Durability	5		3	Contamination possible
6. Ease of use	5		5	Must be applied by practitioner
7. Comfort	4		3	Determined by practitioner
8. Effectiveness	4		4	Determined by practitioner
Total score	4.75		3.5	

Note. The three most important items, in descending order, were dimensions, weight, and safety.

TABLE 2: Wearability evaluation of 3D-printed and plaster of Paris casts for mallet finger (PPP).

| Questionnaire items | | 3D-printed | Plaster of Paris |
No.	Item		
1	I like to use it	5	4
2	It can be used without complicated action or operation	5	0
3	It can be used anywhere and anytime	5	0
4	The procedure for wearing it is simple and uncomplicated	5	0
5	I can understand the principle of the cast	5	5
6	There is no danger or risk of malfunction	5	0
7	Wearing it incorrectly will not cause damage	3	0
8	It is comfortable to wear	5	0
9	Little effort is required to wear it	5	0
10	There are no requirements when using it	5	0
11	It is easy to use the fingers while wearing it	5	5
12	It is an adequate size and shape to protect the fingers	5	3
13	The size and shape are suitable for carrying or keeping it	5	0
14	The colour and shape are good	4	2
15	It is easy to clean and care for	5	2
16	It does not cause skin problems	5	3
17	The cast strength is good	5	5
Total score		4.82	1.70

Note. Scoring: 5 = strongly agree; 4 = agree; 3 = neither agree nor disagree; 2 = disagree; 1 = strongly disagree; 0 = not applicable.

of Paris casts, including oedema, discoloration, hinderance of function and circulation, pain, pulselessness, dysesthesia, and burning from pressure. In future, 3D-printed lattice casts should be used instead of plaster casts to treat mallet finger, based on their many benefits, such as providing patients with the most appropriate, customised treatment.

4. Conclusions

This study produced 3D-printed lattice casts for treatment of tendinous mallet finger based on STL models of the index fingers of randomly selected subjects, obtained using a 3D Systems Sense scanner. The casts were constructed from PLA resin using a 3D Edison Printer.

The advantages of traditional plaster of Paris casts are the difficulty of taking it off by patients once it is worn and short application time. Disadvantages include possible pain, skin oedema, discoloration, burning, infection, and necrosis; the complications of splint treatments are mainly skin-related.

Complications occurring in 123 cases of mallet finger treated both surgically and nonsurgically were reviewed. The 84 cases of splint treatment had a complication ratio of 45%; these complications were almost always temporary. Among the 45 cases of surgical treatment, 53% experienced complications and 76% of complications developed during the average monitoring period of 38 months. Six cases that involved surgical treatment after splinting (for a minimum of six weeks) were counted in both groups. Major complications experienced by surgically treated patients were deep infection (4%), total joint incongruity (18%), and nail deformity (18%). Seven patients (16%) required reoperation, and all had unsatisfactory results [13] except for one whose result was unknown.

The 3D-printed lattice cases were compared with plaster of Paris casts in treatment of patients with mallet finger. The results of PPP evaluation indicated that 3D-printed lattice casts allow for accurate, rapid production of customised orthoses, improving upon existing production methods. The 3D-printed casts can additionally resolve problems associated with plaster of Paris casts, namely, hyperextension and skin problems, because production is customised to the patient using 3D scanning. The size is very appropriate for 3D printer output, and it uses less material than a plaster of Paris cast and requires little output time. The ability of 3D-printed casts to overcome the disadvantages of traditional plaster of Paris casts makes them beneficial for clinical application.

Development of 3D-printed lattice casts is meaningful because they have the potential to help many patients if produced in clinical practice using 3D printers. Improvements in body scanning technology and product design software are expected to bring benefits to clinical practice. Future research should investigate the production of orthoses with various structures using the processes developed in this study. The investigators hope that the present study may serve as a reference for research on the production methods of finger orthoses based on various diseases and their treatment in clinical practice, such as the various types of 3D-printed finger casts in Figure S1.

Data Availability

The data used for evaluation purposes are uploaded and made publicly available.

Conflicts of Interest

The authors declare that there are no conflicts of interest regarding the publication of this paper.

Supplementary Materials

Figure S1: various types of 3D-printed finger casts. (*Supplementary Materials*)

References

[1] B. Ripley, T. Kelil, M. K. Cheezum et al., "3D printing based on cardiac CT assists anatomic visualization prior to transcatheter aortic valve replacement," *Journal of Cardiovascular Computed Tomography*, vol. 10, no. 1, pp. 28–36, 2016.

[2] K. H. Lee, S. J. Kim, Y. H. Cha, J. L. Kim, D. K. Kim, and S. J. Kim, "Three-dimensional printed prosthesis demonstrates functional improvement in a patient with an amputated thumb: a technical note," *Prosthetics and Orthotics International*, vol. 42, no. 1, pp. 107–111, 2018.

[3] D. Gu and J. Lee, "Development of a wrist protector using a 3D scanner and a 3D printer," *Journal of the Korean Medical Industry Society*, vol. 19, no. 3, pp. 312–319, 2017.

[4] D. S. Koo and J. R. Lee, "The development of a wrist brace using 3D scanner and 3D printer," *Fashion & Textile Research Journal*, vol. 19, no. 3, pp. 312–319, 2017.

[5] K. Chang, J. H. Chang, M. W. Huang, and L. Y. Lee, "Innovative orthosis for phalanx extension neurofacilitation (iOPEN)—development of a 3D-printed hand orthosis for chronic stroke patient," in *Proceedings of the 2018 IEEE International Conference on Applied System Innovation (ICASI)*, pp. 13–17, Institute of Electrical and Electronics Engineers, Chiba, Japan, April 2018.

[6] D. Palousek, J. Rosicky, D. Koutny, P. Stoklásek, and T. Navrat, "Pilot study of the wrist orthosis design process," *Rapid Prototyping Journal*, vol. 20, no. 1, pp. 27–32, 2014.

[7] A. P. Fitzpatrick, M. I. Mohanned, P. K. Collins, and I. Gibson, "Design of a patient specific, 3D printed arm cast," in *Proceedings of the International Conference on Design and Technology*, pp. 135–142, Knowledge E, Dubai, United Arab Emirates, December 2017.

[8] Y.-H. Seoung, "3-dimensional printing for mesh types of short arm cast by using computed tomography," *Journal of the Korea Contents Association*, vol. 15, no. 1, pp. 308–315, 2015.

[9] A. Bandyopadhyay, S. Bose, and S. Das, "3D printing of biomaterials," *MRS Bulletin*, vol. 40, no. 2, pp. 108–115, 2015.

[10] F. Rengier, A. Mehndiratta, H. von Tengg-Kobligk et al., "3D printing based on imaging data: review of medical applications," *International Journal of Computer Assisted Radiology and Surgery*, vol. 5, no. 4, pp. 335–341, 2010.

[11] C. L. Ventola, "Medical applications for 3D printing: current and projected uses," *Pharmacy and Therapeutics*, vol. 39, no. 10, pp. 704–711, 2014.

[12] Y. H. Cha, K. H. Lee, H. J. Ryu et al., "Ankle-foot orthosis made by 3D printing technique and automated design software," *Applied Bionics and Biomechanics*, vol. 2017, Article ID 9610468, 6 pages, 2017.

[13] P. J. Stern and J. J. Kastrup, "Complications and prognosis of treatment of mallet finger," *Journal of Hand Surgery*, vol. 13, no. 3, pp. 329–334, 1988.

Research Article

A New Method for Biostatistical *miRNA* Pattern Recognition with Topological Properties of Visibility Graphs in 3D Space

Matej Babič [ID],[1] **Ninoslav Marina,**[2] **Andrej Mrvar,**[3] **Kumar Dookhitram** [ID],[4] **and Michele Calì** [ID][5]

[1]*Faculty of Information Studies, Novo Mesto, Slovenia*
[2]*University of Information Science and Technology "St Paul the Apostle", Skopje, North Macedonia*
[3]*Faculty of Social Sciences, University of Ljubljana, Ljubljana, Slovenia*
[4]*University of Technology, Mauritius, Port Louis, Mauritius*
[5]*Electric, Electronics and Computer Engineering Department, University of Catania, Catania, Italy*

Correspondence should be addressed to Matej Babič; babicster@gmail.com

Visibility is a very important topic in computer graphics and especially in calculations of global illumination. Visibility determination, the process of deciding which surface can be seen from a certain point, has also problematic applications in biomedical engineering. The problem of visibility computation with mathematical tools can be presented as a visibility network. Instead of utilizing a 2D visibility network or graphs whose construction is well known, in this paper, a new method for the construction of 3D visibility graphs will be proposed. Drawing graphs as nodes connected by links in a 3D space is visually compelling but computationally difficult. Thus, the construction of 3D visibility graphs is highly complex and requires professional computers or supercomputers. A new method for optimizing the algorithm visibility network in a 3D space and a new method for quantifying the complexity of a network in DNA pattern recognition in biomedical engineering have been developed. Statistical methods have been used to calculate the topological properties of a visibility graph in pattern recognition. A new *n*-hyper hybrid method is also used for combining an intelligent neural network system for DNA pattern recognition with the topological properties of visibility networks of a 3D space and for evaluating its prospective use in the prediction of cancer.

1. Introduction

Manufacturing the visibility network (graph) [1] is a fundamental geometric structure which has useful applications in several fields including illumination and rendering, motion planning, pattern recognition, and sensor networks. A graph G is called a visibility graph when there is a polygon P such that the vertices of P are the vertices of G and two vertices are adjacent in G if they are visible in P. A visibility graph can be used in spatial analysis of urban and building spaces and applied to landscapes, as well. It is formed by taking a set of points across the space and forming graph edges between those points, if they are mutually visible. Visibility graphs have been widely used for 2D applications so far, but in this paper, an application to complex 3D visibility problems is advanced.

Visibility calculations are central to any computer graphics application. The relevance of statistics [2] has been much more recognized in the biomedical engineering field. Statistics can provide technicians of laboratories with important instruments for a scientific analysis of biomedical phenomena, allowing to understand the observed phenomena more correctly and to obtain more reliable results.

Biomedical engineering [3] being one of the fastest growing engineering disciplines aims at applying engineering expertise and advances to the field of medical needs and bioscience for the enhancement of healthcare.

Deoxyribonucleic acid (*DNA*) pattern recognition constitutes one of the most important works in biomedical engineering. Pattern recognition [4] is a branch of machine learning that focuses on the recognition of patterns and regularities in data, although it is in considered to be in some

cases nearly synonymous with machine learning. In pattern recognition, labels are assigned to objects and all objects are described by features, also called attributes. A classic example is the recognition of handwritten digits for the purpose of automatic mail sorting. Pattern recognition methods based on machine learning techniques [5] have been shown to be a promising approach to the analysis of network data. Intelligent computing has attracted many scientists and researchers working on intelligent techniques for solving complex real-world problems.

The graphical representations of the *DNA* as a method for *DNA* pattern recognition have been introduced to facilitate comparison of *DNA* sequences and to observe differences in their structure [6–10]. A novel method is thus explored in this study to generate and characterize complex networks by means of analysis of their *miRNA* sequences.

A new hybrid method [11] that combines three types of intelligent neural network systems [12] has been used. This paper explores the use of an intelligent system [13] with a new hybrid method that improves the existing ones. It is based on the *n*-hyper hybrid method. The aim of this work is to outline possibilities for applying an *n*-hyper hybrid system method for *miRNA* pattern recognition [14] with topological properties of visibility graphs in a 3D space and to evaluate its prospective use in biomedical engineering.

The proposed method can be utilized to approach more systematically problems of visibility of *miRNA* sequences, in the comparison of *DNA* sequences and in the analysis of complex networks such as *miRNA* networks in the biomedical field. The method is based on an algorithm which is built for optimizing the visibility in a 3D space and an *n*-hyper hybrid system for *miRNA* cancer pattern recognition which allows to register more precisely the risk of various types of cancer.

In particular, the proposed method can be used to analyze the transformation of 1D *miRNA* sequences into 3D *miRNA* sequences for predicting cancer. More specifically, a new type of intelligent system, the *n*-hyper hybrid system, has been developed to describe *miRNA* sequences and the difference between cancer and noncancer *miRNA*. Thanks to this method, some more information on a complex network derived from the visibility network in a 3D space, compared to the visibility graph, can be obtained in the application of *miRNA* pattern recognition. The utility of applying 3D visibility graphs in biomedical engineering for a more precise prediction of cancer will be thus discussed in this paper.

Finally, this new method permits to obtain a physical visualization of the three-dimensional *miRNA* sequences. Through additively manufactured (3D printing) techniques, which are much used in the biomedical field for building and analysis of implantable devices [15–18], it is possible indeed to have a reconstruction of the 3D space network as a lattice structure as well as a view of the relationships between *miRNA* sequences.

This paper is organized as follows: Section 2 is devoted to a description of the methods and the materials used. In Section 3, the results and discussions are illustrated. Final considerations and conclusions are drawn in Section 4.

2. Materials and Methods

2.1. A New Method for Statistical miRNA Pattern Recognition. *DNA* [19–23] is composed of an extremely long array of nucleotides. MicroRNAs [23–27] constitute a recently discovered class of noncoding *RNAs* playing some key roles in the regulation of gene expression. In this article, we have developed a new method to describe the transformation of 1D *miRNA* sequences into 3D *miRNA* sequences. This means that we have transformed the *miRNA* sequences into a 3D coordinate system.

For better presentation, four colours are used to denote the nucleotides adenine (A), cytosine (C), guanine (G), and thymine (T). We have replaced each nucleotide by different colours, namely, A by white, C by light purple, G by gray, and T by black. Initially, we have transformed each nucleotide of the *DNA* sequences into a 2D array by using a spiral curve. Figure 1 presents the coloured *miRNA* sequences (miR-612 gene) and transformation of each nucleotide of the *miRNA* sequences into a 2D array by using a spiral curve. We have also denoted the *miRNA* sequences by two coordinates (x, y).

Furthermore, we have denoted each nucleotide of the *miRNA* sequences with a number. An example of an *miRNA* sequence is ... *TGCCAATCGTTGT* .... This sequence of letters can be converted with the function f. We have denoted $\{A, C, G, T\} \in M$ and $\{1, 2, 3, 4\} \in N$. Also, $f : M \longrightarrow N$. We have denoted with n_A, n_C, n_G, and n_T the number of all nucleotides A, C, G, and T in some sequences. We have determined linear arrangement $\{n_A, n_C, n_G, n_T\}$ from the largest to the smallest value. For example, if $n_A > n_C > n_G > n_T$, then we have function f, $f : A \longrightarrow 4$, $f : C \longrightarrow 3$, $f : G \longrightarrow 2$, and $f : T \longrightarrow 1$ or $f(A) = 4$, $f(C) = 3$, $f(G) = 2$, and $f(T) = 1$. When using function f, we can write $f(... TGCCAATCGTTGT ...) = ... 1233441231121 ....$ Also, the function f denotes the third coordinate of the *miRNA* nucleotides in a 3D space, (x, y, z). In the third step, we have used a new method for optimizing the algorithm visibility graph in a 3D space (Figure 2).

For each visibility graph of the *miRNA* sequences, we have calculated the statistical property chi-square of triads [28].

If ν independent variables x_i are each normally distributed with mean μ_i and variance σ_i^2, then the quantity known as chi-square (χ^2) is denoted by

$$\chi^2 = \frac{\sum(x_i - \mu_i)^2}{\sigma_i^2}. \tag{1}$$

2.2. A New Method for Optimizing the Algorithm Visibility Graph in 3D Space. We have developed a new algorithm for the construction of visibility graphs in a 3D space [29]. Two arbitrary data values (x_a, y_a) and (x_b, y_b) will have visibility and will consequently become two connected nodes of the associated graph if any other data (x_c, y_c) placed between them fulfil the following relation [30]:

$$y_c < y_b + \frac{(y_a - y_b)(x_b - x_c)}{x_b - x_a}. \tag{2}$$
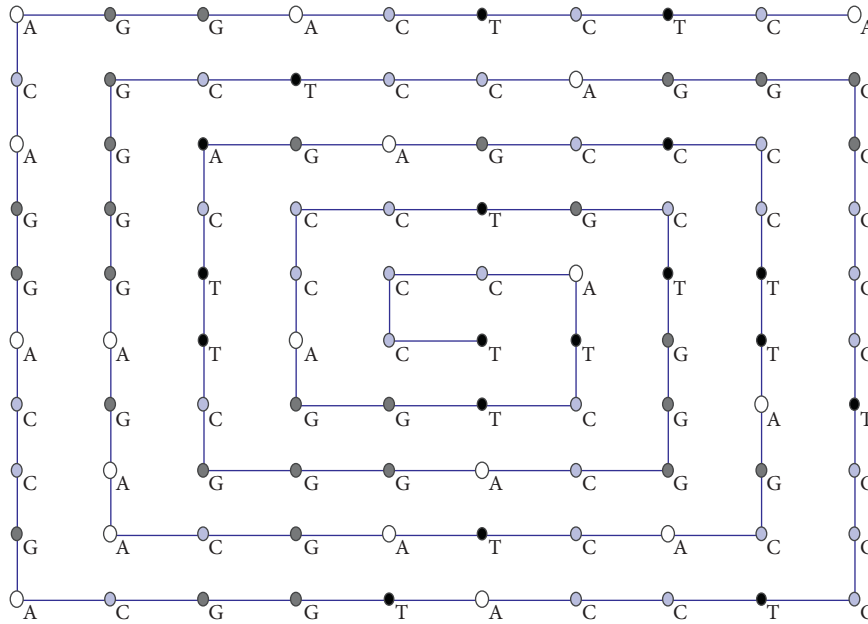
FIGURE 1: Coloured *miRNA* sequences (miR-612 gene) and transformation of each nucleotide of the *DNA* sequences into a 2D array by using a spiral curve.
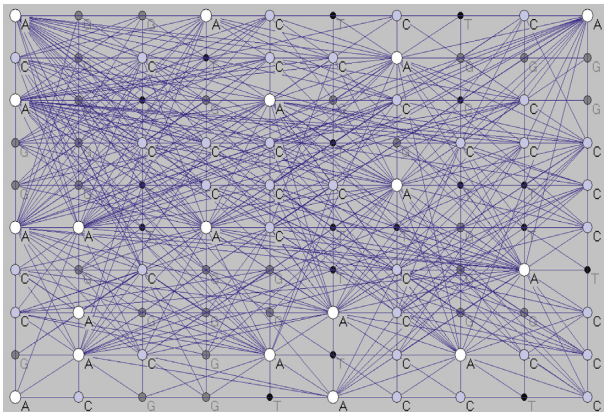
FIGURE 2: Visibility graph of *miRNA* sequences (miR-612 gene).

FIGURE 3: Visibility nodes (blue line) and unrelated nodes (red line).

We wanted to know how to connect the nodes in Figure 3. Nodes $v_{i,j}$ and $v_{k,l}$ of the 3D graph, where $i < k$ and $j < l$, are connected by a link if and only if they are visible.

This means that the path from $v_{i,j}$ to $v_{k,l}$ has no points on the graph. An example is presented in Figure 3, in which the nodnes connected by the blue line are visible to each other and those connected by the red line are an example of unrelated nodes (the straight line that connects the two nodes pierces the graph, which is contrary to the definition of the visibility graph). The following section describes how to construct a 3D visibility graph. The open problem of visibility graphs in a 2D space has thus been presented (Figure 4). Also, we have transformed all 3D points by perpendicular projection on the *xy* plane.

As a first step, we have the 3D points which are transformed into a 2D plane. A graphical solution on a 5×5 grid is given because it provides a better visual representation. Figure 5 presents the nodes of the graph.

In the second step, we have connected neighbouring nodes. Also, node $T_{i,j}(x_i, y_j)$ is connected with nodes $T(x_{i-1}, y_j)$, $T(x_{i+1}, y_j)$, $T(x_i, y_{j+1})$, and $T(x_i, y_{j-1})$ if node $T_{i,j}(x_i, y_j)$ is not located on the edge of a complex network. If node $T_{i,j}(x_i, y_j)$ is on the edge of a complex network, then it is connected with two or three nodes only, as presented in Figure 6.

In the third step, nodes $T_{i,j}(x_i, y_j)$, $T(x_{i+1}, y_j)$, $T(x_{i+1}, y_{j+1})$, and $T(x_i, y_{j+1}, z_{i,j+1})$ present quadrilaterals, and it is possible to see many quadrilaterals in Figure 7. In all quadrilaterals, nodes from a higher z coordinate are connected with other nodes by diagonal lines.

In the fourth step (Figure 8), we have broken the set of all nodes $(x_i, y_i, z_{i,j})$ into two sets. The first set presents all nodes $(x_i, 0, z_{i,j})$, and the second set presents all nodes $(0, y_i, z_{i,j})$.
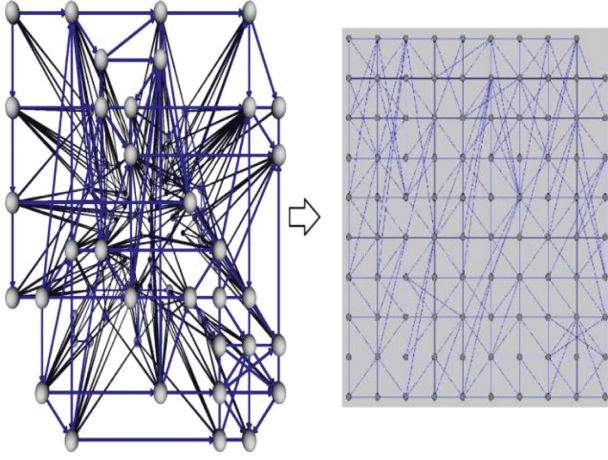
FIGURE 4: Solution of the 3D visibility graph presented as a 3D graph in a 3D space and in a 2D space.
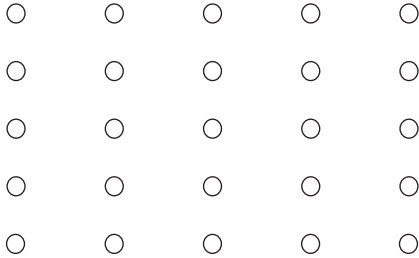
FIGURE 5: 3D nodes which are transformed into a 2D plane.
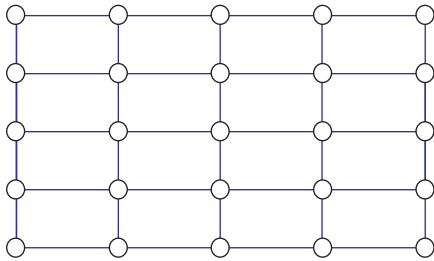
FIGURE 6: Neighbouring nodes.
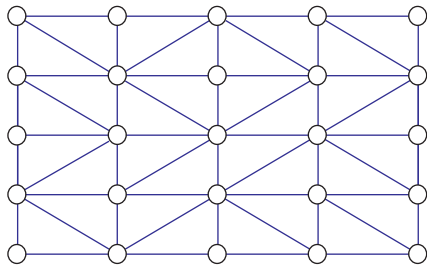
FIGURE 7: Nodes connected with other nodes by diagonal lines.

We have presented those nodes that are visible in the first set and those that are visible in the second set. In the first set, two nodes $T_{i,j}(x_i, y_j, z_{i,j})$ and $T_{k,l}(x_k, y_l, z_{k,l})$ are visible and will consequently become connected nodes on the associated
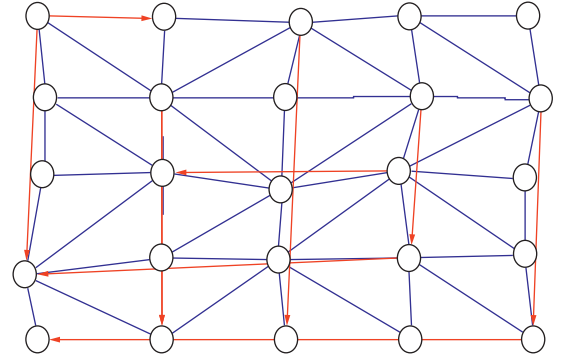
FIGURE 8: Fourth step of visibility graph creation.

graph if any other node $T(x_m, 0, z_{m,0})$ placed between them fulfils the following relation:

$$z_{m,0} < z_{k,l} + \frac{(z_{i,j} - z_{k,l})(x_k - x_m)}{(x_k - x_i)}. \tag{3}$$

In the second set, two nodes $T_{i,j}(x_i, y_j, z_{i,j})$ and $T_{k,l}(x_k, y_l, z_{k,l})$ are visible and will consequently become two connected nodes on the associated graph if any other node $T_{0,n}(0, y_n, z_{0,n})$ placed between them fulfils the following relation:

$$z_{m,0} < z_{k,l} + \frac{(z_{i,j} - z_{k,l})(y_k - y_m)}{(y_k - y_i)}. \tag{4}$$

In the fifth step, we have connected all other visible nodes. Two nodes $T_{i,j}(x_i, y_j, z_{i,j})$ and $T_{k,l}(x_k, y_l, z_{k,l})$ will be visible if no nodes exist on the line between $T_{i,j}(x_i, y_j, z_{i,j})$ and $T_{k,l}(x_k, y_l, z_{k,l})$. Figure 9 presents the solution of the 3D visibility graph on a 5×5 grid.

2.3. Optimizing the Algorithm Visibility Network in 3D Space

(i) All 3D points transform into 2D points $\{(x, y, z) \longrightarrow (x, y)\}$

(ii) Node $T_{i,j}(x_i, y_j)$ is connected with nodes $T(x_{i-1}, y_j)$, $T(x_{i+1}, y_j)$, $T(x_i, y_{j+1})$, and $T(x_i, y_{j-1})$, if node $T_{i,j}(x_i, y_j)$ is not located on the edge of a complex network

(iii) If node $T_{i,j}(x_i, y_j)$ is on the edge of a complex network, then it is connected with two or three nodes only

(iv) Nodes from a higher z coordinate of all nodes $T_{i,j}(x_i, y_j)$, $T(x_{i+1}, y_j)$, $T(x_{i+1}, y_{j+1})$, and $T(x_i, y_{j+1}, z_{i,j+1})$ in quadrilaterals are connected with other nodes by diagonal lines

(v) Two nodes $T_{i,j}(x_i, y_j, z_{i,j})$ and $T_{k,l}(x_k, y_l, z_{k,l})$ are connected, if any other node $T(x_m, 0, z_{m,0})$ placed between them fulfils $z_{m,0} < z_{k,l} + (z_{i,j} - z_{k,l})(x_k - x_m)/(x_k - x_i)$

(vi) Two nodes $T_{i,j}(x_i, y_j, z_{i,j})$ and $T_{k,l}(x_k, y_l, z_{k,l})$ are connected, if any other node $T_{0,n}(0, y_n, z_{0,n})$ placed between them fulfils $z_{m,0} < z_{k,l} + (z_{i,j} - z_{k,l})(y_k - y_m)/(y_k - y_i)$

(vii) Two nodes $T_{i,j}(x_i, y_j, z_{i,j})$ and $T_{k,l}(x_k, y_l, z_{k,l})$ are connected, if no nodes exist on the line between $T_{i,j}(x_i, y_j, z_{i,j})$ and $T_{k,l}(x_k, y_l, z_{k,l})$
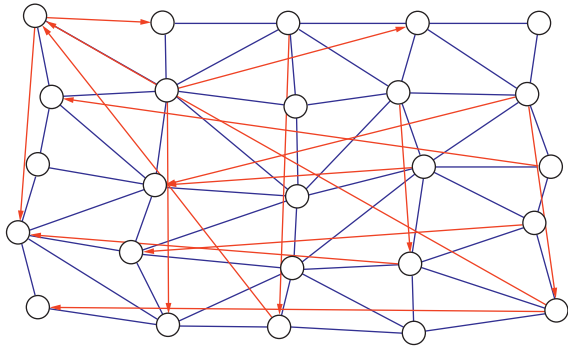
FIGURE 9: Solution of the 3D visibility graph on a 5×5 grid.

2.4. A New n-Hyper Hybrid Method. Hybrid evolutionary computation is a generic, flexible, robust, and versatile method for solving complex global optimization problems and can also be used in practical applications. Only three methods are adopted using intelligent systems, namely, the neural networks NN1 (present prediction with 33%; also, we use 67% of the data for the learning set and 33% for the test set), NN2 (present prediction with 50%; also, we use 50% of the data for the learning set and 50% for the test set), and NN3 (present leave-one-out cross-validation method). We have used a four-layer network with a learning rate of 0.7, moment of learning of 0.6, tolerance of test set of 0.02, and tolerance of learning set of 0.2. Hybrid 1 presents the sequence hybrid method. In this hybrid, methods are connected in series in the direction of the entrance to the method *n*. All methods work independently of the other methods. The results of input method 1 are transferred to input method 2, and the results of input method 2 are transferred to input method 3. Hybrid 2 presents the cyclic hybrid method. In Hybrid 2, methods are connected in series in the direction of the entrance to the method *n*. All methods work independently of the other methods.

The results of input method 1 are transferred to input method 2, the results of input method 2 are transferred to input method 3, and the results of input method 3 are transferred to input method 1. In Hybrid 3, all methods work independently of the other methods. The results of input method 1 are transferred to input method 2, the results of input method 2 are transferred to input method 3, the results of input method 3 are transferred to input method 2, and the results of input method 2 are transferred to input method 1. 1-hyper hybrid methods are similar to hybrid methods. Also, we have repeated the process up to *n*, where $n \in N$. In the end, we have *n*-hyper hybrid methods. Figure 10 presents all the processes of building *n*-hyper hybrids.

3. Results and Discussion

The visibility graph problem itself has long been studied in computational geometry and has been applied to a variety of areas. We present a new method for describing the transformation of 1D *miRNA* sequences into 3D *miRNA* sequences. We combine this method with a new method for optimizing the algorithm visibility graph in a 3D space.

Based on the variation network, several topological properties, such as different types of triads, are calculated for natural *miRNA* sequences. Also, the correlations between types of triads over the variation network are obtained.

It is well known that there is an individual cancer susceptibility despite equivalent environmental exposure, likely due to polymorphisms in genes involved in carcinogenesis. Table 1 presents a list of *miRNA* gene polymorphisms associated with cancer. We use the miR-146a, hsa-mir-149, hsa-mir-196a-2, hsa-mir-608, and hsa-miR-612 genes from the *miRNA* base. MiR-146a is a family of microRNA precursors found in mammals, including humans. MiR-146a is primarily involved in the regulation of inflammation and other processes that function in the innate immune system. Loss of functional miR-146a (and mir-145) could predispose an individual to suffer from chromosome 5q deletion syndrome. MiR-146 has also been reported to be highly upregulated in the osteoarthritis cartilage and could be involved in its pathogenesis. An increasing body of evidence points to a possible role of microRNAs (*miRNAs*) in hereditary cancer syndromes [31, 32].

Recently, variations of the miR-146a gene have drawn increasing attention in cancer etiologies, and altered expression levels have been observed in inflammatory diseases as well as in cancers [33, 34]. MicroRNA hsa-mir-149 is located on chromosome 2. It is an intronic *miRNA* and is located in sense orientation relative to its protein-coding host gene glypican 1 (*GPC1*). Our integrated review of *miRNA*-SNPs revealed that polymorphisms of hsa-mir-149 have previously been associated with increased or decreased risk of seven cancer types: renal cell carcinoma and breast, colorectal, gastric, hepatocellular, papillary, and thyroid cancers. miR149 rs71428439 predisposes its carriers to CCRCC, and miR149 rs71428439 may be a new biomarker for predicting the risk of CCRCC [35]. miR-196 appears to be a vertebrate-specific microRNA and has now been predicted or experimentally confirmed in a wide range of vertebrate species (MIPF0000031). The hairpin precursors are predicted based on base pairing and cross-species conservation—their extents are not known. Many studies demonstrated that the hsa-miR-196a2 rs11614913 SNP was significantly associated with the susceptibility of breast cancer [36–38]. MicroRNA hsa-mir-608 is located on chromosome 10. It is an intronic *miRNA*, located in sense orientation relative to its host gene semaphorin 4G (*SEMA4G*) and in antisense orientation to the mitochondrial ribosomal protein *L43M* (*RPL43*) gene. Several studies [39–46] examined the impact of miR-608 rs4919510C>G on the risk of various cancers, but the results were inconsistent.

Additionally, it has also been associated with increased risk of breast, nasopharyngeal, and papillary thyroid carcinomas. MicroRNA hsa-mir-612 is located on chromosome 11. It is an exonic *miRNA*, located in sense orientation relative to its host gene, nuclear paraspeckle assembly transcript 1 (*NEAT1*). Polymorphism with pre-*miRNA* regions has been associated with B-cell acute lymphoblastic leukemia [47–49].

Also, we have used a new method for optimizing the algorithm visibility graph in a 3D space and a new method
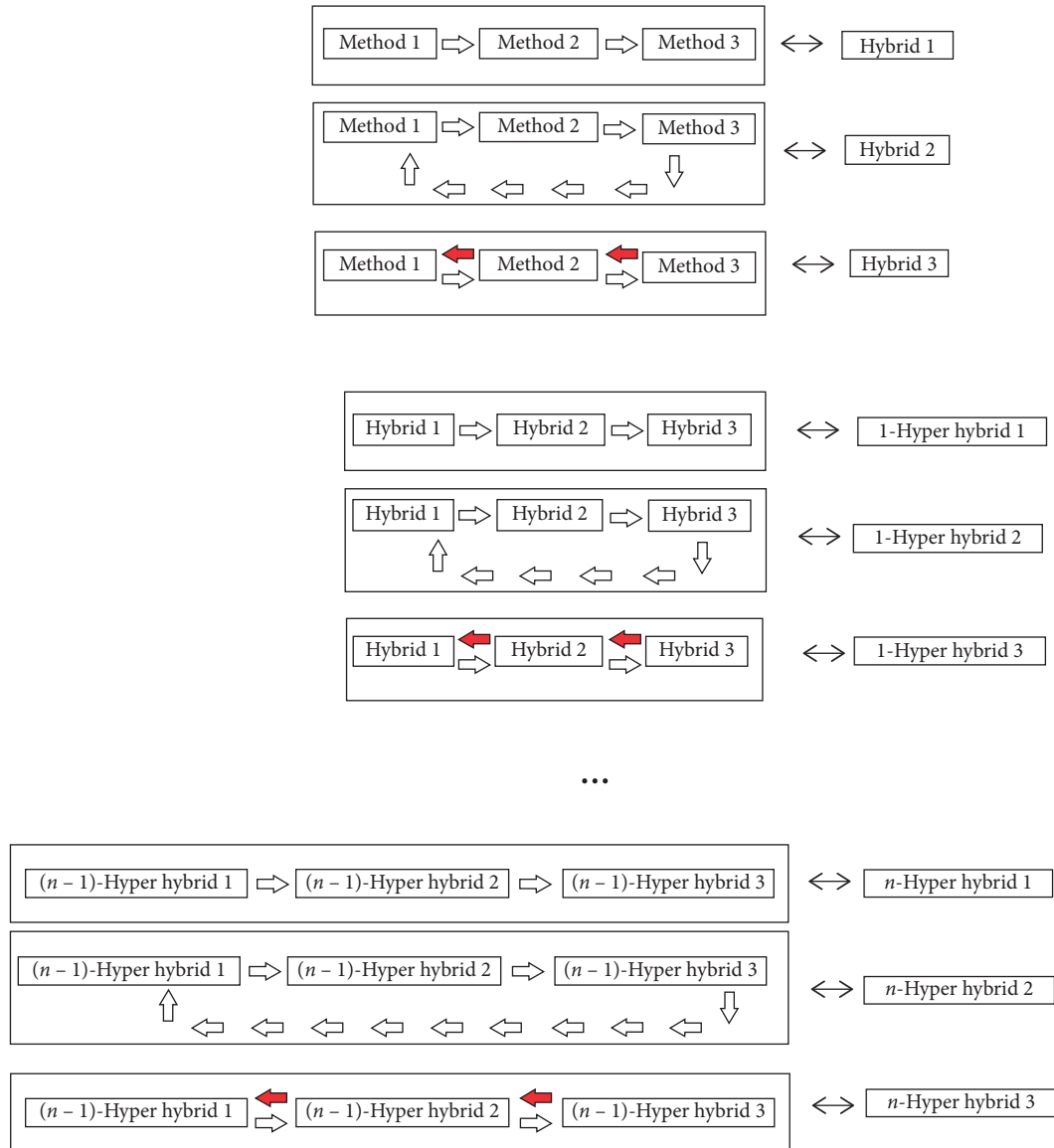
Figure 10: n-Hyper hybrid method.

Table 1: List of *miRNA* gene polymorphisms associated with cancer.

miRNA name	Mark	rs number	Nucleotide change	Cancer type
hsa-mir-146a	D1	2910164	A>G	Increased risk for gastric cancer
hsa-mir-149	D2	71428439	A>G	Increased risk for chronic lymphocytic leukemia
hsa-mir-196a-2	D3	11614913	C>T	Breast cancer
hsa-mir-608	D4	4919510	C>G	Increased risk for breast cancer
hsa-mir-612	D5	12803915	G>A	B-cell acute lymphoblastic leukemia

for *miRNA* cancer pattern recognition. We have determined the topological properties of the triad patterns, in *miRNA* networks [50]. The analysis of triads and the prevalence of different types of triads in populations has been a staple of most network analyses. The input data of neural networks are the topological properties, namely, the triads of *miRNA* patterns and function *f* of sequences of *miRNA*. The output data (*Y*) of the neural data decide whether the *miRNA* is

associated with cancer: if the *miRNA* is not associated with cancer, then 1 is output, else 0 is output.

Table 2 presents the topological properties of the visibility graphs in a 3D space of *DNA* patterns. D1–D5 present the mark of *DNA*. C1–C5 present cancer D1–D5 *DNA*. TP1–TP10 [51] present the types of topological properties of triads: TP1 presents type 1-102, TP2 presents type 1-003, TP3 presents type 2-012, TP4 presents type 6-021C, TP5

TABLE 2: Topological properties of the graph of *miRNA* patterns.

N	TP1	TP2	TP3	TP4	TP5	TP6	Y
D1	15359	126096	17484	489	505	522	0
C1	15372	126020	17446	486	509	525	1
D2	15511	126406	17240	497	514	469	0
C2	15611	126482	17082	490	509	470	1
D3	18875	167586	20947	424	530	522	0
C3	18886	167784	20753	421	524	525	1
D4	15601	125597	18093	402	488	480	0
C4	15603	125596	18085	401	487	481	1
D5	15611	126952	16657	454	493	469	0
C5	15639	126953	16655	453	492	473	1

TABLE 3: Statistical properties of the graph of *miRNA* patterns.

N	X	S1	S2	S3
D1	A	50	395	251228
C1	G	50	396	249883
D2	A	83	392	265112
C2	G	83	390	269117
D3	C	78	425	365987
C3	T	78	423	368945
D4	C	37	399	265911
C4	G	37	399	266532
D5	G	51	386	273025
C5	A	51	386	272976

TABLE 4: Experimental and predicted cancers of *miRNA* patterns.

N	D1	C1	D2	C2	D3	C3	C4	D4	C5	D5
E	0	1	0	1	0	1	0	1	0	1
NN1	1	0	0	0	0	1	1	0	1	0
NN2	1	1	1	1	0	0	0	1	1	1
NN3	0	1	0	1	0	0	0	1	1	1
H1	0	0	1	0	1	1	1	0	1	0
H2	1	1	1	1	1	1	0	1	1	0
H3	0	1	0	0	0	0	1	1	1	1
1-HH1	1	0	1	0	1	1	1	0	0	0
1-HH2	0	1	1	0	0	0	0	1	1	0
1-HH3	1	1	0	1	0	0	0	0	0	1
2-HH1	1	0	0	0	1	1	1	1	1	0
2-HH2	1	1	1	1	1	1	1	0	0	1
2-HH3	0	1	0	0	0	0	0	1	0	1
10-HH1	1	0	0	1	1	1	1	1	1	1
10-HH2	1	0	0	1	0	0	0	1	0	1
10-HH3	1	1	0	1	0	1	0	1	0	1

presents type 7-111D, and TP6 presents type 8-111U. For each constructed variation *miRNA* network, the related topological properties are shown in Table 2. We can see that triad TP1 type 1-102 increases for cancer *miRNA* (rows C1–C5). In the third column, we can see that triad TP3 type 2-012 decreases for cancer *miRNA* (rows C1–C5). In the fourth column, we can see that triad TP4 type 6-021C decreases for cancer *miRNA* (rows C1–C5). In the fifth column, we can see that triad TP6 type 8-111U decreases for cancer *miRNA* (rows C1–C5). Also, these three types of triads present a significant correlation between *miRNA* and cancer *miRNA*.

Table 3 presents the statistical properties of the graph of *miRNA* patterns. X presents the modification of the nucleotide position. S1 presents the place number of changed nucleotides in *miRNA*. S2 presents the number of all edges in the graph. S3 presents the chi-square of triads. In hsa-mir-146a, nucleotide A changes into G on the 50th place, which is described in column S1. The chi-square of the triads increases on hsa-mir-149, hsa-mir-196a-2, and hsa-mir-608 in another decrease.

Table 4 presents the experimental and predicted cancers of *miRNA* patterns. Column C presents the decision of cancer *miRNA* with different methods. In Table 4, rows NN1, NN2, and NN3 present the data predicted with the neural network, rows H1, H2, and H3 present the data predicted with the hybrid system, 1-H1, 1-H2, and 1-H3 present the data predicted with the 1-hyper hybrid system, 2-H1, 2-H2, and 2-H3 present the data predicted with the 2-hyper hybrid system, and 10-H1, 10-H2, and 10-H3 present the data predicted with the 10-hyper hybrid system.

The first row is equal to column Y in Table 2, which determines whether the *miRNA* is cancer or noncancer *miRNA*. Modeling with NN1 presents a 30% precision from the set of measured data, modeling with NN2 presents a 60% precision from the set of measured data, modeling with NN3 presents a 70% precision from the set of measured data, modeling with H1 presents a 30% precision from the set of measured data, modeling with H2 presents a 30% precision from the set of measured data, modeling with H3 presents a 30% precision from the set of measured data, modeling with 1-HH1 presents a 30% precision from the set of measured data, modeling with 1-HH2 presents a 50% precision from the set of measured data, modeling with 1-HH3 presents a 60% precision from the set of measured data, modeling with 2-HH1 presents a 30% precision from the set of measured

data, modeling with 2-HH2 presents a 50% precision from the set of measured data, modeling with 2-HH3 presents a 70% precision from the set of measured data, modeling with 10-HH1 presents a 50% precision from the set of measured data, modeling with 10-HH2 presents a 70% precision from the set of measured data, and modeling with 10-HH3 presents a 90% precision from the set of measured data. Therefore, we can see that 10-HH3 presents the best prediction.

4. Conclusions

In this paper, a novel concept entitled "optimizing the algorithm visibility graph in a 3D space network" is introduced to analyze the relationships between *miRNA* sequences and the type of cancer *miRNA*. We have developed a new method for describing the transformation of 1D *miRNA* sequences into 3D *miRNA* sequences. Using the topological properties of different types of triads, we have determined *miRNA* sequences and the difference between cancer and noncancer *miRNA*. From the results obtained, we are able to conclude that the variation network is a complex network and that it has some dynamic information for further researches. The visibility network in a 3D space, which contains more information than the visibility graph, has been used for the application of *miRNA* pattern

recognition in biomedical engineering. This new method permits to obtain also a physical visualization of the tri-dimensional *miRNA* sequences through additively manufactured techniques.

Finally, we have built a new type of intelligent system, the *n*-hyper hybrid system, that can be used for cancer *miRNA* prediction.

Data Availability

The data in Table 1 are available online at http://www.ncbi.nlm.nih.gov/pmc/articles/PMC4586796/.

Conflicts of Interest

The authors declare that there are no conflicts of interest regarding the publication of this paper.

Acknowledgments

References

[1] Ben-Moshe, O. Hall-Holt, M. J. Katz, and J. S. B. Mitchell, "Computing the visibility graph of points within a polygon," in *Proceedings of the 20th ACM Symposium on Computational Geometry*, pp. 27–35, Brooklyn, NY, USA, June 2004.

[2] D. A. Freedman, *Statistical Models: Theory and Practice*, Cambridge University Press, Cambridge, UK, 2005, ISBN 978-0-521-67105-7.

[3] J. D. Enderle and J. D. Bronzino, *Introduction to Biomedical Engineering*, p. 16, Academic Press, Cambridge, MA, USA, 2012, ISBN 978-0-12-374979-6.

[4] N. Easterbrook, "Alternate presents: the ambivalent historicism of pattern recognition," *Science Fiction Studies*, vol. 33, no. 100, pp. 483–504, 2006, ISSN 0091-7729.

[5] Y. Wernick, Y. Brankov, and S. Strother, "Machine learning in medical imaging," *IEEE Signal Processing Magazine*, vol. 27, no. 4, pp. 25–38, 2010.

[6] E. Hamori, "Graphical representation of long DNA sequences by methods of H curves, current results and future aspects," *Biotechniques*, vol. 7, pp. 710–720, 1989.

[7] B. Liao and T. Wang, "3-D graphical representation of DNA sequences and their numerical characterization," *Journal of Molecular Structure: THEOCHEM*, vol. 681, pp. 209–212, 2004.

[8] A. Nandy, "A new graphical representation and analysis of DNA sequence structure," *Current Science*, vol. 66, pp. 309–314, 1994.

[9] M. Randić, M. Vračko, N. Lerš, and D. Plavšić, "Novel 2-D graphical representation of DNA sequences and their numerical characterization," *Chemical Physics Letters*, vol. 368, pp. 1–6, 2003.

[10] M. Randić, M. Vračko, J. Zupan, and M. Novič, "Compact 2-D graphical representation of DNA," *Chemical Physics Letters*, vol. 373, pp. 558–562, 2003.

[11] V. Ravi, N. Naveen, and M. Pandey, "Hybrid classification and regression models via particle swarm optimization auto associative neural network based nonlinear PCA," *International Journal of Hybrid Intelligent Systems*, vol. 10, no. 3, 2013.

[12] M. El Hafnawi and M. Mysara, *Recurrent Neural Networks and Soft Computing*, Intech, Rijeka, Croatia, 2012.

[13] A. Jameson and J. Riedl, "Introduction to the transactions on interactive intelligent systems," *ACM Transactions on Interactive Intelligent Systems*, vol. 1, no. 1, pp. 1–6, 2011.

[14] P. Gagniuc, P. D. Cristea, R. Tuduce, C. Ionescu-Tîrgovişte, and L. Gavrila, "DNA patterns and evolutionary signatures obtained through Kappa Index of Coincidence," *Revue Roumaine Des Sciences Techniques Série Électrotechnique et Énergétique*, vol. 57, no. 1, pp. 100–109, 2012.

[15] E. M. Zanetti, A. Aldieri, M. Terzini, M. Calì, G. Franceschini, and C. Bignardi, "Additively manufactured custom load-bearing implantable devices: grounds for caution," *Australasian Medical Journal*, vol. 10, no. 8, pp. 694–700, 2017.

[16] D. Speranza, D. Citro, F. Padula et al., "Additive manufacturing techniques for the reconstruction of 3D fetal faces," *Applied Bionics and Biomechanics*, vol. 2017, Article ID 9701762, 10 pages, 2017.

[17] J. De Krijger, C. Rans, B. Van Hooreweder, K. Lietaert, B. Pouran, and A. A. Zadpoor, "Effects of applied stress ratio on the fatigue behavior of additively manufactured porous biomaterials under compressive loading," *Journal of the Mechanical Behavior of Biomedical Materials*, vol. 70, pp. 7–16, 2017.

[18] T. Stanković, J. Mueller, P. Egan, and K. Shea, "A generalized optimality criteria method for optimization of additively manufactured multimaterial lattice structures," *Journal of Mechanical Design*, vol. 137, no. 11, 2015.

[19] B. Alberts, A. Johnson, J. Lewis, M. Raff, K. Roberts, and P. Walter, *Molecular Biology of the Cell, Chapter 4*, DNA, Chromosomes and Genomes, Garland, TX, USA, 6th edition, 2014, ISBN 9780815344322.

[20] R. Nuwer, *Counting All the DNA on Earth*, The New York Times Company, New York, NY, USA, 2015, ISSN 0362-4331.

[21] A. Mashaghi and A. Katan, "A physicist's view of DNA," *De Physicus*, vol. 24e, no. 3, pp. 59–61, 2013, http://arxiv.org/abs/1311.2545v1.

[22] R. N. Irobalieva, J. M. Fogg, D. J. Catanese Jr. et al., "Structural diversity of supercoiled DNA," *Nature Communications*, vol. 6, no. 1, p. 8440, 2015.

[23] S. G. Gregory, K. F. Barlow, K. E. McLay et al., "The DNA sequence and biological annotation of human chromosome 1," *Nature*, vol. 441, no. 7091, pp. 315–321, 2006.

[24] N. J. Kenny, E. K. Namigai, F. Marlétaz, J. H. Hui, and S. M. Shimeld, "Draft genome assemblies and predicted microRNA complements of the intertidal lophotrochozoans *Patella vulgata* (Mollusca, Patellogastropoda) and *Spirobranchus* (*Pomatoceros*) *lamarcki* (Annelida, Serpulida)," *Marine Genomics*, vol. 24, no. 2, pp. 139–146, 2015.

[25] A. Wagschal, "Genome-wide identification of microRNAs regulating cholesterol and triglyceride homeostasis," *Nature Medicine*, vol. 21, no. 11, pp. 1290–1297, 2015.

[26] Y. L. Phua, J. Y. Chu, A. K. Marrone, A. J. Bodnar, S. Sims-Lucas, and J. Ho, "Renal stromal miRNAs are required for normal nephrogenesis and glomerular mesangial survival," *Physiological Reports*, vol. 3, no. 10, article e12537, 2015.

[27] N. D. Amin, G. Bai, J. R Klug et al., "Loss of motoneuron-specific microRNA-218 causes systemic neuromuscular failure," *Science*, vol. 350, no. 6267, pp. 1525–1529, 2015.

[28] H. John, *MC Donald Biological Statistics*, University of Delaware, Sparky House Publishing, Baltimore, MD, USA, 2008.

[29] M. Babič, *Analiza kaljenih materialov s pomočjo fraktalne geometrije*, Doctoral dissertation, University of Maribor, Maribor, Slovenia, 2014.

[30] L. Lacasa, B. Luque, F. Ballesteros, J. Luque, and J. C. Nuno, "From time series to complex networks: the visibility graph," *Proceedings of the National Academy of Sciences*, vol. 105, no. 13, pp. 4972–4975, 2008.

[31] P. Dikeakos, G. Theodoropoulos, S. Rizos, N. Tzanakis, G. Zografos, and M. Gazouli, "Association of the miR-146aC>G, miR-149T>C, and miR-196a2T>C polymorphisms with gastric cancer risk and survival in the Greek population," *Molecular Biology Reports*, vol. 41, no. 2, pp. 1075–1080, 2014.

[32] J. Kupcinskas, T. Wex, A. Link et al., "Gene polymorphisms of micrornas in Helicobacter pylori-induced high risk atrophic gastritis and gastric cancer," *PLoS One*, vol. 9, Article ID e87467, 2014.

[33] M. M. Perry, S. A. Moschos, A. E. Williams, N. J. Shepherd, H. M. Larner-Svensson, and M. A. Lindsay, "Rapid changes in microRNA-146a expression negatively regulate the IL-1beta-induced inflammatory response in human lung alveolar epithelial cells," *Journal of Immunology*, vol. 180, no. 8, pp. 5689–5698, 2008.

[34] L. O. Reis, T. C. Pereira, I. Lopes-Cendes, and U. Ferreira, "MicroRNAs: a new paradigm on molecular urological oncology," *Urology*, vol. 76, no. 3, pp. 521–527, 2010.

[35] Z. Wang, M. Wei, Y. Ren et al., "miR149 rs71428439 polymorphism and risk of clear cell renal cell carcinoma: a case-control study," *Tumour Biology*, vol. 35, no. 12, pp. 12127–12130, 2014.

[36] Z. Hu, J. Liang, Z. Wang et al., "Common genetic variants in pre-microRNAs were associated with increased risk of breast cancer in Chinese women," *Human Mutation*, vol. 30, no. 1, pp. 79–84, 2009.

[37] A. E. Hoffman, T. Zheng, C. Yi et al., "microRNA miR-196a-2 and breast cancer: a genetic and epigenetic association study and functional analysis," *Cancer Research*, vol. 69, no. 14, pp. 5970–5977, 2009.

[38] I. Catucci, R. Yang, P. Verderio et al., "Evaluation of SNPs in miR-146a, miR196a2 and miR-499 as low-penetrance alleles in German and Italian familial breast cancer cases," *Human Mutation*, vol. 31, pp. E1052–E1057, 2010.

[39] Z. M. Dai, H. F. Kang, W. G. Zhang et al., "The associations of single nucleotide polymorphisms in miR196a2, miR-499, and miR-608 with breast cancer susceptibility: a STROBE-compliant observational study," *Medicine*, vol. 95, article e2826, 2016.

[40] W. J. Wei, Y. L. Wang, D. S. Li et al., "Association study of single nucleotide polymorphisms in mature microRNAs and the risk of thyroid tumor in a Chinese population," *Endocrine*, vol. 49, no. 2, pp. 436–444, 2015.

[41] L. Jiao, J. Zhang, Y. Dong et al., "Association between miR-125a rs12976445 and survival in breast cancer patients," *American Journal of Translational Research*, vol. 6, pp. 869–875, 2014.

[42] J. Kupcinskas, I. Bruzaite, S. Juzenas et al., "Lack of association between miR-27a, miR-146a, miR-196a-2, miR-492 and miR-608 gene polymorphisms and colorectal cancer," *Scientific Reports*, vol. 4, no. 1, p. 5993, 2014.

[43] M. Lin, J. Gu, C. Eng et al., "Genetic polymorphisms in microRNA-related genes as predictors of clinical outcomes in colorectal adenocarcinoma patients," *Clinical Cancer Research*, vol. 18, no. 14, pp. 3982–3991, 2012.

[44] B. M. Ryan, A. C. McClary, N. Valeri et al., "rs4919510 in hsa-mir-608 is associated with outcome but not risk of colorectal cancer," *PLoS One*, vol. 7, Article ID e36306, 2012.

[45] R. Wang, J. Zhang, Y. Ma et al., "Association study of miR149 rs2292832 and miR608 rs4919510 and the risk of hepatocellular carcinoma in a largescale population," *Molecular Medicine Reports*, vol. 10, no. 5, pp. 2736–2744, 2014.

[46] P. Zhang, J. Wang, T. Lu et al., "miR-449b rs10061133 and miR-4293 rs12220909 polymorphisms are associated with decreased esophageal squamous cell carcinoma in a Chinese population," *Tumour Biology*, vol. 36, no. 11, pp. 8789–8795, 2015.

[47] A. Gutierrez-Camino, E. Lopez-Lopez, I. Martin-Guerrero et al., "Noncoding RNA-related polymorphisms in pediatric acute lymphoblastic leukemia susceptibility," *Pediatric Research*, vol. 75, no. 6, pp. 767–773, 2014.

[48] Z. Li, W. Zhang, M. Wu et al., "Gene expression-based classification and regulatory networks of pediatric acute lymphoblastic leukemia," *Blood*, vol. 114, no. 20, pp. 4486–4493, 2009.

[49] L. R. Treviño, W. Yang, D. French et al., "Germline genomic variants associated with childhood acute lymphoblastic leukemia," *Nature Genetics*, vol. 41, no. 9, pp. 1001–1005, 2009.

[50] D. Michieletto, D. Marenduzzo, and E. Orlandini, "Is the kinetoplast DNA a percolating network of linked rings at its critical point?," *Physical Biology*, vol. 12, no. 3, article 036001, 2015.

[51] W. De Nooy, A. Mrvar, and V. Batagelj, *Exploratory Social Network Analysis with Pajek*, Cambridge University Press, Structural Analysis in Social Sciences, New York, NY, USA, 2005.

Research Article

Application of 3D Printing Technology for Design and Manufacturing of Customized Components for a Mechanical Stretching Bioreactor

Giovanni Putame [iD],[1] **Mara Terzini** [iD],[1] **Dario Carbonaro,**[1] **Giuseppe Pisani,**[1]
Gianpaolo Serino,[1] **Franca Di Meglio** [iD],[2] **Clotilde Castaldo,**[2] **and Diana Massai** [iD][1]

[1]*PolitoBIOMed Lab, Department of Mechanical and Aerospace Engineering, Politecnico di Torino, Turin 10129, Italy*
[2]*Department of Public Health, University of Naples "Federico II", Naples, Italy*

Correspondence should be addressed to Diana Massai; diana.massai@polito.it

Giovanni Putame and Mara Terzini contributed equally to this work.

Three-dimensional (3D) printing represents a key technology for rapid prototyping, allowing easy, rapid, and low-cost fabrication. In this work, 3D printing was applied for the in-house production of customized components of a mechanical stretching bioreactor with potential application for cardiac tissue engineering and mechanobiology studies. The culture chamber housing and the motor housing were developed as functional permanent parts, aimed at fixing the culture chamber position and at guaranteeing motor watertightness, respectively. Innovative sample holder prototypes were specifically designed and 3D-printed for holding thin and soft biological samples during cyclic stretch culture. The manufactured components were tested in-house and in a cell biology laboratory. Moreover, tensile tests and finite element analysis were performed to investigate the gripping performance of the sample holder prototypes. All the components showed suitable performances in terms of design, ease of use, and functionality. Based on 3D printing, the bioreactor optimization was completely performed in-house, from design to fabrication, enabling customization freedom, strict design-to-prototype timing, and cost and time effective testing, finally boosting the bioreactor development process.

1. Introduction

Tissue engineering aims to generate *in vitro* functional biomimetic substitutes to repair or replace damaged biological tissues and organs [1]. The three main components for *in vitro* tissue development are as follows: (1) cells, responsible for new tissue synthesis; (2) scaffolds, providing physical and structural support and biochemical cues for cells; and (3) biomimetic *in vitro* culture environment, for replicating the *in vivo* milieu and signals [2]. Numerous mechanobiology studies demonstrated that, in addition to cells, biomaterials, and chemical signals, physical stimuli play a fundamental role during the development of native tissues and for the generation of tissue engineered substitutes [3–7]. In this perspective, bioreactors are innovative

and technological devices appositely engineered for providing *in vivo*-like culture conditions, by coping with limitations of conventional two-dimensional, static, and manual cell/tissue cultures. In particular, bioreactors are designed to culture cells/tissues in a three-dimensional (3D) environment, under monitored and controlled conditions (e.g., pH, O_2, glucose, and lactate) and user-defined physical stimuli (e.g., stretching, compression, electrical pulse, and fluid shear stress). They can be used both as culture model systems, to investigate *in vitro* cell/tissue development and the effects of chemicophysical stimuli on tissue maturation, or as production systems, for finally directing stem cell fate and engineered tissue formation *in vitro* [8–14]. Moreover, when equipped with technological solutions for real-time closed-loop monitoring and control of culture conditions,

bioreactors could allow for automated culture processes, leading to high quality, reproducible, and standardized cell/tissue cultures as required by industrial and clinical applications.

Since this is a relatively young and multifaceted research field, bioreactors are often high-cost customized devices designed and developed in-house, but usually prototypes and/or permanent parts are outsource manufactured by external companies. Indeed, they must satisfy strict design, quality, and functionality requirements imposed by the Good Laboratory Practices (GLP) adopted in cell biology/tissue engineering laboratories [15]. In particular, in such laboratories cell/tissue cultures are performed by using sterile equipment, working under laminar flow hood for sterility maintenance, and using incubators for temperature (37°C), humidity (85–95%), and carbon dioxide (5%) maintenance. Therefore, bioreactors should guarantee biocompatibility, sterilizability (preferentially by autoclave), ease of assembling and use, watertightness, and reliability for long-term culture processes in the incubator [16]. In this scenario, three-dimensional (3D) printing, based on computer-controlled layer-by-layer deposition of materials, represents a key technology both for rapid prototyping of components to be tested and for fabricating permanent functional parts. Indeed, unlike conventional subtractive machining processes (i.e., milling, turning, and drilling), 3D printing allows easy, rapid, and low-cost manufacturing of complex geometries by single-step processes. This entails clear advantages for the definition of the final bioreactor design and during the fabrication phase, in terms of design customization and flexibility, in-house manufacturing, and reduced times and costs for production and testing, leading to an overall improvement of the bioreactor development process. Recently, a small but growing number of groups are adopting 3D printing for the development of customized culture systems. Raveling and colleagues used fused deposition modelling (FDM) to manufacture a low-cost, highly customizable mechanical bioreactor for investigating soft tissue mechanics [17]. Schneidereit et al. 3D-printed a culture chamber with included electrodes for electrical stimulation and parallel microscopic evaluation [18]. Smith and colleagues developed a 3D-printed bioreactor platform designed for 3D-bioprinted tissue construct culture, perfusion, observation, and analysis [19].

In this work, we applied FDM-oriented design and manufacturing for the optimization of a recently developed mechanical stretching bioreactor with potential application for cardiac tissue engineering and mechanobiology studies, designed to provide cyclic uniaxial stretch to biological samples [20]. In particular, 3D printing was used to in-house fabricate the bioreactor culture chamber housing and the motor housing, functional parts designed to fix the culture chamber position and to guarantee motor watertightness, respectively. Moreover, innovative sample holder prototypes were specifically designed and 3D-printed for holding thin and soft biological samples and experimentally and computationally tested in terms of ease of use and gripping performance, before final production with biocompatible and autoclavable materials. Assembling, usability and functionality tests confirmed the excellent performances of all 3D-printed components, which strongly contributed to the bioreactor development process.

2. Materials and Methods

2.1. Bioreactor Setup. The bioreactor, which has been designed to be incubated and has been optimized with respect to a previous version [20], is composed of three modular subsystems: the culture unit, the motor unit and the control unit (Figure 1). The culture unit is dedicated to house the samples for sterile culture under mechanical stimulation. The motor unit, which has been modified and reduced in size, houses the motor, which is connected to the culture unit via a shaft for providing uniaxial mechanical stimulation. The control unit, whose development goes beyond the purpose of this study, enables the setting of the mechanical stimulation parameters and the motor control and must be located outside the incubator. In this setup, four bioreactor components (culture chamber housing, motor housing, and two sample holders) were designed following specific requirements and manufactured by FDM to be used either as permanent functional parts (culture chamber housing and motor housing) within the incubator or as working prototypes (sample holders) to test functionality and ease of use before to produce the final components in biocompatible and autoclavable materials.

2.2. FDM-Oriented Design and Manufacturing

2.2.1. Design Requirements. The bioreactor design process was guided by the need to satisfy specific design requirements in terms of GLP-compliance, use, performance, and FDM manufacturing (Table 1). In particular, the whole bioreactor system should meet the GLP principles, which are rules and criteria for a quality system of organisational and working conditions in research laboratories to ensure consistency, reliability, reproducibility, and quality of nonclinical health studies [15]. Therefore, the bioreactor should be easy to assemble, to use, and to clean with the standard equipment (laminar hood, autoclave, incubator, gloves, and tweezers) and procedures of a cell biology/tissue engineering laboratory. With regard to dimensional requirements, the bioreactor must be placed on an incubator shelf (max 40 cm × 50 cm × 30 cm), and moreover, the new FDM-printed components must couple with preexisting parts (i.e., culture chamber, motor shaft, and connections). Due to the high humidity levels within the incubator, watertightness is mandatory in case of electrical and electronic parts for assuring reliable operation, especially for long-term culture processes. Modularity requirement comes from the need to guarantee accessibility and ease of use during assembling/disassembling and cleaning procedures, and together with customization, it allows providing adaptable, interchangeable, and scalable solutions for different cell/tissue applications to be used with the same bioreactor system. In particular, in this case, a specific design requirement for the gripping system came from the need to hold and culture under cyclic stretch thin and soft
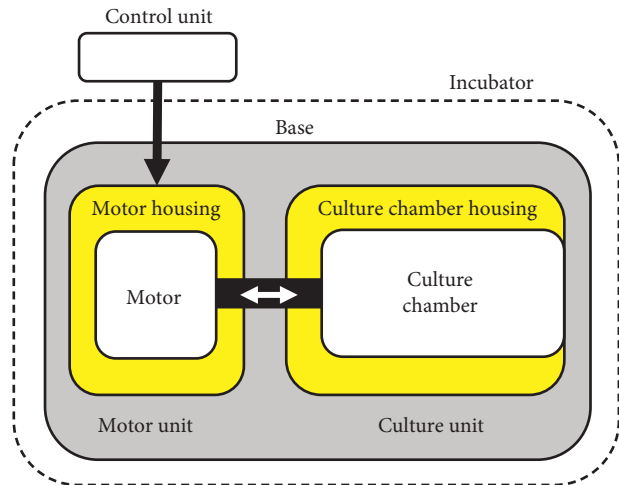
FIGURE 1: Schematic drawing of the bioreactor setup with the three modular subsystems: the culture unit, the motor unit, and the control unit. The functional FDM-printed components are represented in yellow. Both the motor housing and the culture chamber housing are bolted on a rigid planar base (represented in grey).

TABLE 1: Design requirements.

Design requirements
Bioreactor system
Ease of assembling, use, and cleaning
Small footprint (max 40 cm × 50 cm × 30 cm to fit in an incubator)
Watertightness (85–95% humidity in an incubator)
Modularity and customization
Reliability of culture processes (weeks in an incubator)
Culture chamber components (in contact with the culture medium and/or cells/tissues)
Cytocompatibility
Sterilizability (preferably by an autoclave)
Water/sterility tightness
Ease of assembly/disassembly under laminar flow hood
Ease of cleaning
FDM manufacturing
Supported and unsupported walls minimum thickness (0.66 mm)
Maximum overhang inclination (45°)
Minimum diameter of vertical holes (2 mm)
Backlash between connecting parts (0.1 mm)

substrates/tissues for cardiac tissue engineering and mechanobiology studies. Finally, as regards the already existing culture chamber, where the components are in direct contact with the culture medium and/or with cells/tissues, the specific design requirements listed in Table 1 were previously fulfilled [20].

In parallel, because of the need to produce in-house customized components by a rapid, flexible, and low-cost process, FDM technology was selected for manufacturing. The FDM technology, developed by Stratasys Inc. (Eden Prairie, Minnesota, United States), is based on a filament of the thermoplastic material, and most commonly ABS [21], heated over its melting point, extruded through a nozzle and finally deposited to form structures composed of solidified layers [22]. Specific manufacturing design requirements are imposed by FDM technology, for which limitations exist in terms of minimum manufacturable size and features, such as holes and engraved details [23]. In detail, the thickness of supported and unsupported walls should be at least 0.66 mm. As regards the overhang inclination, for printability reasons, the maximum value is 45°; however, in this work, inclined surfaces and consequent stair-stepping effect were avoided for ease of cleaning needs. The minimum diameter for vertical holes is 2 mm, and the backlash between connecting parts is set equal to 0.1 mm. Lastly, threaded holes were avoided due to possible wear and tear caused by repeated assembling procedures.

2.2.2. Design and Manufacturing. Taking into account the previously described design requirements, the culture chamber housing, the motor housing, and the sample holder prototypes were designed using the commercial computer-aided design (CAD) software Solidworks 2017 (Dassault Systemes, Vélizy-Villacoublay, France). In detail, the culture chamber housing was designed to fix the position of the removable culture chamber, to maintain a precise alignment and a defined distance between the culture unit and the motor unit and to fit the whole system within the incubator shelf. The motor housing was designed to be a watertight box protecting motor and electrical connections from incubator humidity. The sample holder prototypes, to be mounted within the culture chamber, were specifically designed to test the functionality of an innovative gripping system aimed at holding thin and soft biological samples [24, 25].

The FDM manufacturing was performed uploading the design STL files on the printer software CatalystEX and using the 3D printer Stratasys uPrint SE Plus (Stratasys, Eden Prairie, Minnesota, United States). The ABS plus-P430 thermoplastic printing material (Stratasys, Eden Prairie, Minnesota, United States), durable enough to perform virtually the same as production parts (as declared by the manufacturer, physical properties listed in Table 2 [26]), was used in combination with the SR30 soluble support material. All components were printed setting the minimum layer thickness (0.254 mm) to minimize surface roughness and to optimize accuracy, imposing backlash (0.1 mm) to avoid interference during the mounting procedure and setting the solid fill option and the smart support strategy. For each component, the printing direction was defined balancing the resolution on circular features and the support material/time consumption, leading to different printing durations (the printer can build faster across the XY plane than it can along the Z axis) [27]. The support material was then removed manually, avoiding the use of the detergent bath. Figure 2 shows the adopted design-to-manufacturing workflow. Printed components were then connected through nuts and bolts.

2.3. Testing. The 3D-printed components were tested in terms of assembly, coupling, and functionality of the whole bioreactor setup. Preliminary tests were performed in-house. In particular, the coupling between the culture chamber and the chamber housing was checked, and this

TABLE 2: Physical properties of ABS plus-P430 [26].

Mechanical properties*	
Yield stress (MPa)	31.0
Ultimate stress (MPa)	33.0
Elastic modulus (MPa)	2.2
Elongation at break (%)	6
Elongation at yield (%)	2
Thermal properties	
Glass transition temperature (°C)	108

*Uniaxial tensile tests performed along the printing direction of the specimens.

latter was screwed on the rigid planar base. The motor housing was assembled and screwed on the rigid planar base. The sample holder prototypes were assembled and mounted within the culture chamber. The culture chamber mobile shaft was connected to the motor unit. Finally, the control unit was electrically connected to the motor unit, and an explanatory cyclic mechanical stimulation (displacement = 1 mm and frequency = 1 Hz) was run. In this phase, the following features were checked: coupling with preexisting components, holes alignment, culture unit, and motor unit alignment. Successively, trained laboratory operators tested the whole bioreactor system in a cell biology laboratory. In detail, the bioreactor culture chamber components were autoclaved, and the assembling procedure of the whole system was performed under laminar flow hood. To test the bioreactor functionality (including sterility maintenance), the culture chamber was filled with the culture medium, the assembled system was placed in an incubator, and the mechanical stimulation was switched on and run for 5 days. During the stimulation process, possible interferences between moving and fixed components were checked. At the end of the test, the watertightness of the motor unit, potential deformations of the 3D-printed components, and possible contamination were assessed.

Finally, the gripping performance of the sample holder prototypes was assessed performing both uniaxial tensile tests and finite element analysis (FEA) and compared with the performance of commercial titanium grips appositely designed for soft tissue characterization (TA Instruments, Inc, New Castle, DE, United States). For the experimental tests, one sample holder prototype was mounted on the material testing machine QTest10 (MTS Systems Corporation, Eden Prairie, Minnesota, United States) together with a contra-lateral commercial titanium grip. In order to assess the suitability of the prototype to hold thin and soft biological samples, two samples of human decellularized skin (length = 10 mm, width = 5 mm, and thickness = 0.6 mm) [28] were clamped between the sample holder and the titanium grip and then uniaxially stretched imposing a straining rate of $3.2\% \, s^{-1}$ (gauge length = 5 mm) [29]. For comparison purposes, two additional samples were tested imposing the same conditions but using two titanium grips. Both loads and displacements were recorded to monitor the curve trend [30] because decreases in slope or sudden steps are indicators of gripping failure and slipping.

In addition, to investigate the contact pressure distributions exerted by the sample holder or the titanium grip configuration on the clamped samples, nonlinear FE analyses were performed using the software HyperMesh/HyperView 2017 (Altair Engineering, Troy, Michigan) and Abaqus 2017 (Dassault Systemes, Vélizy-Villacoublay, France). The sample holder and the titanium grip were modelled as rigid bodies, and only the surfaces in contact with the sample were discretized with the R3D4 elements. The sample was modelled as a rectangular parallelepiped (width = 5 mm and thickness = 0.6 mm), meshed with C3D8 elements, and considered as a linear-elastic material. To compare contact pressure results, the same sample contact surface (width = 5 mm and length = 3.2 mm) was modelled for both configurations. A frictionless contact between sample holder/grip surface and the sample was imposed. A force of 1 N was applied to the mobile part of the sample holder/grip, while the respective fixed parts were totally constrained.

3. Results and Discussion

3.1. FDM-Oriented Design and Manufacturing. The culture chamber housing is a L-shaped chassis (width = 118 mm, length = 147 mm and height = 78 mm) composed of a planar base to house the culture chamber, two lateral edges, and a vertical wall designed to maintain the alignment and a defined distance between the culture unit and the motor unit (Figure 3). The coupling between the culture chamber and its housing is performed by sliding the culture chamber into the housing and fixing it through a screw (Figure 3).

The motor housing is a watertight box (length = 130 mm, width = 95 mm, and height = 65.5 mm) designed for protecting the motor and electrical connections from incubator humidity and consists of two main parts: a container and a lid (Figure 4). To fix the lid on the container, four screw and nut sets are adopted. To guarantee watertightness, (i) a silicon gasket is placed between the container and the lid, (ii) a waterproof socket (including a gasket) for the connection with the control unit cable is screwed in a counterbore on the container lateral wall, and (iii) a rubber bellow for the motor through shaft fits on a protrusion of the container wall in front of the culture unit.

Guided by the design requirement of gripping thin and soft samples and inspired by commercial solutions for testing thin wires, the innovative design of the sample holder prototypes (maximum width = 54 mm, maximum height = 39.5 mm) is based on a guided moving cylindrical rod that, when pushed by a central screw connected to a planar guide, slides along two lateral guides against a grip base (Figure 5(a)). For gripping, the moving rod pushes the sample end against the grip base causing the sample wrapping around the cylindrical rod. To ensure a stable gripping of the sample, the proper coupling between the moving rod and the grip base is guaranteed by an appositely-sized hemicylindrical groove on the grip base (Figures 5(a), and 5(c)). The sample holder allows the gripping of samples with a maximum width of 20 mm. A maximum open position of 6.2 mm allows the positioning of the sample by using tweezers (Figure 5(b)). To fix the lateral guides on the grip base, dedicated cavities were designed to accommodate threaded nuts (Figure 5(b)).

Figure 6 shows the assembled bioreactor system (with the exception of the control unit), composed of the culture
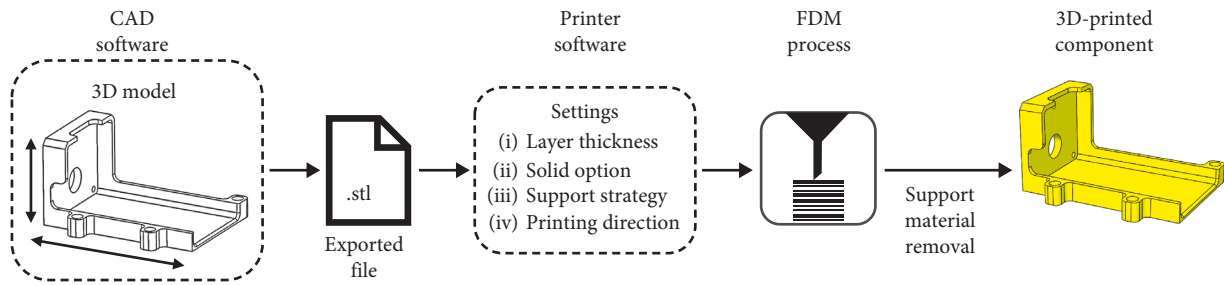
FIGURE 2: Design-to-manufacturing workflow.
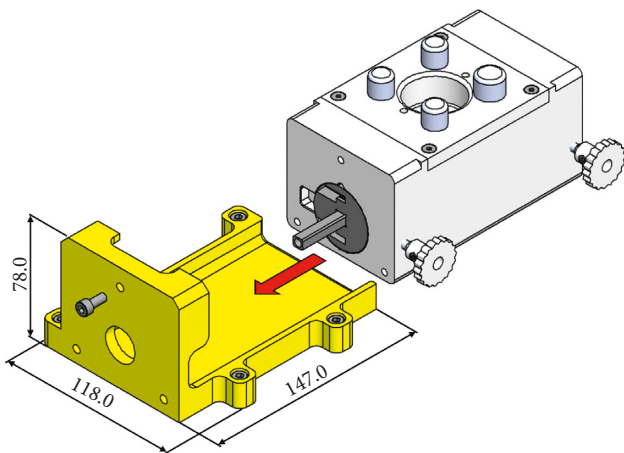
FIGURE 3: 3D model of the culture chamber and its housing (in yellow). The red arrow shows the sliding direction for the coupling.
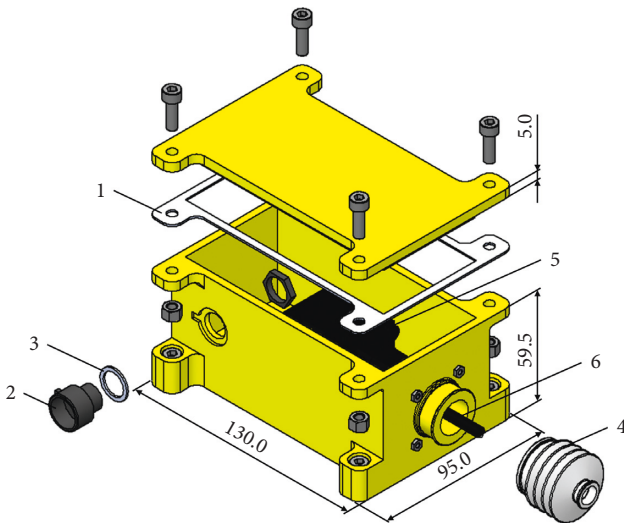
FIGURE 4: Exploded view of the 3D model of the motor unit. 1, silicon gasket; 2, waterproof socket; 3, gasket; 4, rubber bellow; 5, motor; 6, motor through shaft.

unit and the motor unit screwed on the rigid planar base (length = 342 mm and width = 128 mm). The culture chamber is mounted on its housing and connected through a shaft to the motor placed inside the motor housing. The gripping system within the culture chamber consists of one

mobile sample holder, screwed on the motor through-shaft, and a fixed sample holder screwed at the opposite culture chamber wall (Figure 6(b)).

The FDM manufacturing process required different durations depending on the printed component. For instance, notwithstanding their similar volumes, the printing process of the moving rod resulted more than four times longer than the process for manufacturing the planar guide, mainly due to the printing direction. Indeed, to guarantee the highest resolution on the rod surface, this component was printed with its long axis parallel to the Z printer axis. In Table 3 are listed printing times, printing material volumes, and support material volumes used for each component.

3.2. Testing. The in-house assembling of the 3D-printed components and their coupling with preexisting bioreactor parts did not show any issues. In detail, the position of the holes allowed screwing easily both the culture chamber housing and the motor housing on the rigid planar base. Similarly, the motor housing lid was easily coupled to the motor container. The culture chamber was slid into its housing, and the correct alignment with the motor unit was verified. The sample holder prototypes were assembled and mounted within the culture chamber. For all components, a suitable coupling with preexisting parts was confirmed.

Ease of use and performance of the whole bioreactor system were tested in a cell culture laboratory by trained laboratory operators. The assembling of the bioreactor components under laminar flow hood was easy and fast (Figure 7(a)). A performance test was carried out placing the bioreactor in incubator and running the mechanical stimulation for 5 days (Figure 7(b)). During working conditions, the system did not show any malfunction, no interferences between moving and fixed components were noticed, and the watertightness of the motor housing was confirmed. At the end of the test, neither deformations nor culture medium contamination was observed.

To test the gripping performance of the novel sample holder prototypes, uniaxial tensile tests of biological samples were performed using the testing machine QTest10 and two different gripping configurations: (i) sample holder–titanium grip (Figure 8(a)); (ii) titanium grip–titanium grip (Figure 8(b)). In the first configuration, each sample was easily positioned on the sample holder by using tweezers and firmly clamped by acting on the central screw, with the
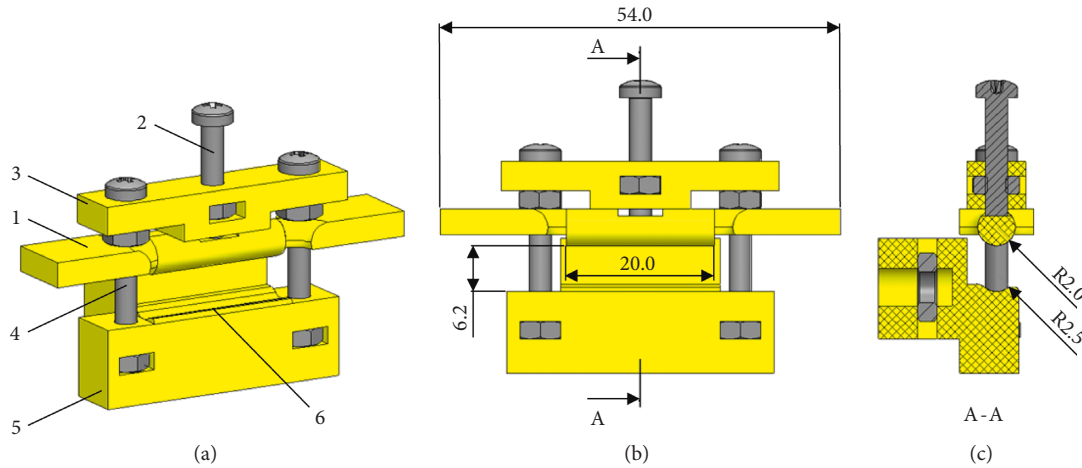
FIGURE 5: 3D model of the sample holder prototype in open configuration. (a) Axonometric projection: 1, moving rod; 2, central screw; 3, planar guide; 4, lateral guide; 5, grip base; 6, hemicylindrical groove. (b) Front view. (c) Section view.
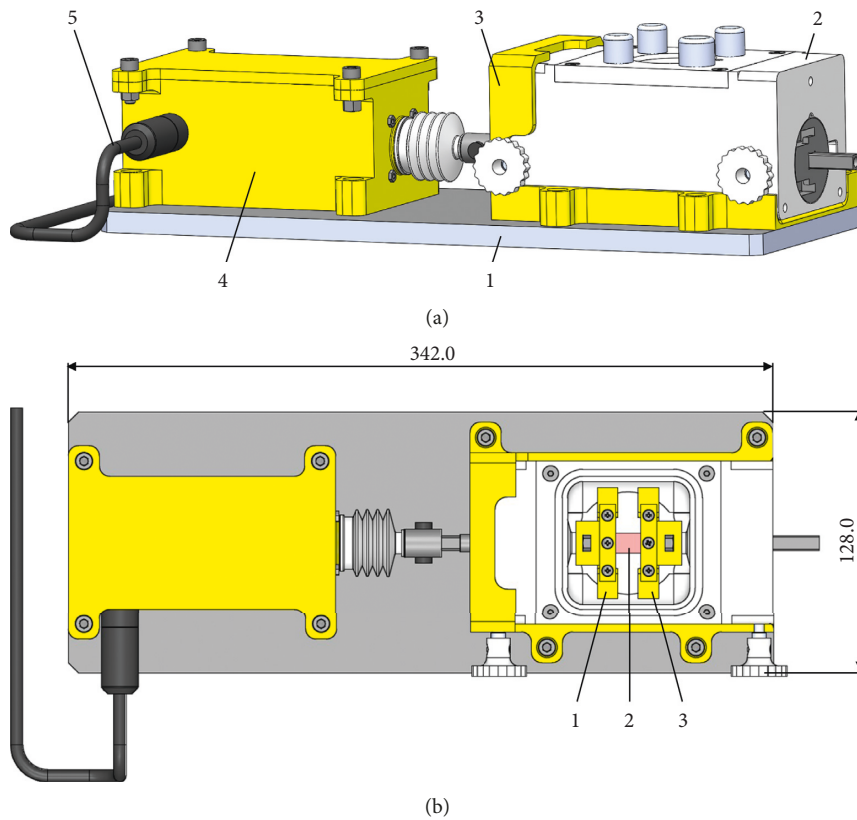
FIGURE 6: 3D model of the whole bioreactor system. (a) Axonometric projection of the bioreactor with the following parts: 1, rigid planar base; 2, culture chamber; 3, culture chamber housing; 4, motor housing; 5, control unit cable. (b) Top view of the bioreactor 3D model without the culture chamber lid: 1, mobile sample holder; 2, sample; 3, fixed sample holder.

TABLE 3: Printing time, printing material volume, and support material volume for each 3D-printed component.

Component	Part	Printing time (h:min)	Printing material volume (cm^3)	Support material volume (cm^3)
Motor housing	Container	11:19	177.8	2.1
	Lid	2:29	83.5	7.8
Culture chamber housing		9:00	133.9	27.6
Sample holder	Moving rod	1:43	1.6	2.4
	Grip base	1:50	7.5	2.8
	Planar guide	0:23	1.8	0.6

(a)

(b)

Figure 7: Assembled bioreactor: (a) top view of the bioreactor setup; (b) bioreactor within the incubator for the 5-day performance test.

(a)

(b)

(c)
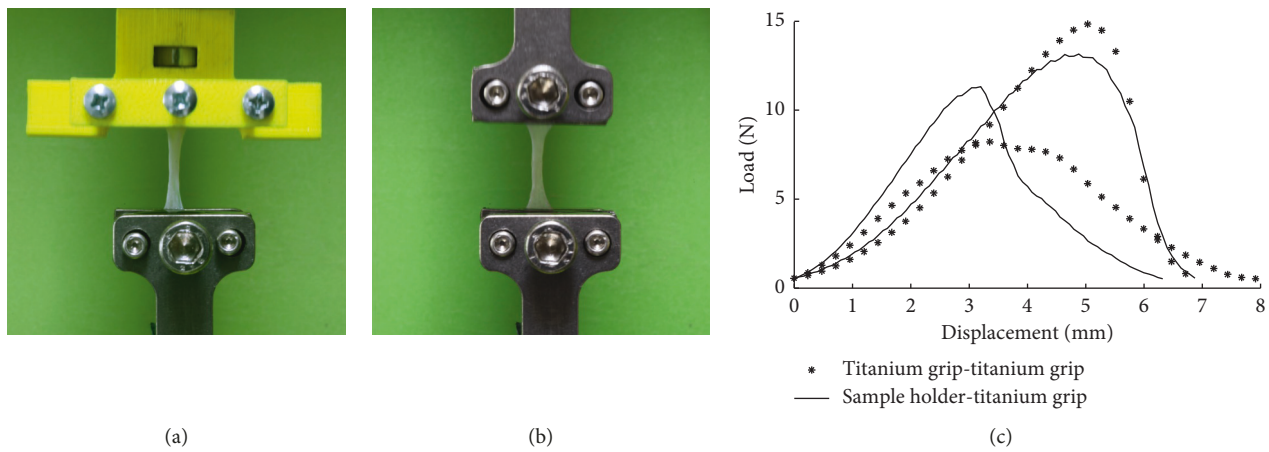
Figure 8: Gripping performance test of the sample holder prototype: setup of the testing machine QTest10 with the biological sample clamped by (a) the sample holder-titanium grip configuration and (b) the titanium grip-titanium grip configuration; (c) load-displacement curves obtained from the tensile tests performed with both configurations.

sample end wrapped around the moving rod. During the tests, no sample slipping was observed, and at rupture, each sample broke in the central cross section, confirming the proper load distribution in the gripping area. Similar results were obtained with the second configuration. Figure 8(c) shows the four load-displacement curves, realigned at 0.5 N load, obtained from the tensile tests performed with both configurations. Besides the observable intra-variability of mechanical behaviour typical of soft tissues, each curve increases smoothly up to rupture, with no sudden slope decrease, for both configurations. Tensile tests confirmed that the sample holder prototype is comparable to the commercial titanium grip in terms of gripping performance, and it is suitable in terms of FDM-based manufacturing.

In addition, FE analyses were performed to investigate the distributions of the contact pressure on the sample surface clamped by the sample holder or the titanium grip configurations. The FE results show that the sample holder configuration guarantees a more uniform contact pressure distribution on the sample surface (Figures 9(a) and 9(c); maximum contact pressure = 0.097 MPa) compared to the titanium grip, which causes a pressure concentration along the grip external edge (Figures 9(b) and 9(d); maximum contact pressure = 0.222 MPa). In case of thin and

soft samples, contact pressure concentrations should be absolutely prevented since they could trigger sample break. The FEA results provided further confirmation of the suitability of the sample holder design.

With regard to possible limitations, components fabricated by FDM technology can be characterized by anisotropic behaviour, high surface roughness, poor geometry accuracy, and the presence of internal defects [31]. However, in this work, the manufactured components and the performed tests were not affected by such limitations.

4. Conclusions

In this work, 3D printing was applied for in-house designing and producing two functional parts and two prototype components for a mechanical stretching bioreactor with potential application for cardiac tissue engineering and mechanobiology studies. In detail, the 3D-printed culture chamber housing and motor housing met the design requirements of ease of use and functionality, guaranteeing alignment between the culture unit and the motor unit as well as the motor unit watertightness. The innovative sample holder prototypes, designed specifically for holding thin and soft biological samples, demonstrated their excellent performance in terms of ease of
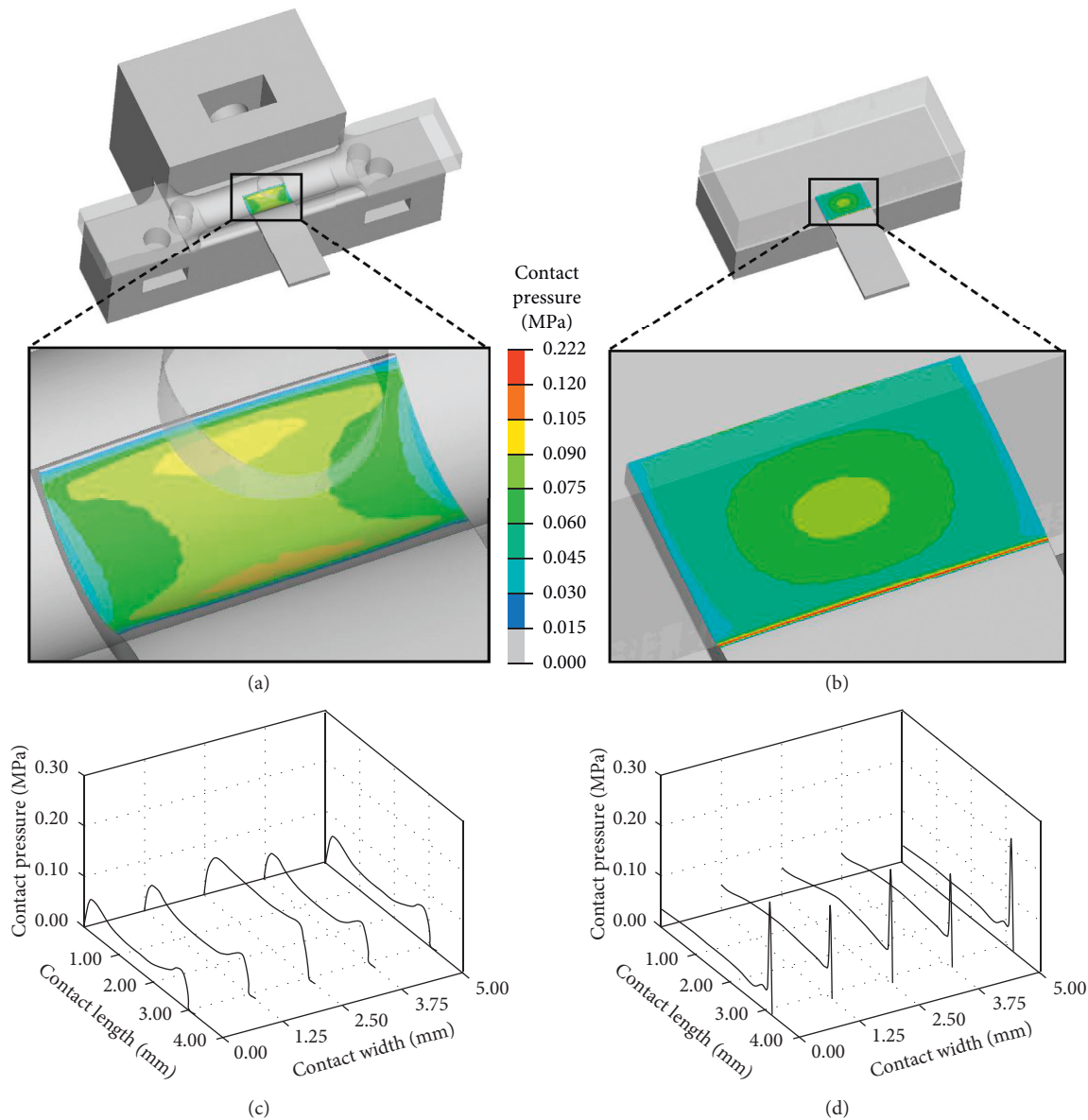
FIGURE 9: FEA results on contact pressure distributions on the sample surface exerted by (a, c) sample holder configuration and (b, d) titanium grip configuration.

use and gripping, thus confirming the suitability of the design for future manufacturing in biocompatible and autoclavable materials. This approach enabled to perform in-house the entire bioreactor optimization process, from design to fabrication, providing customization freedom, strict design-to-prototype timing, and rapid and inexpensive testing. In conclusion, 3D printing technology allowed to manufacture low-cost, customized bioreactor components, and to reduce the risk of failure at later stages in new concept development, improving design and manufacturing process efficiency. In the next future, the increasing performances of printable materials in terms of biocompatibility, autoclavability, and transparency will further boost the development of low-cost bioreactors and customized culture devices. This will lead to more reproducible, standardized, and efficient basic studies, with

great potential for the future routine production of tissue engineering strategies for clinical application.

Data Availability

The data used to support the findings of this study are available from the corresponding author upon request.

Conflicts of Interest

The authors declare that there are no conflicts of interest regarding the publication of this paper.

Authors' Contributions

G. P. and M. T. contributed equally to this work. G. P., M. T., D. C., and D. M. conceived the design of the 3D-printed

components and their testing. G. P. and D. C. 3D-printed the components. F. D. M. and C. C. prepared the biological samples for the uniaxial tensile tests and tested the system in a cell biology laboratory. M. T., G. P., and G. S. performed the experimental testing. D. C. performed the finite element analysis. M. T., G. P., and G. Pi. analyzed the data. D. M. and D. C. reviewed the current state of the art. G. P., M. T., and D. C. prepared the figures. D. M. conceived and coordinated the study. G. P., M. T., and D. M. wrote the manuscript.

Acknowledgments

References

[1] A. S. Goldstein and G. Christ, "Functional tissue engineering requires bioreactor strategies," *Tissue Engineering Part A*, vol. 15, no. 4, pp. 739-740, 2009.

[2] F. Lyons, S. Partap, and F. J. O'Brien, "Part 1: scaffolds and surfaces," *Technology and Health Care*, vol. 16, no. 4, pp. 305–317, 2008.

[3] A. Goldstein, T. M. Juarez, C. D. Helmke, M. C. Gustin, and A. G. Mikos, "Effect of convection on osteoblastic cell growth and function in biodegradable polymer foam scaffolds," *Biomaterials*, vol. 22, no. 11, pp. 1279–1288, 2001.

[4] G. Cerino, E. Gaudiello, T. Grussenmeyer et al., "Three dimensional multi-cellular muscle-like tissue engineering in perfusion-based bioreactors," *Biotechnology and Bioengineering*, vol. 113, no. 1, pp. 226–236, 2016.

[5] N. Y. Liaw and W.-H. Zimmermann, "Mechanical stimulation in the engineering of heart muscle," *Advanced Drug Delivery Reviews*, vol. 96, pp. 156–160, 2016.

[6] W. L. Stoppel, D. L. Kaplan, and L. D. Black III, "Electrical and mechanical stimulation of cardiac cells and tissue constructs," *Advanced Drug Delivery Reviews*, vol. 96, pp. 135–155, 2016.

[7] R. F. Canadas, A. P. Marques, R. L. Reis, and J. M. Oliveira, "Bioreactors and microfluidics for osteochondral interface maturation," in *Osteochondral Tissue Engineering*, vol. 1056, pp. 395–420, Springer, Cham, Switzerland, 2018.

[8] I. Martin, D. Wendt, and M. Heberer, "The role of bioreactors in tissue engineering," *Trends in Biotechnology*, vol. 22, no. 2, pp. 80–86, 2004.

[9] N. Plunkett and F. J. O'Brien, "Bioreactors in tissue engineering," *Studies in Health Technology and Information*, vol. 152, pp. 152–214, 2010.

[10] J. Hambor, "Bioreactor design and bioprocess control for industrialized cell processing," *Bioprocess International*, vol. 10, pp. 22–33, 2012.

[11] D. Massai, G. Cerino, D. Gallo et al., "Bioreactors as engineering support to treat cardiac muscle and vascular disease," *Journal of Healthcare Engineering*, vol. 4, no. 3, pp. 329–370, 2013.

[12] D. Massai, G. Isu, D. Madeddu et al., "A versatile bioreactor for dynamic suspension cell culture. Application to the culture of cancer cell spheroids," *PLoS One*, vol. 11, no. 5, Article ID e0154610, 2016.

[13] C. Kropp, D. Massai, and R. Zweigerdt, "Progress and challenges in large-scale expansion of human pluripotent stem cells," *Process Biochemistry*, vol. 59, pp. 244–254, 2017.

[14] I. Chimenti, D. Massai, U. Morbiducci, A. P. Beltrami, M. Pesce, and E. Messina, "Stem cell spheroids and ex vivo niche modeling: rationalization and scaling-up," *Journal of Cardiovascular Translational Research*, vol. 10, no. 2, pp. 150–166, 2017.

[15] https://www.ema.europa.eu/en/human-regulatory/research-development/compliance/good-laboratory-practice-compliance.

[16] C. F. Mandenius, *Bioreactors: Design, Operation and Novel Applications*, Wiley, Weinheim, Germany, 2016.

[17] A. R. Raveling, S. K. Theodossiou, and N. R. Schiele, "A 3D printed mechanical bioreactor for investigating mechanobiology and soft tissue mechanics," *MethodsX*, vol. 5, pp. 924–932, 2018.

[18] D. Schneidereit, J. Tschernich, O. Friedrich, M. Scharin-Mehlmann, and D. F. Gilbert, "3D-printed reusable cell culture chamber with integrated electrodes for electrical stimulation and parallel microscopic evaluation," *3D Printing and Additive Manufacturing*, vol. 5, no. 2, pp. 115–125, 2018.

[19] L. J. Smith, P. Li, M. R. Holland, and B. Ekser, "FABRICA: a bioreactor platform for printing, perfusing, observing & stimulating 3D tissues," *Scientific Reports*, vol. 8, no. 1, article 7561, 2018.

[20] G. Pisani, A. Rodriguez, G. Cerino et al., "Automated bioreactor for biomimetic adaptive culture and in situ mechanical characterization of cardiac tissue models," *Tissue Engineering Part A*, vol. 21, p. S376, 2015.

[21] B. N. Turner, R. Strong, and S. A. Gold, "A review of melt extrusion additive manufacturing processes: I. process design and modeling," *Rapid Prototyping Journal*, vol. 21, no. 3, pp. 192–204, 2015.

[22] S. H. Huang, P. Liu, A. Mokasdar, and L. Hou, "Additive manufacturing and its societal impact: a literature review," *International Journal of Advanced Manufacturing Technology*, vol. 67, no. 5-8, pp. 1191–1203, 2013.

[23] T. Chen, S. Fritz, and K. Shea, "Design for mass customization using additive manufacture: case-study of a balloon-powered car," in *Proceedings of the 20th International Conference on Engineering Design (ICED15)*, vol. 4, Milan, Italy, July 2015.

[24] M. Terzini, A. Aldieri, E. M. Zanetti, D. Massai, A. L. Audenino, and C. Bignardi, "Native human dermis versus human acellular dermal matrix: a comparison of biaxial mechanical properties," *Australasian Medical Journal*, vol. 11, no. 8, pp. 434–442, 2018.

[25] C. Castaldo, D. Nurzynska, V. Romano et al., "From cover to core: acellular human dermis for the regeneration of human heart," *Tissue Engineering Part A*, vol. 23, no. S1, p. S-67, 2017.

[26] http://usglobalimages.stratasys.com/Main/Files/Material_Spec_Sheets/MSS_FDM_ABSplusP430.pdf.

[27] http://articles.stratasys.com/user-guides/fdm-3d-printers/uprint-se-uprint-se-plus-user-guide.pdf.

[28] M. Terzini, C. Bignardi, C. Castagnoli, I. Cambieri, E. M. Zanetti, and A. L. Audenino, "Dermis mechanical behaviour after different cell removal treatments," *Medical Engineering & Physics*, vol. 38, no. 9, pp. 862–869, 2016.

[29] M. Terzini, C. Bignardi, C. Castagnoli, I. Cambieri, E. M. Zanetti, and A. L. Audenino, "Dermis mechanical behavior in relation to decellularization treatment length," *Open Biomedical Engineering Journal*, vol. 10, no. 1, pp. 34–42, 2016.

[30] E. M. Zanetti, M. Perrini, C. Bignardi, and A. L. Audenino, "Bladder tissue passive response to monotonic and cyclic loading," *Biorheology*, vol. 49, no. 1, pp. 49–63, 2012.

[31] E. M. Zanetti, A. Aldieri, M. Terzini, M. Calì, G. Franceschini, and C. Bignardi, "Additively manufactured custom load-bearing implantable devices: grounds for caution," *Australasian Medical Journal*, vol. 10, no. 8, pp. 694–700, 2017.

Research Article

Robocasting of Bioactive SiO$_2$-P$_2$O$_5$-CaO-MgO-Na$_2$O-K$_2$O Glass Scaffolds

Francesco Baino [iD],[1] Jacopo Barberi,[1] Elisa Fiume,[1,2] Gissur Orlygsson,[3] Jonathan Massera,[4] and Enrica Verné[1]

[1]*Department of Applied Science and Technology (DISAT), Politecnico di Torino, Turin, Italy*
[2]*Department of Mechanical and Aerospace Engineering (DIMEAS), Politecnico di Torino, Turin, Italy*
[3]*Department of Materials, Biotechnology and Energy, Innovation Center Iceland (ICI), Reykjavik, Iceland*
[4]*Faculty of Medicine and Health Technology, University of Tampere, Tampere, Finland*

Correspondence should be addressed to Francesco Baino; francesco.baino@polito.it

Bioactive silicate glass scaffolds were fabricated by a robocasting process in which all the movements of the printing head were programmed by compiling a script (text file). A printable ink made of glass powder and Pluronic F-127, acting as a binder, was extruded to obtain macroporous scaffolds with a grid-like three-dimensional structure. The scaffold architecture was investigated by scanning electron microscopy and microtomographic analysis, which allowed quantifying the microstructural parameters (pore size 150–180 μm and strut diameter 300 μm). In vitro tests in simulated body fluid (SBF) confirmed the apatite-forming ability (i.e., bioactivity) of the scaffolds. The compressive strength (around 10 MPa for as-produced scaffolds) progressively decreased during immersion in SBF (3.3 MPa after 4 weeks) but remains acceptable for bone repair applications. Taken together, these results (adequate porosity and mechanical strength as well as bioactivity) support the potential suitability of the prepared scaffolds for bone substitution.

1. Introduction

Bone substitution in critical- and medium-sized defects, resulting from injuries, degenerative pathologies, and tumor removal, is still considered one of the major clinical challenges of our time. Hence, there has been a considerable increase in the demand for bone grafts over the last years [1]. Autologous bone is still considered the "gold standard" in realizing bone grafting procedures mainly due to its excellent biocompatibility, but the need to overcome the limits related to tissue availability and donor site morbidity is driving researchers towards other options. Allografts and xenografts are available in a virtually unlimited amount but can carry the risk of disease transmission, are often resorbed more quickly as compared to the host bone healing rate, and may be refused by the patient due to ethical or religious concerns [2]. Hence, many efforts have been carried out in the last two decades for the development of engineered tissues created by bioreactors [3] as well as synthetic bone grafts exhibiting osteoconductive, osteoinductive, and osteogenetic properties [4–6].

Up to now, among all the available synthetic materials used in the production of bone grafts (i.e., polymers, ceramics, and composites [7]), undoubtedly bioactive glasses (BGs) show highly attractive properties as basic materials for the fabrication of three-dimensional (3D) scaffolds based on bone tissue engineering (BTE) strategies [8, 9]. The suitability of BGs relies on their unique capability to both create a stable material-device interface by inducing the formation of a hydroxyapatite (HA) layer on their surface and promote the expression of osteogenetic factors by osteoprogenitor cells [10, 11].

When designing scaffolds for BTE, interconnected pores with mean diameter ≥100 μm and open porosity ≥50 vol.%

are considered to be the minimum requirements to have a proper tissue ingrowth and cell migration within the grafting material [12–14]. Moreover, achieving a suitable mechanical response of the device is essential in order to guarantee both structural integrity and adequate support over the whole duration of the healing process [15]. Unfortunately, almost all the traditional manufacturing processes, deeply reviewed elsewhere [16–18], do not allow achieving an accurate control on such parameters.

As safety and reliability of the implant-manufacturing process represent moral imperatives in health sciences, methods for the production of complex geometries and patient-specific devices are strongly required. As a result, starting from the early '80s, solid freeform fabrication (SFF) techniques, also known as additive manufacturing (AM) technologies, gained increasing scientific interest because of the possibility to easily tailor the device properties by simply acting on process parameters [19, 20]. Such technologies, in fact, are based on bottom-up approaches, where the object is produced layer by layer starting from a computer-aided design (CAD) file (.stl file) or text scripts [15]. All these aspects are of particular interest in BTE where obtaining customized devices is a primary goal [21]. A high control on porosity, pore size, and interpore interconnectivity can actually be achieved by relatively simple SFF processes. These techniques show also promise for large-scale manufacturing, where high reproducibility of the devices is required.

Moreover, having a high control on the scaffold architecture makes it possible to tailor the mechanical response of the device during the design phase [22]. In this regard, it should be pointed out that both compressive strength and elastic modulus of the bone should ideally be matched by the scaffold. These parameters depend on both the extruded material properties and the scaffold pore/strut structure.

Several SFF techniques have already been used for BTE scaffold fabrication, including 3D printing (3DP), fused deposition modeling (FDM), ink-jet printing, stereolithography (SL), and selective laser sintering (SLS) [20]. However, very little information is available in the literature regarding the processing of bioactive glasses by SFF techniques. Probably, robocasting is the most common and powerful direct ink-writing technique for the processing of glass and glass-ceramic scaffolds. This technique is based on the continuous extrusion of a filament (ink) from a robot-controlled nozzle onto a building platform [22]. The ink is a slurry, composed of glass or ceramic particles and a polymeric binder to form a colloidal suspension, characterized by well-defined rheological properties [23]. Usually, the process does not require the use of a high concentration of binder, allowing sintered parts to be obtained in a short time [22]. Pluronic F-127 is one of the three most commonly used binders for robocasting in bone applications [24–26], together with ethyl cellulose/polyethylene glycol and carboxymethyl cellulose [27–30].

Robocast bioceramic scaffolds were produced for the first time in 2010 by Franco et al., who developed a hydrogel-based ink containing calcium phosphates (HA and β-TCP) [24]. Since then, both commercial 45S5 Bioglass® and 13-93

glass were processed by robocasting by several research groups. In 2013, Liu et al. used robotic deposition to produce 13-93 glass-based grid-like microstructured scaffolds with 47 vol.% porosity and $300 \, \mu$m pore width. Flexural and compressive mechanical tests were performed before and after both bioactivity tests in simulated body fluid (SBF) and in vivo tests in a rat subcutaneous model. It was found that compressive strength decreased both after 2-week immersion in SBF and in vivo implantation. Moreover, a shift from brittle to elastoplastic response was observed after 2- and 4-week implantation in vivo, thus demonstrating the bone-like behaviour of such devices and their suitability in load-bearing applications [26].

In 2014, fully vitreous 45S5 Bioglass®-based scaffolds with interconnected porosity ranging from 60 to 80 vol.% were successfully produced for the first time. All the scaffolds showed compressive strength comparable to that of the trabecular bone (2–13 MPa), even when sintered below the crystallization temperature [27].

More recently, 45S5 Bioglass®-based scaffolds reinforced by HA/PCL nanocomposite coatings were obtained by Motealleh et al. [30], who interestingly investigated the effects of different postprocessing thermal treatments on the scaffold mechanical response. The CAD-derived original architecture was successfully retained upon sintering both in amorphous and highly crystallized scaffolds, with compressive strengths of 2 MPa and 11 MPa, respectively, which are definitely in the range of the trabecular bone.

In a recent study, functionally graded porous devices were successfully obtained by Mattioli-Belmonte et al. [31] who used a robocasting system, called the pressure-assisted microsyringe (PAM), to produce bioactive glass/poly(lactic-co-glycolic acid) (PLGA) 2D porous structures characterized by a well-defined topology. The layers were then assembled in order to obtain a 3D bone-like scaffold [31]. It was demonstrated that the elastic modulus was comparable to that of the cancellous bone, and osteoblastic differentiation of human periosteal precursor cells was observed, showing great promise for bone tissue engineering applications.

In the present work, highly bioactive and fully amorphous grid-like scaffolds for bone regeneration were produced by robocasting using a six-oxide silicate glass as the basic material for the ink formulation. The aim was to demonstrate that it is possible to obtain 3D structures with suitable porosity with a rather simple method, avoiding the use of ultrafine powders, thin nozzles, and complex ink preparation.

2. Materials and Methods

2.1. Glass Preparation. The basic material used to manufacture the scaffolds was a silicate glass (composition 47.5SiO$_2$-10Na$_2$O-10K$_2$O-10MgO-20CaO-2.5P$_2$O$_5$ mol.%) originally developed by Verné et al. [32] at Politecnico di Torino. This glass, referred to as 47.5B, was produced by a standard melting method in a platinum crucible. The raw precursors (SiO$_2$, Na$_2$CO$_3$, K$_2$CO$_3$, (MgCO$_3$)$_4$·Mg(OH)$_2$· 5H$_2$O, CaCO$_3$, and Ca$_3$(PO$_4$)$_2$ high-purity powders purchased from Sigma-Aldrich) were homogeneously mixed in

the crucible and melted in air at 1500°C for 30 min. The melt was then quenched in deionized water to produce a frit that was ball-milled (Pulverisette 0, Fritsch, Germany) and sieved to obtain a final particle below 32 μm by using a stainless steel sieve (Giuliani Technologie Srl; mesh 32 μm).

2.2. Scaffold Fabrication by Robocasting. The 47.5B glass was thought to be very suitable to produce completely amorphous—and hence highly bioactive—porous scaffolds due to its large hot-working range (difference between onset of crystallization (T_x) and glass transition temperature (T_g), $T_x - T_g = 260$°C), as determined in a previous study [32].

Pluronic F-127 (Sigma-Aldrich) was used as a binder for the preparation of the glass-based ink. The ink formulation was optimized through some preliminary trials and involved the addition of 35 vol.% of glass to an optically clear water-based solution containing 27.5 wt.% of Pluronic F-127. Prior to adding the glass, the Pluronic F-127 solution was stirred overnight while being maintained at low temperature in an ice bath due to the thermosensitive behaviour of the binder. The glass-containing ink was then mixed for 1 min by using a vortex mixer (Ika-Werk shaker, type Vibrofix VF1 electronic) at 2500 rpm and cooled for 1 min in the ice bath. Five mixing-cooling cycles were performed to allow achieving good dispersion of the glass particles.

The plastic cartridge connected to the robocasting machine (3Dn-Tabletop, nScrypt Inc., Orlando, FL, USA) was filled with the ink, which was left to stabilize for 1 h before printing. The only movement that was allowed to the printing tower was along the (vertical) z-axis, and its position determined the printing height. Plastic tips with an inner diameter of 410 μm (Nordson EFD Optimum® SmoothFlow™) were used to extrude the ink. The plate under the nozzle was moved on the x-y plane with respect to the printing tower so that the ink was extruded according to the correct pattern. The printing accuracy was 10 μm along the x- and y-axes and about 5 μm along the z-axis [33].

Acetate sheets (Colour Copier and Laser Transparency OHP Film, Folex AG, Seewen, Switzerland) were used as the printing substrate due to their flatness, good adhesions they have with the ink, and easiness to detach the scaffolds from them once they are dry [34].

Once the cartridge was loaded and fitted in position and the acetate sheet was placed on the platform, the processing parameters were adjusted using the software (MachineTools 3.0) provided by nScrypt. The desired structure was obtained by programming every single movement that the print head must do along the x-, y-, and z-axes through compiling a design script, written as a text file. The printing speed was 2 mm/s, and the pressure used to extrude the ink was in the range of 1.24–1.51 bar; the raster pattern is shown in Figure 1.

Robocast 47.5B scaffolds were porous cuboids (length = width = 7.5 mm) with a grid-like structure and were made of 20 glass layers (height about 4.5 mm). Once the printing was completed, the scaffolds were left to dry for 48 h in air and finally detached from the acetate sheet. A multistep thermal treatment (three stages at 200, 400, and 500°C for 30 min each followed by a final stage at 600°C for 1 h;
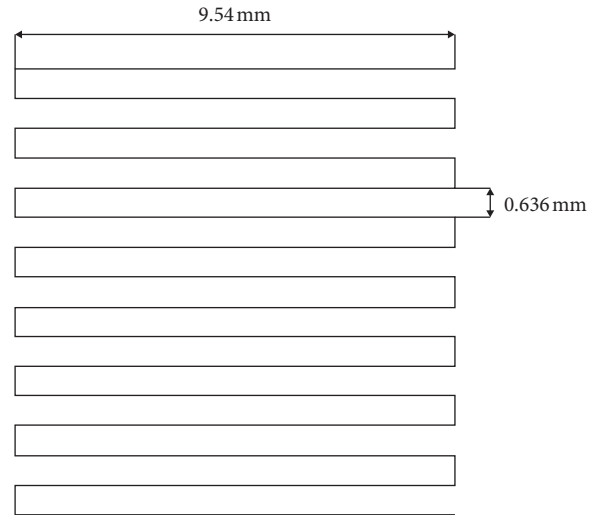
Figure 1: Raster pattern used to print the scaffolds.

heating rate 1°C/min) was eventually performed to allow the removal of the organic binder and the sintering of glass particles. Only the last heat treatment, being performed at a temperature higher than T_g, led to glass sintering, while the others were part of the burning-out process of the binder, which was carried out slowly to ensure the complete removal of any organic residue and avoid cracking phenomena due to sudden shrinkage.

2.3. Characterizations

2.3.1. X-Ray Diffraction. Both as-quenched glass and sintered scaffolds (after being crushed into powder) underwent wide-angle X-ray diffraction (XRD; 2θ within 20–70°) to detect the presence of crystalline phases. A X'Pert Pro PW3040/60 diffractometer (PANalytical, Eindhoven, Netherlands) was used; the experimental setup included operating voltage 40 kV, filament current 30 mA, Bragg-Brentano camera geometry with Cu Kα incident radiation (wavelength $\lambda = 0.15405$ nm), step size 0.02°, and fixed counting time per step 1 s.

2.3.2. In Vitro Bioactivity. The bioactivity of the robocast scaffolds, in terms of HA formation and ionic release in vitro, was carried out by properly adapting the testing procedure proposed by Macon et al. [35]. The experiments involved the immersion of triplicate samples in Kokubo's SBF [36] for 6, 24, 48, 72, 168, and 336 h. The ratio between sample mass and SBF volume at the beginning of the experiments was fixed at 1.5 mg/ml. The specimens were placed into an orbital shaker incubator (Multitron AJ 118 g, Infors, Bottmingen, Switzerland) at 37°C under a constant speed of 100 rpm. The solution was analyzed at each time point by means of inductively coupled plasma optical emission spectroscopy (ICP-OES) (5110 ICP-OES, Agilent Technologies) in order to evaluate the concentration of ions in the solution. After being extracted from the solution, the samples were gently rinsed with distilled water and left to dry overnight at room temperature. The results were expressed as mean ± standard deviation.

2.3.3. Morphology and Porosity. The scaffolds were investigated before and after in vitro tests by a field-emission scanning electron microscope (FE-SEM; Supra™ 40, Zeiss, Oberkochen, Germany) equipped with an energy dispersive spectroscopy (EDS) detector in order to evaluate the pore-strut morphology and the formation of new phases on the surface of SBF-treated samples. The specimens were sputter-coated with chromium prior to the analysis and inspected at an accelerating voltage of 15 kV.

The total porosity of the scaffolds was assessed by mass-volume measurements as $(1 - \rho/\rho_0) \times 100$, where ρ is the apparent density of the scaffold and ρ_0 is the bulk density. The porosity was expressed as mean ± standard deviation calculated on five specimens.

For micro-CT analysis, the samples were X-ray scanned in the dry state in a Phoenix Nanotom S machine (General Electric Measurement and Control), at a source voltage of 110 kV and a source current of 110 μA. No X-ray filters were used. The scanning modalities for the robocast 47.5B scaffolds before and after immersion in SBF are reported in Table 1. A translational motion compensation was performed in order to guarantee a perfect matching of the 0° and 360° shadow images. Thereafter, the projection images were used to reconstruct the investigated scaffolds by means of the Radon transform [37, 38] as algorithmized in the software datos|x reconstruction provided by the manufacturer. VGStudio Max 2.0 from Volume Graphics was employed for visual evaluation and detail measurements on strut and void sizes as well as for calculations of porosity. An automated calibration routine integrated into VGStudio Max 2.0 was used to define material boundaries. The software determines the background peak and the material peak in the grey value histogram and calculates the grey value of the material boundary. VGStudio Max 2.0 was also used to export image stacks in the DICOM format. This format can be read into the BoneJ plugin [39] running under the ImageJ software package (version 1.51t) [40]. BoneJ (version 1.4.2) was used to extract information following an approach used for the trabecular bone where bone volume, total volume, trabecular thickness, and trabecular spacing (i.e., pore size) are determined [41].

2.3.4. Mechanical Characterization. The compressive strength of the scaffolds before and after in vitro tests (2 and 4 weeks in SBF) was evaluated through crushing tests by using an MTS machine (Model 43, MTS, Minnesota, USA; cell load 5 kN and cross-head speed 1 mm·min^{-1}). The failure stress was calculated as the ratio between the maximum load registered during the test and the resistant cross-sectional area measured by callipers. The compressive strength was expressed as mean ± standard deviation calculated on five specimens for each type.

3. Results and Discussion

3.1. Microstructure and Morphology. Figure 2 shows the XRD spectra of both the as-quenched material and the sintered scaffolds. As expected, no diffraction peaks can be detected, but only a broad amorphous halo in the range of 20 to 35° is visible, which is typical of silicate glasses (red pattern). No microstructural changes in the material were revealed after the thermal treatment at 600°C, which demonstrates that 47.5B scaffolds remain in an amorphous state (black pattern). This is beneficial for the bioactivity, as suggested by some studies reporting that devitrification can reduce the apatite-forming ability of bioactive glass-derived materials [42].

The scaffold structure obtained by robocasting is highly regular with a grid-like arrangement of the pores (Figure 3(a)). The struts (rods) remained straight during the sintering process and exhibited a quite regular circular section. The porosity is made of regular macrochannels, both vertical and horizontal, generated by the separation between glass lines and the tilting of each newly juxtaposed layer with respect to the underlying one.

More accurate morphological investigations were carried out by SEM, especially in order to understand the level of sintering reached during the thermal treatment. The scaffolds exhibit well-densified struts (rods) in which the glass particles are no more distinguishable (Figure 3(b)). High-magnification analysis reveals that the interparticle porosity almost completely disappeared as a result of sintering and the glass particles are fused together, also in the areas of contact between adjacent rods (Figure 3(c)). Few small spherical pores derived from air bubbles entrapped in the ink can also be observed. The cross-sectional size of the channels (100–200 μm) is potentially suitable to support new bone formation. In fact, pores above 100 μm allow osteoblastic cell colonization and proper vascularization, thus avoiding hypoxic growth conditions of the bone [9].

The total porosity of the scaffolds was 42.5 ± 4.5 vol.%, which is close to the minimum threshold of acceptability recommended for bone tissue engineering applications (about 50 vol% [43]). Further optimizations of the robocasting process could allow increasing the porosity without negatively affecting the structural integrity. The low value of standard deviation demonstrates the good reproducibility of the fabrication process.

Micro-CT reconstructions of two-dimensional sections of the scaffolds are reported in Figure 4.

The tomographic images showed good regularity of the pore-strut structure and rod diameter: the voids that are visible in the filaments are due to air bubbles that remained entrapped inside the ink. In some cases, these voids originated from full-thickness cracks in the filaments as a consequence of the scaffold volumetric shrinkage upon sintering. Quantification of microstructural parameters yielded the following results: pore width 180 ± 25 μm, pore height 147 ± 19 μm, and strut diameter 300 ± 10 μm. These findings are consistent with those from SEM observations; the low values of standard deviation confirmed the good reproducibility of the robocasting process.

A slight curvature in the rods of the scaffold structure is visible in Figure 4(a). This could be due to (i) the slight bending of the ink filaments under their own weight prior to sintering and (ii) shrinkage phenomena that occur during sintering.

Three-dimensional reconstructions of the whole scaffold volume are also displayed in Figure 5.

TABLE 1: Micro-CT scanning parameters.

Scaffold	Magnification	Voxel size (μm)	Rotation step (°)	Exposure time (s)	Tube mode	Frame averaging number	Frame skipped
Scaffold as-such	10.00x	5.00	0.50	1.5	0	3	1
Scaffold soaked for 2 weeks in SBF	11.11x	4.50	0.50	1.5	0	3	1
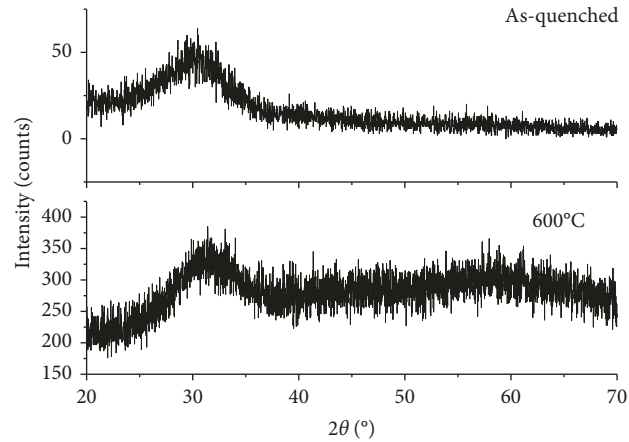
FIGURE 2: XRD patterns. Both the as-quenched 47.5B glass powders (red) and the powdered scaffolds sintered at 600°C for 1 h (black) are characterized by the amorphous structure since no crystallization peaks were observed.

(a)

(b)

(c)
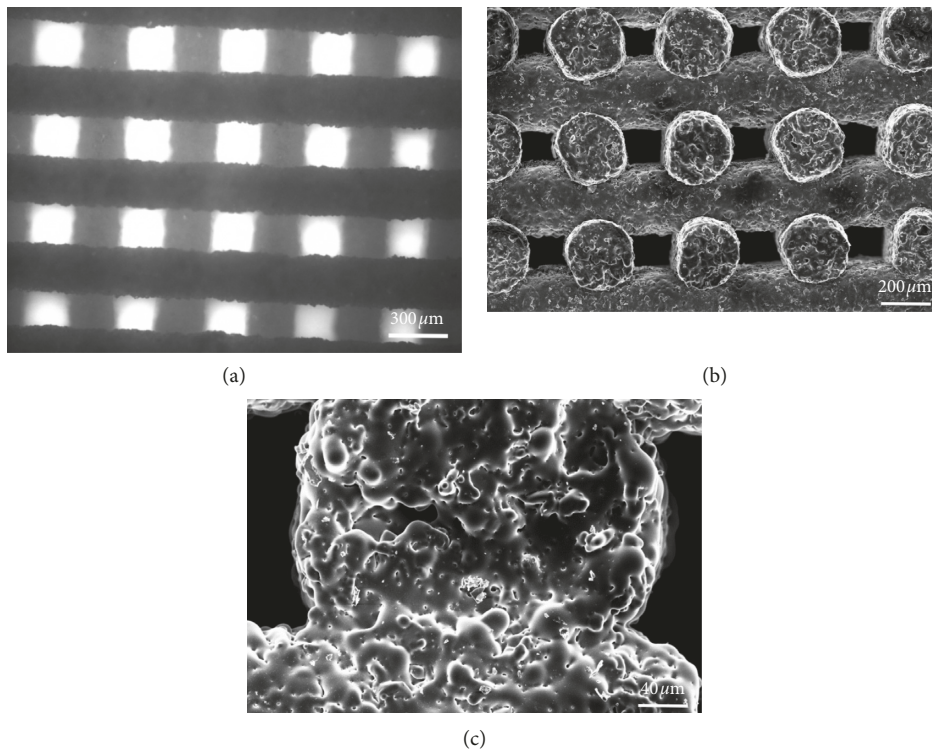
FIGURE 3: Morphological evaluation of the scaffold. Top view of the grid-like structure obtained by optical microscopy (a); SEM micrograph of the channel porous structure (b) and of the trabecular section (c).

3.2. In Vitro Bioactivity.

A biomaterial for bone repair is defined "bioactive" if HA precipitates onto its surface once it is implanted inside a living body or during immersion in solutions that simulate the body environment (in vitro) [44]. XRD analyses on the samples soaked in SBF for different time frames actually

(a)

(b)

(c)
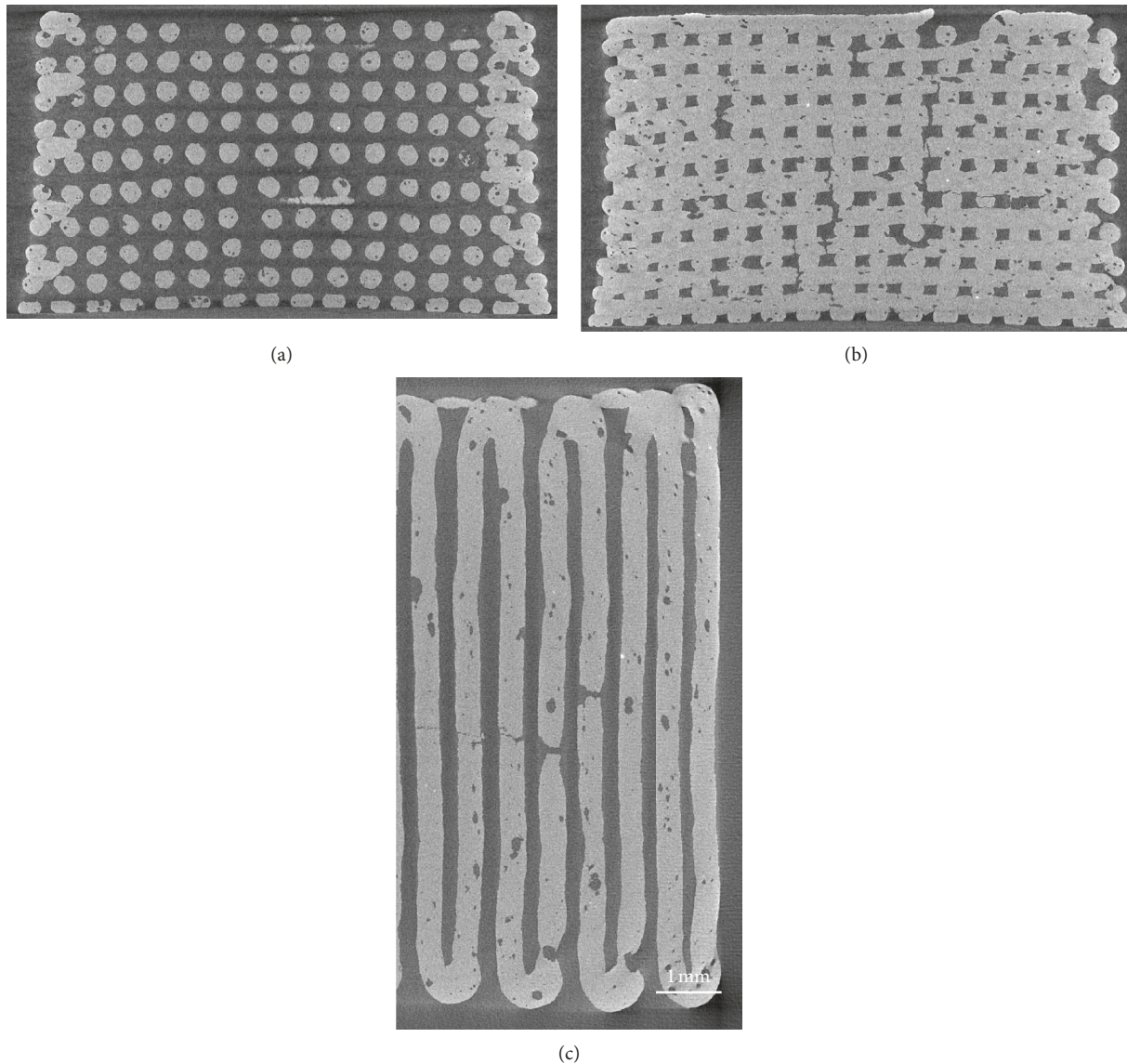
FIGURE 4: Micro-CT images of 47.5B scaffolds. Vertical section on a plane that passes through the gap between 2 central rods (a); vertical section on a plane that cuts through the rods parallel to the image plane (b); horizontal section on the midheight of the scaffold, showing also the border of the scaffold (c) (nominal strut diameter: 300 μm).

revealed the formation of HA on the scaffold surface (Figure 6).

Specifically, there was a progressive disappearance of the amorphous halo typical of the glass and the appearance of the HA characteristic diffraction peaks. The two main peaks of HA (PDF code no. 01-073-1731) were detected, the highest at 31.79° (corresponding to the (2 1 1) reflection) and the other one at 25.68° ((0 0 2) reflection). These peaks are not sharp but have a quite broad appearance, suggesting that the HA formed on the scaffold struts has a nanocrystalline nature.

A better understanding of the in vitro bioactivity mechanism of 47.5B scaffolds was obtained performing morphological and compositional analyses by SEM and EDS assisted by micro-CT imaging. Thus, it was possible to follow the stepwise evolution of the scaffold surface, including the

formation of the silica gel, the precipitation of the amorphous calcium-phosphate layer, and the nucleation and growth of HA crystals, according to the bioactivity mechanism proposed by Hench [45]. After 6 h, it is possible to see the formation of the silica gel (the typical surface-cracked layer in Figure 7(a)), and at 24 h, small calcium-phosphate nuclei are visible as brighter globules on the surface of the underlying gel (Figure 7(b)). This layer evolved leading to the formation of needle-like HA crystals that grew and joined together to form large globular crystals with "cauliflower morphology," which is typical of bone-like HA (Figures 7(c)–7(e)). After 1 week, the scaffold struts are thicker as compared to those of untreated scaffolds and are covered by HA globular aggregates. After 2 weeks, no significant thickening of the scaffold rods is observed, suggesting that a process of HA detachment from the scaffold

(a)   (b)
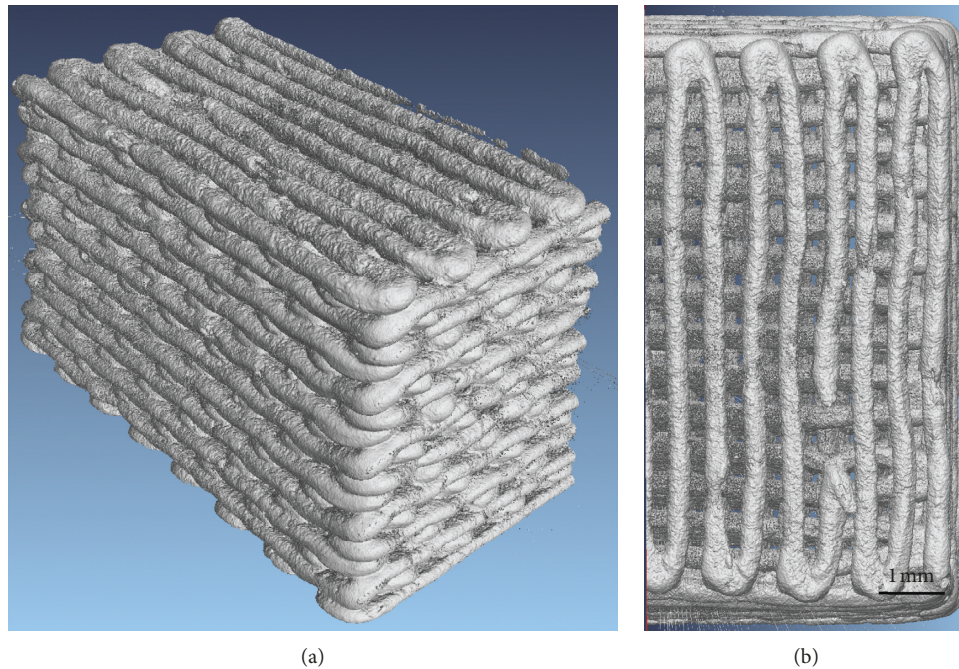
FIGURE 5: 3D reconstruction of scaffold volume obtained by micro-CT. Lateral view (a); top view (b) (nominal strut diameter: 300 μm).
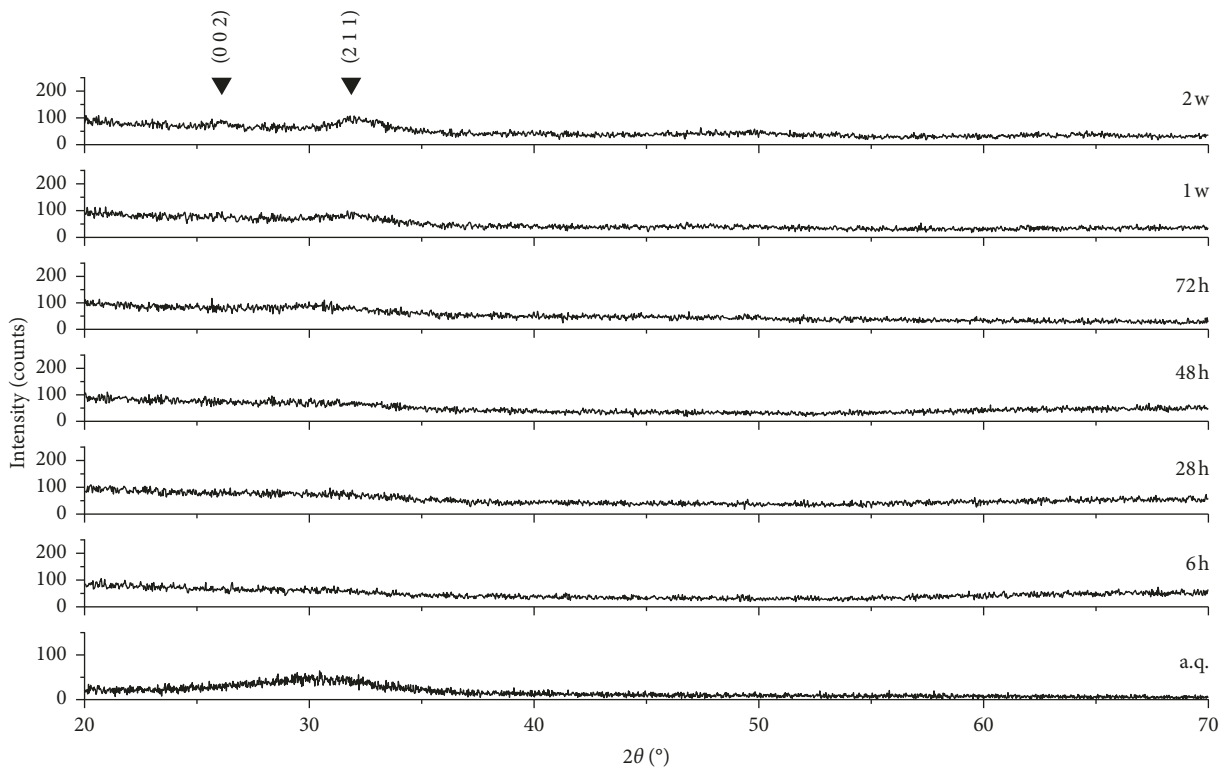
FIGURE 6: XRD spectra of 47.5B scaffolds after different immersion times in SBF. The characteristic peaks of HA are indicated by Miller indices ($h\ k\ l$).

might have taken place. This is evidenced by the fact that the HA crystals detected on the scaffold walls are smaller compared to the ones that covered the 1-week specimen, as it is possible to see in Figure 7(d). The Ca-to-P atomic ratio increases with soaking time from 0.46 at 24 h to 1.47 at 2 weeks. The Ca-to-P ratio at the end of the experiments is still lower that the value of stoichiometric HA (Ca/P = 1.67), revealing the presence of Ca-deficient HA as already observed previously for other bioactive glass compositions [46–48]. However, as Mg^{2+} ions are released from the glass
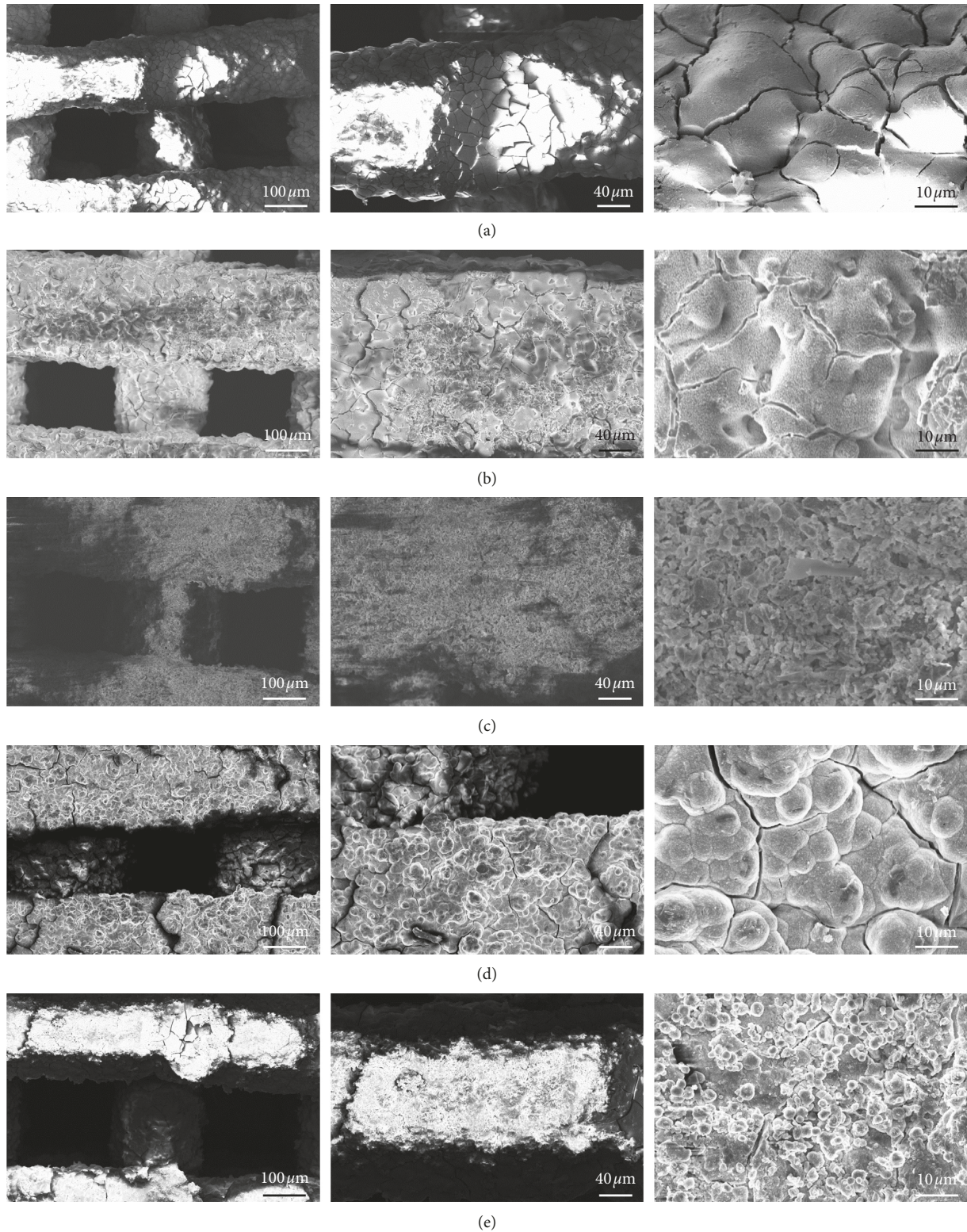
FIGURE 7: SEM morphological analysis performed after immersion in SBF at different time points. Typical silica gel layer observed on the surface of the material after soaking for 6 h (a); small calcium-phosphate nuclei formed after 24 h (b); gel layer evolution upon soaking observed after 72 h (c); formation of a thick layer of globular HA characterized by the typical cauliflower morphology after 1-week immersion (d); morphology evaluation of the surface after 2 weeks revealed a partial detachment of the HA with no significant changes in the rod diameter (e).
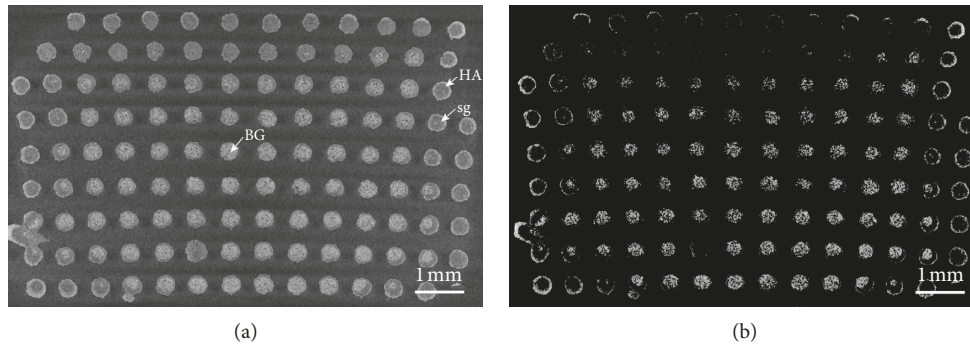
FIGURE 8: Cross section of a 47.5B scaffold soaked in SBF for two weeks obtained by micro-CT. (a) Standard condition and (b) augmented contrast. HA, hydroxyapatite layer; sg, silica gel; BG, unmodified bioactive glass.

surface during immersion in SBF, a small amount of Ca in HA has been substituted by Mg, as confirmed by compositional analysis. Therefore, the atomic ratio between the amounts of bivalent cations and phosphorus $(Ca + Mg)/P$ yields 1.64, which is closer to the Ca/P value of stoichiometric HA.

The micro-CT analysis of the scaffold structure after 2 weeks in SBF highlighted the presence of different reaction layers in the rods resulting from the bioactivity mechanism (Figure 8).

Some rods clearly exhibit a thick silica gel layer (grey tones) with a thin converted outer layer of HA (white tones). Other struts, mainly at the scaffold periphery, present a quite thick HA coating and a core converted to silica gel. A third type of rods is represented by the trabeculae in the center of the scaffold which are almost unmodified. HA and bioactive glass, which have higher densities than silica gel, are highlighted in Figure 8(b).

Ions are released from the glass surface during the reaction stages of the bioactivity mechanism; therefore, it is possible to gain some additional information about this process by monitoring the evolution of the ionic concentration in SBF during the dissolution test. In fact, it was previously shown that greater changes in ionic concentrations can be related to higher bioactivity [49].

Silicon concentration increases steadily over the first week (Figure 9), when the glass converts into silica gel releasing soluble $Si(OH)_4$, and reaches the equilibrium at 1 week after the formation of an HA layer. Also, a similar trend was observed for calcium ions within 1 week, but a plateau was not reached.

The trend of phosphorus is indicative of the sequestration of phosphate ions from the solution, which means that calcium phosphate—and then HA—precipitates for the whole soaking period. This is in good agreement with the SEM and micro-CT observations (Figures 6 and 8). The trends of magnesium and potassium ions are in accordance with the evolution of the silicon concentration in the first week, confirming a progressive dissolution of the glass. However, while silicon concentration reaches a plateau after 1 week, the concentrations of magnesium and potassium in SBF still tend to increase over the whole testing period. The evolution of the ionic concentrations of Si, Ca, and P is in

agreement with previous studies on the dissolution of bioactive silicate glasses [50]. The release of sodium is not reported because its concentration, extremely high within the SBF solution, oversaturated the detector.

The pH of the solution was also monitored during the test as its variations are strongly related to the ionic exchanges between glass and SBF. The pH values, shown in Figure 9, exhibit a rapid increase in the first 24 h, and then the increase in pH slowed down. This is consistent with the morphological observations of the sample: since the pH is modified by the ionic exchanges between the glass and the solution, once the HA layer starts to form and limit the glass-SBF interactions, the ion exchange rate decreases too.

3.3. Mechanical Strength.
The compressive strength of as-printed scaffolds was in the range of 5.6–16.5 MPa $(9.9 \pm 4.6\,MPa)$, which is comparable to the typical range assessed for the human cancellous bone (2–12 MPa [51]). Future optimizations in the process of scaffold fabrication could allow reducing the high variability of the mechanical strength.

The mechanical properties of scaffolds should ideally match those of the host bone, and this is challenging especially in load-bearing applications. The advent of additive manufacturing technologies disclosed fascinating scenarios in this regard. An interesting study carried out by Rainer et al. [52] established the basis for successfully achieving the design of scaffolds with the microarchitecture predicted through a priori finite-element analysis (FEA) of the implant site geometry under physiological loads. This approach, called the load-adaptive scaffold architecturing (LASA), uses FEA for obtaining the principal stress directions under a physiologically derived load system and can easily be coupled to CAD-based manufacturing technologies. Although the applications of LASA are currently limited to polymeric materials, extension to glasses and ceramics would be highly beneficial for the field of BTE scaffolds.

When a scaffold is implanted in a load-bearing site, its major function is to act as a template for the new bone growth while supporting the surrounding tissues, exactly as a healthy bone does. Thus, the mechanical properties of the scaffold need to be suitable at the moment of the implantation and, furthermore, should not decrease too fast during

(a)

(b)

(c)

(d)

(e)

(f)
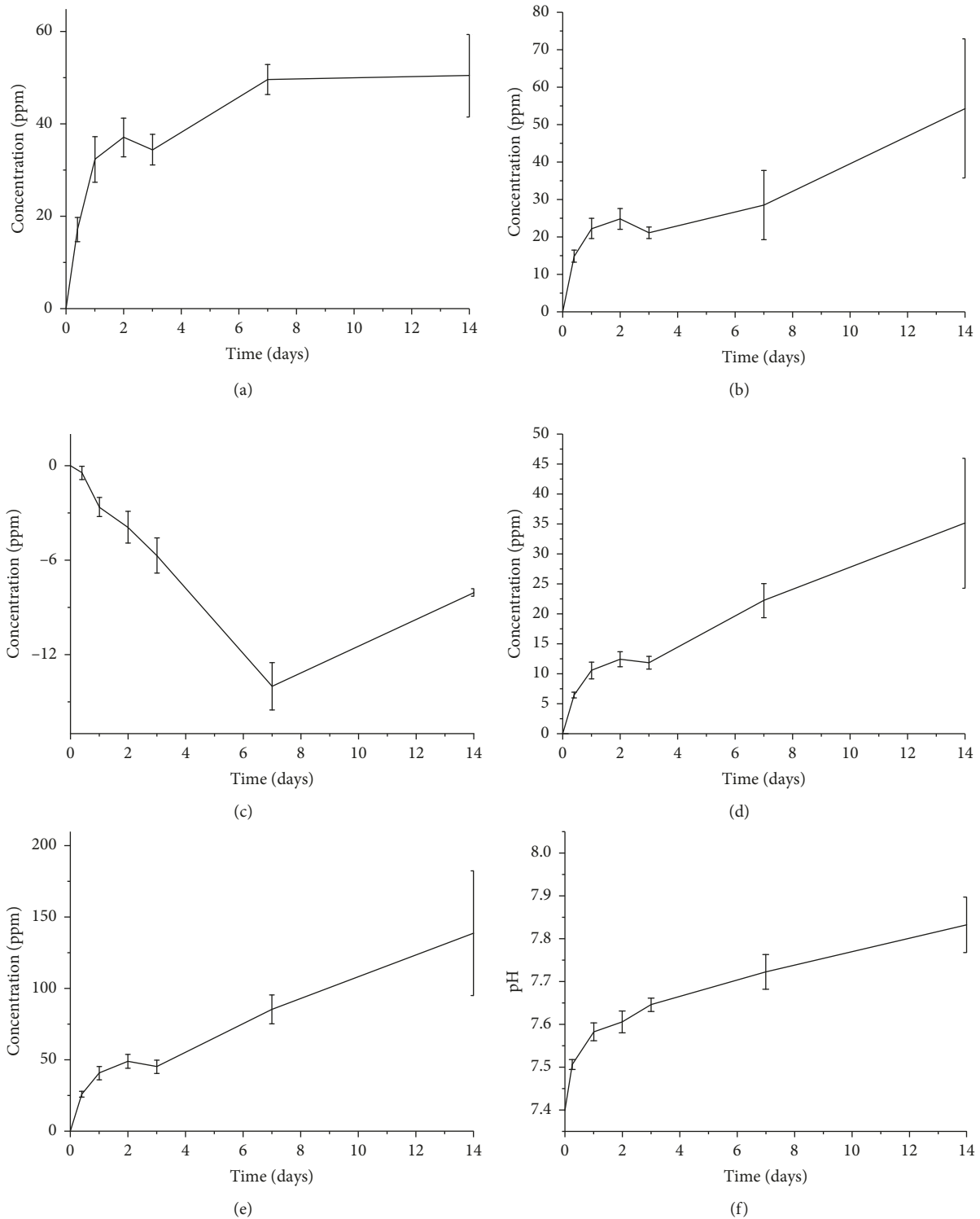
FIGURE 9: Ion-release profiles related to Si (a), Ca (b), P (c), Mg (d), and K (e) and pH (f) trend upon soaking in SBF. The variation of ionic concentration in the solution is reported after the subtraction of the ion concentration of blank SBF.

the healing time. The compressive strength of the scaffolds decreases as the immersion time in SBF increases (5.6 ± 2.2 MPa after 2 weeks and 3.3 ± 0.7 MPa after 4 weeks) but still remains within the typical range of the trabecular

bone (2–12 MPa [51]). This trend is in agreement with the results reported by Motealleh et al. [30] who used robocasting to fabricate 45S5 Bioglass® scaffolds with a grid-like structure.

4. Conclusions

Bioactive glass scaffolds were obtained by a relatively simple robocasting process that does not require the use of ultrafine glass powder, very thin nozzles, and a complex experimental setup, which are usually needed in the processes reported in the literature. The process allowed fabricating macroporous scaffolds with well-reproducible microstructural features, such as pore size and rod diameter. The compressive strength of the scaffolds, which remains comparable to that of the cancellous bone even after prolonged immersion in SBF with ionic dissolution phenomena, combined with a clear apatite-forming capability supports the potential suitability of the material for bone repair applications.

Data Availability

The data used to support the findings of this study are included within the article.

Conflicts of Interest

The authors declare that there are no conflicts of interest regarding the publication of this paper.

Acknowledgments

References

[1] O. Johnell and J. A. Kanis, "An estimate of the worldwide prevalence and disability associated with osteoporotic fractures," *Osteoporosis International*, vol. 17, no. 12, pp. 1726–1733, 2006.

[2] W. Schlickewei and C. Schlickewei, "The use of bone substitutes in the treatment of bone defects—the clinical view and history," *Macromolecular Symposia*, vol. 253, no. 1, pp. 10–23, 2007.

[3] I. E. De Napoli, E. M. Zanetti, G. Fragomeni, E. Giuzio, A. L. Audenino, and G. Catapano, "Transport modeling of convection-enhanced hollow fiber membrane bioreactors for therapeutic applications," *Journal of Membrane Science*, vol. 471, pp. 347–361, 2014.

[4] P. V. Giannoudis, H. Dinopoulos, and E. Tsiridis, "Bone substitutes: an update," *Injury*, vol. 36, no. 3, pp. S20–S27, 2005.

[5] W. R. Moore, S. E. Graves, and G. I. Bain, "Synthetic bone graft substitutes," *ANZ Journal of Surgery*, vol. 71, no. 6, pp. 354–361, 2001.

[6] V. Campana, G. Milano, E. Pagano et al., "Bone substitutes in orthopaedic surgery: from basic science to clinical practice," *Journal of Materials Science: Materials in Medicine*, vol. 25, no. 10, pp. 2445–2461, 2014.

[7] M. M. Stevens, "Biomaterials for bone tissue engineering," *Materials Today*, vol. 11, no. 5, pp. 18–25, 2008.

[8] M. N. Rahaman, D. E. Day, B. Sonny Bal et al., "Bioactive glass in tissue engineering," *Acta Biomaterialia*, vol. 7, no. 6, pp. 2355–2373, 2011.

[9] L.-C. Gerhardt and A. R. Boccaccini, "Bioactive glass and glass-ceramic scaffolds for bone tissue engineering," *Materials*, vol. 3, no. 7, pp. 3867–3910, 2010.

[10] D. C. Greenspan, "Bioactive glass: mechanisms of bone bonding," *Tandläkartidningen Årk*, vol. 91, no. 8, pp. 1–32, 1999.

[11] L. L. Hench, "The story of Bioglass®," *Journal of Materials Science: Materials in Medicine*, vol. 17, no. 11, pp. 967–978, 2006.

[12] D. Massai, F. Pennella, P. Gentile et al., "Image-based three-dimensional analysis to characterize the texture of porous scaffolds," *BioMed Research International*, vol. 2014, Article ID 161437, 8 pages, 2014.

[13] F. Pennella, G. Cerino, D. Massai et al., "A survey of methods for the evaluation of tissue engineering scaffold permeability," *Annals of Biomedical Engineering*, vol. 41, no. 10, pp. 2027–2041, 2013.

[14] E. M. Zanetti, A. Aldieri, M. Terzini, M. Calì, G. Franceschini, and C. Bignardi, "Additively manufactured custom load-bearing implantable devices: grounds for cautions," *Australasian Medical Journal*, vol. 10, no. 8, pp. 694–700, 2017.

[15] Q. Fu, E. Saiz, M. N. Rahaman, and A. P. Tomsia, "Bioactive glass scaffolds for bone tissue engineering: state of the art and future perspectives," *Materials Science and Engineering: C*, vol. 31, no. 7, pp. 1245–1256, 2011.

[16] E. Fiume, J. Barberi, E. Verné, and F. Baino, "Bioactive glasses: from parent 45S5 composition to scaffold-assisted tissue-healing therapies," *Journal of Functional Biomaterials*, vol. 9, no. 1, p. 24, 2018.

[17] F. Baino, E. Fiume, M. Miola, and E. Verné, "Bioactive sol-gel glasses: processing, properties, and applications," *International Journal of Applied Ceramic Technology*, vol. 15, no. 4, pp. 841–860, 2018.

[18] F. Baino and C. Vitale-Brovarone, "Three-dimensional glass-derived scaffolds for bone tissue engineering: current trends and forecasts for the future," *Journal of Biomedical Materials Research Part A*, vol. 97A, no. 4, pp. 514–535, 2011.

[19] S. Bose, S. Vahabzadeh, and A. Bandyopadhyay, "Bone tissue engineering using 3D printing," *Materials Today*, vol. 16, no. 12, pp. 496–504, 2013.

[20] J. W. Lee, J. Y. Kim, and D.-W. Cho, "Solid free-form fabrication technology and its application to bone tissue engineering," *International Journal of Stem Cells*, vol. 3, no. 2, pp. 85–95, 2010.

[21] G. Ambrogio, R. Conte, L. De Napoli, G. Fragomeni, and F. Gagliardi, "Forming approaches comparison for high customised skull manufacturing," *Key Engineering Materials*, vol. 651–653, pp. 925–931, 2015.

[22] R. Gmeiner, U. Deisinger, J. Schönherr et al., "Additive manufacturing of bioactive glasses and silicate bioceramics," *Journal of Ceramic Science and Technology*, vol. 6, no. 2, pp. 75–86, 2015.

[23] J. Cesarano, "Robocasting of ceramics and composites using fine particle suspensions," December 2018, https://www.researchgate.net/publication/236517891_Robocasting_of_Ceramics_and_Composites_Using_Fine_Particle_Suspensions.

[24] J. Franco, P. Hunger, M. E. Launey, A. P. Tomsia, and E. Saiz, "Direct write assembly of calcium phosphate scaffolds using a water-based hydrogel," *Acta Biomaterialia*, vol. 6, no. 1, pp. 218–228, 2010.

[25] Q. Fu, E. Saiz, and A. P. Tomsia, "Direct ink writing of highly porous and strong glass scaffolds for load-bearing bone defects repair and regeneration," *Acta Biomaterialia*, vol. 7, no. 10, pp. 3547–3554, 2011.

[26] X. Liu, M. N. Rahaman, G. E. Hilmas, and B. S. Bal, "Mechanical properties of bioactive glass (13–93) scaffolds fabricated by robotic deposition for structural bone repair," *Acta Biomaterialia*, vol. 9, no. 6, pp. 7025–7034, 2013.

[27] S. Eqtesadi, A. Motealleh, P. Miranda, A. Pajares, A. Lemos, and J. M. F. Ferreira, "Robocasting of 45S5 bioactive glass scaffolds for bone tissue engineering," *Journal of the European Ceramic Society*, vol. 34, no. 1, pp. 107–118, 2014.

[28] S. Eqtesadi, A. Motealleh, A. Pajares, F. Guiberteau, and P. Miranda, "Improving mechanical properties of 13–93 bioactive glass robocast scaffold by poly (lactic acid) and poly (ε-caprolactone) melt infiltration," *Journal of Non-Crystalline Solids*, vol. 432, pp. 111–119, 2016.

[29] A. M. Deliormanli and M. N. Rahaman, "Direct-write assembly of silicate and borate bioactive glass scaffolds for bone repair," *Journal of the European Ceramic Society*, vol. 32, no. 14, pp. 3637–3646, 2012.

[30] A. Motealleh, S. Eqtesadi, A. Civantos, A. Pajares, and P. Miranda, "Robocast 45S5 bioglass scaffolds: in vitro behavior," *Journal of Materials Science*, vol. 52, no. 15, pp. 9179–9191, 2017.

[31] M. Mattioli-Belmonte, C. De Maria, C. Vitale-Brovarone, F. Baino, M. Dicarlo, and G. Vozzi, "Pressure-activated microsyringe (PAM) fabrication of bioactive glass/poly(lactic-co-glycolic acid) composite scaffolds for bone tissue regeneration," *Journal of Tissue Engineering and Regenerative Medicine*, vol. 11, no. 7, pp. 1986–1997, 2017.

[32] E. Verné, O. Bretcanu, C. Balagna et al., "Early stage reactivity and in vitro behavior of silica-based bioactive glasses and glass-ceramics," *Journal of Materials Science: Materials in Medicine*, vol. 20, no. 1, pp. 75–87, 2009.

[33] "nScrypt", December 2017, https://www.nscrypt.com/wp-content/uploads/2018/11/2018-3Dn-Brochure.pdf.

[34] A. Nommeots-Nomm, P. D. Lee, and J. R. Jones, "Direct ink writing of highly bioactive glasses," *Journal of the European Ceramic Society*, vol. 38, no. 3, pp. 837–844, 2018.

[35] A. Macon, T. B. Kim, E. M. Valliant et al., "A unified in vitro evaluation for apatite-forming ability of bioactive glasses and their variants," *Journal of Materials Science: Materials in Medicine*, vol. 26, no. 2, p. 115, 2015.

[36] T. Kokubo and H. Takadama, "How useful is SBF in predicting in vivo bone bioactivity?," *Biomaterials*, vol. 27, no. 15, pp. 2907–2915, 2006.

[37] J. Radon, "Uber die bestimmung von funktionen durch ihre integralwerte langs geweisser mannigfaltigkeiten," *Berichte Saechsische Akad. der Wissenschaften*, vol. 29, pp. 262–277, 1917.

[38] J. Beyerer and F. Puente León, "Die Radontransformation in der digitalen Bildverarbeitung," *at—Automatisierungstechnik*, vol. 50, p. 472, 2002.

[39] M. Doube, M. M. Kłosowski, I. Arganda-Carreras et al., "BoneJ: free and extensible bone image analysis in ImageJ," *Bone*, vol. 47, no. 6, pp. 1076–1079, 2010.

[40] W. S. Rasband, *ImageJ*, U.S. National Institutes of Health, Bethesda, MD, USA, 2018, https://imagej.nih.gov/ij/.

[41] T. Hildebrand and P. Ruegsegger, "A new method for the model-independent assessment of thickness in three-dimensional images," *Journal of Microscopy*, vol. 185, no. 1, pp. 67–75, 1997.

[42] O. P. Filho, G. P. La Torre, and L. L. Hench, "Effect of crystallization on apatite-layer formation of bioactive glass 45S5," *Journal of Biomedical Materials Research*, vol. 30, no. 4, pp. 509–514, 1996.

[43] V. Karageorgiou and D. Kaplan, "Porosity of 3D biomaterial scaffolds and osteogenesis," *Biomaterials*, vol. 26, no. 27, pp. 5474–5491, 2005.

[44] T. Kokubo, H. Kushitani, S. Sakka, S. Kitsugi, and T. Yamamuro, "Solutions able to reproducein vivo surface-structure changes in bioactive glass-ceramic A-W3," *Journal of Biomedical Materials Research*, vol. 24, no. 6, pp. 721–734, 1990.

[45] L. L. Hench, "Bioactive ceramics," *Annals of the New York Academy of Sciences*, vol. 523, no. 1 Bioceramics, pp. 54–71, 1988.

[46] A. López-Noriega, D. Arcos, I. Izquierdo-Barba, Y. Sakamoto, O. Terasaki, and M. Vallet-Regí, "Ordered mesoporous bioactive glasses for bone tissue regeneration," *Chemistry of Materials*, vol. 18, no. 13, pp. 3137–3144, 2006.

[47] F. Baino, M. Marshall, N. Kirk, and C. Vitale-Brovarone, "Design, selection and characterization of novel glasses and glass-ceramics for use in prosthetic applications," *Ceramics International*, vol. 42, no. 1, pp. 1482–1491, 2016.

[48] F. Baino, E. Fiume, M. Miola, F. Leone, B. Onida, and E. Verné, "Fe-doped bioactive glass-derived scaffolds produced by sol-gel foaming," *Materials Letters*, vol. 235, pp. 207–211, 2019.

[49] R. Brückner, M. Tylkowski, L. Hupa, and D. S. Brauer, "Controlling the ion release from mixed alkali bioactive glasses by varying modifier ionic radii and molar volume," *Journal of Materials Chemistry B*, vol. 4, no. 18, pp. 3121–3134, 2016.

[50] A. Nommeots-Nomm, S. Labbaf, A. Devlin et al., "Highly degradable porous melt-derived bioactive glass foam scaffolds for bone regeneration," *Acta Biomaterialia*, vol. 57, pp. 449–461, 2017.

[51] L. L. Hench, "Bioceramics: from concept to clinic," *Journal of the American Ceramic Society*, vol. 74, no. 7, pp. 1487–1510, 1991.

[52] A. Rainer, S. M. Giannitelli, D. Accoto, S. D. Porcellinis, E. Guglielmelli, and M. Trombetta, "Load-adaptive scaffold architecturing: a bioinspired approach to the design of porous additively manufactured scaffolds with optimized mechanical properties," *Annals of Biomedical Engineering*, vol. 40, no. 4, pp. 966–975, 2012.

Research Article

Additive Manufacturing Applications on Flexible Actuators for Active Orthoses and Medical Devices

Michele Gabrio Antonelli,[1] **Pierluigi Beomonte Zobel** [ID],[1] **Francesco Durante,**[1] **and Terenziano Raparelli**[2]

[1]*Department of Industrial and Information Engineering and Economics, University of L'Aquila, via G. Gronchi n. 18, 67100 L'Aquila, Italy*
[2]*Department of Mechanical and Aerospace Engineering, Politecnico di Torino, Corso Duca degli Abruzzi 24, 10129 Torino, Italy*

Correspondence should be addressed to Pierluigi Beomonte Zobel; pierluigi.zobel@univaq.it

This paper describes the results of research projects developed at the University of L'Aquila by the research group of the authors in the field of biomedical engineering, which have seen an important use of additive manufacturing technologies in the prototyping step and, in some cases, also for the realization of preindustrialization prototypes. For these projects, commercial 3D printers and technologies such as fused deposition modelling (FDM) were used; the most commonly used polymers in these technologies are acrylonitrile butadiene styrene (ABS) and polylactic acid (PLA). The research projects concern the development of innovative actuators, such as pneumatic muscles and soft pneumatic actuators (SPAs), the development of active orthoses, such as a lower limb orthosis and, finally, the development of a variable-stiffness grasper to be used in natural orifice transluminal endoscopic surgery (NOTES). The main aspects of these research projects are described in the paper, highlighting the technologies used such as the finite element analysis and additive manufacturing.

1. Introduction

The authors have been engaged for several years in the development of innovative nontraditional actuators, and some of the research conducted on nontraditional pneumatic actuators, for example, for safety reasons, when the movements must take place avoiding that the moving parts constitute a danger to user, will be illustrated in this article. This is the case in the medical sector of assistive and rehabilitation devices, for example, an active orthosis, in which the patient interfaces directly with the device that has an autonomous movement capacity. In these cases, it is necessary that the actuator is intrinsically safe; therefore, it must not constitute a rigid system in movement but rather present adequate compliance for a greater system safety because this minimizes the risk of injury. Several researchers have developed compliant actuators able to perform a bending or a rotary movement and suitable for use in the biomedical and/or robotic field. These actuators are made of an elastomeric

material and are pneumatically powered. Different solutions are proposed for deformation: an element of appropriate shape made only of soft material or the combination of an element in soft material with a reinforcement of adequate internal stiffness. In [1], two categories of soft pneumatic actuators (SPAs), the bending SPA and the rotary SPA, are presented and characterized and a procedure for the design of the types of actuators shown is described. In [2], the concept of assembling modular units of fabric-based rotary actuators for the construction of soft pneumatic structures, interesting for the realization of gripping systems with performances suitable for different types of objects, is illustrated. In the following sections, the term SPAs will be used for these nontraditional pneumatic actuators. The SPAs shown here are made of silicone rubber or natural lattice, due to their high deformability and simplicity of processing, inside which one or more chambers are obtained to contain the compressed air. When the latter is sent into the chamber, the structure deforms symmetrically or asymmetrically, if

stiffness elements have been used (which can also be used to control the maximum deformation) or in the case of different thicknesses of the elastomeric material, as shown in Figure 1. The external load is applied through contact with the deformable surfaces. The power-to-weight ratio is higher than traditional actuators because they are very light materials. The force developed depends on the dimensions of the deformable chamber, the compressed air pressure value, the magnitude of the deformation caused, and the material used.

The intrinsic yielding of the elastomeric material makes these SPAs suitable for applications in the biomedical sector and makes it possible to realize actuators with geometries developed according to the specific application. These actuators require, for their realization, the preparation of a technological setup with the design and production of molds to which the silicone compound is poured, which allows the coupling of the half-shells. For the molds of various types of actuators realized, the additive manufacturing technology is frequently used. This technology has allowed the rapid and economic realization of the molds and the possibility of a simple optimization of the process even when it was necessary to modify the mold for a new realization. The properties of the polymeric materials used in 3D printers, such as ABS and PLA, meet the necessary strength and quality specifications, such as machining tolerances and surface finish, and they are easily operated with the usual design tools such as finite element analysis. Computer-aided design and finite element analysis have been among the most used tools for designing and sizing these innovative actuators and the manufacturing process. This paper shows some original development of SPAs, including applications in biomedical engineering, and of pneumatic muscle actuators, which are made up of elastomeric materials too. The McKibben pneumatic muscle is the most common type of braided muscle [3], and it will be discussed here. It is made of an inner elastomer tube surrounded by a braided shell and two ends. The straight fibres pneumatic muscle received less interest from the researchers [4], and it is formed by an elastomer tube inside in which there is an axial texture of cables, from one end to the other, and externally by circumferential rings that constrain the radial expansion. For both types of pneumatic muscles, the air inlet causes a radial expansion followed by an axial contraction of the heads, which allows an external traction work. This paper will also describe the research activity that led to the design and prototype realization of a remote-controlled surgical grasper, and of its variable-stiffness actuation (VSA) system, for whose technological development, the additive manufacturing was used. The robotics for the NOTES, also called natural orifice transluminal endoscopic robotic surgery (NOTERS), requires specific and customized solutions, such as a snail-like robot and the variable-stiffness actuation (VSA) implementation proposed in [5, 6]. Snail architecture uses a chain of elements connected to each other: the driver is placed near each joint, and the end effector can be guided with high dexterity in the peritoneal cavity. The VSA is recommended for developing high-performance devices for NOTERS, where intrinsic safety is required for both involuntary impact with internal organs and gripping, avoiding any potential damage to the soft tissue that is grasped. The use of SPA in the surgical gripper has proved to be very useful for the necessity of the VSA and for the extreme compactness required. With the NOTES, the abdominal cavity is reached in the absence of external incisions, exploiting the natural cavities such as the mouth, the rectum, and the vaginal conduit.

2. Materials and Methods

About the material used for soft pneumatic actuators and pneumatic muscles, since the constitutive law of the elastomeric material is nonlinear, as well as the behaviour of the air, being a compressible fluid, it is very complex to identify analytical correlations, assigned a geometry, among the deformation, the developed force and the pressure within the actuator chamber. Therefore, for the design of the actuators, the numerical modelling by the finite element method is carried out and, in some cases, for pneumatic muscles, the dimensional analysis is carried out, which allowed building a design graph based on three dimensionless parameters, which contain the quantities that influence the behaviour of the actuator. Several authors have developed models of pneumatic muscles of the braided type with the finite element method: the nonlinearity of the rubber tube has been simulated with the Mooney–Rivlin formulation with two coefficients as the mechanism for transferring the load to the braided shell [7]. Some authors [8] have proposed a nonlinear model to analyze the relationship between different muscles arranged in parallel and the total contraction ratio of each of them. This model examined geometric nonlinearity, while the behaviour of the rubber material was considered linear. Other authors [9] proposed a model to optimize the angle of the braided shell, and in [10], a method of quantitative optimization of the project is shown. The analysis of the scientific literature highlights the lack of a numerical model of the braided pneumatic muscle that is built on the real geometrical characteristics of the braided shell, as it is commercially available. In these models, the braided shell is analysed with average parameters available in the literature. The finite element model of the braided pneumatic muscle developed by the authors has been experimentally validated [11]. The model developed is nonlinear and based on real muscle parameters. It is proposed to predict the muscle behaviour and act as a reliable design tool. Several prototypes have been made of this muscle, and they have been applied in research projects for the development of orthoses. In Figures 2(a)–2(c), an example of numerical results of an isotonic test simulation, based on the model proposed, is shown. A research work was also carried out for straight fibres pneumatic muscles [12], and in Figure 2(d), an example of a characteristic graph obtained with the design curve is shown together with the curve required by the designer (traction force F vs. shortening ΔL) for a biomedical application.

The soft pneumatic actuators (SPAs), the straight fibres, and the braided pneumatic muscles require the experimental
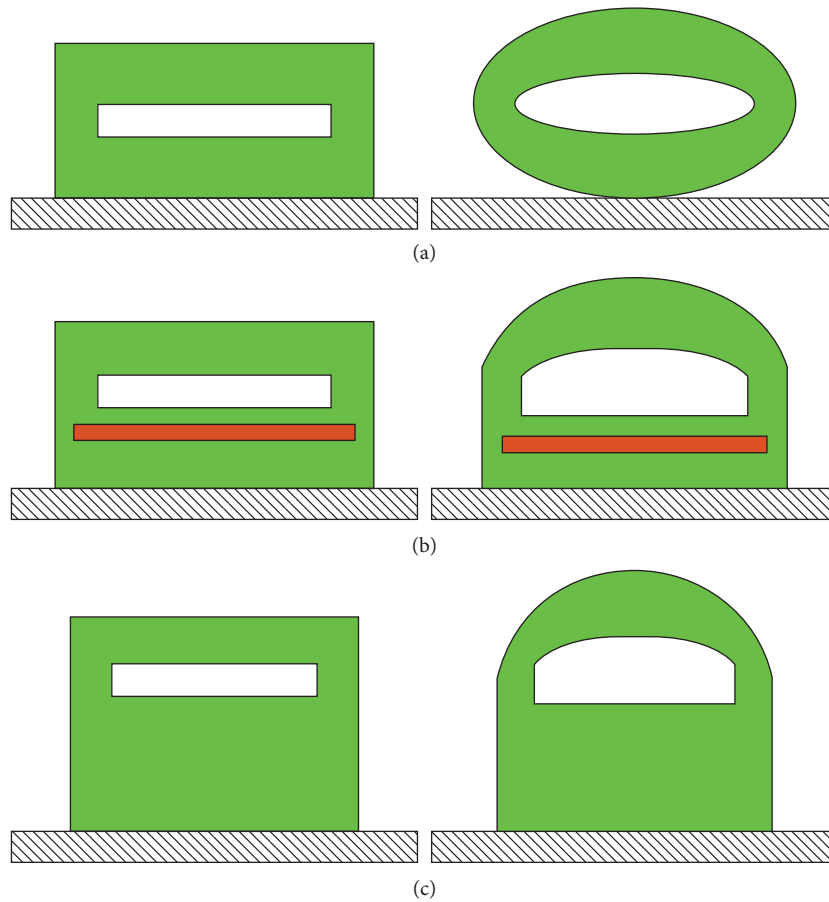
FIGURE 1: Mode of SPA deformation: (a) symmetrical; (b) unilateral, by inserting stiffness material or (c) through increase in thickness.
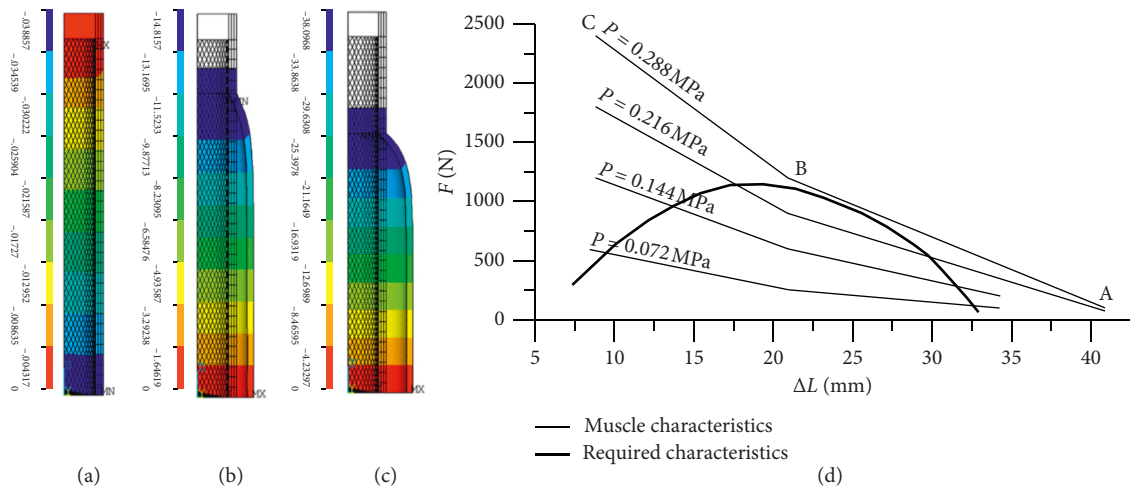
FIGURE 2: Numerical results of an isotonic test simulation with the braided pneumatic muscle model: (a) rest muscle; (b) during shortening; (c) at maximum inflation speed (side view). Graph obtained by connecting the design curve of the straight fibre pneumatic muscle together with the curve desired by the designer (d).

identification of the constitutive law of the elastomeric material used (e.g., Silastic E of Dow Corning). In the presence of actuator symmetries, the geometry modelled by the finite elements can represent half or a quarter of the entire geometry (Figure 3).

Usually, it is sufficient to create two models: a model that simulates the isometric test conditions and the one that simulates isotonic ones. In the first case, with constant deformation, the force value developed by the actuator is correlated to the air pressure; in the second, at constant load,

Ansys 5.4
May 29, 2005
18:43:26
Nodal solution
Step = 1
Sub = 10
Time = 1
USUM
RSYS = 0
DMX = 19.359
SMX = 19.359

- 0
- 2.151
- 4.302
- 6.453
- 8.604
- 10.755
- 12.906
- 15.057
- 17.208
- 19.359

(a) (b)
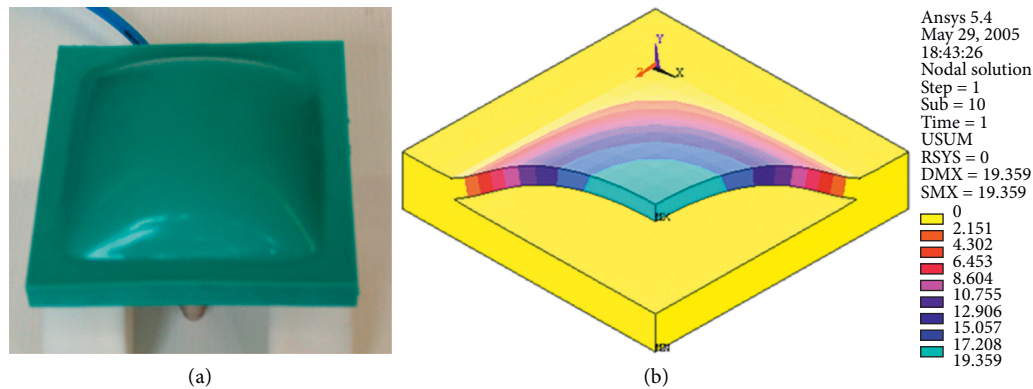
FIGURE 3: Example of a SPA prototype with an output of the finite element model.

the deformation of the actuator correlates with the air pressure. The finite elements used for the silicone rubber modelling are of the brick type, and the elastomeric material is modelled by the Mooney–Rivlin formulation with two coefficients. Once the actuator has been sized, the first step is the designing of the mold, made of polymeric materials by additive manufacturing. Then, the preparation of the silicone rubber starts as follows: before the catalysis takes place, the rubber has a very fluid consistency and is easily pourable. Before casting, it is advisable to proceed with the removal of air bubbles present in the silicone rubber mix, to avoid inclusions inside the actuator. Thus, the casting is carried out. Depending on the type of SPA, the construction can take place in a single casting or in successive phases. The second mode occurs when a metal plate or a bar is incorporated into the actuator to limit deformation in an assigned direction or when multichamber actuators are to be made. Thus, the construction of a first layer of the actuator is carried out. And the mixture is expected to start to solidify, and the high stiffness material is deposited; then, a second casting is carried out; the second casting is expected to start to solidify and the material for the construction of the chamber is laid below another casting until the entire mold is filled. Typically, the construction of the chamber is carried out by a sheet of paper or by wax, according to requirements. An example of embodiment of a square-shaped SPA is shown in Figure 4. The conduit for air supply and discharge can be integrated with the actuator (in this case, it is made of silicone rubber during the casting process) or the mold is designed with a cavity inside the actuator, where the valve will be placed.

3. Results and Discussion

3.1. Actuators and Active Orthoses.
The types of pneumatic actuators presented here belong to two different families: pneumatic muscles and soft pneumatic actuators (SPAs). The former have been the subject of research activities and find space in some industrial applications, as they are available in the automation components market; the latter are not present in the market but are often designed ad hoc and integrated into commonly used devices such as blood pressure measurement systems and other medical devices,

such as car seats and massage chairs. Two types of pneumatic muscles have been developed [11, 12]: straight fibres and braided, also known as McKibben muscle. The straight fibres pneumatic muscle (Figure 5(a)) is made of a silicone cylindrical chamber in the wall in which a cage consists of 40 Kevlar threads, arranged longitudinally and held in position by two end rings, in which one is buried inside the silicone and the other is connected to the head that contains the air supply/discharge pipe. The pneumatic and mechanical seal is ensured by means of clamping systems with the tube at the heads. To limit the radial deformation of the muscle, metal circumferential rings are arranged externally of the cylindrical chamber. The pneumatic muscle of the McKibben type (Figure 5(b)) is formed by using a cylindrical chamber made of the elastomeric material, a sheath consisting of a rhomboidal mesh that covers the chamber externally, and two heads which have the function of isolating the chamber, blocking the sheath on the outside of the chamber, and allowing the anchorage of the muscle to the device. On one of the two heads, the air supply/discharge hole is made. The sheath is of the braided type and has a cylindrical shape: the wires, in polyamide, are placed side by side in numbers of six and wound to form 42 spirals that create rhomboidal meshes. Sending air into the chamber causes an increase in volume so that the outer surface of it comes into contact with the outer sheath; the muscle contracts due to the high axial rigidity of the wires forming the sheath. Table 1 shows the characteristics of the silicone muscles made. Pneumatic muscles have been used in research applications in the biomedical sector: those with straight fibres for the movement of an anthropomorphic rehabilitation robot of the upper limb and with the braided muscles for the movement of an inferior and upper limb orthosis.

The active orthosis for inferior limb is a research project born with the aim of developing a solution to allow the elderly, and people with weak strength in the legs, to have a wearable device under the pants that can give them additional strength in the legs to allow them to get up from a sitting position. The result of this research activity [13] is an optimized prototype of a one degree-of-freedom lower limb orthosis with a light structure; it is made of carbon fibre and naturally activated with a sensor that detects the contraction of the quadriceps femoris of the user.
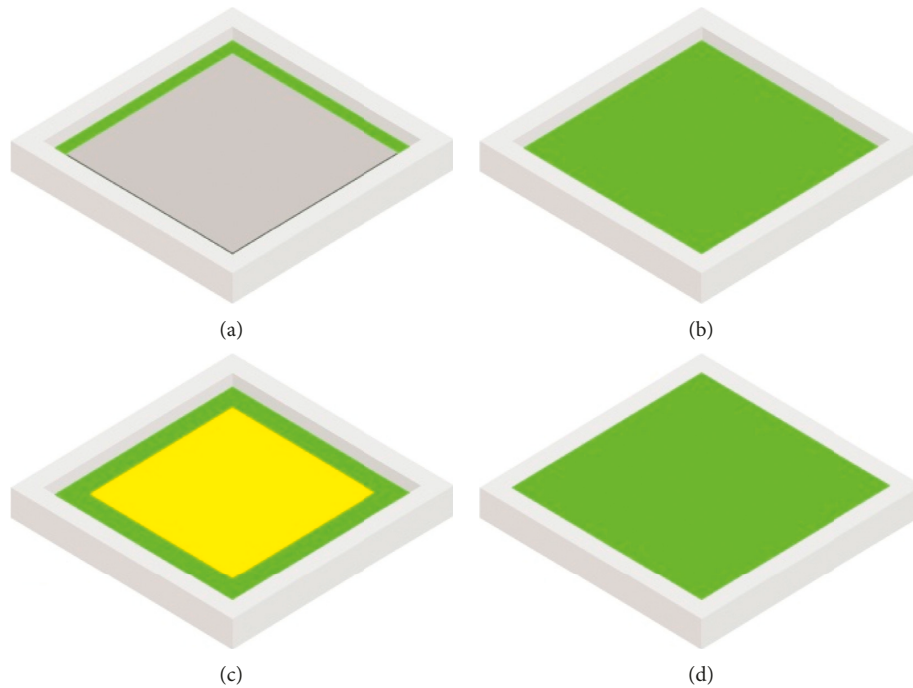
Figure 4: Steps of manufacturing a square-shaped SPA: after solidification of the first silicone layer, (a) deposition of an element with high rigidity; (b) deposition of a second layer of silicone; (c) deposition of a sheet of paper or wax for the realization of the volume; (d) filling the mold with another layer of silicone.
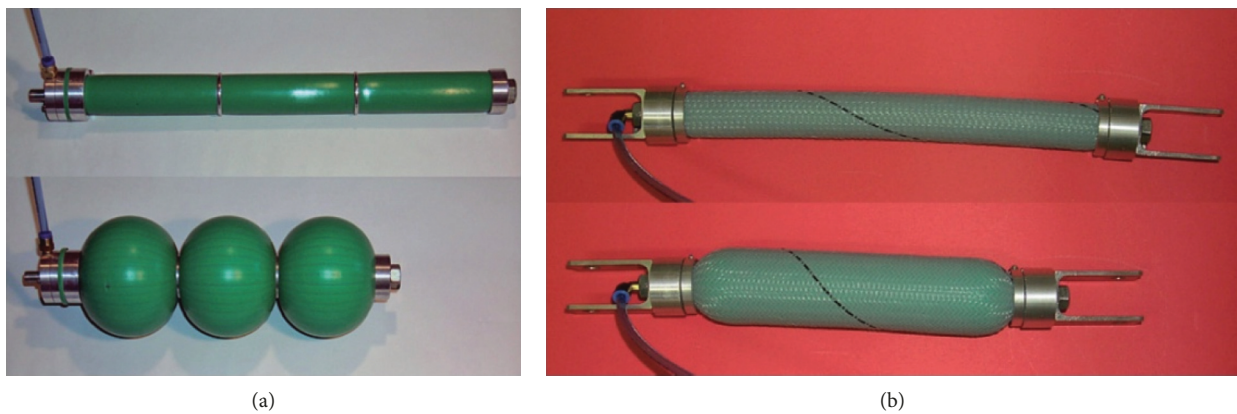
Figure 5: Prototypes of pneumatic muscles developed: straight fibres (a) and braided (b), also known as McKibben muscle.

Table 1: Main characteristics of silicone pneumatic muscles made.

Type of pneumatic muscle	Length (mm)		External diameter (mm)		P_{max} (bar)	F_{max} (N)
	At rest	At maximum contraction	At rest	At maximum contraction		
Straight fibres	300	217	30	91	1.5	1000
Braided	285	209	30	54	2.5	500

This type of command allows the orthosis to be activated even when the user is sitting, avoiding the impact on the seat that can cause traumas. The carbon fibre structure is made in laboratories using a fibre sock, suitable for making tubular structures with a diameter from 20 to 45 mm, impregnated with epoxy resin through an ABS mold manufactured by additive manufacturing. The mold is hollow and made of two shells. To allow the correct polymerization of the fibre inside the mold in the desired thicknesses, a rubber cylinder was inserted and subsequently filled with pressurized air so as to obtain an adequate thrust of the fibre against the inner surface of the mold. During the polymerization, the vertical arrangement was used which guaranteed the best surface finish of the product. In Figure 6(a), one of the orthotics
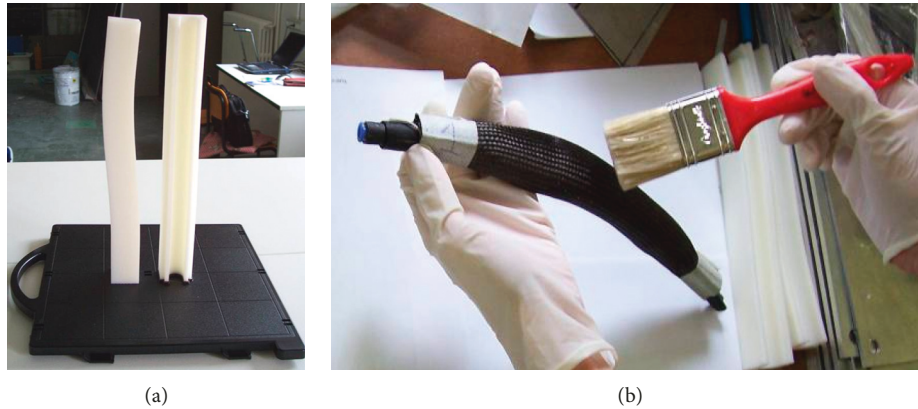
Figure 6: Mold shells made of ABS by additive manufacturing (a) and an impregnation step of the carbon fibre braided with the resin (b).

molds, 244 mm long, is visible, while in Figure 6(b), the resin application on the socks of carbon fibre, after having inserted them into the rubber cylinder, is shown.

Figure 7(a) shows the rubber cylinder coated by the socks into the mold, while in Figure 7(b), the manufactured tube in carbon fibre is shown and, finally, the prototype of orthosis assembled is shown in Figure 8. The sock in carbon fibre has a thickness of about 0.5 mm and, to obtain a thickness of about 2 mm for the structure, it was necessary to use 4 layers of sock, at whose ends an adhesive was applied to keep the fibres in the desired arrangement. The impregnation with the epoxy resin takes place after the insertion of the first sock on the rubber cylinder and continued after the insertion of each of the following carbon fibre socks. On the inside wall of the mold, it was necessary to apply a detaching wax to prevent adhesion between the carbon fibre and the ABS mold. After the mold has been closed, the cylinder has been brought to a pressure of 1 bar and therefore kept in the oven for a thermal cycle of 20 hours at 45°C. Once the polymerization was finished and the product was extracted, an acrylic finishing layer was applied.

Square-shaped SPAs were made and inside which a chamber is located to fill compressed air. The planar geometry of the SPAs can be different depending on the application: square, rectangular, circular, semicircular, and toroidal. The geometry of the chamber reproduces the geometry of the external shape of the actuator, but in some cases, it may be different. Regardless of the profile of the perimeter, the actuators are characterized by having the nondeformable perimeter. Inside the SPA can be located a single volume or several volumes, each with its own air supply/discharge channel or connected to each other but with a single air channel. Simple types of single-chamber SPA have been designed for applications in the medical field. A series of actuators has been installed inside a scoliosis brace in order to apply a push action on the spine [14]. These are SPAs with a single square-shaped chamber. The chamber deforms unilaterally, having placed a metal plate at the other end. The air supply/exhaust channel was obtained by means of a common tire tube valve for bicycle use and mounted on the side where the metal plate is present, as shown in Figure 9.
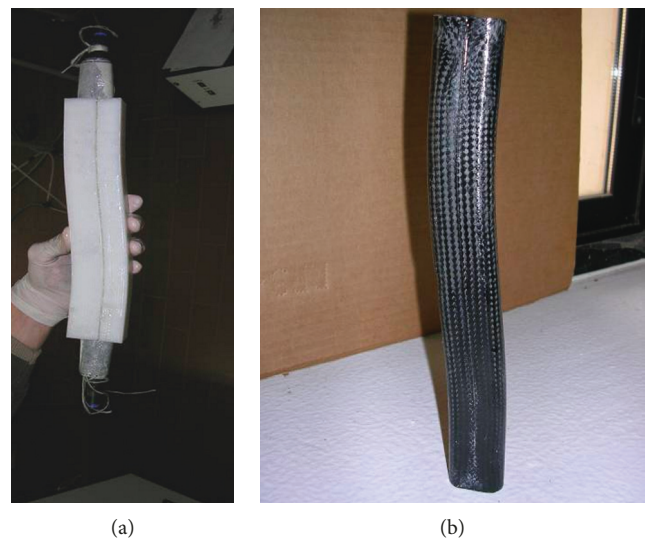
Figure 7: Mold of the pneumatic core coated with the impregnated carbon fibre socks (a) and the result obtained after polymerization (b).

The therapist using a manual bag to inflate adjusts the air pressure for each soft pneumatic actuator. A SPA with several chambers, each having its air supply/discharge channel, has been designed and manufactured for the massage device shown in Figure 10 [15].

The multichamber SPA, mounted on a structure that is worn by the subject and which is in contact with the lumbar segment of the spine, applies a compression action. The intensity of this thrust is adjusted by varying the pressure value inside the chamber. Each multichamber SPA has 6 small actuators. The actuator is deformed from one side; on the opposite side, a metal plate is placed and the silicone air supply/discharge channel is obtained. The massage device consists of 8 SPAs with a total of 48 actuators. By suitably filling the different volumes, the common massage techniques used by the physiotherapist are reproduced. The order of feeding the chambers and the pressure and the frequency of air supply/discharge are managed by a programmable logical controller. In Figure 11, the result of the

FIGURE 8: Prototype of lower limb orthosis made of carbon fibre with aluminum joints.

(a)

(b)
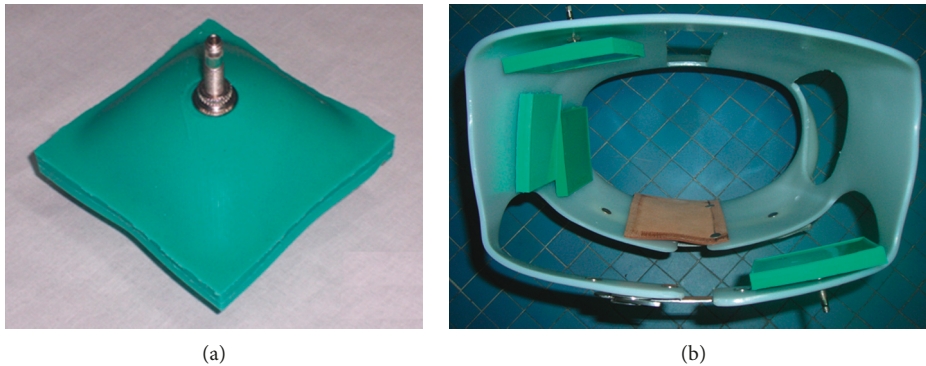
FIGURE 9: Square-shaped SPA (a) and application in a brace for scoliosis with the thrusts in specific points of the spine (b).

(a)

(b)
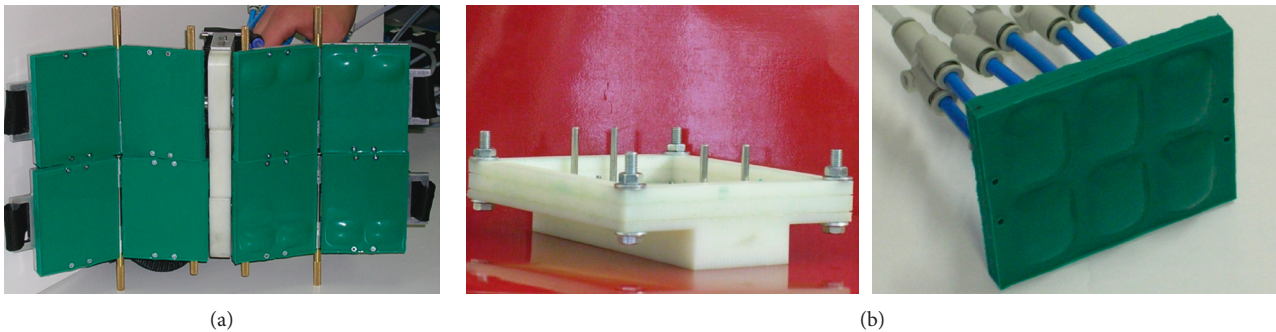
FIGURE 10: Spine massage device (a) and details of the multichamber SPA and of the processing mold (b).

characterization tests carried out on the multichamber SPA is shown. Similar technology has been used for developing an articulated finger for a gripper device [16] and for an active brace for the unloading of the lumbar spine [17]. The brace is made with two rigid elements, one lower and one upper, respectively, in contact with the iliac crests and with the thoracic sockets. Distancing the two elements from each other produces an unloading of the lumbar spine section. The movement of the rigid elements is entrusted to the actuators, interposed between them, and positioned at the sides of the user.

The SPAs with several chambers, located on different planes in a parallel disposition, joined together by a single air supply/discharge channel, and made of silicone rubber during the casting phase of the actuator, are shown in Figure 12(a). In Figure 12(b), the prototype of the active brace is shown, and the characteristic curve of strength F vs. displacement Δh is shown in Figure 13.

Each multichamber SPA consists of 5 chambers of semicircular geometry, symmetrically deformable. The therapist using a manual bag to inflate adjusts the air pressure value, following the medical prescription. Table 2 shows the dimensional and functional characteristics of the realized silicone rubber SPAs.

3.2. Medical Devices. Additive manufacturing is spreading more and more for manufacturing medical devices with the aim of using them as customized prostheses that the single surgeon adapts and prints for the specific patient. At present, the critical issues are related not so much to static loads as to cyclic loads, as was shown for load-bearing implants [18]. By using the additive manufacturing for the soft pneumatic actuator (SPA), the research project on a surgical grasper has been carried out. It has the focus in the natural orifice transluminal endoscopic surgery (NOTES) where the

(a)

(b)
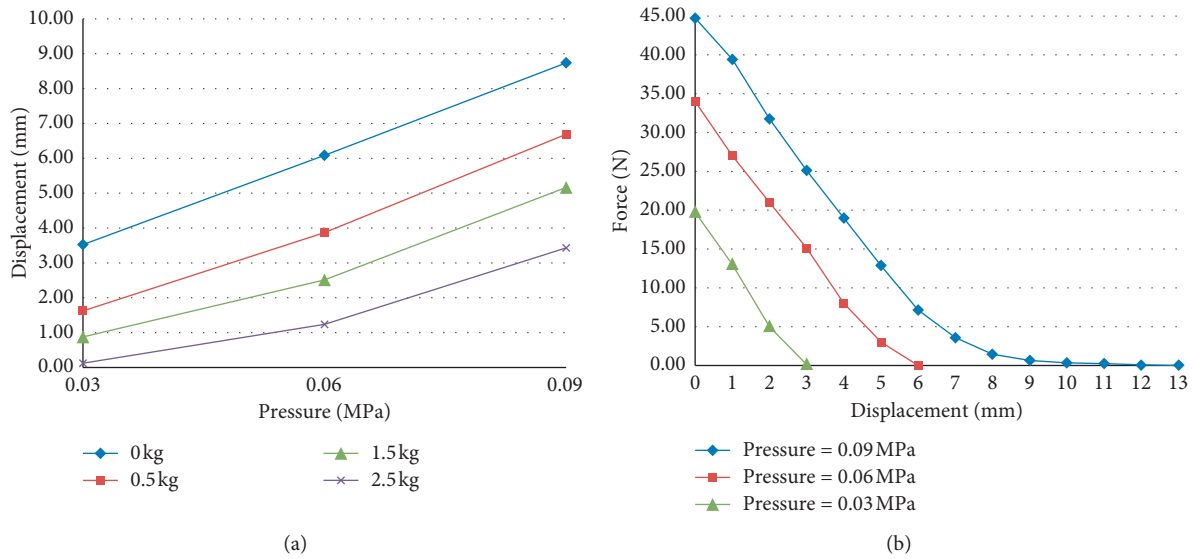
FIGURE 11: Results of characterization tests on multichamber SPA: isotonic displacement vs. pressure and isometric force vs. displacement.

(a)

(b)

FIGURE 12: Multichamber SPA (a) and the prototype of the active brace (b).
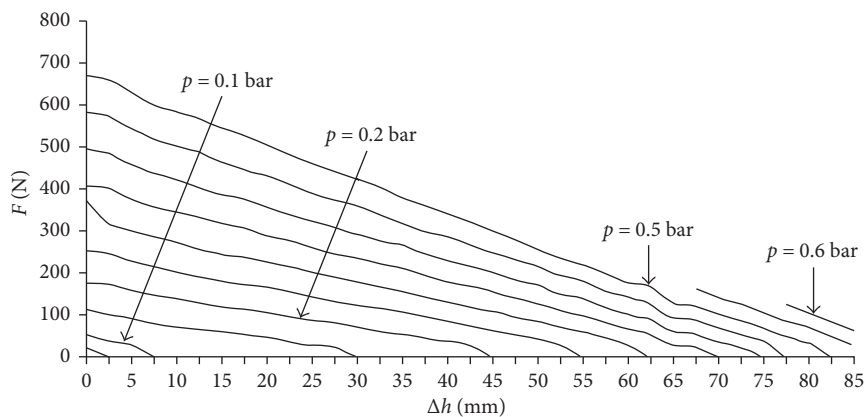
FIGURE 13: Characteristic curve of the brace built in the laboratory as strength F vs. displacement Δh at different pressure values.

abdominal cavity is reached, exploiting the natural cavities such as the mouth, the rectum, and the vaginal conduit. The advantage of this type of surgery is represented by the absence of scars, the reduction of the recovery time, and the recovery of the patient. Due to the limitations of current surgical instruments for laparoscopy, NOTES must necessarily resort to robotic systems operated by the surgeon and become natural orifice transluminal endoscopic robotic surgery (NOTERS). In the NOTERS, collision safety can be ensured by yielding devices that reduce the effects of the

TABLE 2: Main features of the silicone rubber SPAs.

Field of application	Dimensions, $b \times h \times s$ (mm^3)	Type of deformation	Maximum deformation (mm)	P_{max} (bar)	F_{max} (N)
Brace for scoliosis	$80 \times 80 \times 10$	Monolateral	40	0.6	100
Grasper	$60 \times 40 \times 10$	Symmetrical	14	0.8	90
Massage device	$44 \times 36 \times 9^*$ $104 \times 123 \times 9^{**}$	Monolateral	10	1	30
Brace for unloading the spine	$128 \times 88 \times 6^{***}$	Symmetrical	20	0.5	800

*Dimension of the single-channel SPA; **dimension of the multichannel SPA; ***external radius × internal radius × thickness.

(a)   (b)
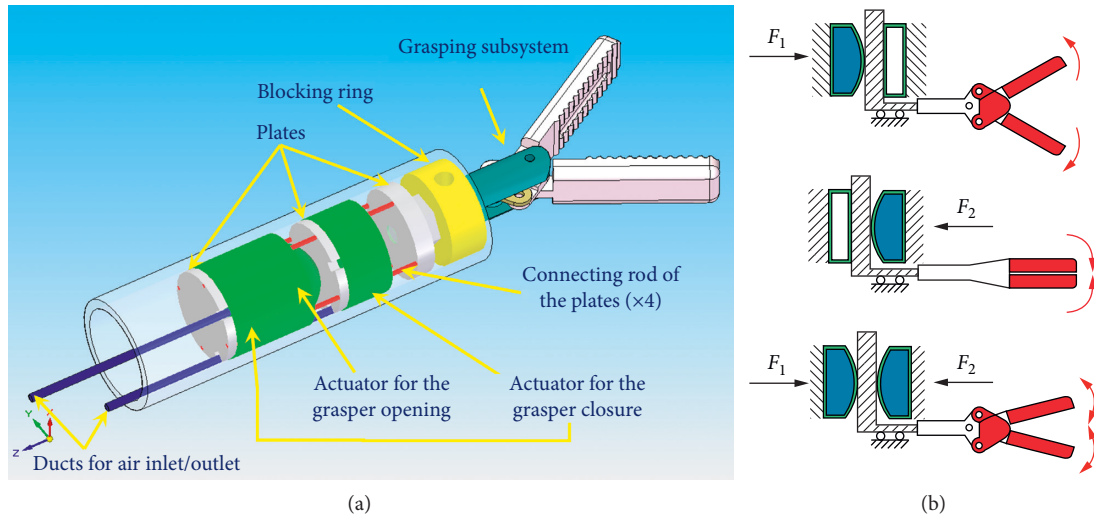
FIGURE 14: Axonometric view of the developed surgical grasper (a) and the principle of operation of the actuation module (b).

impact on the patient; performance depends heavily on the interaction of the operating mechanics of the surgical instrument with the control system. To meet both requirements, several solutions have been proposed: decoupling the inertia of the instrument implementation system from the inertia of its structure, by means of an elastic transmission; the use of a pair of actuators, one of which is used in low-frequency and the other in high-frequency applications; the use of variable-stiffness systems [19], which is the solution chosen for the developed prototype of the surgical grasper presented here with the focus on the SPA. The main technical specifications underlying the implementation of this surgical grasper, for the type of grip adopted, are as follows: variable stiffness, ability to exert a maximum force equal to 11.50 N, and ability to allow a maximum displacement of the rod of the subassembly of 2.4 mm. Furthermore, the outer diameter of the entire prototype implementation subassembly must not exceed 12 mm. The operating principle of the SPA is shown in Figure 14(b). The solution developed for the implementation of a variable-stiffness device for the miniaturized graspers (Figure 14(a)) is pneumatic actuation by means of a SPA, made of silicone rubber, mounted in line, and arranged in agonist-antagonist position, as shown in Figure 15(b). The prototype of the gasper is shown in Figure 15(a).

These circular-shaped SPAs are characterized by having inside them an air chamber formed between two circular silicone rubber surfaces, connected to each other along the circumference: sending air into the chamber causes a

deformation of the actuator, due to the silicone's compliance, which can occur at both the surfaces or only one, depending on the construction mode. The agonist-antagonist mode of the actuator system is necessary for opening and closing of the grasper. by acting on the air pressure inside the chambers, it is possible to control the stiffness of the transmission, as shown in Figure 14(b). The realization of the SPAs has been facilitated by the use of FDM technology of additive manufacturing with different materials, and the best results for the application have been obtained with the ABS. The designing of the actuators was carried out by means of numerical modelling by finite elements technique, also thanks to the know-how of the authors on the modelling of silicone rubber SPAs. Isometric models were simulated to derive the force developed by the actuator as a function of the pressure, for an assigned deformation. The optimal solution was provided by the actuator model characterized by an external diameter of 10 mm, a diameter of the deformable surface equal to 8 mm, and a thickness of the deformable surface equal to 1 mm. From the analysis of the results, it is observed that, for a typical stroke of 1.8 mm, only one actuator is able to exert a force equal to 7 N at 0.3 MPa, sufficient to close the clamp when the load is applied to it externally with a maximum load of 3 N. For the maximum stroke of 2.4 mm, the 0.3 MPa actuator exerts a force of 6 N. In compliance with the specifications, it was established to adopt a pair of SPAs for closing the clamp and a single SPA for opening. The latter requires a minimum of negligible force. The prototype grasper shown in

(a)

(b)
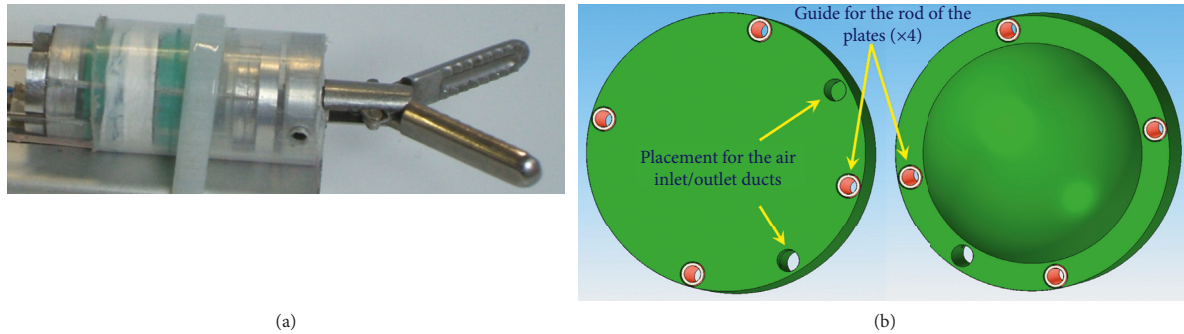
FIGURE 15: Prototype of NOTERS grasper realized (a) and view of the circular-shaped SPA (b).

Figure 15(a) was submitted to a campaign of laboratory validation tests that gave very positive results.

4. Conclusion

This paper shows the main results of the research activities carried out by the authors in the field of pneumatic muscles and soft pneumatic actuators for use in active orthoses and medical devices. In this field, a wide use was made of additive manufacturing technology, for the realization of the molds, and of computer-aided design tools and of the finite element method for designing and sizing of the actuators and devices in which they have been applied. The actuators presented are pneumatic muscles and square-sized and circular-sized SPAs. The latter were applied to a scoliosis brace, to a massage device, to a spinal unloading brace, and to a surgical grasper, the main results of which have been described in the paper. The application of additive manufacturing in the construction of molds for the manufacturing of the prototype of lower limb orthosis in carbon fibre is also presented. The results obtained are of scientific interest, and the applications presented demonstrate the effectiveness of additive manufacturing technology in the field of assistive devices and rehabilitation systems, as well as computer-aided design and the finite element method. The research work is in progress for some applications with the study of other elastomers such as natural latex, which allow a better resistance to fatigue than silicone.

Data Availability

The authors state that the results cited in this research work are related to numerical simulations and to experimental test campaigns. Data supporting the findings of this study are available from the corresponding author [PBZ] on request.

Conflicts of Interest

The authors declare that they have no conflicts of interest regarding the publication of this manuscript.

Acknowledgments

References

[1] Y. Sun, Y. S. Song, and J. Paik, "Characterization of silicone rubber based soft pneumatic actuators," in *Proceedings of the IEEE/RSJ International Conference on Intelligent Robots and Systems*, pp. 4446–4453, Tokyo, Japan, November 2013.

[2] P. M. Khin, H. K. Yap, M. H. Ang, and C.-H. Yeow, "Fabric-based actuator modules for building soft pneumatic structures with high payload-to-weight ratio," in *Proceedings of the IEEE/RSJ International Conference on Intelligent Robots and Systems (IROS)*, pp. 2744–2750, Vancouver, Canada, September 2017.

[3] F. Daerden and D. Lefeber, "Pneumatic artificial muscles: actuators for robotics and automation," *European Journal of Mechanical and Environmental Engineering*, vol. 47, no. 1, pp. 11–21, 2002.

[4] A. Morecki, "Polish artificial pneumatic muscles," in *Proceedings of the 4th International Conference on Climbing and Walking Robot*, Karlsruhe, Germany, September 2001.

[5] F. E. Cepolina and M. Zoppi, "Design of multi-degrees-of-freedom dexterous modular arm instruments for minimally invasive surgery," *Proceedings of the Institution of Mechanical Engineers, Part H: Journal of Engineering in Medicine*, vol. 226, no. 11, pp. 827–837, 2012.

[6] M. Zoppi, R. Molfino, and P. Cerveri, "Modular micro robotic instruments for transluminal endoscopic robotic surgery: new perspectives," in *Proceedings of the 2010 IEEE/ASME Conference on Mechatronics and Embedded Systems and Applications (MESA)*, pp. 440–445, Qingdao, China, July 2010.

[7] A. Manuello Bertetto and M. Ruggiu, "Characterization and modeling of air muscles," *Mechanics Research Communications*, vol. 31, no. 2, pp. 185–194, 2004.

[8] S. Wakimoto, K. Suzumori, and J. Takeda, "Flexible artificial muscle by bundle of McKibben fiber actuators," in *Proceedings of the 2011 IEEE/ASME International Conference on Advanced Intelligent Mechatronics (AIM)*, pp. 457–462, Budapest, Hungary, July 2011.

[9] K. Iwata, K. Suzumori, and S. Wakimoto, "A method of designing and fabricating McKibben muscles driven by 7 MPa

hydraulics," *International Journal of Automation Technology*, vol. 6, no. 4, pp. 482–487, 2012.

[10] T. Nozaki and T. Noritsugu, "Motion analysis of McKibben type pneumatic rubber artificial muscle with finite element method," *International Journal of Automation Technology*, vol. 8, no. 2, pp. 147–158, 2014.

[11] M. G. Antonelli, P. Beomonte Zobel, F. Durante, and T. Raparelli, "Numerical modelling and experimental validation of a McKibben pneumatic muscle actuator," *Journal of Intelligent Material Systems and Structures*, vol. 28, no. 19, pp. 2737–2748, 2017.

[12] F. Durante, M. G. Antonelli, P. B. Zobel, and T. Raparelli, "Development of a straight fibers pneumatic muscle," *International Journal of Automation Technology*, vol. 12, no. 3, pp. 413–423, 2018.

[13] F. Durante, P. B. Zobel, and T. Raparelli, "Development of an active orthosis for inferior limb with light structure," *Advances in Service and Industrial Robotics*, vol. 49, pp. 833–841, 2018.

[14] M. G. Antonelli, P. Beomonte Zobel, P. Raimondi, T. Raparelli, and G. Costanzo, "An innovative brace with pneumatic thrusts for scoliosis treatment," *International Journal of Design & Nature and Ecodynamics*, vol. 5, no. 4, pp. 354–367, 2010.

[15] M. G. Antonelli, P. Beomonte Zobel, F. Durante, and T. Raparelli, "Development and pre-clinical investigation of a massage device for the low back," *International Journal of Mechanical Engineering and Technology*, vol. 9, no. 2, pp. 742–754, 2018.

[16] M. G. Antonelli, W. D'Ambrogio, and F. Durante, "Development of a pneumatic soft actuator as a hand finger for a collaborative robot," in *Proceedings of the 2018 2nd International Conference on Mechatronics Systems and Control Engineering (ICMSCE 2018)*, pp. 67–71, Amsterdam, Netherlands, February 2018.

[17] T. Raparelli, P. Beomonte Zobel, F. Durante, M. G. Antonelli, P. Raimondi, and G. Costanzo, "First clinical investigation on a pneumatic lumbar unloading orthosis," in *Proceedings of the IEEE/ICME International Conference on Complex Medical Engineering (CME)*, article 4381959, pp. 1327–1330, Beijing, China, May 2007.

[18] E. M. Zanetti, A. Aldieri, M. Terzini, M. Calì, G. Franceschini, and C. Bignardi, "Additively manufactured custom load-bearing implantable devices: grounds for caution," *Australasian Medical Journal*, vol. 10, no. 8, pp. 694–700, 2017.

[19] M. G. Antonelli, P. Beomonte Zobel, F. Durante, and F. Gaj, "Development and testing of a grasper for NOTES powered by variable stiffness pneumatic actuation," *International Journal of Medical Robotics and Computer Assisted Surgery*, vol. 13, no. 3, article e1796, 2017.

Review Article

The Role of 3D Printing in Medical Applications: A State of the Art

Anna Aimar [ID],[1] **Augusto Palermo,**[2] **and Bernardo Innocenti** [ID][3]

[1]*Aid4Med S.r.l., Udine 33100, Italy*
[2]*Head 3 Orthopaedic Department, Istituto Auxologico Italiano IRCCS Capitanio Hospital, Milan 20122, Italy*
[3]*BEAMS Department, Université Libre de Bruxelles, Bruxelles 1050, Belgium*

Correspondence should be addressed to Anna Aimar; anna.aimar@aid4med.com

Three-dimensional (3D) printing refers to a number of manufacturing technologies that generate a physical model from digital information. Medical 3D printing was once an ambitious pipe dream. However, time and investment made it real. Nowadays, the 3D printing technology represents a big opportunity to help pharmaceutical and medical companies to create more specific drugs, enabling a rapid production of medical implants, and changing the way that doctors and surgeons plan procedures. Patient-specific 3D-printed anatomical models are becoming increasingly useful tools in today's practice of precision medicine and for personalized treatments. In the future, 3D-printed implantable organs will probably be available, reducing the waiting lists and increasing the number of lives saved. Additive manufacturing for healthcare is still very much a work in progress, but it is already applied in many different ways in medical field that, already reeling under immense pressure with regards to optimal performance and reduced costs, will stand to gain unprecedented benefits from this good-as-gold technology. The goal of this analysis is to demonstrate by a deep research of the 3D-printing applications in medical field the usefulness and drawbacks and how powerful technology it is.

1. Introduction

Among the different manufacturing processes that are currently adopted by the industry, the 3D printing is an additive technique. It is a process through which a three-dimensional solid object, virtually of any shape, is generated starting from a digital model. Medical 3D printing was once an ambitious pipe dream. However, time and investment made it real. Nowadays, the 3D printing technology represents a big opportunity to help pharmaceutical and medical companies to create more specific drugs, enabling a rapid production of medical implants and changing the way that doctors and surgeons plan procedures [1]. This technology has multiple applications, and the fastest growing innovation in the medical field has been represented by the advent of the 3D printing itself [2]. Five technical steps are required to finalize a printed model. They include selecting the anatomical target area, the development of the 3D geometry through the processing of the medical images coming from a CT/MRI scan, the optimization of the file for

the physical printing, and the appropriate selection of the 3D printer and materials (Figure 1). This file represents the guidance for the subsequent printing, "slicing" that digital design model into cross sections. That "sliced" design is then sent to a 3D printer, which manufactures the object by starting at the base layer and building a series of layers on top until the object is built using the raw materials that are needed for its composition. A patient-specific model with anatomical fidelity created from imaging dataset is finally obtained.

In this way, the 3D printing has the potential to significantly improve the research knowledge and the skills of the new generation of surgeons, the relationship between patient and surgeon [3], increasing the level of understanding of the disease involved, and the patient-specific design of implantable devices and surgical tools [4–6] and optimize the surgical process and cost [7]. Nowadays, different printing techniques and material are available in order to better reproduce the patient anatomy. Most of the available printing materials are rigid and therefore not
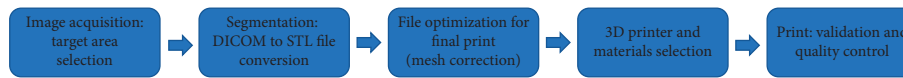
FIGURE 1: 3D-printing workflow.

optimum for flexibility and elasticity, unlike biological tissue [8]. Therefore, there are nowadays materials able to close the gap between the real anatomy and the reproduced one, especially considering the soft tissue [9, 10]. In this analysis, an overview of the 3D printing application in medical field is presented, highlighting the usefulness and limitations and how it could be useful for surgeons.

2. Additive Manufacturing Technologies

The 3D-printing techniques have grown in the last decades starting from 1986 when the first stereolithographic (SLA) systems were introduced in practice. Seven are the technical processes related to the 3D printing, each of which is represented by one or more commercial technologies, as shown by the ASTM International [11]. All the processes are listed in Table 1 that reported information about the technologies involved, the materials used, and the medical applications related to each process [12]. A comparison among all the seven techniques is proposed in the same table showing the advantages and disadvantages related to all the processes. Each process uses specific materials with specific properties that relate to medical applications, which are also summarized in Table 1. This general information helps the users to better choose the right technology depending on the application needed.

These technologies and the related advantages enable the researchers to improve existing medical applications that use 3D-printing technology and to explore new ones. The medical goal that has been already reached is significant and exciting, but some of the more revolutionary applications, such as bio/organ printing, require more time to evolve [2].

3. Transformation Process and Materials Used

Materials used in 3D printing are transformed during the production of the specific model by changing their consistency. This process is named cure and can be done in different ways: a melting of a hard filament in order to give the desired form to the model by the material distortion, liquid solidification for the construction of the structure and powder solidification. All these processes require filler or support material in lattice forms avoiding distortion of the model while the material is being cured. The support material can be easily removed by hand with a cutting tool; however, there is the risk to leave impression on the surface requiring an additional polishing in order to obtain a good-quality printing. The risk of damaging the model, losing details, or break the geometry is really high [23].

The correct selection of the material is directly linked to the selection of the 3D-printing process and printer, as well as the requirements of the model. Related to medical application, similarly to other applications, different

anatomical structures need different mechanical properties of the materials to fulfill the required performance of the printed object [8]. The main distinction among the different materials that characterize the human body is between rigid and soft materials. Human bones are an example of rigid tissue and ligaments or articular cartilage are examples of soft materials. Bones are the simplest and easiest biological tissue to be produced by 3D printing as the majority of the materials are rigid. The materials used in 3D printing to model the bone structure are for example acrylonitrile butadiene styrene (ABS) [23], powder of plasters [24], and hydroquinone [8].

Relating to soft tissues, deeper research is still needed in order to decrease the gap between a 3D-printed anatomical model and the human structure. Most of the 3D-printing materials present a lack of realism to mimic adequately a soft human biological tissue. Thus, postprocessing may be necessary in order to soften the printed structures. Some examples are given in the reproduction of cartilaginous tissues [25], arteries for practicing valve replacement [26], hepatic segment [27], and hearts [28]. An interesting example is the development of a 3D-printed brain aneurysm using the flexible TangoPlus™ photopolymer [29] that represented a useful tool to plan the operative strategy in order to treat congenital heart disease. Furthermore, some of the materials used are urethane and rubber-like material, mixed with a rigid photopolymer, to reasonably mimic the artery structure due to their Shore value and elastic properties similar to the physiological one [30, 31].

For a promising future, the multimaterial composites seem to represent a good chance for the 3D printing of human tissues since none of the current available material is able to fully mimic elastic and biological tissues. Multimaterial composites may be designed based on the capacity of the selected biological material to replicate the mechanical properties of human tissue [32]. Mechanical testing may represent a necessary tool to analyze the biomechanical response and validate the artificial material.

Moreover, it is also important to mention that 3D printing allows the reproduction of implantable custom device, but still deeper research needs to be done in order to examine the differences between the traditional and additive manufacturing in terms of mechanical and structural properties, especially fatigue limit needs to be examined further [33].

4. Role of 3D Printing in Medical Field

Every year, 3D printing offers more and more applications in the healthcare field helping to save and improve lives in ways never imagined up to now. In fact, the 3D printing has been used in a wide range of healthcare settings including, but not limited to cardiothoracic surgery [34], cardiology [26], gastroenterology [35], neurosurgery [36], oral and

Table 1: Summary of the 3D-printing process and technologies, focus on materials needed and medical applications, and comparison among the 3D-printing technologies.

Designation additive-manufacturing process	Process description	Technologies	Materials	Medical use	Pros	Cons
Vat photo-polymerisation	Vat polymerisation uses a vat of liquid photopolymer resin, out of which the model is constructed layer by layer	Stereolithography (SLA) Digital light processing (DLP)	(i) Photopolymer resin	Bone, dental models [13], dental implant guides [14], hearing aids [15]	(i) High resolution and accuracy (ii) Complex parts (iii) Decent surface finish: smoother finish (iv) Flexible printing setup	(i) Lacking in strength and durability (ii) Still affected by UV light after print (iii) Not for heavy use
Material jetting	Material jetting creates objects in a similar method to a two-dimensional ink jet printer. Material is jetted onto a build platform using either a continuous or drop on demand (DOD) approach	Multijet modelling (MJM)	(i) Plastics (ii) Polymers: polypropylene, HDPE, PS, PMMA, PC, ABS, HIPS, EDP	Medical models [16], dental casts, dental implant guides [17]	(i) High accuracy (ii) Low waste of material (iii) Multiple material parts and colours in one process	(i) Required support material (ii) Limited materials: only polymers and waxes are supported
Binder jetting	The binder-jetting process uses two materials; a powder-based material and a binder. The binder is usually in liquid form and the build material in powder form. A print head moves horizontally along the x and y axes of the machine and deposits alternating layers of the build material and the binding material	Powder bed and inkjet head 3D printing (PDIH) Plaster-based 3D printing (PP)	(i) Stainless steel (ii) Polymers: ABS, PA, PC (iii) Ceramics: glass	Colour models especially colour coding of anatomy [18]	(i) Range of colours (ii) Multiple materials supported (iii) Faster (iv) Different binder-powder combination for various mechanical properties	(i) Not always suitable for structural parts (ii) The cleaning of the 3D-printing result needs time and increases the time of the procedure
Material extrusion	Fuse deposition modelling (FDM) is a common material extrusion process and is trademarked by the company Stratasys. Material is drawn through a nozzle, where it is heated and is then deposited layer by layer. The nozzle can move horizontally, and a platform moves up and down vertically after each new layer is deposited	Fused deposition modelling (FDM) Fused filament fabrication (FFF)	(i) Plastics; (ii) Polymers: ABS, nylon, PC, AB	Medical instruments and devices [19], rapid prototyping exoskeleton [20]	(i) Inexpensive process (ii) Widespread (iii) ABS plastic supported: good structural properties and easily accessible	(i) Dependence of quality on the noozle radius: bigger nozzle leads to less quality (ii) Low accuracy and dependence on the nozzle thickness (iii) Low speed (iv) Contact pressure needed to increase quality

TABLE 1: Continued.

Designation additive-manufacturing process	Process description	Technologies	Materials	Medical use	Pros	Cons
Powder bed fusion	The powder bed fusion process includes the following commonly used printing techniques: direct metal laser sintering (DMLS), electron beam melting (EBM), selective heat sintering (SHS), selective laser melting (SLM) and selective laser sintering (SLS)	Selective laser sintering (SLS) Direct metal laser sintering (DMLS) Selective heat sintering (SHS) Selective laser melting (SLM) Electron beam melting (EBM)	Powder-based materials. Common metals and polymers used are (i) SHS: nylon (ii) DMLS, SLS, SLM: stainless steel, titanium, aluminium, cobalt chrome, steel (iii) EBM: titanium, cobalt chrome, stainless steel material, aluminium and copper	Models that require a lattice, medical devices such as implants and fixations [21]	(i) Inexpensive (ii) Small technology: office size machine (iii) Large range of material options	(i) Low speed; lack of structural properties in materials (ii) Limited sizes (iii) Dependence on powder grain size
Sheet lamination	Sheet lamination processes include ultrasonic additive manufacturing (UAM) and laminated object manufacturing (LOM). The ultrasonic additive manufacturing process uses sheets or ribbons of metal, which are bound together using ultrasonic welding	Laminated object manufacturing (LOM) Ultrasonic consolidation (UC)	Paper, plastic and sheet metals	Orthopaedic modelling of bone surfaces [22]	(i) Speed (ii) Inexpensive (iii) Ease of materials handling	(i) Dependence on paper or plastic material (ii) Need of postprocessing (iii) Limited material range
Direct energy deposition	Directed energy deposition (DED) covers a range of terminology: "Laser engineered net shaping, directed light fabrication, direct metal deposition, 3D laser cladding" it is a more complex printing process commonly used to repair or add additional material to existing components	Laser metal deposition (LMD)	Metals: cobalt chrome, titanium	Limited. Commonly used to repair existing parts and build very large parts	(i) High control of grain structure (ii) High-quality-dependent on speed (iii) High-accuracy-dependent on accuracy (iv) Fast built with rapid material deposition (v) Fully dense parts; no need for supports (vi) Best process for part repair	(i) Limited range of materials; (ii) Poor surface quality; (iii) Wire process is less accurate

maxillofacial surgery [37], ophthalmology [38], otolaryngology [39], orthopaedic surgery [22], plastic surgery [40], podiatry [41], pulmonology [42], radiation oncology [43], transplant surgery [44], urology [45], and vascular surgery [46].

Thanks to the different benefits that this technology could induce in the field, the main direct applications of 3D printing in the medical and clinical field are as follows [47]:

(i) Used for personalized presurgical/treatment and for preoperative planning. This will lead to a multistep procedure that, integrating clinical and imaging information, will determine the best therapeutic option. Several studies have demonstrated that patient-specific presurgical planning may potentially reduce time spent in the operating room (OR) and result in fewer complications [48, 49]. Moreover, this may lead to reduced postoperative stays, decreased reintervention rates, and lower healthcare costs. The 3D-printing technology allows to provide to the surgeon a physical 3D model of the desired patient anatomy that could be used to accurately plan the surgical approach along with cross-sectional imaging or, alternatively, modelling custom prosthetics (or surgical tool) based on patient-specific anatomy [50–54]. In this way, a better understanding of a complex anatomy unique to each case is allowed [52–56]. Furthermore, the 3D printing gives the possibility to choose before the implantation the size of the prostheses components with very high accuracy [57–59].

(ii) Customize surgical tools and prostheses: the 3D printing can be used to manufacture custom implants or surgical guides and instruments. Therefore, the customization of surgical tools and prostheses means a reduction of cost given by the additive manufacturing technique [52–54, 60].

(iii) Study of osteoporotic conditions: following a pharmacological treatment, 3D printing is useful in validating the results achieved by the patient. This enables a more accurate estimation of patient's bone condition and a better decision on the surgical treatment [15].

(iv) Testing different device in specific pathways: a clear example is the reproduction of different vascular patterns to test the effectiveness of a cardiovascular system used to treat peripheral and coronary artery disease [61]. In this way, the 3D printing enables us to quickly produce prototypes of new design concepts or improvements to existing devices.

(v) Improving medical education: 3D-printed patient-specific models have demonstrated that they can increase performance and foster rapid learning [62], while significantly ameliorating the knowledge, management, and confidence of the trainees regardless of the area of expertise [8]. The benefits of 3D printing in education are the reproducibility and safety of the 3D-printed model with respect to the cadaver dissection, the possibility to model different physiologic and pathologic anatomy from a huge dataset of images, and the possibility to share 3D models among different institutions, especially with ones that have fewer resources [63]. 3D printers that have the capability to print with different densities and colours can be used to accentuate the anatomical details [64, 65].

(vi) Patient education: patient-centered cares makes patient education one of the top priorities for most healthcare providers. However, communicating imaging reports verbally or by showing patients their CT or MRI scans may not be effective; the patients may not fully understand 2D images representation of a 3D anatomy. On the contrary, 3D printing may improve the doctor-patient communication by showing the anatomic model directly [66, 67].

(vii) Storage of rare cases for educational purposes: this role is closely linked to the previous one. This allows the generation of a large dataset composed by datasets of patients affected by rare pathologies, allowing the training of surgeons in specific applications [52–54].

(viii) Improve the forensic practice: in the courtroom, a 3D model could be used to easily demonstrate various anatomic abnormalities that may be difficult to jury members to understand using cross-sectional imaging [68].

(ix) Bioprinting: the 3D printing allows also the modelling of implantable tissue. Some examples are the 3D printing of synthetic skin for transplanting to patients, who suffered burn injuries [69]. It may also be used for testing of cosmetic, chemical, and pharmaceutical products. Another example is the replicating of heart valves using a combination of cells and biomaterials to control the valve's stiffness [26] or the replicating of human ears using molds filled with a gel containing bovine cartilage cells suspended in collagen [70].

(x) Personalized drug 3D printing: the 3D printing of drugs consists of the printing out the powdered drug layer to make it dissolve faster than average pills [71]. It allows also personalization of the patient's needed quantity [2].

(xi) Customizing synthetic organs: the 3D printing may represent an opportunity to save life reducing the waiting list of patients that need transplantation [72]. Bioprinted organs may also be used in the future by pharmaceutical industries to replace animal models for analyzing the toxicity of new drugs [73].

Therefore, these examples clearly demonstrated that 3D printing is one of the most disruptive technologies that have the potential to change significantly the clinical field, improving medicine and healthcare, making care affordable, accessible, and personalized. As printers evolve, printing biomaterials get safety regulated and the general public acquires a common sense about how 3D printing works.

4.1. Lack of Regulation. The biomedical field is one of the areas in which 3D printing has already shown its potentialities and that, in not too distant future, may be one of the key elements for the resolution of important problems related to human health that still exist.

Nowadays, despite the additive manufacturing offers a great potential for the manufacturing, the 3D-printing products do not have a proper legal status that defines them, both for implantable and nonimplantable devices. All the 3D-printed products are categorized as custom-made device under the Regulation (EU) 2017/745 of the European Parliament and of the Council of the 5 April 2017 [74]. They are defined as follow: "*any device specifically made in accordance with a written prescription of any person authorized by national law by virtue of that person's professional qualifications which gives, under that person's responsibility, specific design characteristics, and is intended for the sole use of a particular patient exclusively to meet their individual conditions and needs*". Differently for mass-produced devices "*which need to be adapted to meet the specific requirements of any professional user and devices which are mass-produced by means of industrial manufacturing processes in accordance with the written prescriptions of any authorized person shall not be considered to be custom-made devices*" [75]. Indeed, manufacturers of custom-made devices shall only be guaranteed by an obligation of conformity assessment procedures upon which the device shall be compliant with safety and performance requirements [76]. Furthermore, the regulation states that "*Devices, other than custom-made or investigational devices, considered to be in conformity with the requirements of this Regulation shall bear the CE marking of conformity*" [77]. Thus, these medical devices do not require affixation of CE markings: a significant and constraining procedure demonstrating the safety and the performance of the device for the patient. Moreover, the custom-made devices do not require the UDI System (Unique Device Identification system) as reported in the Article 27, Comma 1 of the regulation.

A different approach has to be applied for custom-made implants, such as dental prostheses, that are defined as "*any device, including those that are partially or wholly absorbed, which is intended*:

(i) *to be totally introduced into the human body, or*

(ii) *to replace an epithelial surface or the surface of the eye,*

by clinical intervention and which is intended to remain in place after the procedure.

Any device intended to be partially introduced into the human body by clinical intervention and intended to remain in place after the procedure for at least 30 days shall also be deemed to be an implantable." [78]. The custom-made implantable devices require the CE marking in order to guarantee the safety and to be commercialized.

The EU has been working for many years on an update to the Medical Devices Directive. This proposed legislation has many noble attributes in addition to overcoming the gaps of the existing Medical Devices Directive, such as supporting technology and science innovation, while simultaneously strengthening patient safety. However, the current version of the draft Regulation lacks some depth that is mandatory to safeguard safe usage of 3D-printing technology and, thus, enable its increasing prevalence in medicine.

4.2. Examples of Application of 3D Printing in Paediatric Cases. Three-dimensional (3D) modelling and printing greatly supports advances in individualized medicine and surgery. Looking to the field of paediatrics, it is possible to identify four main applications categories: surgical planning, prostheses, tissue construct, and drug printing.

There are many successful cases that demonstrate the potential of the additive manufacturing in surgical planning in paediatric cases. In particular, most of the applications of 3D printing reported in the literature are related to the congenital heart disease [29]. This is due to the fact that children have a smaller chest cavity than adults, and the surgical treatment in paediatric cases may be much more difficult. The additive manufacturing helps the surgeons to have more information than the only ones that imaging technologies can afford. It helps the surgeon in the spatial orientation inside the cavities of a small infant heart and in simulating the surgical approach and steps of the operation with high fidelity [79]. This leads to shorter intraoperative time that per se has significant impact on complication rate, blood loss, postoperative length-of-stay, and reduced costs [80]. An example of the application of the 3D printing in the paediatric congenital heart disease treatment is a study reported in the literature based on the development of a 3D heart model of a 15-years-old boy to improve interventional simulation and planning in patient with aortic arch hypoplasia. The 3D-printed model allowed simulation of the stenting intervention. The assessment of optimal stent position, size, and length was found to be useful for the actual intervention in the patient. This represents one of the most technically challenging surgical procedures which opens the door for potential simulation applications of a 3D model in the field of catheterization and cardiovascular interventions [81].

Another study proposed in which the 3D printing had a relevant role consists in a clinical preoperative evaluation on five patients ranged from 7 months to 11 years of age affected by a double outlet right ventricle with two well-developed ventricles and with a remote ventricular septal defect. The three-dimensional printed model based on the data derived from computed tomography (CT) or magnetic resonance (MRI) contributed to a more complete appreciation of the intracardic anatomy, leading to a successful surgical repair for three of the five patients. [82] Lastly, CT and MRI data were used to construct 3D digital and anatomical models to plan a heart transplantation surgical procedure of two patients of 2 and 14 years old affected relatively by hypoplastic left heart syndrome and pulmonary atresia with a hypoplastic right ventricle. These physical models allowed the surgeon and the paediatric cardiologist to develop the optimal surgical treatment during the heart transplantation

anticipating problems that may arise during the procedure. The specific dimensions and distances can be measured, and heart transplantation can be planned [83].

The importance of three-dimensional printing has been demonstrating also in other application. The additive manufacturing in fact has been used to plan surgical treatment of paediatric orthopaedic disorders [84]. The 3D model of a 2-year-old male child was produced in order to plan the surgical treatment for his multisutural craniosynostosis with a history of worsening cranial deformity. Other than the turribrachycephalic skull, the child also had greatly raised intracranial pressure with papilledema and copper beaten appearance of the skull. Thorough preoperative planning enabled faster surgery and decreased anesthesia time in a compromised patient [85].

Another study, based on 13 cases of multiplane spinal or pelvic deformity, was developed in order to demonstrate that the three-dimensional printing may represent a useful tool in the surgical planning of complex paediatric spinal deformities treatment [86].

Changing the final goal of the additive manufacturing, other applications cases are reported in the literature to demonstrate the usefulness in the production of paediatric patient-specific prostheses. An example in the literature is given by the development of a low-cost three-dimensional printed prosthetic hand for children with upper-limb reductions using a fitting methodology that can be performed at a distance [87]. This specific case demonstrates that the advancements in computer-aided design (CAD) programs, additive manufacturing, and imaging editing software offer the possibility of designing, printing, and fitting prosthetic hands devices overcoming the costs limitation. As a consequence, the advantages of 3D-printed implants over conventional ones are in terms of customizability and cost as seems to be clear from the previous example. On the contrary, the major adversity is related to the rapid physical growth that makes the customize prostheses outsized frequently. This leads to the production of advanced technological implant that, due to their high complexity and weight, increases cost. The additive manufacturing can be used to fabricate rugged, light-weight, easily replaceable, and very low-cost prostheses for children [88]. The major prostheses lack is related to the ability to communicate with the brain in terms of sensibility. With the advent of bioprinting, cellular prostheses could be an interesting area of research, which can lead to integrated prostheses in the brain communication system, and exhibit more biomimicry with tissue and organ functionalities [89].

Related to bioprinting, there are few applications nowadays involved in the tissues production in regenerative medicine. Many different tissues have been successfully bioprinted as reported in many journal articles [90] including bone, cartilage, skin, and even heart valves. However, the bioprinted tissues and organs are at the laboratory level; a long way needs to be travelled to achieve successful clinical application [91].

Last but not the least, the additive manufacturing in terms of drug printing may also represent an innovative technique in the production of patient-specific medicine with regard to the composition and the dose needed by the patients. The drug-printing introduces the concept of tailor-made drugs in order to make drugs safer and more effective. Especially for children, furthermore, drug-printing represents the possibility of choosing colour, shape, and design of the medication, reducing the resistance in taking them. Imagine a paediatrician talking to a four-year-old child who is having trouble adjusting to taking daily doses of steroids after being diagnosed with Duchenne muscular dystrophy the previous month. 3D printing allows us to design in particular shape the drug, making medicine more appealing to the child [92]. It is amental to note that changing the shape of a capsule does not have to lead to different dose and drug properties, such as drug release or dissolution rate [93].

5. Conclusions

The 3D printing in medical field and design needs to think outside the norm for changing the health care. The three main pillars of this new technology are the ability to treat more people where it previously was not feasible, to obtain outcomes for patients and less time required under the direct case of medical specialists. In few words, 3D printing consists in "enabling doctors to treat more patients, without sacrificing results" [94].

Therefore, like any new technology, 3D printing has introduced many advantages and possibilities in the medical field. Each specific case in which 3D printing has found application shown in this analysis is a demonstration of this. However, it must be accompanied by an updated and current legislation in order to guarantee its correct use.

Conflicts of Interest

The authors declare that there are no conflicts of interest regarding the publication of this paper.

Acknowledgments

References

[1] H. Arun, *Healthcare 3D Printing Market 2018 Prominent Players-Aprecia Pharmaceuticals, Aspect Biosystems, Bio 3D Technologies, Biobots, Cyfuse Biomedical, Digilab, 3 Dynamics Systems, Envision Tec, Luxexcel, Materialise NV, Nano 3D Biosciences, Oceanz, Organovo Ho*, http://www.openpr.com.

[2] C. L. Ventola, "Medical applications for 3D printing: current and projected uses," *Pharmacy and Therapeutics*, vol. 39, no. 10, pp. 704–711, 2014.

[3] D. B. Jones, R. Sung, C. Weinberg, T. Korelitz, and R. Andrews, "Three-dimensional modeling may improve surgical education and clinical practice," *Surgical Innovation*, vol. 23, no. 2, pp. 189–195, 2016.

[4] I. M. Mazher, P. F. Angus, K. M. Santosh, and I. Gibson, "Customised design and development of patient specific 3D printed whole mandible implant," in *Proceedings of the 27th*

Annual International Solid Freeform Fabrication Symposium, Austin, TX, USA, August 2016.

[5] D. C. Ackland, D. Robinson, M. Redhead, P. Vee Sin Lee, A. Moskaljuk, and G. Dimitoulis, "A personalized 3D-printed prosthetic joint replacement for the human temporomandibular joint: From implant design to implantation," *Journal of the Mechanical Behavior of Biomedical Materials*, vol. 69, pp. 404–411, 2017.

[6] K. Phan, A. Sgro, M. M. Maharaj, P. D'Urso, and R. J. Mobbs, "Application of a 3D custom printed patient specific spinal implant for C1/2 arthrodesis," *Journal of Spine Surgery*, vol. 2, no. 4, pp. 314–318, 2016.

[7] L. E. Diment, M. S. Thompson, and J. H. M. Bergmann, "Clinical efficacy and effectiveness of 3D printing: a systematic review," *BMJ Open*, vol. 7, no. 12, article e016891, 2017.

[8] J. Garcia, Z. Yang, R. Mongrain, R. L. Leask, and K. Lachapelle, "3D printing materials and their use in medical education: a review of current technology and trends for the future," *BMJ Simulation and Technology Enhanced Learning*, vol. 4, no. 1, pp. 27–40, 2017.

[9] R. J. Mondschein, A. Kanitkar, C. B. Williams, S. S. Verbridge, and T. E. Long, "Polymer structure-property requirements for stereolithographic 3D printing of soft tissue engineering scaffolds," *Biomaterials*, vol. 140, pp. 170–188, 2017.

[10] W. Zhu, X. Ma, M. Gou, D. Mei, K. Zhang, and S. Chen, "3D printing of functional biomaterials for tissue engineering," *Current opinion in biotechnology*, vol. 40, pp. 103–112, 2016.

[11] ASTM, *Standard Technology for Additive Manufacturing-General Principles/Terminology*, ASTM ISO/ASTM 52900: 2015 (E), West Conshohocken, PA, USA, 2015.

[12] H. J. Chen and M. Gariel, *A roadmap from Idea to Implementation–3D Printing for Pre-Surgical Applications*, CreateSpace Independent Publishing Platform, Scotts Valley, CA, USA, 1st edition, 2012.

[13] A. Cohen, A. Laviv, P. Berman, R. Nashef, and J. Abu-Tair, "Mandibular reconstruction using stereolithographic 3-dimensional printing modeling technology," *Oral Surgery, Oral Medicine, Oral Pathology, Oral Radiology, and Endodontology*, vol. 108, no. 5, pp. 661–666, 2009.

[14] D. Whitley, R. S. Eidson, I. Rudek, and S. Bencharit, "In-office fabrication of dental implant surgical guides using desktop stereolithographic printing and implant treatment planning software: a clinical report," *Journal of Prosthetic Dentistry*, vol. 118, no. 3, pp. 256–263, 2017.

[15] H. Dodziuk, "Application of 3D printing in healthcare," *Kardiochirurgia i Torakochirurgia Polska*, vol. 13, no. 3, pp. 283–293, 2017.

[16] D. Ibrahim, T. L. Broilo, C. Heitz et al., "Dimensional error of selective laser sintering, three-dimensional printing and PolyJet models in the reproduction of mandibular anatomy," *Journal of Cranio-Maxillofacial Surgery*, vol. 37, no. 3, pp. 167–173, 2009.

[17] https://www.sys-uk.com/news/3d-printed-surgical-guides-and-dental-implants/.

[18] J. S. Matsumoto, J. M. Morris, T. A. Foley et al., "Three-dimensional physical modelling: applications and experience at mayo clinic," *RadioGraphics*, vol. 35, no. 7, pp. 1989–2006, 2015.

[19] *Medtronic case study, Custom surgical instruments becoming working prototypes using FDM 3D printing technology.*

[20] K. S. Tanaka and N. Lightdale-Miric, "Advances in 3d-printed pediatric prostheses for upper extremity differences," *Journal of Bone and Joint Surgery*, vol. 98, no. 15, pp. 1320–1326, 2016.

[21] S. L. Sing, J. An, W. Y. Teong, and F. E. Wiria, "Laser and electron beam powder-bed additive manufacturing of metallic implants: a review on processes, materials and designs," *Journal of Orthopaedic Research*, vol. 34, no. 3, pp. 369–385.

[22] F. Auricchio and S. Marconi, "3D printing: clinical applications in orthopaedics and traumatology," *EFORT Open Reviews*, vol. 1, no. 5, pp. 121–127, 2016.

[23] C. G. Helguero, V. M. Mustahsan, S. Parmar et al., "Biomechanical properties of 3D-printed bone scaffolds are improved by treatment by CRFP," *Journal of Orthopaedic Surgery and Reasearch*, vol. 12, no. 1, p. 195, 2017.

[24] M. Asadi-Edyvand, M. Solati-Hasjin, A. Farzad, and N. A. A. Osman, "Effect of technical parameters on porous structure and strength of 3D printed calcium sulfate prototypes," *Robotics and Computer-Integrated Manufacturing*, vol. 37, pp. 57–67, 2015.

[25] M. S. Mannoor, Z. Jiang, T. James et al., "3D printed bionic ears," *Nano Letters*, vol. 13, no. 6, pp. 2634–2639, 2013.

[26] M. Vukievic, B. Mosadegh, J. K. Little, and S. H. Little, "Cardiac 3D printing and its future directions," *JACC: Cardiovascular Imaging*, vol. 10, no. 2, pp. 171–184, 2017.

[27] D. S. C. Soon, M. P. Chae, C. H. C. Pilgrim, W. M. Rozen, R. T. Spychal, and D. J. Hunter-Smith, "3D haptic modelling for preoperative planning of hepatic resection: a systematic review," *Annals of Medicine and Surgery*, vol. 10, pp. 1–7, 2016.

[28] I. Abudayyeh, B. Gordon, M. M. Ansari, K. Jutzy, L. Stoletniy, and A. Hilliard, "A practical guide to cardiovascular 3D printing in clinical practice: overview and examples," *Journal of Interventional Cardiology*, vol. 31, no. 3, pp. 375–383, 2017.

[29] M. Cantinotti, I. Valverde, S. Kutty, and J. Eckert, "Three-dimensional printed models in congenital heart disease," *International Journal of Cardiovacuolar Imaging*, vol. 33, no. 1, pp. 137–144, 2016.

[30] Stratasys, Case study, *Dante Pazzanese Cardiology Institute uses 3D printed arteries to diagnose and treat diseases.*

[31] Stratasys, Case study, *Shaping Young Hearts. Stratasys Helps a Surgeon Save More Kids.*

[32] K. Qiu, G. Haghiashtiani, and M. C. McAlpine, "3D printed organ models for surgical applications," *Annual Review of Analytical Chemistry*, vol. 11, no. 1, pp. 287–306, 2018.

[33] E. M. Zanetti, A. Aldieri, M. Terzini, M. Calì, G. Franceschini, and C. Bignardi, "Additively manufactured custom load-bearing implantable devices: grounds for caution," *Australasian Medical Journal*, vol. 10, no. 8, pp. 694–700, 2017.

[34] S. N. Kurenov, C. Ionita, D. Sammons, and T. L. Demmy, "Three-dimensional printing to facilitate anatomic study, device development, simulation, and planning in thoracic surgery," *Journal of Thoracic and Cardiovascular Surgery*, vol. 149, no. 4, pp. 973–979, 2015.

[35] H. Jeon, K. Kang, S. A. Park et al., "Generation of multilayered 3D structures of HepG2 cells using a bio-printing technique," *Gut and Liver*, vol. 11, no. 1, pp. 121–128, 2017.

[36] M. Randazzo, J. M. Pisapia, N. Singh, and J. P. Thawani, "3D printing in neurosurgery: a systematic review," *Surgical Neurology International*, vol. 7, no. 34, pp. 801–809, 2016.

[37] H. Lino, K. Igawa, Y. Kanno et al., "Maxillofacial reconstruction using custom-made artificial bones fabricated by inkjet printing technology," *Journal of artificial organ*, vol. 12, no. 3, pp. 200–205, 2009.

[38] W. Huang and X. Zhang, "3D printing: print the future of ophthalmology," *Investigative Opthalmology & Visual Science*, vol. 55, no. 8, pp. 5380-5381, 2014.

[39] T. D. Crafts, S. E. Ellsperman, T. J. Wannemuehler, T. D. Bellicchi, T. Z. Shipchandler, and A. V. Mantravadi,

"Three-dimensional printing and its applications in otorhinolaryngology-head and neck surgery," *Otolaryngology-Head and Neck Surgery*, vol. 156, no. 6, pp. 999–1010, 2017.

[40] M. P. Chae, W. M. Rozen, P. G. McMenamin et al., "Emerging applications of bedside 3D printing in plastic surgery," *Frontiers in Surgery*, vol. 16, no. 2, p. 25, 2015.

[41] C. Williams, A. James, M. P. Chae, and D. J. Hunter-Smith, "3D printing in clinical podiatry: a pilot study and review," *Journal of Foot and Ankle Research*, vol. 8, no. 2, p. 41, 2015.

[42] N. Guilbert, L. Mhanna, A. Didier et al., "Integration of 3D printing and additive manufacturing in the interventional pulmonologist's toolbox," *Respiratory Medicine*, vol. 134, pp. 139–142, 2018.

[43] S. Su, K. Moran, and J. L. Robar, "Design and production of 3D printed bolus for electron radiation therapy," *Journal of Applied Clinical Medical Physics*, vol. 15, no. 4, pp. 194–211, 2014.

[44] N. N. Zein, I. A. Hanouneh, P. D. Bishop et al., "Three-dimensional print of a liver for preoperative planning in living donor liver transplantation," *Liver transplantation*, vol. 19, no. 12, pp. 1304–1310, 2013.

[45] Y. Soliman, A. H. Feibus, and N. Baum, "3D printing and its urologic applications," *Urology*, vol. 17, no. 1, pp. 20–24, 2017.

[46] P. Hangge, Y. Pershad, A. A. Witting, H. Albadawi, and R. Oklu, "Three-dimensional (3D) printing and its applications for aortic diseases," *Cardiovascular Diagnosis & Therapy*, vol. 8, no. 1, pp. 19–25, 2018.

[47] D. H. Ballard, A. P. Trace, S. Ali et al., "Clinical applications of 3D printing," *Academic Radiology*, vol. 25, no. 1, pp. 52–65, 2018.

[48] E. Perica and Z. Sun, "Patient-specific three-dimensional printing for pre-surgical planning in hepatocellular carcinoma treatment," *Quantitative Imaging in Medicine and Surgery*, vol. 7, no. 6, pp. 668–677, 2017.

[49] E. O'Brien, D. B. Wayne, K. A. Barsness, W. C. McGaghie, and J. H. Barsuk, "Use of 3D printing for medical education models in transplantation medicine: a critical review," *Current Transplantation Reports*, vol. 3, no. 1, pp. 109–119, 2016.

[50] K. C. Wong, "3D-printed patient-specific applications in orthopedics," *Orthopedic Research and Reviews*, vol. 8, pp. 57–66, 2016.

[51] J. P. Costello, R. J. Olivieri, L. Su et al., "Incorporating three-dimensional printing into a simulation-based congenital heart-disease and critical care training curriculum for resident physicians," *Congenital Heart Disease*, vol. 10, no. 2, pp. 185–190, 2015.

[52] M. Frame and J. S. Huntley, "Rapid prototyping in orthopaedic surgery: a user's guide," *Scientific World Journal*, vol. 2012, Article ID 838575, 7 pages, 2012.

[53] B. Mahaisavariya, K. Sitthiseripratip, P. Oris, and T. Tongdee, "Rapid prototyping model for surgical planning of corrective osteotomy for cubitus varus: report of two cases," *Injury Extra*, vol. 37, no. 5, pp. 176–180, 2006.

[54] U. Sheth, J. Theodoropoulos, and J. Abouali, "Use of 3-dimensional printing for preoperative planning in the treatment of recurrent anterior shoulder instability," *Arthroscopy Techniques*, vol. 4, no. 4, pp. 311–316, 2015.

[55] Stratasys, Case study, *3D Printing for Vascular Health. Shaping Breakthroughs in Brain Aneurysm Treatments*.

[56] Y.-T. Wang, X.-J. Yang, B. Yan, T.-H. Zeng, Y.-Y. Qiu, and S.-J. Chen, "Clinical application of three-dimensional printing in the personalized treatment of complex spinal disorders,"

Chinese Journal of Traumatology, vol. 19, no. 1, pp. 31–34, 2016.

[57] A. Hosny, J. D. Dilley, M. Mathur et al., "Pre-procedural fit-testing of TAVR valves using parametric modeling and 3D printing," *Journal of Cardiovascular Computed Tomography*, vol. 18, 2018.

[58] R. Vaishya, V. Vijay, A. Vaish, and A. K. Agarwal, "Computed tomography based 3D printed patient specific blocks for total knee replacement," *Journal of Clinical Orthopaedics and Trauma*, vol. 9, no. 3, pp. 254–259, 2018.

[59] X. Chen, J. K. Possel, C. Wacongne, A. F. Van Ham, P. C. Klink, and P. R. Roelfsema, "3D printing and modelling of customized implants and surgical guides for non-human primates," *Journal of Neuroscience Methods*, vol. 286, no. 286, pp. 38–55, 2017.

[60] A. De La Pena, J. De La Pena-Brambila, J. Perez-De La Torre, M. Ochoa, and M. J. Gallardo, "Low-cost customized craniolplasty using a 3D digital printing model: a case report," *3D Printing in Medicine*, vol. 4, no. 1, 2018.

[61] Stratasys, Case study, *Printing Pathways to Medical Innovation. 3D Printing's Versatility Paves the Way for Medical Advancements by Cardiovascular Systems, Inc.*.

[62] K. R. Rosen, "The history of medical simulation," *Journal of Critical Care*, vol. 23, no. 2, pp. 157–166, 2008.

[63] V. Walker, "Implementing a 3D printing service in a biomedical library," *Journal of the Medical Library Association*, vol. 105, no. 1, pp. 55–60, 2017.

[64] K. Wang, C. Wu, Z. Qian, C. Zhang, B. Wang, and M. A. Vannan, "Dual-material 3D printed metamaterials with tunable mechanical properties for patient-specific tissue-mimicking phantoms," *Additive Manufacturing*, vol. 12, pp. 31–37, 2016.

[65] K. H. A. Lim, Z. Y. Loo, S. J. Goldie, J. W. Adams, and P. G. McMenamin, "Use of 3D printed models in medical education: a randomized control trial comparing 3D prints versus cadaveric materials for learning external cardiac anatomy," *Anatomical Sciences Education*, vol. 9, no. 3, pp. 213–221, 2015.

[66] J.-C. Bernhard, S. Isotani, T. Matsugasumi et al., "Personalized 3D printed model of kidney and tumor anatomy: a useful tool for patient education," *World Journal of Urology*, vol. 34, no. 3, pp. 337–345, 2016.

[67] C. Andolfi, A. Plana, P. Kania, P. P. Banerjee, and S. Small, "Usefulness of three-dimensional modeling in surgical planning, resident training, and patient education," *Journal of Laparoendoscopic & Advanced Surgical Techniques*, vol. 27, no. 5, pp. 512–515, 2017.

[68] W. Baier, J. M. Warnett, M. Payne, and M. A. Williams, "Introducing 3D printed models as demonstrative evidence at criminal trials," *Journal of Forensic Sciences*, vol. 63, no. 4, pp. 1298–1302, 2017.

[69] P. He, J. Zhao, J. Zhang et al., "Bioprinting of skin constructs for wound healing," *Burns & Trauma*, vol. 6, no. 1, 2018.

[70] G. Zhou, H. Jiang, Z. Yin et al., "In vitro regeneration of patient-specific ear-shaped cartilage and its first clinical application for auricular reconstruction," *EBioMedicine*, vol. 28, pp. 287–302, 2018.

[71] A. Konta, M. García-Piña, and D. Serrano, "Personalised 3D printed medicines: which techniques and polymers are more successful?," *Bioengineering*, vol. 4, no. 4, p. 79, 2017.

[72] S. Ji and M. Guvendiren, "Recent advances in bioink design for 3D bioprinting of tissues and organs," *Frontiers in Bioengineering and Biotechnolgy*, vol. 5, no. 5, p. 23, 2017.

[73] N. Charbe, P. A. McCarron, and M. M. Tambuwala, "Three-dimensional bio-printing: a new frontier in oncology research," *World Journal of Clinical Oncology*, vol. 8, no. 1, pp. 21–36, 2017.

[74] Regulation (EU) 2017/745 of the European Parliament and of the Council of 5 April 2017 on medical devices, amending Directive 2001/83/EC, Regulation (EC) No 178/2002 and regulation (EC) No 1223/2009 and repealing Council Directive 90/985/EEC and 93/42/EEC.

[75] Article 2, Comma 3 of the Regulation (EU) 2017/745.

[76] Article 20, Comma 1 of the Regulation (EU) 2017/745.

[77] Article 10 of the Regulation (EU) 2017/745.

[78] Article 2, Comma 5 of the Regulation (EU) 2017/745.

[79] L. Kiraly and S. Khalifa, "Three-dimensional modelling and three-dimensional printing in pediatric and congenital cardiac surgery," *Translational Pediatrics*, vol. 7, no. 2, pp. 129–138, 2018.

[80] M. Maruthappu, A. Duclos, S. R. Lipsitz, and D. Orgill, "Surgical learning curves and operative efficiency: a cross-speciality observational study," *BMJ Open*, vol. 5, no. 3, article e006679, 2015.

[81] I. Valverde, G. Gomez, J. F. Coserria et al., "3D printed models for planning endovascular stenting in transverse aortic arch hypoplasia," *Catheterization and Cardiovascular Interventions*, vol. 85, no. 6, pp. 1006–1012, 2015.

[82] S. Garekar, A. Bharati, M. Chokhandre et al., "Clinical application and multidisciplinary assessment of three dimensional printing in double outlet right ventricle with remote ventricular septal defect," *World Journal for Pediatric and Congenital Heart Surgery*, vol. 7, no. 3, pp. 344–350, 2016.

[83] R. Sodian, S. Weber, M. Markert et al., "Pediatric cardiac transplantation: three-dimensional printing of anatomic models for surgical planning of heart transplantation in patients with univentricular heart," *Journal of Thoracic and Cardiovascular Surgery*, vol. 136, no. 4, pp. 1098-1099, 2008.

[84] Z. A. Starosolski, J. H. Kan, S. D. Rosenfeld, R. Krishnamurthy, and A. Annapragada, "Application of 3-D printing (rapid prototyping) for creating physical models of pediatric orthopedic disorders," *Pediatric Radiology*, vol. 44, no. 2, pp. 216–221, 2014.

[85] D. A. Mendonca, V. Deraje, R. S. Gujjalanavar, and S. Gopal, "Case series of three-dimensional printing technology applied in complex craniofacial deformity surgery," *Journal of Lip Palate and Craniofacial Anamalies*, vol. 3, no. 2, pp. 88–94, 2016.

[86] J. Guarino, S. Tennyson, G. McCain, L. Bond, K. Shea, and H. King, "Rapid prototyping technology for surgeries of the pediatric spine and pelvis," *Journal of Pediatric Orthopaedics*, vol. 27, no. 8, pp. 955–960, 2007.

[87] J. Zuniga, D. Katsavelis, J. Peck et al., "Cyborg beast: a low-cost 3D-printed prosthetic hand for children with upper-limb differences," *BMC Research Notes*, vol. 8, no. 1, pp. 8–10, 2015.

[88] M. B. Burn and G. R. Gogola, "Three-dimensional printing of orosthetic hands for children," *Journal of Hand Surgery*, vol. 41, no. 5, pp. 103–109, 2016.

[89] Stratasys, Case Study, *Skull Reconstruction. CTI Renato Archer 3D Prints Prototypes of an Accident Victim's Skull.*

[90] J. An, J. E. M. Teoh, R. Suntornnond, and C. K. Chua, "Design and 3D printing of scaffolds and tissues," *Engineering*, vol. 1, no. 2, pp. 261–268, 2015.

[91] E. S. Bishop, S. Mostafa, M. Pakvasa et al., "3-D bioprinting technologies in tissue engineering and regenerative medicine: current and future trends," *Genes & Diseases*, vol. 4, no. 4, pp. 185–195, 2017.

[92] K. Sanderson, "3D printing: the future of manufacturing medicine," *Pharmaceutical Journal*, vol. 294, no. 7865, pp. 590–592, 2015.

[93] V. Sanjairaj, W. F. Lu, and J. Y. H. Fuh, "3D printing and 3D bioprinting in paediatrics," *Bioengineering*, vol. 4, no. 4, p. 63, 2017.

[94] S. Dunham, *Surgeon's Helper: 3D Printing is Revolutionizing Health Care (Op-Ed)*, SmarTech Markets, Charlottesville, VA, USA, 2015, https://www.livescience.com/49913-3d-printing-revolutionizing-health-care.html.

Review Article

Design of Additively Manufactured Structures for Biomedical Applications: A Review of the Additive Manufacturing Processes Applied to the Biomedical Sector

Flaviana Calignano [ID], **Manuela Galati** [ID], **Luca Iuliano, and Paolo Minetola** [ID]

Department of Management and Production Engineering, Politecnico di Torino, Turin 10129, Italy

Correspondence should be addressed to Manuela Galati; manuela.galati@polito.it

Additive manufacturing (AM) is a disruptive technology as it pushes the frontier of manufacturing towards a new design perspective, such as the ability to shape geometries that cannot be formed with any other traditional technique. AM has today shown successful applications in several fields such as the biomedical sector in which it provides a relatively fast and effective way to solve even complex medical cases. From this point of view, the purpose of this paper is to illustrate AM technologies currently used in the medical field and their benefits along with contemporary. The review highlights differences in processes, materials, and design of additive manufacturing techniques used in biomedical applications. Successful case studies are presented to emphasise the potentiality of AM processes. The presented review supports improvements in materials and design for future researches in biomedical surgeries using instruments and implants made by AM.

1. Introduction

Additive manufacturing (AM), also known as 3D printing, is a relatively new technology that includes a large number of processes based on the layer-by-layer strategy to fabricate components. In contrast to conventional subtractive technologies, in which the component is fabricated by removing material from a larger raw part, using AM techniques, the final shape of the part is obtained by adding material one layer at a time. This approach has revolutionised manufacturing, and AM is today recognised as a pillar of the third industrial revolution. In line with the digital era, the only information needed to create a part by AM processes is its 3D digital model. The advantage of this kind of approach is clearly demonstrated by the design freedom [1]. Therefore, even 3D complex geometries can be easily and directly transformed into an end-usable part in only one manufacturing step without using specific tools, moulds, or dies [2]. This kind of flexibility has attracted the attention of many fields especially the medical one which was the first user of AM technologies [3]. From this point of

view, what makes AM even more attractive is the possibility to use reverse engineering (RE) methodologies to obtain almost directly the 3D models for the production; for instance, of customised parts which match the patient's anatomy. Medical images acquired by tools such as computer tomography (CT) [4] or magnetic resonance imaging (MRI) are in fact currently used for such scope. On the other hand, since the AM processes are well known as rapid prototyping (RP) technique, the integration between RE and RP techniques allows the production of physical, real 3D hard copy, models of any anatomical shape for use in surgical trial, and preoperative planning of surgery and/or simulation [5]. This helps the surgeon to clearly understand the clinical situation, to train, and to be more confident during the surgery with a decrease in the operation time. The medical field constitutes a large world to be exploited for AM processes because no extra cost is needed for customization, which is the most important aspect to be considered [6]. For all of these reasons, today AM technologies play a key role in several biomedical applications that can be resumed as follows:

(i) Equipment [7–9] for the production of surgical supports, instruments, and tools [10]

(ii) Physical models for visualisation [8], preoperative planning [5], testing, and educational aims

(iii) Fabrication of customised implants for several scopes such as prostheses [11] and devices

(iv) Biostructures for scaffolds and tissue engineering

In addition, since AM uses a digital file, the creation of a knowledge sharing platform, which is another pillar of the third industrial revolution, is facilitated. From this point of view, activities have been undertaken to create online free and open-access repositories for 3D-printable models in the fields of biology and medicine, such as the NIH 3D print exchange [12].

2. From Medical Data to the 3D Model for AM Processes

The literature review aims to present and discuss in detail the most representative AM technologies, covering the main research areas and case studies of applications in medicine. The AM processes present numerous features that make them suitable for biomedical applications especially if specific materials, design, and procedure are considered.

Figure 1 shows the workflow for manufacturing customized medical devices through AM starting from the acquisition of the specific patient's anatomy. In the medical field, the discipline of reverse engineering for digital data capture and processing can be combined with the one of additive manufacturing for the fabrication of the customized part directly from a 3D digital model. Three main phases can be distinguished. The first phase is the one of reverse engineering and acquisition of the patient's anatomy to convert it to digital data (point cloud). The second phase is the design phase that involves computer-aided activities such as 3D modelling with a CAD tool [13] and finite element analysis for validation of the structural resistance of the designed part [14]. In this phase, another benefit of AM can be exploited by generating complex lightweight shapes such as lattices or trabecular structures. The design parts do not have to be fully dense, and load bearing lattice structures can be integrated into portions of the part volume to reduce overall material consumption and part weight in the specific case of customised implants with an advantage for the patient's comfort.

The third and final phase is the manufacturing of the customised part by means of an AM technique, including the postprocessing operations and sterilization that are necessary for the part to be compliant with the medical specifications and requirements.

3. AM Processes for Medical Applications

Nowadays, AM processes that are currently used for medical applications can be grouped into two categories according to the raw material: polymers and metals. Selective laser sintering, stereolithography, and material extrusion are the most common AM techniques for polymers, while laser
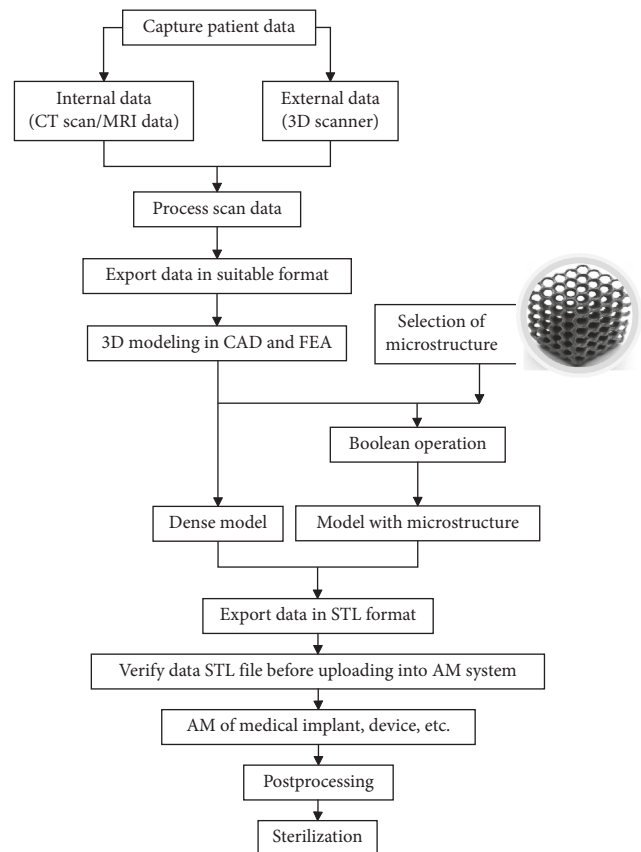
FIGURE 1: Flowchart from medical data to the final part.

powder bed fusion (L-PBF) and electron beam melting (EMB) are those for metals.

3.1. Selective Laser Sintering. Selective laser sintering (SLS) is a powder bed technology in which a laser beam selectively sinters thin layers (from about 60 to 100 μm or more) of thermoplastic powder. After a layer is finished, the build table is lowered by the layer height, fresh powder is spread over the building bed, and a new layer is defined and sintered. The build chamber can be heated during the process as well as the powder bed can be preheated before local melting with the spot of the laser. A large range of thermoplastic powders is today available for SLS. In the medical sector, this technique is mostly used for the fabrication of visualisation models, surgical tools, and customised implants. A polyamide guide to position the osteotomized bony fragments during a zygomatic osteotomy has been developed by Herlin et al. [15]. Pilot models for preoperative planning and testing have been produced using nylon powders [16]. Mixes between oxide ceramics and a PEEK and PLC compound have been studied by Shishkovsky and Scherbakov [17] to produce porous tissue engineering scaffolds. Scaffolds for growing specific tissues have been also studied by several researchers [18–25]. Most of them demonstrated the efficiency to sustain cell growth by studying different structures and postprinting functionalization. Recent overviews [26, 27] resumed the current applications of this technology

in tissue engineering. The potentiality of the SLS process compared to traditional milling has been showed by Probst et al. [28], while Pallari et al. [29] demonstrated the feasibility of customised orthosis for large production.

3.2. Stereolithography.

The stereolithography (SLA) process first appeared in 1981, when the Japanese researcher Dr. Hideo Kodama of Nagoya Municipal Industrial Research Institute published his account of a functional rapid-prototyping system using photopolymers. Three years later, in 1984, Charles (Chuck) W. Hull made 3D-printing history by inventing SLA and co-founding the 3D Systems company to commercialize it. SLA is today referred to a certain number of AM technologies in which a liquid resin is converted into a solid part by exposing the material to a light source which selectively activates the polymerisation of the material. The older system utilises a vat of liquid photopolymer resin cured by an ultraviolet (UV) laser to create a solid 3D model. A UV laser beam is directed by a computer-controlled mirror onto the surface of the photopolymer resin to draw one cross-section of the CAD model of the part. After creating one layer, the building platform is lowered into the vat and then the laser beam tracing process is repeated. Generally, a blade is used to make a smooth resin layer. The process continues layer-by-layer until the fabrication of the part is completed. Once the model is complete, the platform rises out of the vat and the excess resin is drained. The model is then removed from the platform and placed in a UV oven for final curing in order to meet the required strength of the material. Subsequently, the supports are finally detached.

Another SLA system is known as inverted SLA because the object is built using an upside-down approach. In this case, the light source hits the material through the bottom of the vat. The process starts lowering the build platform to touch the bottom of the resin-filled vat and then moving upward of a quantity equal to the layer thickness. The UV laser then acts on the bottom-most layer through the transparent vat bottom. An advantage of this kind of system is that the build volume can be bigger than the vat itself. In addition, since the object is incrementally raised, the resin that is not solidified by the laser remains in the vat and can be reused for the next layer. One similar approach is adopted for the digital light processing (DLP) [30], another SLA system in which the UV laser is replaced by a digital projector [31]. The projector is a digital screen which flashes a single image of each layer across the entire platform. Since each layer will be composed of square pixels, the resolution of a DLP printer corresponds to the pixel size, whereas in the SLA system, the resolution is determined by the spot size of the laser.

Several resins have been developed over the past two decades, and the properties of SLA parts are continuously improving, making them not only useful as prototypes but also as functional parts. Photopolymers lack of stability in the long-time period. The high precision of the process, with a layer thickness that can be adjusted from 25 to $100 \, \mu m$, makes SLA suitable for producing accurate models.

The combination of medical imaging and SLA has been used to fabricate models or moulds for the preparation of implants in cranial surgery [29, 32], customized heart valves [33], ear-shaped implants [34], and aortas [35]. Dental applications are increasing [36] as well as the fabrication of tissue engineering scaffolds [37, 38], thanks also to the development of biodegradable macromers and resins [39].

3.3. Material Extrusion.

Fused deposition modeling (FDM) is an AM process that belongs to the material extrusion category. This technology was developed by Scott Crump in the late eighties of last century, and it was marketed in the 90s by Stratasys company, of which Crump was the co-founder [40]. Stratasys holds this trade name for FDM even if the patent expired in 2009. For this reason, the subsequent printer manufacturers exploiting the same extrusion principle have coined the alternative acronym of FFF (fusion filament fabrication). FDM printers build parts layer-by-layer using a thermoplastic filament that is heated to a semiliquid state, extruded, and deposited on the printing bed along with a computer-controlled path [41]. The FDM filaments come in two standard sizes with a diameter of 1.75 mm or 2.85 mm. Depending on the size of the extrusion nozzle, the layer thickness can vary from about 50 to $500 \, \mu m$. As for all AM processes, the smaller is the thickness of the layer, the higher is the part accuracy but also the longer the manufacturing time. Thanks to the solid material that feeds the 3D printer, multiple extruders can be used to combine diverse materials with different properties (e.g., rigid and flexible) or colours in the single layer or in different layers.

Polylactic acid (PLA) and acrylonitrile butadiene styrene (ABS) are the two thermoplastic materials most commonly used in FDM. Lactic acid-based polymers, including PLA and PCL, have biocompatible and biodegradable properties, and hence are extensively used for medical and pharmaceutical applications. Polycarbonate-ISO (PC-ISO), in its raw state, is compliant with ISO 10993 and USP Class VI certifications used to establish biocompatibility. These biocompatible materials enable manufacturers of medical devices to rely on the FDM technique to produce devices that can be used safely for clinical trials and for low-volume productions of end-use parts. Polymethyl methacrylate (PMMA) filament was used for 3D-printing of porous patient-tailored implants for craniofacial reconstructions and orthopedic spacers [42]. On modified FDM printers [43, 44], the possibility to directly extrude polymeric compounds from pellet feedstocks offers the potentiality to extend the range of materials for biomedical applications. However, there is no evidence of specific case studies so far.

3.4. Laser Powder Bed Fusion (L-PBF).

Laser powder bed fusion (L-PBF), also known as selective laser melting (SLM), is an AM process that uses a high-energy density laser, usually an ytterbium fibre laser, to fuse selected areas on a single layer according to the processed data and create 3D metal parts layerwise. The building process begins with laying a fine metallic powder layer on a substrate plate in a controlled inert environment. After selective melting, the

building platform is lowered, and a new layer is applied. The process is repeated until the part build height is reached. The layer thickness can vary from 15 to 150 μm. The laser beam focus is controlled by a galvanometer, and the movement of the beam is controlled by an F-theta lens. In L-PBF, laser power, scanning speed, hatching distance, and layer thickness are the common process parameters adjusted to optimize the process. These parameters affect the volumetric energy density that is available to heat up and melt the powders, mechanical properties, and surface roughness of the parts produced [45]. The alloys currently available for this process include stainless steel, cobalt chromium (Co-Cr alloys), Ni-based alloys, aluminium (Al-Si-Mg alloys), and titanium (Ti6Al4V alloy). Compared with the cast and forged components, a part produced by the L-PBF process has excellent mechanical properties, thanks to characteristics of grain refinement, extended solid solubility, chemical homogeneity, reduction in quantity, and size of phase segregation [46]. However, due to the Marangoni convection induced by high thermal capillary forces, the melt pool may be unstable causing microstructures uncontrollability [47]. Therefore, to meet the current clinical requirements in parts of Ti6Al4V produced by L-PBF, heat treatment is needed to adapt the physiochemical properties and to homogenize the metal microstructures, trying to possibly improve the cytocompatibility in vitro.

3.5. Electron Beam Melting. Electron beam melting (EBM) or electron powder bed fusion (E-PBF) is an AM process for metal powders. In this case, the energy of an electron beam is used to melt the powder, after a preheating phase of the powder layer. The mechanic of an EBM system mixes the hardware of a welding machine and the operating base of an electron microscope [48]. The EBM® technology is still an exclusive of ARCAM AB [48], which recently introduced a specific line of machines for biomedical application such as the Q10 plus model in which the improved beam control allows a better definition of the spot size [49]. If compared to the previous model (A-machines), the Q-machines have a camera, Q-Cam, which takes a picture of each layer after the melting phase. With the aid of image-processing software, the machine provides a report about the final quality of the printed parts. In this way, defects or errors can be detected and recognised immediately, without the need for additional part inspection after production. The EBM systems work under vacuum to avoid the beam to be deflected by the air molecules. Due to the vacuum and the preheating step, the build chamber is warm during the process. Therefore, after the process, the parts need to be cooled down. At the end of the process, when the part is removed from the building chamber, a soft agglomerate of powder adheres to the surface of the built and covers it completely [50]. This agglomerate is removed by sandblasting in which the same powder of the EBM process is used in order to avoid powder contamination. After this phase of cleaning, the unused powder can be recycled several times without altering its chemical composition or physical properties, because no oxygen is present inside the building chamber during the

melting process, thanks to the vacuum [50]. Because of the warm environment during the process, the part shows low residual stress as compared to laser-based L-PBF systems, which require the postprocessing of built parts by a stress-relieving treatment [51]. On the other hand, the L-PBF technique offers a better surface finish, thanks to a smaller beam size and smaller layer thickness when compared to the EBM technology [51]. However, the surface roughness resulting from the EBM process represents an advantage for medical applications. In general, Ti6Al4VELI and CoCr are the most frequently used material for medical implants produced by EBM. Patient-customised implants with high biocompatibility and structures with osseointegration properties have been developed and implemented [52–58]. A significant successful example is the large-scale production of titanium acetabular cups manufactured by two Italian companies, Lima Ltd, and Ala Ortho Srl.

4. Conclusions

The purpose of the current review is to provide a short summary that can give an overview of the AM applications in the medical field even to a reader who approaches the topic for the first time. The main features of each AM process have been presented also by highlighting its peculiarities and differences. Numerous references have been provided to show applicative case studies, demonstrating the potentiality of AM in the medical sector. A special effort was dedicated to providing case studies which reported not only the feasibility for large-volume production but also the indication of industries which already use additive technologies as the only manufacturing system to fabricate their medical products. Even if applications in the biomedical sector have been the first for layerwise technologies almost 20 years ago, this review showed that the research is currently active and aimed at improving the part design and extending the number of materials available for AM, as supported by the numerous studies.

Conflicts of Interest

The authors declare that there are no conflicts of interest regarding the publication of this paper.

References

[1] I. Gibson, D. W. Rosen, and B. Stucker, *Additive Manufacturing Technologies*, Springer, Berlin, Germany, 2010.

[2] N. Hopkinson and P. Dickens, "Emerging rapid manufacturing processes," in *Rapid Manufacturing: An Industrial Revolution for the Digital Age*, pp. 55–80, John Wiley & Sons, Hoboken, NJ, USA, 2006.

[3] J. Giannatsis and V. Dedoussis, "Additive fabrication technologies applied to medicine and health care: a review," *International Journal of Advanced Manufacturing Technology*, vol. 40, no. 1-2, pp. 116–127, 2009.

[4] N. Vitković, S. Mladenović, M. Trifunović et al., "Software framework for the creation and application of personalized bone and plate implant geometrical models," *Journal of Healthcare Engineering*, vol. 2018, Article ID 6025935, 11 pages, 2018.

[5] S. Singare, Q. Lian, W. Ping Wang et al., "Rapid prototyping assisted surgery planning and custom implant design," *Rapid Prototyping Journal*, vol. 15, no. 1, pp. 19–23, 2009.

[6] E. M. Zanetti, A. Aldieri, M. Terzini et al., "Additively manufactured custom load-bearing implantable devices: grounds for caution," *Australasian Medical Journal*, vol. 10, no. 8, p. 694, 2017.

[7] S. R. Patel, K. Ghose, and E. N. Eskandar, "An open source 3-D printed modular micro-drive system for acute neurophysiology," *PLoS One*, vol. 9, no. 4, Article ID e94262, 2014.

[8] R. A. McDougal and G. M. Shepherd, "3D-printer visualization of neuron models," *Frontiers in Neuroinformatics*, vol. 9, p. 18, 2015.

[9] T. Baden, A. M. Chagas, G. Gage et al., "Open Labware: 3-D printing your own lab equipment," *PLoS Biology*, vol. 13, no. 3, article e1002086, 2015.

[10] M. Salmi, K.-S. Paloheimo, J. Tuomi, J. Wolff, and A. Mäkitie, "Accuracy of medical models made by additive manufacturing (rapid manufacturing)," *Journal of Cranio-Maxillofacial Surgery*, vol. 41, no. 7, pp. 603–609, 2013.

[11] J. Parthasarathy and J. Parthiban, "Rapid prototyping in custom fabrication of titanium mesh implants for large cranial defects," in *Proceedings of RAPID*, pp. 20–22, May 2008.

[12] NIH 3D Print Exchange, "Online repository for 3D-printable models for biology and medicine," November 2018, https://3dprint.nih.gov/.

[13] G. Venne, G. Esau, R. T. Bicknell et al., "3D printed anatomy-specific fixture for consistent glenoid cavity position in shoulder simulator," *Journal of Healthcare Engineering*, vol. 2018, Article ID 2572730, 6 pages, 2018.

[14] A. Salmi, F. Calignano, M. Galati et al., "An integrated design methodology for components produced by laser powder bed fusion (L-PBF) process," *Virtual and Physical Prototyping*, vol. 13, no. 3, pp. 191–202, 2018.

[15] C. Herlin, M. Koppe, J.-L. Béziat, and A. Gleizal, "Rapid prototyping in craniofacial surgery: using a positioning guide after zygomatic osteotomy—a case report," *Journal of Cranio-Maxillofacial Surgery*, vol. 39, no. 5, pp. 376–379, 2011.

[16] E. Berry, J. M. Brown, M. Connell et al., "Preliminary experience with medical applications of rapid prototyping by selective laser sintering," *Medical Engineering & Physics*, vol. 19, no. 1, pp. 90–96, 1997.

[17] I. Shishkovsky and V. Scherbakov, "Selective laser sintering of biopolymers with micro and nano ceramic additives for medicine," *Physics Procedia*, vol. 39, pp. 491–499, 2012.

[18] C. K. Chua, K. F. Leong, K. H. Tan, F. E. Wiria, and C. M. Cheah, "Development of tissue scaffolds using selective laser sintering of polyvinyl alcohol/hydroxyapatite biocomposite for craniofacial and joint defects," *Journal of Materials Science: Materials in Medicine*, vol. 15, no. 10, pp. 1113–1121, 2004.

[19] K. H. Tan, C. K. Chua, K. F. Leong et al., "Scaffold development using selective laser sintering of polyetheretherketone-hydroxyapatite biocomposite blends," *Biomaterials*, vol. 24, no. 18, pp. 3115–3123, 2003.

[20] C. Adamzyk, P. Kachel, M. Hoss et al., "Bone tissue engineering using polyetherketoneketone scaffolds combined with autologous mesenchymal stem cells in a sheep calvarial defect model," *Journal of Cranio-Maxillofacial Surgery*, vol. 44, no. 8, pp. 985–994, 2016.

[21] H.-T. Liao, M.-Y. Lee, W.-W. Tsai, H.-C. Wang, and W.-C. Lu, "Osteogenesis of adipose-derived stem cells on polycaprolactone-β-tricalcium phosphate scaffold fabricated via selective laser sintering and surface coating with collagen type I," *Journal of Tissue Engineering and Regenerative Medicine*, vol. 10, no. 10, pp. 337–353, 2016.

[22] S. Lohfeld, S. Cahill, V. Barron et al., "Fabrication, mechanical and in vivo performance of polycaprolactone/tricalcium phosphate composite scaffolds," *Acta Biomaterialia*, vol. 8, no. 9, pp. 3446–3456, 2012.

[23] W. Y. Zhou, S. H. Lee, M. Wang, W. L. Cheung, and W. Y. Ip, "Selective laser sintering of porous tissue engineering scaffolds from poly(l-lactide)/carbonated hydroxyapatite nano-composite microspheres," *Journal of Materials Science: Materials in Medicine*, vol. 19, no. 7, pp. 2535–2540, 2008.

[24] R. L. Simpson, F. E. Wiria, A. A. Amis et al., "Development of a 95/5 poly(L-lactide-co-glycolide)/hydroxylapatite and β-tricalcium phosphate scaffold as bone replacement material via selective laser sintering," *Journal of Biomedical Materials Research Part B: Applied Biomaterials*, vol. 84, no. 1, pp. 17–25, 2008.

[25] S. Saska, L. C. Pires, M. A. Cominotte et al., "Three-dimensional printing and in vitro evaluation of poly(3-hydroxybutyrate) scaffolds functionalized with osteogenic growth peptide for tissue engineering," *Materials Science and Engineering: C*, vol. 89, pp. 265–273, 2018.

[26] S. Miar, A. Shafiee, T. Guda et al., "Additive Manufacturing for Tissue Engineering," in *3D Printing and Biofabrication*, pp. 3–54, Springer, Berlin, Germany, 2018.

[27] A. Youssef, S. J. Hollister, and P. D. Dalton, "Additive manufacturing of polymer melts for implantable medical devices and scaffolds," *Biofabrication*, vol. 9, no. 1, article 012002, 2017.

[28] F. A. Probst, M. Metzger, M. Ehrenfeld, and C.-P. Cornelius, "Computer-assisted designed and manufactured procedures facilitate the lingual application of mandible reconstruction plates," *Journal of Oral and Maxillofacial Surgery*, vol. 74, no. 9, pp. 1879–1895, 2016.

[29] J. H. P. Pallari, K. W. Dalgarno, and J. Woodburn, "Mass customization of foot orthoses for rheumatoid arthritis using selective laser sintering," *IEEE Transactions on Biomedical Engineering*, vol. 57, no. 7, pp. 1750–1756, 2010.

[30] E. Fantino, A. Chiappone, I. Roppolo et al., "3D printing of conductive complex structures with in situ generation of silver nanoparticles," *Advanced Materials*, vol. 28, no. 19, pp. 3712–3717, 2016.

[31] R. De Santis, U. D'Amora, T. Russo et al., "3D fibre deposition and stereolithography techniques for the design of multifunctional nanocomposite magnetic scaffolds," *Journal of Materials Science: Materials in Medicine*, vol. 26, no. 10, p. 250, 2015.

[32] P. S. D'Urso, P. S., D. J. Earwaker et al., "Custom cranioplasty using stereolithography and acrylic," *British Journal of Plastic Surgery*, vol. 53, no. 3, pp. 200–204, 2000.

[33] G. Wurm, B. Tomancok, K. Holl, and J. Trenkler, "Prospective study on cranioplasty with individual carbon fiber reinforced polymere (CFRP) implants produced by means of stereolithography," *Surgical Neurology*, vol. 62, no. 6, pp. 510–521, 2004.

[34] R. Sodian, M. Loebe, A. Hein et al., "Application of stereolithography for scaffold fabrication for tissue engineered heart valves," *ASAIO Journal*, vol. 48, no. 1, pp. 12–16, 2002.

[35] A. Naumann, J. Aigner, R. Staudenmaier et al., "Clinical aspects and strategy for biomaterial engineering of an auricle based on three-dimensional stereolithography," *European Archives of Oto-Rhino-Laryngology*, vol. 260, no. 10, pp. 568–575, 2003.

[36] A. Dawood, B. M. Marti, V. Sauret-Jackson, and A. Darwood, "3D printing in dentistry," *British Dental Journal*, vol. 219, no. 11, pp. 521–529, 2015.

[37] J. Wallace, M. O. Wang, P. Thompson et al., "Validating continuous digital light processing (cDLP) additive manufacturing accuracy and tissue engineering utility of a dye-initiator package," *Biofabrication*, vol. 6, no. 1, article 015003, 2014.

[38] D. Dean, J. Wallace, A. Siblani et al., "Continuous digital light processing (cDLP): highly accurate additive manufacturing of tissue engineered bone scaffolds," *Virtual and Physical Prototyping*, vol. 7, no. 1, pp. 13–24, 2012.

[39] R. Sodian, P. Fu, C. Lueders et al., "Tissue engineering of vascular conduits: fabrication of custom-made scaffolds using rapid prototyping techniques," *Thoracic and Cardiovascular Surgeon*, vol. 53, no. 3, pp. 144–149, 2005.

[40] T. Matsuda, M. Mizutani, and S. C. Arnold, "Molecular design of photocurable liquid biodegradable copolymers. 1. Synthesis and photocuring characteristics," *Macromolecules*, vol. 33, no. 3, pp. 795–800, 2000.

[41] P. Minetola and M. Galati, "A challenge for enhancing the dimensional accuracy of a low-cost 3D printer by means of self-replicated parts," *Additive Manufacturing*, vol. 22, pp. 256–264, 2018.

[42] D. Espalin, K. Arcaute, D. Rodriguez, F. Medina, M. Posner, and R. Wicker, "Fused deposition modeling of patient-specific polymethylmethacrylate implants," *Rapid Prototyping Journal*, vol. 16, no. 3, pp. 164–173, 2010.

[43] N. Volpato, D. Kretschek, J. Foggiatto et al., "Experimental analysis of an extrusion system for additive manufacturing based on polymer pellets," *International Journal of Advanced Manufacturing Technology*, vol. 81, no. 9–12, pp. 1519–1531, 2015.

[44] X. Liu, B. Chi, Z. Jiao, J. Tan, F. Liu, and W. Yang, "A large-scale double-stage-screw 3D printer for fused deposition of plastic pellets," *Journal of Applied Polymer Science*, vol. 134, no. 31, p. 45147, 2017.

[45] F. Calignano, G. Cattano, and D. Manfredi, "Manufacturing of thin wall structures in AlSi10Mg alloy by laser powder bed fusion through process parameters," *Journal of Materials Processing Technology*, vol. 255, pp. 773–783, 2018.

[46] F. Trevisan, F. Calignano, A. Aversa et al., "Additive manufacturing of titanium alloys in the biomedical field: processes, properties and applications," *Journal of Applied Biomaterials & Functional Materials*, vol. 16, no. 2, pp. 57–67, 2018.

[47] K. Antony and N. Arivazhagan, "Studies on energy penetration and Marangoni effect during laser melting process," *Journal of Engineering Science and Technology*, vol. 10, no. 4, pp. 509–525, 2015.

[48] M. Galati and L. Iuliano, "A literature review of powder-based electron beam melting focusing on numerical simulations," *Additive Manufacturing*, vol. 19, pp. 1–20, 2018.

[49] M. Galati, A. Snis, and L. Iuliano, "Experimental validation of a numerical thermal model of the EBM process for Ti6Al4V," *Computers & Mathematics with Applications*, 2018.

[50] S. Biamino, A. Penna, U. Ackelid et al., "Electron beam melting of Ti-48Al-2Cr-2Nb alloy: microstructure and mechanical properties investigation," *Intermetallics*, vol. 19, no. 6, pp. 776–781, 2011.

[51] F. Froes and B. Dutta, "The additive manufacturing (AM) of titanium alloys," in *Advanced Materials Research*, Trans Tech Publications, Zurich, Switzerland, 2014.

[52] O. L. A. Harrysson, O. Cansizoglu, D. J. Marcellin-Little, D. R. Cormier, and H. A. West, "Direct metal fabrication of titanium implants with tailored materials and mechanical properties using electron beam melting technology," *Materials Science and Engineering: C*, vol. 28, no. 3, pp. 366–373, 2008.

[53] A. Palmquist, A. Snis, L. Emanuelsson et al., "Long-term biocompatibility and osseointegration of electron beam melted, free-form–fabricated solid and porous titanium alloy: experimental studies in sheep," *Journal of Biomaterials Applications*, vol. 27, no. 8, pp. 1003–1016, 2013.

[54] P. Heinl, A. Rottmair, C. Körner, and R. F. Singer, "Cellular titanium by selective electron beam melting," *Advanced Engineering Materials*, vol. 9, no. 5, pp. 360–364, 2007.

[55] P. Thomsen, J. Malmström, L. Emanuelsson et al., "Electron beam-melted, free-form-fabricated titanium alloy implants: material surface characterization and early bone response in rabbits," *Journal of Biomedical Materials Research Part B: Applied Biomaterials*, vol. 90, no. 1, pp. 35–44, 2008.

[56] J. Parthasarathy, B. Starly, S. Raman, and A. Christensen, "Mechanical evaluation of porous titanium (Ti6Al4V) structures with electron beam melting (EBM)," *Journal of the Mechanical Behavior of Biomedical Materials*, vol. 3, no. 3, pp. 249–259, 2010.

[57] O. Harrysson, B. Deaton, J. Bardin et al., "Evaluation of titanium implant components directly fabricated through electron beam melting technology," in *Proceedings of the Materials and Processes for Medical Devices Conference*, Boston, MA, USA, November 2005.

[58] P. Heinl, L. Müller, C. Körner, R. F. Singer, and F. A. Müller, "Cellular Ti-6Al-4V structures with interconnected macro porosity for bone implants fabricated by selective electron beam melting," *Acta Biomaterialia*, vol. 4, no. 5, pp. 1536–1544, 2008.

Research Article

Design of Complexly Graded Structures inside Three-Dimensional Surface Models by Assigning Volumetric Structures

Ronny Brünler (ID)**, Robert Hausmann, Maximilian von Münchow, Dilbar Aibibu, and Chokri Cherif**

Institute of Textile Machinery and High Performance Material Technology (ITM), Technische Universität Dresden, Hohe Str. 6, 01069 Dresden, Germany

Correspondence should be addressed to Ronny Brünler; ronny.bruenler@tu-dresden.de

An innovative approach for designing complex structures from STL-datasets based on novel software for assigning volumetric data to surface models is reported. The software allows realizing unique complex structures using additive manufacturing technologies. Geometric data as obtained from imaging methods, computer-aided design, or reverse engineering that exist only in the form of surface data are converted into volumetric elements (voxels). Arbitrary machine data can be assigned to each voxel and thereby enable implementing different materials, material morphologies, colors, porosities, etc. within given geometries. The software features an easy-to-use graphical user interface and allows simple implementation of machine data libraries. To highlight the potential of the modular designed software, an extrusion-based process as well as a two-tier additive manufacturing approach for short fibers and binder process are combined to generate three-dimensional components with complex grading on the material and structural level from STL files.

1. Introduction

Additive manufacturing technologies are based on the layered construction of material into a finished component. The production is carried out by solidification of

   (i) Liquids or gels (curing, drying, crosslinking, etc.) [1–9]

   (ii) Powders or granules (gluing, sintering, etc.) [10–16] or

   (iii) Pasty and belt-shaped or strand-shaped materials (direct deposition without curing processes or solidification, etc.) [17–20]

The limitations for realizing parts with a complex material composition are either found in the process characteristics or in the data formats used.

Technologies using powder beds or liquid baths are limited to a particular material or a particular material composition which is constant throughout the entire component [21, 22].

With these methods, different materials cannot be applied within a part, in particular not within one layer.

In the case of the open-space or layer construction methods, it is possible to use various materials [23, 24].

However, the limitations for parts with complex material and structural composition lie in the properties of the file formats [25]. The most common file format in generative production methods is the STL format (standard tessellation language/standard triangulation language) [26–28]. In niche applications, the AMF format (additive manufacturing format) and the OBJ format (object format) are used as well [29, 30].

A sphere is used to illustrate the file formats. The STL file format provides only surface information and uses triangles, often referred to as vertices, to represent the surfaces as shown in Figure 1(a). In the AMF or OBJ format, the surface information can also be supplemented with properties (material, textures, or metadata), emphasized by a red color scheme in the triangles on the top of the sphere in Figure 1(b).

(a)

(b)
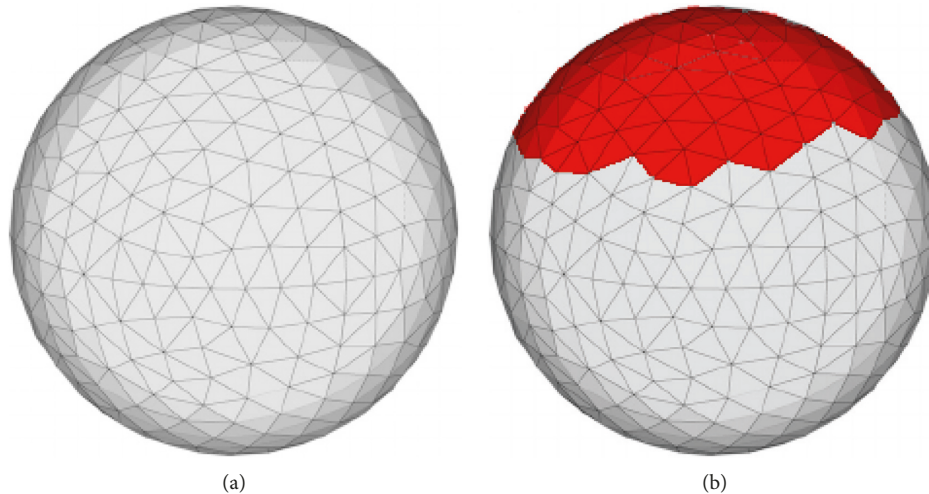
Figure 1: (a) Visualization of the surface representation of a sphere by means of triangles in the STL format [31]. (b) The same sphere in the AMF or OBJ format that allow assigning descriptive metadata to individual triangles, shown here as red color scheme in the upper part of the sphere.

STL files as well as AMF or OBJ files represent geometric bodies exclusively by means of surface information. Regardless of whether the files are stored as surface or solid bodies, they contain no volume data. Basically, the objects are hollow inside and have "outer walls" that are infinitesimally thin. The only difference in solid bodies is the representation of a filled body. Figure 2(a) shows a graphic representation of the previously discussed sphere cut in half using the software Blender (Blender Foundation). As in all other software for editing or displaying STL files or similar formats (Netfabb, Cura, Slic3r, and Repetier, amongst others) as well as CAD software (FreeCAD, SolidWorks, AutoCAD, and CATIA, amongst others), only the surface of the structure can be addressed as it is simply impossible to select or click on other structures than the surface triangles. This points up the decisive limitation of all surface-based file formats: within surface-approximated geometries, for example, from computer tomography recordings (CT) and magnetic resonance tomography representations (MRT) or 3D scans, property assignments cannot be implemented.

In CAD programs, however, objects that contain volume information can be designed and stored in the AMF or OBJ format, but again have to be regarded as individual surfaces approximated by triangles. It is thus possible to realize structures with grading on the material or structural level, supposing that they are designed from scratch as the two-color sphere in Figure 2(b).

However, assigning properties within previously defined or given bodies as obtained from CT scans, MRI scans, or radiographs for the determination of defect geometries in regenerative medicine or 3D scans from reverse engineering cannot be carried out in these programs because of the surface-based representation and the related restrictions. Figure 3(a) shows a CT scan of the lower spine and an STL file derived from that scan containing geometry information of a lumbar vertebra exhibiting a complex geometry. Substantial differences in the structural composition of the STL

file can be observed in comparison with the anatomy of a vertebra (Figure 3(c)). The STL file features a hollow body and shows almost no structures in the area of the spongy bone in the center of vertebral body and infinitesimally thin walls instead of the dense cortical bone around the spongy bone structure. There is no software yet available to fill certain regions with different materials or structural variations within STL, AMF, or OBJ files of parts with complex geometry.

2. Materials and Methods

2.1. Software for Accessing the Inner Structure of Surface-Based Bodies. In addition to surface-based file formats, bodies can also be represented by volumetric elements (voxels). Graphic representations of spheres in voxel format with assigned metadata are shown in Figure 4. This approach is mostly known from video games such as Minecraft (Mojang/Microsoft Studios, 2009) and Blade Runner (Virgin Interactive, 1997) or simulations [34] to represent terrain features and is also widely used in medical imaging formats such as DICOM® [35, 36]. However, the voxel formats are not used for designing implants for regenerative medicine, prosthetic components, or 3D printing applications in reverse engineering as slicer software is usually developed for STL files. Hence, while it is possible to 3D print or display complex geometries with different surfaces, it is not possible to realize grading on the material or structural level inside the structures.

To access the inner structure of surface-based bodies, novel software for segmenting the structures into voxels and manipulating them is developed. The software is capable of processing STL files in ASCII format and is developed in C# within the development environment Visual Studio Community (Microsoft Corp.). Figure 5 shows the graphical user interface (GUI) that was created within the Windows Presentation Foundation (WPF) framework.

(a) (b)
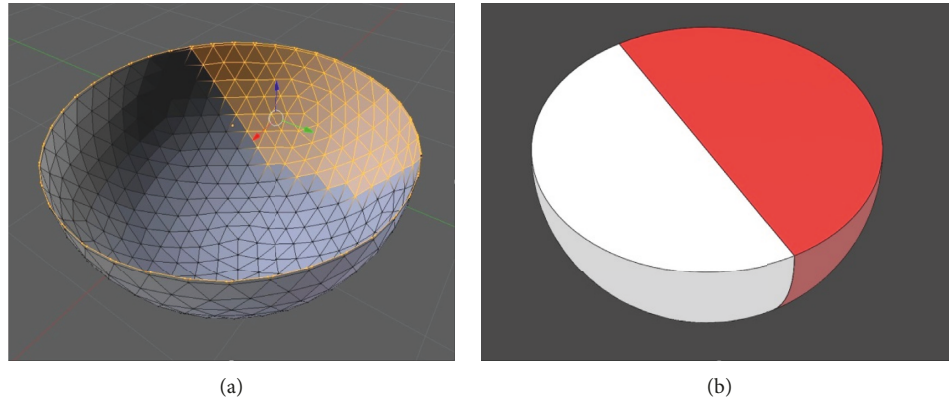
FIGURE 2: (a) Visualization of the structure of the sphere in surface-based formats that solely allow selecting and thus altering the surface triangles. (b) Image of a sphere with two colors designed in a CAD software as a solid body.

(a) (b) (c)
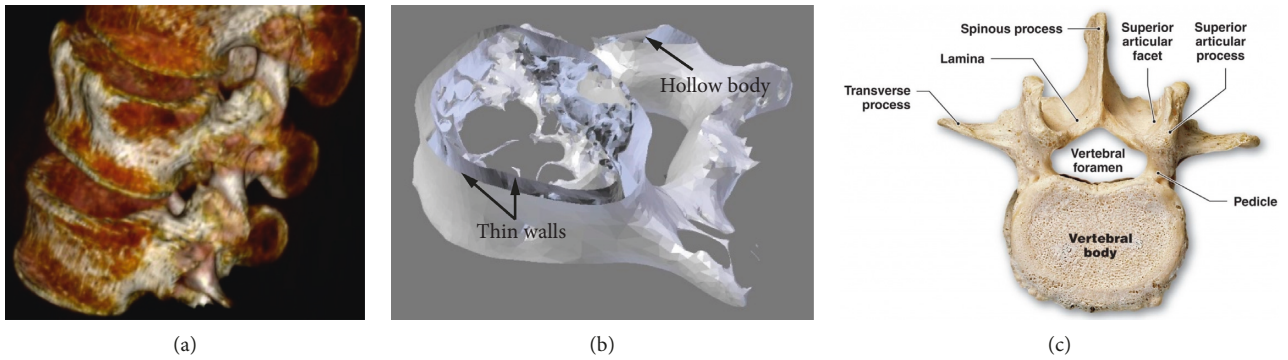
FIGURE 3: (a) CT scan of the lower spine showing the L3 (top), L4 (middle), and L5 (bottom) lumbar vertebrae [32]. (b) View of the STL file of an L5 lumbar vertebra from [32] exhibiting infinitesimally thin walls and a hollow body. (c) Anatomy of the lumbar vertebrae [33].

(a) (b)
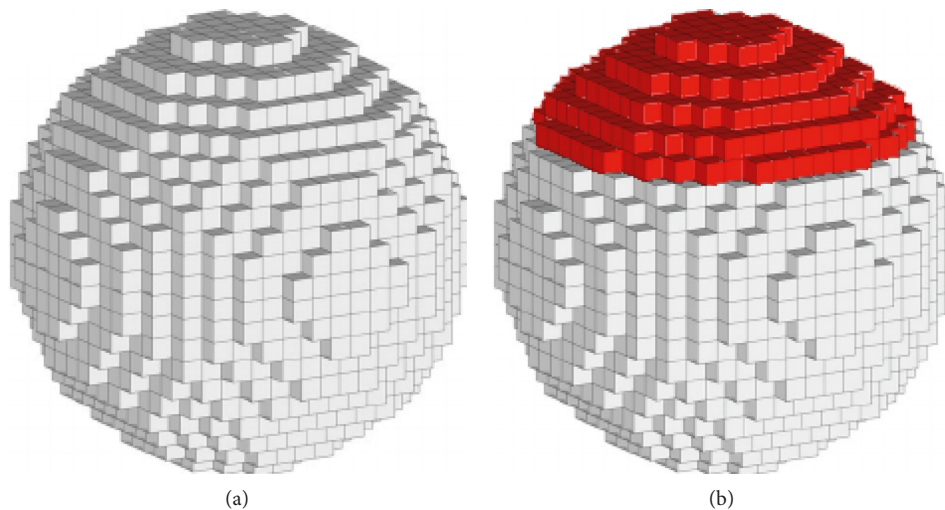
FIGURE 4: (a) Visualization of a sphere in voxel format. (b) The same sphere with a red color scheme in the upper part of the sphere. Descriptive metadata can be assigned to individual voxels even throughout the inner parts of the body.

After importing a file, it is automatically converted into the AMF format and can be viewed, rotated, and zoomed in and out on the "AMF" tab (Figure 5(a)). The "Slice" tab as visualized in Figure 5(b) is used to slice the body and to additionally implement a rectangular grid. Slicing thickness and grid size can be adjusted arbitrarily and separately. In default mode, the grid size matches the slicing thickness. Thus, the grid subdivides the body into cubic voxels.

Generating the slice data for a graphical representation of the contours of the body requires the consideration of

(a)

(b)
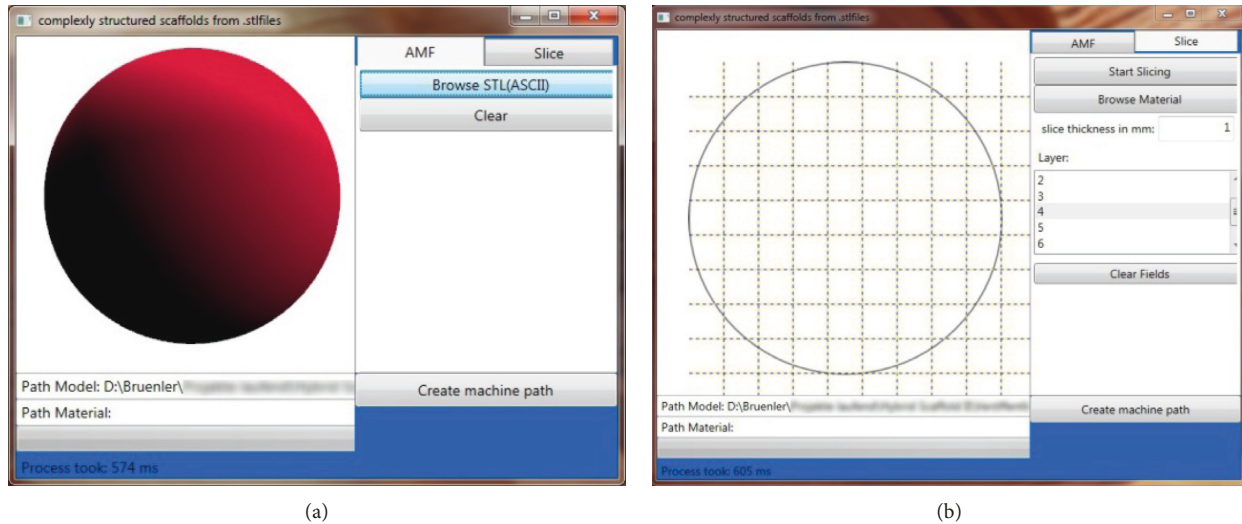
FIGURE 5: Graphical user interface of the developed software: (a) "AMF" tab with imported sphere; (b) "Slice" tab showing the midlayer of the subdivided sphere, the input field for adjusting slicing thickness, and the scroll bar for scrolling through the single slices.

several special cases related to the surface representation by means of triangles. During the generation of a single slice, necessarily some triangles are cut by the section plane as evident in Figure 6(a). In total, there are 10 cases describing the situational relations between section plane and triangles [37]. While simple cases such as triangles located completely above or below the section plane are easy to process, five specific cases have to be considered more closely (Figure 6(b)):

(1) All three edges are located on the section plane

(2) Exactly two edges are located on the section plane

(3) One edge is located above, one below, and one on the section plane

(4) One edge is located above/below the section plane and two edges are located on the other side

(5) Exactly one edge is located on the section plane

These considered cases have a significant effect on the calculation of the intersection points. The coordinates of the edges of all triangles describing the edited body are stored in a separate class (triangle class) within the software. They are processed during slice data generation and serve for intersection point calculation. After using a certain coordinate for calculation, it may be erased from the to-be-processed data. However, depending on the case and on the ratio between slicing thickness and triangle size, certain coordinates have to be used for the calculation of the next layer and must not be erased. To ensure a correct calculation, novel triangles are generated according to Figure 7(a). The triangle (defined by a, b, and c in Figure 7(a)) he is divided into three smaller triangles using the intersection points (P1 and P2) with the current section plane. In the case described here, the coordinates a and b can be erased from the triangle class, and only the triangle defined by P1, P2 and C is used for calculating the intersection points in the next layer.

After calculation of all intersection points, a polygon course is generated automatically and displayed for each

layer in the slice tab. The software layout also allows processing more complex bodies, such as the "test your 3D printer! v2" file from Thingiverse (MakerBot Industries, LLC) as illustrated in Figure 7(b) [38].

3. Results and Discussion

3.1. Assignment of Multiple Properties and g-Code to Subvolumes within Given Complex Geometries. The imported body is divided into voxels by the rectangular grid implemented in the "Slice" tab. Thus, all voxels are accessible by scrolling through the single layers. These features enable assigning arbitrary properties to every single voxel within any given geometry.

The properties assigned to each voxel are used to generate machine-readable code. As g-code is the most common numerical control programming language, it is used for further processing. Specific commands are filed by means of a user-friendly editable .txt file. It can be adjusted depending on the manufacturing technology used. The standard file for extrusion-based additive manufacturing processes is shown in Figure 8(a). It contains the material id (matid), the number of layers necessary to fill one millimeter (fillings/mm), the path distance (hatch), the path arrangement (pattern), the digital output command being used to control the extrusion nozzle (tool), the speed of the tool (speed), and the zero position of the tool used (*X*-, *Y*-, and *Z*-coordinates). The strand thickness can be calculated from the "fillings/mm" column as these values are used for the travel of the *z*-position to lay the strands directly on top of each other. Thus, according to Figure 8(a), 8 fillings/mm are used for a strand thickness of $125\,\mu$m and 4 fillings/mm are used for $250\,\mu$m strands, respectively.

The absolute positions of the voxels and the assigned fillings, hatches, tools, patterns, speeds, and positions are used to generate g-code commands. The black paths in Figure 8(b) directly show the course of the generated path in g-code. Travels in *z* direction are handed over from the

(a)

(b)
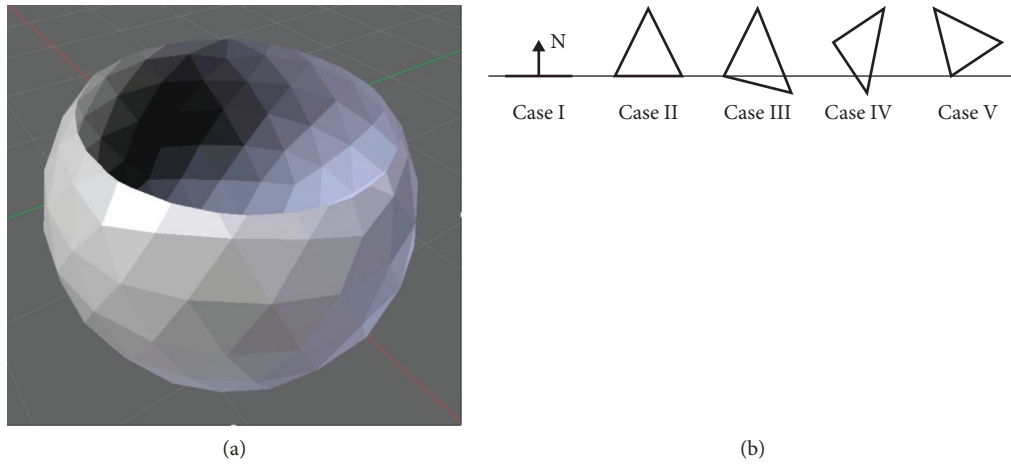
FIGURE 6: (a) Slicing of a sphere with resulting cuts of the surface triangles. (b) Specific cases for situational relations between the section plane and surface triangles during slicing [37].

(a)

(b)
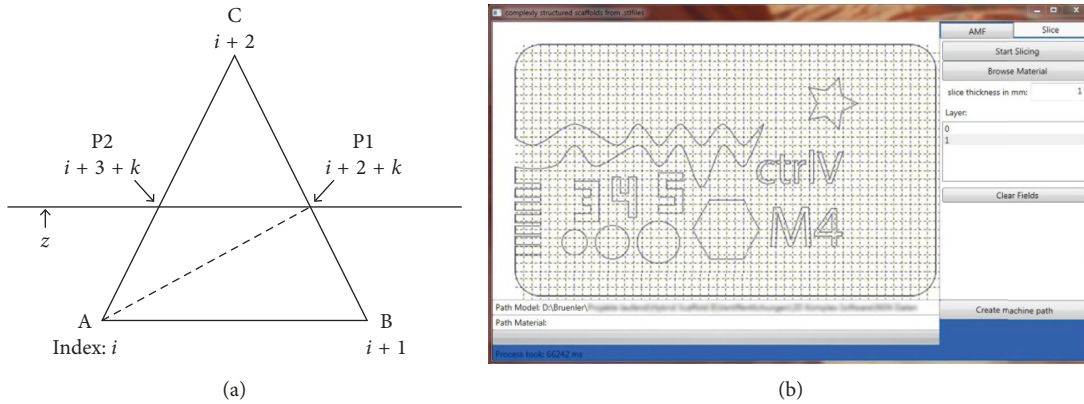
FIGURE 7: (a) Method for calculating the polygon course for a graphic representation of single slices. (b) Polygon course of the base layer of a complex 3D structure [38].

Matid	Filling (mm)	Hatch	Pattern	Tool	Speed	X	Y	Z
1	8	125	zz	1	200	50	50	0
2	8	250	zz	1	200	50	50	0
3	4	250	zz	2	500	150	50	0
4	4	500	zz	2	500	150	50	0

(a)

(b)
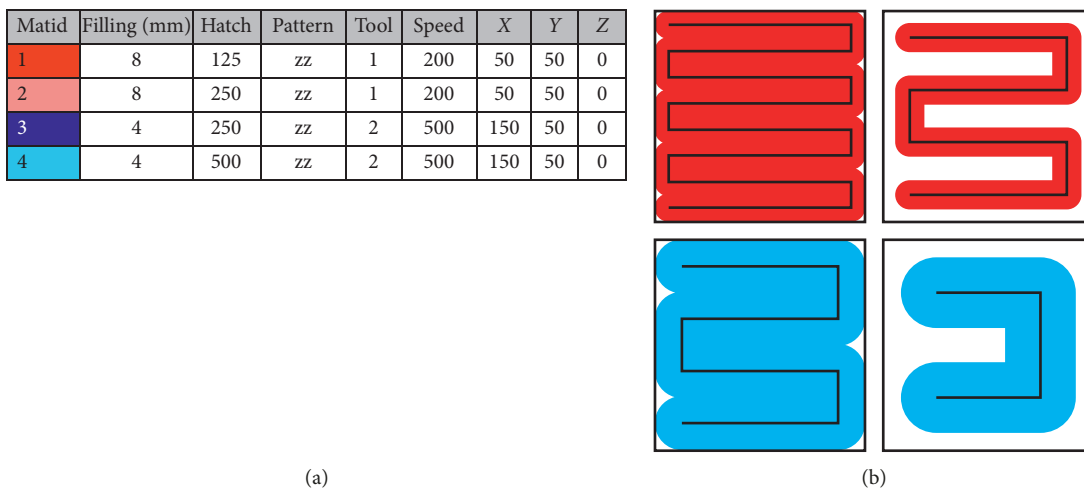
FIGURE 8: (a) Standard file for extrusion-based printing with two different colored materials and different deposition patterns. The voxel size in this figure is 1 mm and is filled in z direction with 8 red material strands (tool 1; red material; strand thickness 125 μm; traversing speed 200 mm/min; zero position of the nozzle with respect to tool installation in our machine) and 4 blue strands (tool 2; blue material; strand thickness 250 μm; traversing speed 500 mm/min; zero position of tool #2), leading to (b) different voxel filling patterns with adjusted path distances (hatch) for the same material used.

information provided by the "fillings/mm" column and the slice thickness.

The file shown in Figure 8(a) leads to different material deposition. The patterns with "matid 1" and "matid 2" are extruded from the same nozzle (tool 1) and with the same speed but in different path distances. For "matid 1," the strand thickness matches the path distance and thus fills the voxel area in top view creating a dense structure (Figure 8(b), top left). "Matid 2" deposits the $125\,\mu$m strands in a path distance of $250\,\mu$m and thus exhibit filling levels of 50%. In "matid 3" and "matid 4," another tool is used to deposit larger strands in different patterns.

Figure 9 shows three different structures manufactured from the same cuboid STL file ($20\,mm \times 20\,mm \times 4\,mm$). Two extruding systems with nozzles 0.4 mm in diameter (Nordson EFD) filled with different colored clay were used to manufacture different structures within the STL file.

The left structure was manufactured with both nozzles using the same path distance leading to a laydown of one material (light-blue colored clay) in the inner zone and the other material (orange colored clay) in the outer part while both regions featuring a dense path spacing. The structure in the middle was manufactured using solely one nozzle following dense path spacing in the outer part and a 0.8 mm path spacing in the inner region leading to 50% porosity. The structure on the right was manufactured with both nozzles using different path distances generating a structure featuring both different materials and different path spacing and thus porosity. The different material grading, porosity grading, or combination of both within the lattice structures were realized within a STL file that usually solely defines the outer geometry by making use of two extrusion nozzles.

3.2. Additive Manufacturing of Complexly Structured Lattice Structures from Surface Models.
The software is designed to assign the information from the editable configuration file to the voxels generated by slicing and gridding of the imported surface based file. An easy-to-use graphical user interface was developed to display the voxels and the boundary curve(s) of the imported body as well as the basic properties of the material deposition as defined in the editable .txt file.

Figure 10(a) shows the GUI of the software during assigning materials from the standard file to one layer of the previously discussed sphere. The standard file is displayed in a reduced form to provide a large area for assigning the materials and patterns.

The voxel size and overall structure size are not limited by the software. However, the voxel size should be dimensioned according to the tools used. In the case of extrusion-based processes, the strand width and the strand spacing should be considered. An appropriate voxel size for the extrusion nozzles used for manufacturing the structures from Figure 9 may lead to different relative disparities in geometries with different sizes. The comparison between Figures 10(a) and 11(a) shows larger relative deviations in the sphere with 9 mm in diameter and good conformity for the life-size vertebra while using the same voxel size. The processing time is dependent on the number of surface
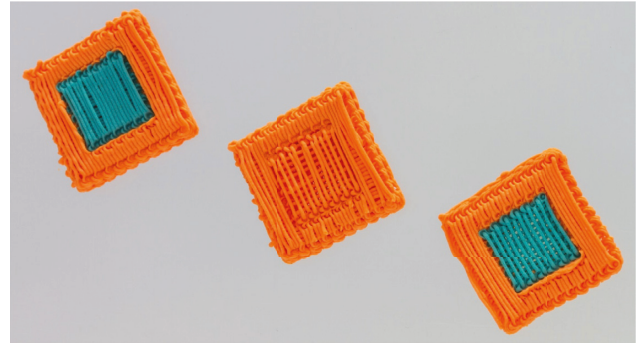
Figure 9: Manufacturing of material grading (left), porosity grading (center), and material and porosity grading (right) by means of assigning different nozzles (tool column) and strand spacings (hatch column).

triangles of the processed structure and the hardware used. The process of loading and processing the vertebra structure that is defined by 34464 surface triangles into voxels took 71.6 seconds on a dual-core 2.4 GHz, 4 GB RAM, 256 MB graphics memory system and 14.5 seconds on an eight-core 3.4 GHz, 32 GB RAM, 1 GB graphics memory system, making the software applicable on a wide range of computing systems. Contiguous areas are processed with continuous paths by using the zig-zag algorithm according to Figure 10(b).

To show the potential of the novel developed software, the surface model of a human lumbar vertebra, extracted from a CT scan and provided as STL file by MarioDiniz on Thingiverse [32] as shown in Figure 3, is subdivided in voxels and filled with different materials and patterns. The software GUI in Figure 11(a) shows polylines based on the calculations presented, showing walls, remains from scanning parts of the trabecular bones, and artefacts within the STL file. These lines function as guidance for assigning the materials and structures from the editable configuration file to the part. For manufacturing the part, two extrusion-based nozzles with a diameter of 0.4 mm (Nordson EFD) as in Figure 9 are used. The example part features an orange pattern with narrow strand spacing of $400\,\mu$m for the areas of the cortical bone (compact bone) and a light-blue pattern with a strand spacing of $800\,\mu$m, leading to a porosity of about 50% in the areas of the cancellous bone (spongy bone) of the vertebral body. Figure 11(b) shows the printed body featuring a material grading (different colors) as well as a porosity grading (strand spacing).

3.3. Combined Additive Manufacturing of Complex Fiber-Based and Strand-Based Structures for Biomedical Applications.
The applications shown so far relate exclusively to the production of extrusion-based structures. The adaptation of the configuration file is used directly to automatically create a g-code with corresponding strand spacing. The software, which also serves as a postprocessor, also allows the use of completely different additive manufacturing processes.

The Net Shape Nonwoven Method (NSN) is a unique technology for the additive production of short fiber-based structures for regenerative medicine [40]. Similar to powder bed printing, this technology is a two-tier process.

(a)

(b)
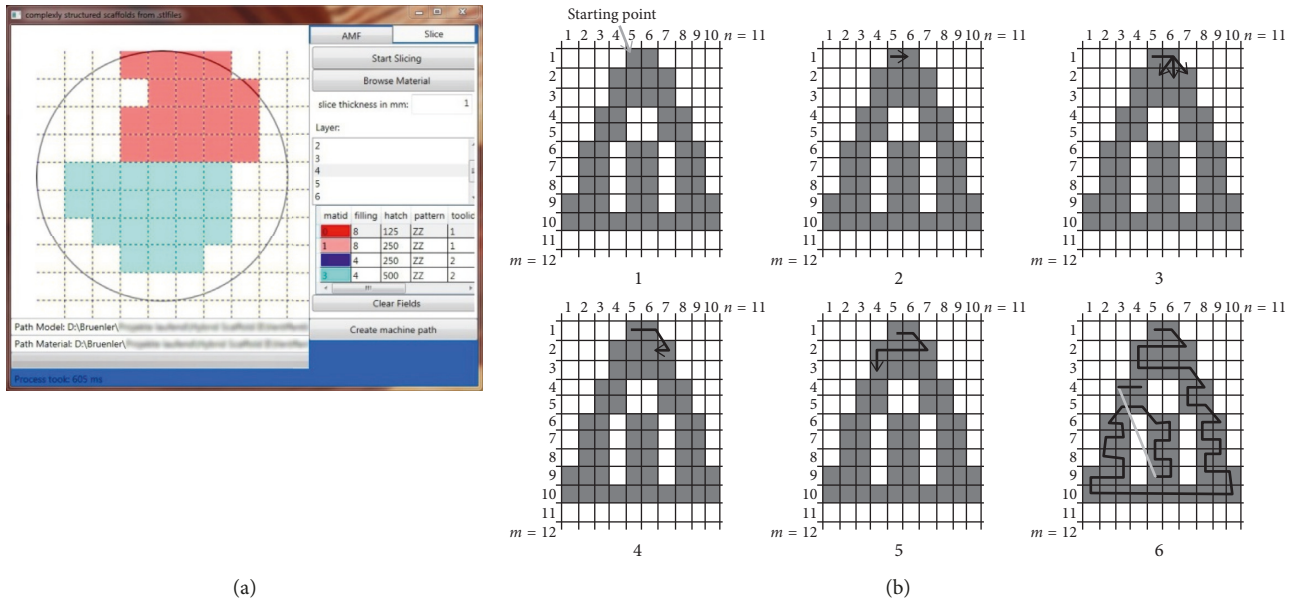
Figure 10: (a) "Slice" tab showing assigned structures from the browsed standard file within the midlayer of a 9 mm sphere. (b) Zig-zag algorithm to create continuous paths in complex slice geometries according to [39].

(a)

(b)
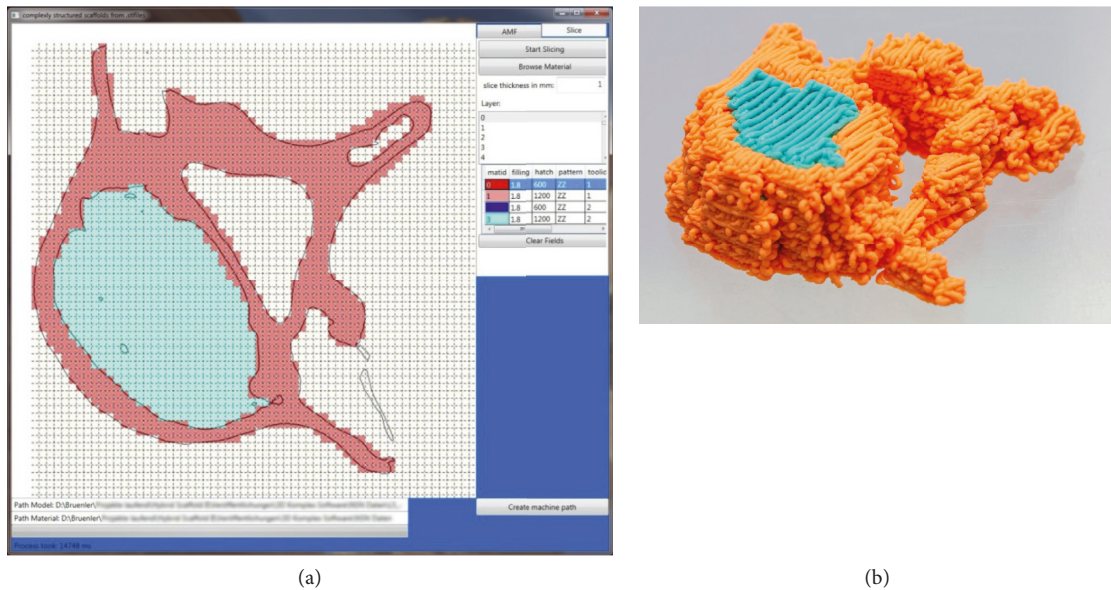
Figure 11: (a) GUI of the software with a large area (left) for assigning the voxel parameters from the standard file (right) with polylines representing the section plane and a field for scrolling through the layers (upper right). (b) Printed body featuring different colors as well as different strand spacing to demonstrate the software's ability to generate different g-codes for different nozzles based on the part geometry and the user's assignments.

First, a thin fiber bed is applied, and subsequently a binder is applied to selectively bonding the fibers together. Using the customizable configuration file, the developed modular software also allows the production of NSN structures. By appropriate selection of the tools for fiber application units (actuated by speed-controlled stepper motors) and the path distances, either a full surface fiber application or a local fiber application can be realized. Clearly, the width of the fiber track depends on the fiber length used and usually ranges from 0.5 mm to 2 mm. With these fiber lengths, which can be estimated simulation-based, suitable pore

sizes and porosities for regenerative medicine can be generated [41]. For the second process step, a piezo-controlled adhesive nozzle is actuated. In order to achieve precise contours and geometries, path distances of about $200\,\mu$m are used.

Due to the flexible controlling of extrusion nozzles, fiber application units, and adhesive nozzles, completely different additive manufacturing processes can be combined to create novel structures. Figure 12 shows different structures on the basis of simple STL files into which different materials have been inscribed.

(a)   (b)   (c)
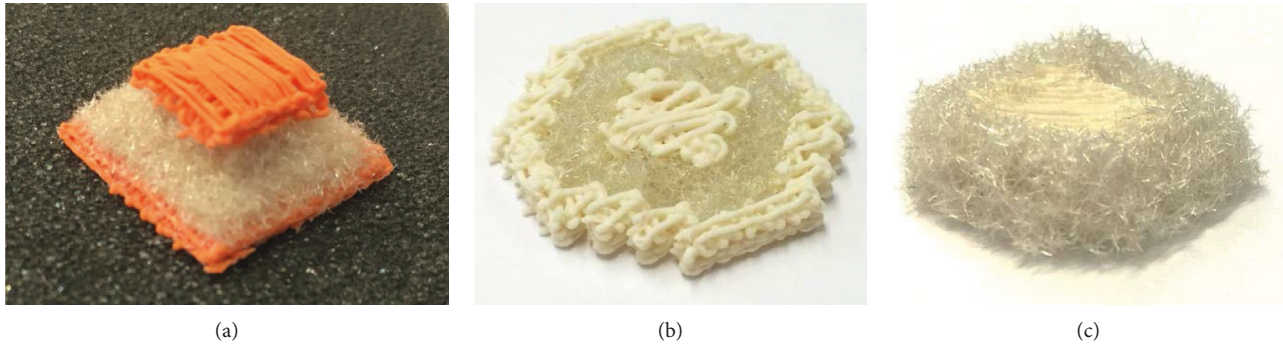
FIGURE 12: Unique structures combining extrusion-based additive manufacturing processes with a fiber-based additive manufacturing approach. (a) Sandwich structure, (b) core-shell-shell structure, and (c) core-shell structure, demonstrating uses in different applications.

The newly developed approach allows assigning volumetric structures in three-dimensional surface models. STL files obtained from CT or MRI scans in medicine, 3D scans from reverse engineering, CAD software, or any other sources solely contain information of the surface of the bodies. With existing software, assigning properties within the bodies is not possible as only triangles on the surface area can be selected.

The hosted editable configuration file allows controlling different extrusion nozzles, fiber application units, and a piezo-driven adhesive nozzle (via tool column). It features arbitrary nozzle diameters, leading to different strand thickness or different fiber layer heights (via filling/mm column). All materials are deposited in a z-pattern (via pattern column) starting in the x direction in the first layer of a voxel and subsequently changing its direction into the y direction which ensure a crossing of the strands and thus structural stability especially for strand deposition. The standard file also allows setting the speed (in mm/min via the speed column) and adjusting the tool position in the machine (in absolute XYZ coordinates (mm) in the respective columns). The "matid" column shows a colored pattern with dark and light colors representing the materials as well as the porosity to simplify the material/pattern choice during assigning the properties from the .txt file to the body.

After assigning the parameters to the voxels, a g-code can be generated automatically by clicking the "Create machine path" button on the lower right (see Figure 11(a)). Machine paths of adjacent voxels featuring the same "matid" are handed over to g-code as a continuous line and are processed according to the zig-zag pattern shown in Figure 10(b).

The possible use of the software goes beyond the usage as a postprocessor for extrusion-based or fiber-based additive manufacturing as it basically allows assigning any control commands to every single voxel:

(i) Positioning and travel commands for axes (e.g., XY tables and XYZ tables)

(ii) On/off and/or speed commands for motors (e.g., material feed/deposition/compaction/removal and applying of substrates)

(iii) Setting/resetting of digital or analog outputs (e.g., connected extruders, nozzles, heaters, coolers, fans, and lasers)

(iv) Transfer information to other units (e.g., bus systems, direct digital controls, robot controls, displays, and user feedback)

Thus, any processing technology or application may be implemented by customizing the spreadsheet file or implementing other (machine-readable) codes according to the users' needs.

Furthermore, the voxel-based approach allows assigning any information (e.g., materials, material morphologies, colors, porosities, and metadata) to the imported files. The information may be stored and used for other applications or further processing.

4. Conclusions

The presented method allows slicing and gridding bodies from STL or AMF files into volumetric elements (voxels) of arbitrary size. The underlying software allows assigning different tools and features such as path distances, strand thicknesses, or traveling speeds to each of these voxels. Adjoining voxels with equal properties are combined to subvolumes and may either be manufactured into structures with material grading, porosity grading as well as combinations of both within the different regions or be stored in AMF format and be used in compatible software or printing technologies.

Strand-based lattice structures with grading on the material and structural level can be designed and manufactured within a multinozzle additive manufacturing approach and can furthermore be combined with a two-tier process for fiber-based additive manufacturing well suited for applications in regenerative medicine. The combination of both approaches enables, e.g., designing press-fit applications with flexible transition areas on the basis of geometry data from complex defects. Furthermore, large defects affecting different tissue types or tissue morphologies, e.g., osteochondral defects involving bone and cartilage, may be addressed.

Data Availability

The software used to support the findings of this study is described extensively within the article. The described findings can be used to replicate the findings of the study.

Furthermore, parts of the software used to support the findings of this study are available from the corresponding author upon request.

Conflicts of Interest

The authors declare that they have no conflicts of interest.

Acknowledgments

References

[1] S.-H. Park, D.-Y. Yang, and K.-S. Lee, "Two-photon stereolithography for realizing ultraprecise three-dimensional nano/microdevices," *Laser & Photonics Review*, vol. 3, no. 1-2, pp. 1–11, 2009.

[2] S. A. Skoog, P. L. Goering, and R. J. Narayan, "Stereolithography in tissue engineering," *Journal of Materials Science: Materials in Medicine*, vol. 25, no. 3, pp. 845–856, 2013.

[3] A. Cazón, P. Morer, and L. Matey, "Polyjet technology for product prototyping: tensile strength and surface roughness properties," in *Proceedings of the Institution of Mechanical Engineers, Part B: Journal of Engineering Manufacture*, vol. 228, no. 12, pp. 1664–1675, 2014.

[4] D. Ibrahim, T. L. Broilo, C. Heitz et al., "Dimensional error of selective laser sintering, three-dimensional printing and polyjet models in the reproduction of mandibular anatomy," *Journal of Cranio-Maxillofacial Surgery*, vol. 37, no. 3, pp. 167–173, 2009.

[5] D. W. Hutmacher, T. Schantz, I. Zein, K. W. Ng, S. H. Teoh, and K. C. Tan, "Mechanical properties and cell cultural response of polycaprolactone scaffolds designed and fabricated via fused deposition modeling," *Journal of biomedical materials research*, vol. 55, no. 2, pp. 203–216, 2001.

[6] S. H. Ahn, M. Montero, D. Odell, S. Roundy, and P. K. Wright, "Anisotropic material properties of fused deposition modeling ABS," *Rapid Prototyping Journal*, vol. 8, no. 4, pp. 248–257, 2002.

[7] K. Thrimurthulu, P. M. Pandey, and N. Venkata Reddy, "Optimum part deposition orientation in fused deposition modeling," *International Journal of Machine Tools and Manufacture*, vol. 44, no. 6, pp. 585–594, 2004.

[8] I. Zein, D. W. Hutmacher, K. C. Tan, and S. H. Teoh, "Fused deposition modeling of novel scaffold architectures for tissue engineering applications," *Biomaterials*, vol. 23, no. 4, pp. 1169–1185, 2002.

[9] R. Anitha, S. Arunachalam, and P. Radhakrishnan, "Critical parameters influencing the quality of prototypes in fused deposition modelling," *Journal of Materials Processing Technology*, vol. 118, no. 1–3, pp. 385–388, 2001.

[10] J. Moon, A. C. Caballero, L. Hozer, Y.-M. Chiang, and M. J. Cima, "Fabrication of functionally graded reaction infiltrated SiC-Si composite by three-dimensional printing (3DP) process," *Materials Science and Engineering: A*, vol. 298, no. 1-2, pp. 110–119, 2001.

[11] K. Lu and W. T. Reynolds, "3DP process for fine mesh structure printing," *Powder Technology*, vol. 187, no. 1, pp. 11–18, 2008.

[12] Q. Wei, Y. Wang, X. Li et al., "Study the bonding mechanism of binders on hydroxyapatite surface and mechanical properties for 3DP fabrication bone scaffolds," *Journal of the Mechanical Behavior of Biomedical Materials*, vol. 57, pp. 190–200, 2016.

[13] B. Caulfield, P. E. McHugh, and S. Lohfeld, "Dependence of mechanical properties of polyamide components on build parameters in the SLS process," *Journal of Materials Processing Technology*, vol. 182, no. 1–3, pp. 477–488, 2007.

[14] J. D. Williams and C. R. Deckard, "Advances in modeling the effects of selected parameters on the SLS process," *Rapid Prototyping Journal*, vol. 4, no. 2, pp. 90–100, 1998.

[15] J. M. Williams, A. Adewunmi, R. M. Schek et al., "Bone tissue engineering using polycaprolactone scaffolds fabricated via selective laser sintering," *Biomaterials*, vol. 26, no. 23, pp. 4817–4827, 2005.

[16] J. P. Kruth, P. Mercelis, J. Van Vaerenbergh, L. Froyen, and M. Rombouts, "Binding mechanisms in selective laser sintering and selective laser melting," *Rapid Prototyping Journal*, vol. 11, no. 1, pp. 26–36, 2005.

[17] R. Landers and R. Mülhaupt, "Desktop manufacturing of complex objects, prototypes and biomedical scaffolds by means of computer-assisted design combined with computer-guided 3D plotting of polymers and reactive oligomers," *Macromolecular Materials and Engineering*, vol. 282, no. 1, pp. 17–21, 2000.

[18] S. A. Park, S. H. Lee, and W. D. Kim, "Fabrication of porous polycaprolactone/hydroxyapatite (PCL/HA) blend scaffolds using a 3D plotting system for bone tissue engineering," *Bioprocess and Biosystems Engineering*, vol. 34, no. 4, pp. 505–513, 2010.

[19] A. Lode, F. Krujatz, S. Brüggemeier et al., "Green bioprinting: Fabrication of photosynthetic algae-laden hydrogel scaffolds for biotechnological and medical applications," *Engineering in Life Sciences*, vol. 15, no. 2, pp. 177–183, 2015.

[20] S. Reitmaier, A. Kovtun, J. Schuelke et al., "Strontium(II) and mechanical loading additively augment bone formation in calcium phosphate scaffolds," *Journal of Orthopaedic Research*, vol. 31, p. 37, 2017.

[21] F. P. W. Melchels, J. Feijen, and D. W. Grijpma, "A review on stereolithography and its applications in biomedical engineering," *Biomaterials*, vol. 31, no. 24, pp. 6121–6130, 2010.

[22] E. O. Olakanmi, R. F. Cochrane, and K. W. Dalgarno, "A review on selective laser sintering/melting (SLS/SLM) of aluminium alloy powders: processing, microstructure, and properties," *Progress in Materials Science*, vol. 74, pp. 401–477, 2015.

[23] Y. Luo, A. Lode, F. Sonntag, B. Nies, and M. Gelinsky, "Well-ordered biphasic calcium phosphate-alginate scaffolds fabricated by multi-channel 3D plotting under mild conditions," *Journal of Materials Chemistry B*, vol. 1, no. 33, p. 4088, 2013.

[24] H.-W. Kang, S. J. Lee, I. K. Ko, C. Kengla, J. J. Yoo, and A. Atala, "A 3D bioprinting system to produce human-scale tissue constructs with structural integrity," *Nature Biotechnology*, vol. 34, no. 3, pp. 312–319, 2016.

[25] J. L. Rosenberg, "Drowning in triangle soup," *XRDS: Crossroads, The ACM Magazine for Students*, vol. 22, no. 3, pp. 58–62, 2016.

[26] C. C. Kai, G. G. K. Jacob, and T. Mei, "Interface between CAD and Rapid Prototyping systems. Part 1: a study of existing interfaces," *International Journal of Advanced Manufacturing Technology*, vol. 13, no. 8, pp. 566–570, 1997.

[27] P. K. Venuvinod and W. Ma, *Rapid Prototyping*, Springer, Boston, MA, USA, 2004.

[28] P. Mohan Pandey, N. Venkata Reddy, S. G. Dhande, and S. G. Dhande, "Slicing procedures in layered manufacturing: a

review," *Rapid Prototyping Journal*, vol. 9, no. 5, pp. 274–288, 2003.

[29] ASTM International, *Specification for Additive Manufacturing File Format (AMF) Version 1.2*, ASTM International, West Conshohocken, PA, USA, 2016.

[30] J. D. Murray and W. Vanryper, *Encyclopedia of Graphics File Formats*, O'Reilly & Associates, Sebastopol, CA, USA, 2nd edition, 1996.

[31] J. Hun, M. Chung, M. Park, S. Woo, X. Zhang, and A. Marie, "Generation of realistic particle structures and simulations of internal stress : a numerical/AFM study of LiMn2O4 particles," *Journal of Electrochemical Society*, vol. 158, no. 4, p. 434, 2011.

[32] Mariodiniz: Thingiverse: Thing: 1984177: Lumbar vertebra - L3, L4 and L5.

[33] Pearson Education, Inc., *Anatomy of the Lumbar Vertebrae*, Pearson Education, Inc., London, UK, 2010.

[34] S. Chmielewski and P. Tompalski, "Estimating outdoor advertising media visibility with voxel-based approach," *Applied Geography*, vol. 87, pp. 1–13, 2017.

[35] C. E. Kahn, J. A. Carrino, M. J. Flynn, D. J. Peck, and S. C. Horii, "DICOM and radiology: past, present, and future," *Journal of American College of Radiology*, vol. 4, no. 9, pp. 652–657, 2007.

[36] Medical Imaging and Technology Alliance, *DICOM®: Digital Imaging and Communications in Medicine*, National Electrical Manufacturers Association, Rosslyn, VA, USA, 2019, http://www.dicomstandard.org/about/.

[37] A. C. Brown and D. de Beer, "Development of a stereolithography (STL) slicing and G-code generation algorithm for an entry level 3-D printer," in *Proceedings of AFRICON 2013*, pp. 1–5, Pointe-Aux-Piments, Mauritius, September 2013.

[38] ctrlV: Thingiverse: Thing: 1019228 : Test your 3D printer! v2.

[39] M. Wojcik, I. Pozniak-Koszalka, L. Koszalka, A. Kasprzak, and V. G. Duffy, "Experimentation system for path planning applied to 3D printing," in *Advances in Intelligent Systems and Computing*, vol. 481, Springer, Berlin, Germany, 2017.

[40] M. Hild, R. Brünler, M. Jäger et al., "Net Shape Nonwoven: a novel technique for porous three-dimensional nonwoven hybrid scaffolds," *Textile Research Journal*, vol. 84, no. 10, pp. 1084–1094, 2014.

[41] R. Brünler, D. Aibibu, M. Wöltje, A.-M. Anthofer, and C. Cherif, "In silico modeling of structural and porosity properties of additive manufactured implants for regenerative medicine," *Materials Science and Engineering: C*, vol. 76, pp. 810–817, 2017.

Research Article

Digital Design of Medical Replicas via Desktop Systems: Shape Evaluation of Colon Parts

Michele Bici, Valerio Cardini, Marco Eugeni, Robinson Guachi, Fabiano Bini, Francesca Campana ⓘD, Franco Marinozzi ⓘD, and Paolo Gaudenzi

Dipartimento di Ingegneria Meccanica e Aerospaziale, Sapienza Università di Roma, via Eudossiana 18, Roma 00184, Italy

Correspondence should be addressed to Francesca Campana; francesca.campana@uniroma1.it

In this paper, we aim at providing results concerning the application of desktop systems for rapid prototyping of medical replicas that involve complex shapes, as, for example, folds of a colon. Medical replicas may assist preoperative planning or tutoring in surgery to better understand the interaction among pathology and organs. Major goals of the paper concern with guiding the digital design workflow of the replicas and understanding their final performance, according to the requirements asked by the medics (shape accuracy, capability of seeing both inner and outer details, and support and possible interfacing with other organs). In particular, after the analysis of these requirements, we apply digital design for colon replicas, adopting two desktop systems. The experimental results confirm that the proposed preprocessing strategy is able to conduct to the manufacturing of colon replicas divided in self-supporting segments, minimizing the supports during printing. This allows also to reach an acceptable level of final quality, according to the request of having a 3D presurgery overview of the problems. These replicas are compared through reverse engineering acquisitions made by a structured-light system, to assess the achieved shape and dimensional accuracy. Final results demonstrate that low-cost desktop systems, coupled with proper strategy of preprocessing, may have shape deviation in the range of ±1 mm, good for physical manipulations during medical diagnosis and explanation.

1. Introduction

The prospect of manufacturing complex shape is the key factor capable of bridging additive manufacturing (AM) with medical applications [1]. AM represents an ideal choice for a small-scale customized production, as the production of patient-specific objects is. In fact, in contrary to conventional manufacturing techniques, variations from the nominal design may have a reduced impact on the AM planning and related costs [2]. This point holds not only in medical applications but also in all cases that need a high level of customization, as, for example, in space applications [3]. To date, medical researchers and clinicians have had limited access to the process knowledge of 3D printing technologies. Now, this is rapidly changing, and many surgery and radiology practitioners are starting their own 3D printing labs. The knowledge of advantages and limitations of the various 3D printing technologies is a key factor to

accomplish successful investment and to extend 3D printing into medical field. In the literature, many works address AM application for medical purposes, as described in [1]. They range different areas from preoperative models up to implants and surgical tools and aids.

AM is currently applied in maxillofacial and orthopedic, both for customized implants and tools and coronary surgery [4, 5]. In [6], it is used for the rapid delivery of the fractured skull model. The effectiveness of the use of this model as a preoperative guide is shown. Time-consuming operative actions for the reduction of fractures can be lessened if the preoperative model of the fractured jaw is provided. In [7], AM is used for a new approach to reduce the eye cavity fracture. Usual procedure provides the surgeon manually shaping metallic plates according to what he finds during the surgery. The proposed procedure allows the fast delivery of skull model of the patient. Based on this, an enhanced implant is designed, allowing for better integration with neighboring

bones. Results show an improved position of the artificial eyeball along with a reduced surgical time, thanks to a better surgical planning. It is also proved that the quality of the 3D models of the skull plays a crucial role since shape inaccuracy may give ineffective implant. In [8], geometric modeling issues are addressed to measure and reproduce fragments of a skull. In [9], AM has been used for getting liver models. Based on these, surgeons get clearer ideas about possible surgical cuts in liver transplantation operations, helping in reducing the risk for the donors. These considerations have been effectively and successfully implemented in liver transplantation operations. High accuracy of the replicas is shown by comparing them with real livers through visual inspections and measurements taken during the operations. Again, model accuracies are of great importance. No reliable surgical cuts could be planned with inaccurate models. In [10], a workflow for digital models of fetal faces is proposed to help diagnosis of cleft lip disease and to investigate affective effects on parents.

Among AM technologies, fused filament fabrication (FFF) is currently the most widespread, in part due to the expiration, in 2007, of the initial patent from Stratasys, the company that invented the technology with the name of fused deposition modeling (FDM). This, along with the simplicity of the system, allowed the proliferation of several companies providing low-cost systems, also called desktop systems [11]. To provide a numerical example, we can just consider that, in 2015, the ratio between expensive commercial systems and low-cost desktop systems (that means below $5000) was about 1 : 20. In addition to cost considerations, desktop systems can be operated with major adaptability. Selected material can be chosen among those from different vendors. Very limited restrictions on available setting values of the process parameters are provided. On the contrary, this freedom does not guarantee any assurance of quality by the vendor, as it usually happens for more expensive solutions, which are properly restricted to guarantee component characteristics and stability in terms of material, size, and shapes.

Desktop systems seem to be advisable for medical replicas that can be adopted as tools for managing surgical planning or for better understanding specific patient-related aspects. They can be able to translate, easily and with low costs, 2D DICOM (Digital Imaging and COmmunications in Medicine) analysis into a physical *replica* (also called *mock-up* [12]), helping a proper perception of actual shapes and lengths. In [13], medical replicas of skull and mandible, made by professional FDM systems, are investigated from the metrological point of view. Applying the comparison between digital models and replicas of different genders and age, authors declare outstanding accuracy (overall absolute average deviation of 0.24%) of FDM in comparison with other rapid prototyping techniques. In [14], the performance of a low cost FDM system for the delivery of 3D models of mandibles are presented and discussed. Even though the performances are satisfying, no discussion is presented on the use of the system, in terms of digital design.

Multiple studies have documented that medical replicas can be produced with spatial errors of less than 1 mm [15–17]. Generally speaking, shape and dimensional inspection are relevant for medical applications due to the necessity of

(i) classification [18]

(ii) quantification of gravity and evolution of malformations [19] and

(iii) interactions among organs and tools.

AM technology involves different sciences and almost every aspect that has been modeled in literature [20, 21]. Nevertheless, also due to the large number of technologies, process knowledge and robustness are not mature yet. This lack of knowledge translates uncertainties in the manufactured object and standard tolerance controls that are still missing.

The digital design workflow asks for a data preprocessing that requires specific skills concerning 3D modeling from DICOM; tessellation for slicing; and definition of process parameters according to functional and quality requests [22].

Part of these topics asks for new oriented approaches and solutions, since they are related to a "new" technology [23]. Although these steps are becoming common skills in the engineering field, they are not always available in the medical field, yet. For these reasons, this paper discusses the most critical aspects (hardware, software, and process parameters) to be accounted for implementing digital design of medical replicas through desktop systems. After their presentation, a test-case consisting of part of a colon, from sigmoid up to the rectum, is presented. It aims at providing an experimental overview of the process and a quantitative evaluation of replicas accuracy, through experimental shape acquisitions made by a structured-light system. For the experimental part, two low-cost desktop systems have been applied and compared, a Sharebot and a Tevo-Little Monster.

According to this aim, in Section 2, we present the general workflow of digital design in the respect of final accuracy; then, in Section 3, we discuss the requirements set by the medical application; finally, we present and discuss the application made and the related experimental results.

2. Digital Design Workflow and Accuracy

Regardless of a specific AM process, in a digital design workflow, we can distinguish the following steps [24]:

(i) preprocessing that concerns with 3D model setup as suitable STL file

(ii) CAM setup of the slicing and processing that consist in the manufacturing of the component

(iii) postprocessing that pertains to the removal of the component from the manufacturing table and also the removal of the outer supports and other operations necessary to guarantee final shape and roughness (gluing of separated parts, surface finishing, etc.).

Each of these steps has its own workflow that can be specialized according to the specific field of application. In Figure 1, some further details have been addressed according to application for medical replicas.

Preprocessing	CAM	Postprocessing
(1) DICOM elaboration (2) Section stack-up (3) 3D points filtering/smoothing (4) 3D surface tessellation (5) *Check and healing* (6) Insert details	(1) Select no. of parts and slicing directions (2) Define supports and filling (3) Define process parameters (4) *Check* (5) Print	(1) Remove from basement (2) Remove supports (3) Smooth surfaces and glue
(i) DICOM segmentation (ii) Filtering/smoothing	(i) Staircase effect due to slicing (ii) Shape variations due to cooling and support/filling (iii) Local defects due to process parameters	(i) Local inaccuracy due to residues (ii) Joint with glue

Sources of error

FIGURE 1: Digital design workflow for medical replicas and related sources of error.

The preprocessing starts from the capture of the area of interest from the medical imaging (DICOM). They can be obtained from different technologies, such as computed tomography (CT), positron emission tomography (PET), X-ray, ultrasound, etc. DICOM images are bidimensional images of transversal sections of the body. These sections are generally taken with a much variable range of steps (we have assumed steps of 3 mm, that represent, in our specific case, a good compromise between time consumption and accuracy for wide areas scanning). They have to be processed by segmentation to isolate the area of interest from the rest of body's sections. Then, the set of sections that pertain to the volume of interest (e.g., part of an organ) are stacked up to obtain the 3D cloud of points, filtered, and/or smoothed so that a suitable tessellation of the 3D model can be achieved. In the majority of cases, especially with X-ray, specific algorithms have to be employed [25]. Errors, during this step, may be wrong segmentation due to misclassified pixels; lack of accuracy due to larger scan step; and 3D cloud of points with holes, thus inaccurate tessellation. It has to be checked according to regularity (no intersecting or non-manifold triangles should be present) and integrity. If not, proper healing functions has to be applied, such as optimization of shape triangles and filling of holes. Absence of this step may result in the incorrectly manufactured objects, or error break of the AM process [2]. After the check, a modeling step can be taken into account if specific functionalities must be provided, for example, the capability of open part of the organ for inner inspection.

CAM setup and processing (CAM) includes *slicing* that pertains to the selection of the layer direction and the subdivision of the 3D model into a set of sections, called slices, one over the other. In this step, also the necessity of splitting the replica into parts must to be evaluated. It can be due to the presence of opened details, which allow inspection or visibility, or due to other manufacturing constraints (e.g., volume of the printing camera). The result of the slicing is an approximated 3D object, given by the stacking of the 2D slices. The height of these is equal to the user-defined *layer-thickness* parameter. External surfaces not aligned with the vertical direction will inevitably exhibit the so-called *staircase* effect. Layer thickness influences this approximation. Normal orientation of the

slicing represents the orientation of the process. It also has effects on the necessity of infill and supports, to avoid collapse of undercuts or unsupported slices not solidified yet. Supports reduce the final quality of the surfaces and ask for post-processing work, to remove them carefully.

Concerning the definition of the process parameters, it is related to the adopted technology. FFF allows to manufacture the slices by extruding fused polymeric filament through a nozzle. Commonly adopted materials are acrylonitrile butadiene styrene (ABS) and polylactic acid (PLA), in the form of loose filament coil. They represent not-expensive solutions, mainly for rapid prototyping [2, 26]. As fundamental component of any FFF hardware, the liquefier nozzle (generally with diameters from 0.2 to 2 mm) allows to melt the filament by reaching the related temperatures (in the range of 100°–200°C, for ABS and PLA). Once liquefied, the polymer pours out through the nozzle, thanks to the pressure applied to the solid filament. It is pushed by the pinch rollers mechanism. The polymer is deposited on a printing plate or on a previously built layer. Polymer melt solidifies as heat is lost to the surrounding environment. The head through which material is poured out can move all along the printing bed plane, i.e., *x-y* directions, as this can be moved independently along height direction (*z* direction). Through this mechanism, a 3D object can be printed. For a deeper discussion of the process, along with state-of-the-art science modeling, the reader can refer to review papers [20, 21]. One of the major drawbacks of this setup is related to the temperature gradients during depositions. If they occur suddenly, not uniform cooling conditions may arise inside the manufactured part and thus residual stresses may occur (shrinkage). To reduce shrinkage, chamber temperature should be guaranteed. For desktop systems, which commonly do not have a closed and controlled chamber, a heated printing plate may help to achieve better conditions. In addition, a correction factor may be applied during the CAM preprocessing to compensate shrinkage, as a function of the selected material. Other problems that may affect this process are the conditions of filament extrusion at the nozzle. The layer thickness may be not uniform and stable at the nominal value. It can change due to problems with the mechanism of

the material supply vector up to the nozzle, or due to friction-thermal discontinuities in the nozzle. These aspects may be of utmost importance for desktop systems, since they are not guaranteed or optimized in respect of all the process variables, as it happens for commercial systems [27–29].

Concerning the postprocessing step, it is necessary to remove the part from the manufacturing platform and possible supports that surround it. Surface finishing can be improved by proper operations, so that residual of the supports and staircase discontinuities are improved. They can be mechanical operation or low-cost chemical solutions such as acetone vapor bath. Chemical solutions provide to be very effective [30], but they are only applicable to certain materials. Acetone vapor bath, for example, does not work with polylactic acid (PLA).

3. Digital Design Requirements for Medical Replicas

Surgeons use tangible life-sized models of individual anatomy for preoperative planning, explanation of the procedure to the patient, and, as a reference, during the surgical procedure. 3D printing offers advantages over conventional manufacturing technologies. Personalized single models can be created, as needed in a clinical setting, with relatively low cost in a fairly short time frame. Medical requirements for the digital design can be summarized as follows:

(1) Area of interest:

  (i) Selection of a single organ/fragment or more than one organ
  (ii) Position of the interesting areas (inner area, outer area, and both inner and outer areas)

(2) Providing pins and positioning elements for exhibition:

  (i) For mounting parts among them
  (ii) For opening/closing interesting areas

(3) Good dimension and shape accuracy

These requirements constraint the preprocessing and the CAM steps as depicted in Figure 2.

More in detail, the first requirement directly derives from DICOM segmentation, and it may have consequences on the material selections (if multiple organs are replicated, multiple materials/colors may be selected [9]). Presence of details inside the organ asks for a replica that has to be opened. It impacts the replica modeling step, asking for (a) modeling the separation of the part in coincident fragments; and (b) modeling the closing pins.

The necessity of parts that have to be opened impacts also the manufacturing step, since in case of complex shapes, it usually asks for supports during slicing. For fast prototyping, supports have to be minimized to avoid postprocessing problems. As a consequence, the shape of the surface to be opened is defined through a criterion that provides a trade-off between the maximization of the inner area dimensions, for visibility and maneuverability, and the minimization of supports, for finishing and aesthetics.

The second requirement (providing pins and positioning elements for exhibition) asks for adding surface details to be embedded in the tessellation of the interesting area, or external volume to be built to maintain the replica fixed. In any case, it may introduce local modification of the model with consequences on the process setup. Positioning elements may be also designed separately from the replicas.

Complex shapes of medical replicas are typical free-form surfaces, characterized by curvatures in different directions and curvilinear axes. In the colon case, no transversal section is equal to any of the others in terms of lengths and morphology (Figure 3).

To guarantee accuracy, the most stringent manufacturing constraint becomes the reduction of supports. Supports must be removed mechanically, and this would inevitably end up in corrupting the quality of the surface where the two structures mate [2]. In addition, mechanical action may induce cracks [31], hidden below a roughly defined surface. To avoid these problems, it is necessary that a subdivision of the axis in linear segments is made, so that each subpart may have proper slicing orientation, suitable for minimizing both staircase effect and request of supports. Figure 4 shows this concept applied to a segment of the colon shown in Figure 3.

In Figure 4(a), its slicing (green) is simulated along the direction able to minimize the supports' height and the difficulties in their removal. In Figure 4(b), although supports are more concentrated, their heights are more relevant and protruded inside the folds, so that major difficulties may arise during removal. Obviously, in case of solution in Figure 4(a), the small area of the replica connected to the supports will be affected of bad finishing after their removal. However, in Figure 4(a) solution, postprocessing operations, in order to improve finishing, can be done more easily than in Figure 4(b) case.

To obtain a better surface accuracy, a longitudinal cut that breaks each segment in two parts can be defined. In this case, a proper slicing orientation means looking for the section plane, along the central axis of the considered segment, which includes the projection of the overall semivolume of the segment. By doing so, the segment will be subdivided in two subparts with minimum height and maximum in-plane surface so that the volume will be self-supporting. In this case, the division will ask for gluing the parts after the process, but it avoids rough surfaces and the necessity of postprocessing, factors that may reduce shape and dimension accuracy. The test case described in the following sections will apply this solution, to minimize postprocessing efforts. Finally, Figure 5 summarizes the concepts behind this reasoning in terms of source of error and efforts necessary in the CAM step of the digital design workflow.

4. Application

4.1. Test-Case Description. The proposed workflow has been applied to evaluate replicas of part of a colon and its final rectum (Figure 3). In the latter, abnormal growths and polyps are internally and externally visible. This justifies two different manufacturing strategies. As there is no interest in
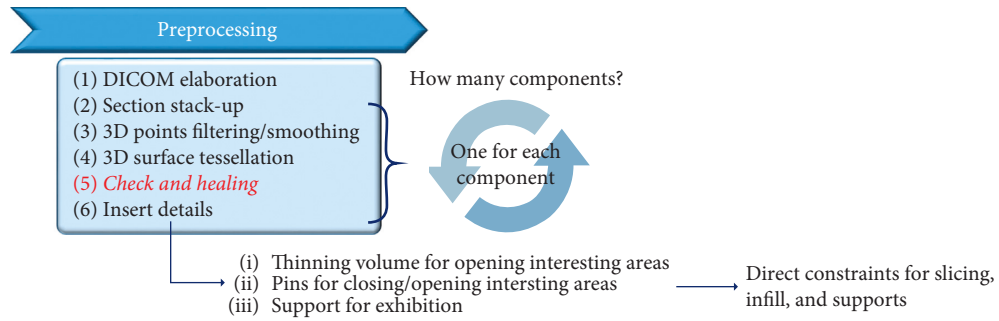
FIGURE 2: Details of the preprocessing substeps for medical replicas.
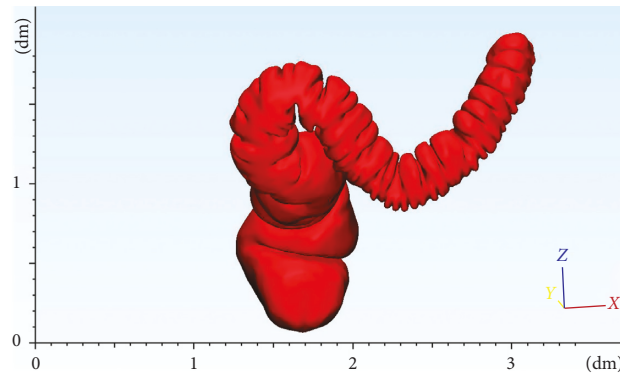
FIGURE 3: 3D model of a descendent/sigmoid colon and rectum after DICOM segmentation and 3D point surface reconstruction.

| (a) | (b) |
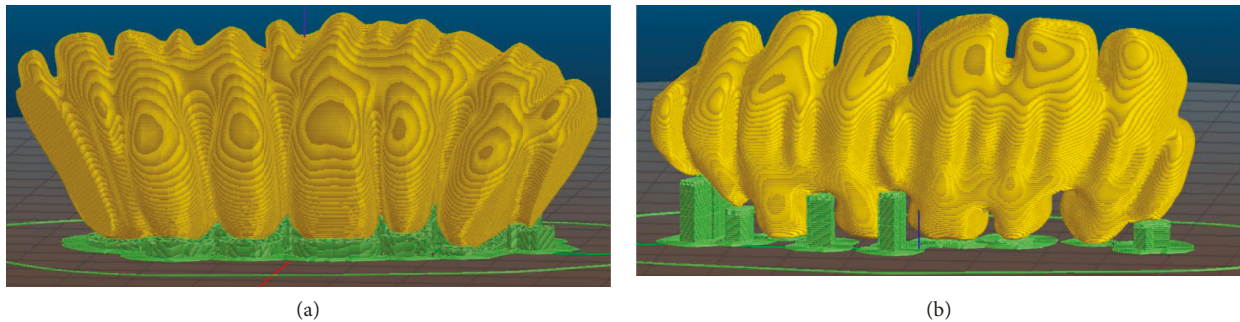
FIGURE 4: (a) Slicing simulation according to optimal direction to minimize height of the supports. (b) Slicing simulation in a different orientation.
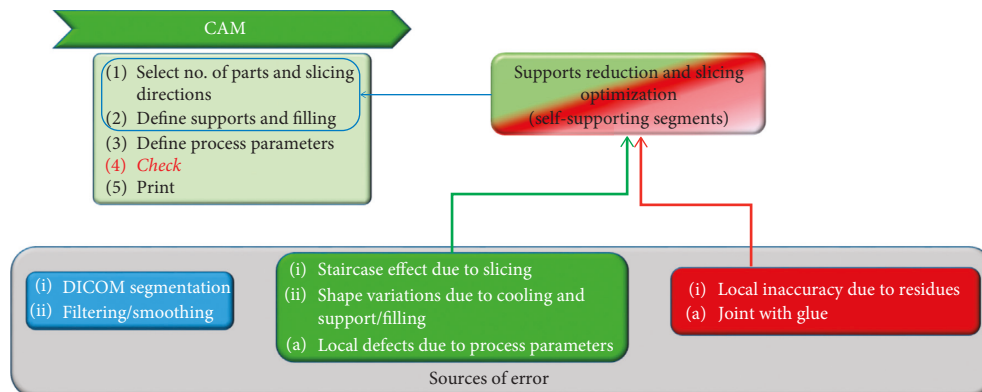
FIGURE 5: Constraints to CAM step in the digital design workflow for medical replicas.

representing the internal part of the colon, this will be built as a dense part. Conversely, the final rectum will be built as a hollow part, with attention given to the polyps and abnormal growths. Their shape and position, together with the specific shape of the colon folds, are fundamental for surgeons, and, ultimately, they justify the manufacture of the medical replica. Parts have been replicated through two different desktop systems: a Sharebot and a Tevo-Little Monster, from now on, respectively, called DS#1 and DS#2. Table 1 shows an overview of their declared plate values.

More in detail, the sigmoid colon has been replicated by DS#1 and DS#2, while the final rectum has been printed by DS#2. Figure 6 shows the final replicas, red parts are related to DS#1 and brown to DS#2.

Adopted material, in both cases, is PLA. For DS#1, selected parameters are layer height of 0.15 mm, with the exception of the first layer (0.30 mm), starting from a filament diameter of 1.75 mm. Temperature at the nozzle was 230°C, at the plate 60°C. We choose to follow the shape for 3 perimeters in each layer, and then, fill the inner part through a honeycomb 2D structure, extruded in Z direction. For DS#2, filament diameter was 1.75 mm with layer height of 0.16 mm. Temperature at the nozzle was 230°C, at the plate 80°C. External perimeters were made at 40 mm/s of speed, otherwise it was higher, up to 650 mm/s for nonprintable areas. In this case, we choose to follow the shape for 4 perimeters in each layer, and then, fill, as previously, the inner part through a honeycomb 2D structure, extruded in Z direction. The honeycomb fill pattern has been chosen with a density of 15%. Supports are the same in both cases.

To assess the quality of the replicas, measurements have been made and compared with the 3D model. They have been carried out both through caliber and reverse engineering acquisitions, made by a structured-light commercial system (Scan in a Box-FX) that declares accuracy of 0.04 mm with a minimum resolution of 0.062 mm.

4.2. Preprocessing and Manufacturing. As said in Section 3, good accuracy can be obtained by reducing the outer supports and minimizing the number of single fragments. Subdivision in fragments is mainly due to the complexity of the shape, that have different planes of maximum envelop surface projection, along its axis. In addition, the subdivision procedure is necessary due to the usage of very simple desktop systems, with one single nozzle. Thus, the component to be printed and the supports, if present, must be of the same material. Due to this, the mechanical removal of supports may cause, also, fractures and breaks in the component. Otherwise, if more than one nozzle is available in the system, other removal techniques and procedures can be developed.

Figure 7 shows, with different colors, the final fragment subdivision of the test-case. The obtained 5 segments, four for the sigmoid colon and the last one for the rectal ampulla, are the result of the localization of the medial axis and the segmentation into parts that can be built minimizing outer supports.

The four colon's segments have been separated again in two parts. This limits inaccuracies on the external surfaces, providing a planar contact area with the printing plate, not involving the external surface. In addition, the cutting planes have been selected as the plane that maximizes the normal projection of the envelop area of the part. In this way, imposing also a slicing orientation orthogonal to the cutting plane, we are able to minimize or completely avoid undercuts, especially in folds, leading to the minimization of supports.

Figure 8 shows details of the subdivision in two parts of the first fragment of the colon at the top of the 3D model. It is clearly shown that, in this case, no supports are necessary, considering the inner volume filled by infill structure. Figure 7(b) shows the subdivisions adopted for the final segment related to the rectum. In contrary to the colon fragments that are bulked, they are related to a thin-wall volume that has to be opened for inner inspection. As a consequence of their free-form shape, supports are necessary to avoid collapse of the inner surfaces with maximum heights from the base and of the prominent details of section, as shown in Figure 9. Also in this case, cutting plane has been found to minimize heights and thus supports, together with the necessity of opening a specific volume, according to the inner area of interest that has to be shown.

Axis analysis, fragment subdivision, and slicing orientation have been made in a CAD environment interactively. Optimization concerning the minimization of the supports has been iteratively checking the added volume of the supports.

5. Experimental Results and Discussion

All the planned parts resulted in a successful outcome. A quantitative comparison of the AM replicas with the tessellation obtained from the DICOM has been obtained by some reverse engineering acquisitions. They are related to the first segment in the upper part of the colon. Due to the possible light reflection on the acquired surfaces, during the acquisition with the structured-light system, the segments were covered with powder. Each segment was acquired in multiple views, aligned via embedded software (IDEA) through best fitting. After this, the cloud of points were superimposed to the 3D model and measured via distance analysis. Acquisitions consists of more than 480×10^3 points that have been analyzed after a selective filtering, based on curvature analysis, which left about 91×10^3 points.

Figure 10 shows the results in terms of color maps. In both cases, the deviation range is less than ±1 mm. Specifically, more than the 95% of points, in each case, are included between +0.48 mm and −0.40 mm. Both in DS#1 and DS#2, the mean deviation is quite close to zero, showing a little negative value (−0.04 mm). Due to this, the shrinkage can be assumed as controlled, even though it is present in blue restricted areas (small entity). This result is consistent with that already found in the literature (value of deviation less than 0.1 mm is defined as absence or controlled shrinkage) [13].

Staircase effect and filament thickness cannot be seen due to the limit of the adopted system; otherwise, along the contour of the glued parts, the discontinuity is clearly shown in DS#2 (Figure 10(b)). While in case of DS#1, the systematic position of the blue areas together with the small values of mean deviation was achieved, let us say that this trend could

TABLE 1: Adopted desktop systems: declared plate values.

	Desktop system DS#1	Desktop system DS#2
Model	Sharebot	Tevo-Little Monster
Printing size	250 mm × 220 mm × 200 mm	340 mm × 340 mm × 500 mm
Material	PLA-S, nylon-carbon, thermoplastic polyurethane	ABS, flexible PLA, HIPS, nylon, PVA
Minimum layer thickness	0.05 mm	0.05 mm up to 0.4 mm
Heated printing plate maximum temperature	90°C	80°C

(a)   (b)
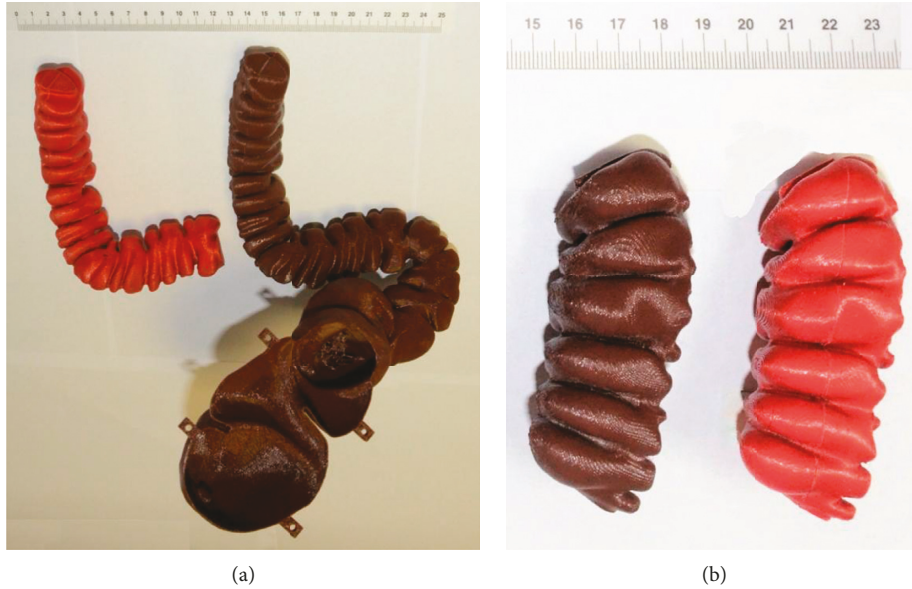
FIGURE 6: DS#1 final replicas (red) and DS#2 final replicas (brown): (a) final assembled models; (b) replications of the first segment of the sigmoid colon.

(a)   (b)
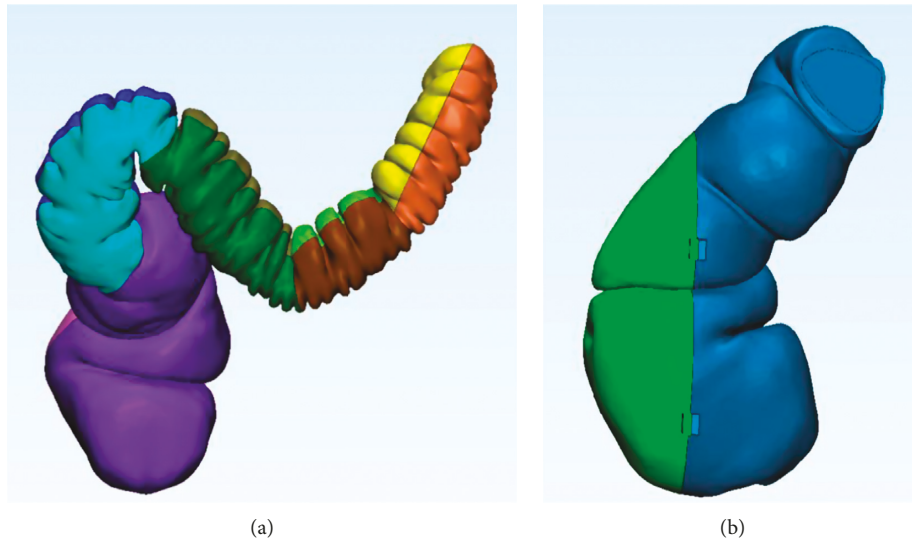
FIGURE 7: 3D model subdivision (one color per manufactured part): (a) spine subdivision in segments; (b) rectum subdivision to see the inner surfaces (part to be opened (represented in green)).

be dependent on possible inaccuracies during alignment or acquisition than on the presence of shrinkage or error during the manufacturing process.

Concerning the rectum ampulla segment, the one that can be opened, a thickness evaluation, made by the caliber, has been performed. It confirms an averaged value of 1 mm, equal to that imposed in the digital design.

These experimental evidences confirm that good shape accuracy can be reached adopting low-cost desktop systems, also for very complex free-form shapes.

(a)   (b)   (c)
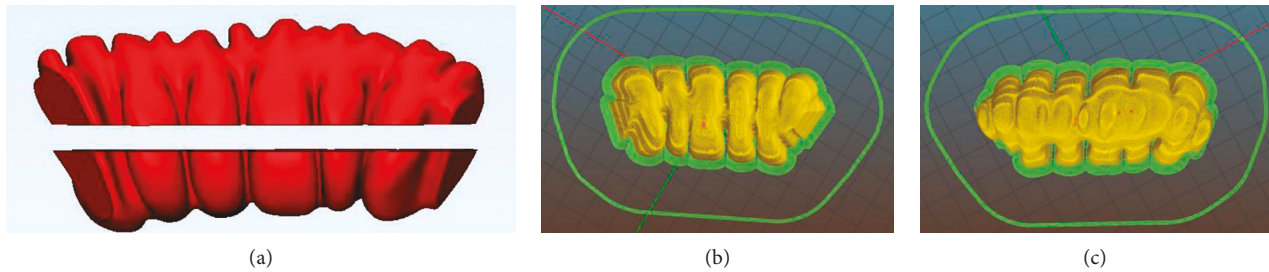
FIGURE 8: First colon segment: (a) model subdivision into two parts and (b, c) related slicing simulations.

(a)   (b)
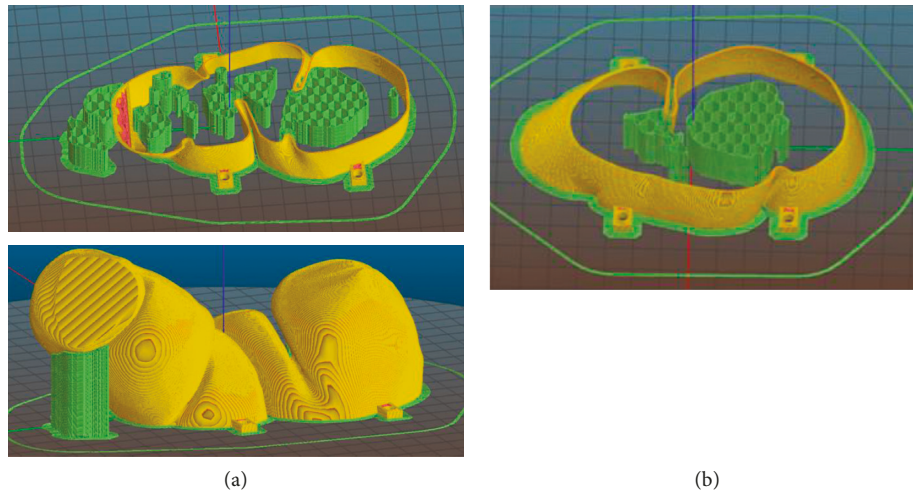
FIGURE 9: Rectum segment: (a) slicing of the part connected to the colon; (b) slicing of the part to be opened.

Taking care of minimizing support presence and avoiding severe cooling conditions of the material (e.g., increasing speed of the deposition of the external surfaces) have allowed to obtain good replicas of all the segments, without the necessity of surface postprocessing. On the contrary, the necessity of gluing the single parts cannot be reduced. Nevertheless, as shown through the experimental results, it induces errors less than 1 mm.

6. Conclusions

In this paper, the digital design workflow of medical replicas has been analyzed and applied to reproduce a large part of the colon. Two low-cost desktop systems, a Sharebot and a Tevo-Little Monster, have been adopted to achieve replicas, made of PLA.

The digital preprocessing of the DICOM data has been approached according to the requirements of (a) making the replica partially opened, and (b) limiting surface postprocessing due to support removal. The opened area is the rectum one, which has been obtained as a thin-walled segment, with one removable shell. The other segments, instead, are filled in by honeycomb fill-in at 15%.

Due to the complex free-form surfaces, avoiding or limiting surface postprocessing mainly means minimizing the presence of supports and thus, optimizing the slicing directions. According to this, the central axis of the overall surface has been divided into 5 segments, suitable for reproducing the related surfaces with the optimal slicing direction. The optimality is found looking for a plane that passes through the central axis of the segment and that is able to define two self-supporting volumes, so that local supports of the complex surfaces on the printing table are avoided. In order to guarantee visibility and accessibility to its inner surface, the fifth segment (related to the rectum) has to be provided as a thinned volume, so that some supports should be necessarily present.

This preprocessing step represents the most consuming part of the workflow, and although the cutting planes may be provided automatically, the overall evaluation of how many segments must be used for the division is, currently, still a manual step, based on integrated product-process skills.

After achieving all the replicas of the segments, they were glued together. The final shapes of the first colon segments, opposite to the rectum, have been digital acquired by a structured-light system. The deviation analysis from the experimental results shows shape errors lower than 1 mm, with more than the 95% of experimental points with errors less than 0.5 mm. Point's statistical distribution shows absence (or high limitation) of shrinkage effects, with an almost symmetrical distribution of the deviation (mean value smaller than 0.1 mm).

To conclude, this paper shows that desktop systems can be used as fast solutions for medical replicas, demonstrating a good level of accuracy in complex shape reproduction. In terms of easiness of workflow, geometrical design criteria have been defined to guarantee surface finishing through the

Doviation DS#1

91246 points (100.00%)
Pos max dev = 0.96 mm
Nag max dev = −0.60 mm
Mean dev = −0.04 mm
Std dev = 0.13 mm
Pos mean dev = −0.09 mm
Neg mean dev = −0.12 mm

0.96 mm
0.13%
0.48 mm
38.62%
0.00 mm
58.30%
−0.30 mm
2.95%
−0.60 mm

(a)

Doviation DS#2

91581 points (100.00%)
Pos max dev = 0.84 mm
Nag max dev = −0.79 mm
Mean dev = −0.04 mm
Std dev = 0.19 mm
Pos mean dev = 0.12 mm
Neg mean dev = 0.17 mm

0.84 mm
0.48%
0.42 mm
44.00%
0.00 mm
51.66%
−0.40 mm
3.85%
−0.79 mm

(b)
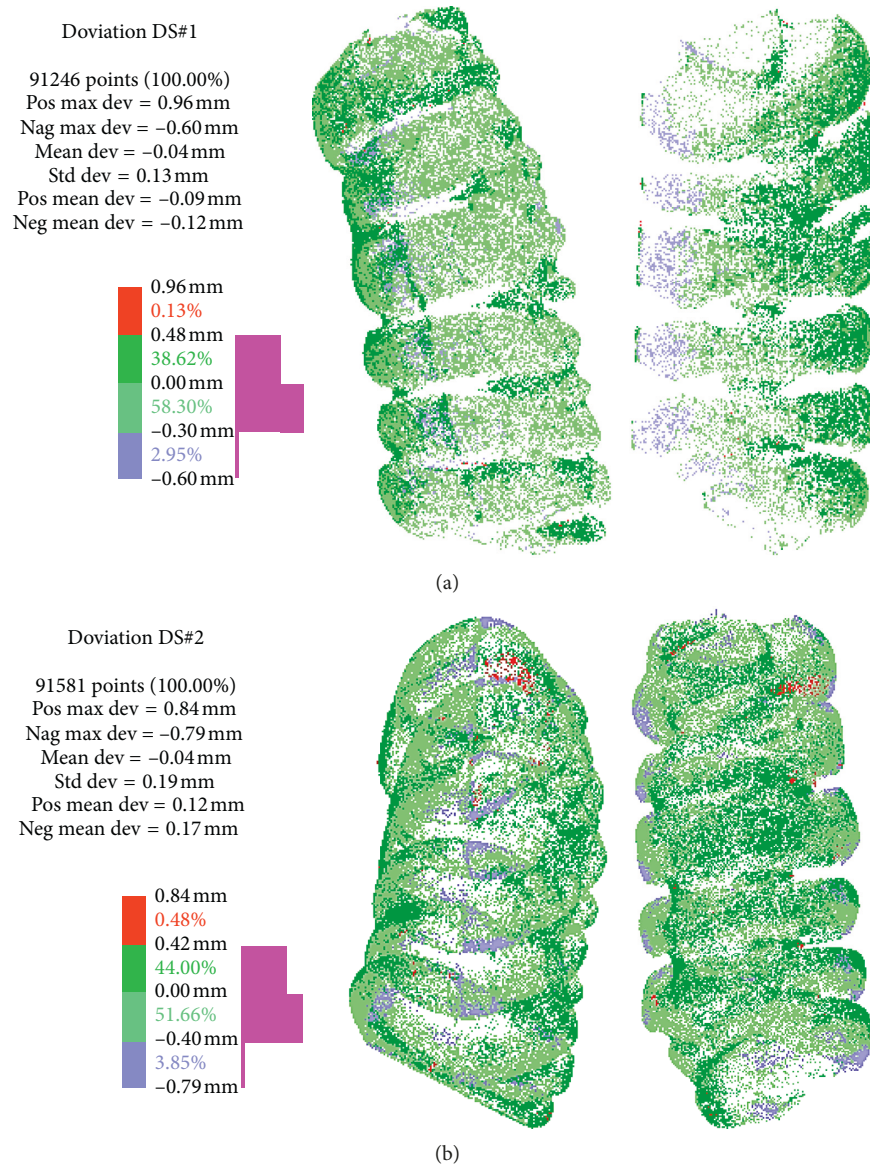
Figure 10: Experimental results related deviation analysis between 3D model and acquired replicas: (a) DS#1; (b) DS#2.

reduction of supports, minimizing the postprocessing efforts. Nevertheless, without a proper automation of the processing of the 3D model to set the segments, preprocessing still represents the bottleneck for medical autonomous applications without added skills from the engineering field. As future work, algorithms to provide the automation of the process will be analyzed and developed. In addition, the research will be moved to the possibility of generalization and reapplication on other different kinds of organs.

Data Availability

The reverse engineering data and manufacturing parameters used to support the findings of this study are included within the article. Input data and all other data used to support the findings of this study are available from the corresponding author upon request.

Conflicts of Interest

The authors declare that there are no conflicts of interest regarding the publication of this paper.

Acknowledgments

Selective Laser Sintering/Melting, macchina nano-fotopolimerizzazione e macchina concept modeler in sinergia con Design Lab Dip. PDTA di Architettura"; and (iv) Grant "SAPIENZA" University no. RM116154CE2CB985, 2016, "Tecniche innovative di progettazione orientata all'additive manufacturing per i settori meccanico-aerospaziale e biomedicale."

References

[1] M. Javaid and A. Haleem, "Additive manufacturing applications in medical cases: a literature based review," *Alexandria Journal of Medicine*, 2017, In press.

[2] I. Gibson, D. Rosen, and B. Stucker, *Additive Manufacturing Technologies. 3D Printing, Rapid Prototyping, and Direct Digital Manufacturing*, Springer, Berlin, Germany, 2nd edition, 2015.

[3] P. Gaudenzi, S. Atek, V. Cardini et al., "Revisiting the configuration of small satellites structures in the framework of 3D additive manufacturing," *Acta Astronautica*, vol. 146, pp. 249–258, 2018.

[4] M. Conner, "3-D medical printer to print body parts," *EDN*, vol. 55, no. 21, pp. 9–18, 2010.

[5] E. M. Zanetti, A. Aldieri, M. Terzini et al., "Additively manufactured custom load-bearing implantable devices: grounds for caution," *Australasian Medical Journal*, vol. 10, no. 8, pp. 694–700, 2017.

[6] J. D. Wagner, B. Baack, G. A. Brown, and J. Kelly, "Rapid 3-dimensional prototyping for surgical repair of maxillofacial fractures: a technical note," *Journal of Oral and Maxillofacial Surgery*, vol. 62, no. 7, pp. 898–901, 2004.

[7] M. Salmi, J. Tuomi, K. S. Paloheimo et al., "Patient-specific reconstruction with 3D modeling and DMLS additive manufacturing," *Rapid Prototyping Journal*, vol. 18, no. 3, pp. 209–214, 2012.

[8] F. Buonamici, R. Furferi, L. Governi et al., "Reverse engineering techniques for virtual reconstruction of defective skulls: an overview of existing approaches," in *Proceedings of CAD'18*, pp. 6–10, Paris, France, July 2018.

[9] N. Zein, I. A. Hanouneh, P. D. Bishop et al., "Three-dimensional print of a liver for preoperative planning in living donor liver transplantation," *Liver Transplantation*, vol. 19, no. 12, pp. 1304–1310, 2013.

[10] D. Speranza, D. Citro, F. Padula et al., "Additive manufacturing techniques for the reconstruction of 3D fetal faces," *Applied Bionics and Biomechanics*, vol. 2017, Article ID 9701762, 10 pages, 2017.

[11] T. Wohlers and T. Caffrey, "Additive manufacturing: the state of the industry," Wohlers Report 2016, Wohlers Associates Inc., Fort Collins, CO, USA, 2016.

[12] E. M. Zanetti and C. Bignardi, "Mock-up in hip arthroplasty pre-operative planning," *Acta of Bioengineering and Biomechanics*, vol. 15, no. 3, pp. 123–128, 2013.

[13] I. El-Katatny, S. H. Massod, and Y. S. Morsi, "Error analysis of FDM fabricated medical replicas," *Rapid Prototyping Journal*, vol. 16, no. 1, pp. 36–43, 2010.

[14] F. Maschio, M. Pandya, and R. Olszewski, "Experimental validation of plastic mandible models produced by a "low-cost" 3-dimensional fused deposition modeling printer," *Medical Science Monitor: International Medical Journal of Experimental and Clinical Research*, vol. 22, pp. 943–957, 2016.

[15] J. Y. Choi, J. H. Choi, N. K. Kim et al., "Analysis of errors in medical rapid prototyping models," *International Journal of Oral and Maxillofacial Surgery*, vol. 31, no. 1, pp. 23–32, 2002.

[16] M. Salmi, K. S. Paloheimo, J. Tuomi, J. Wolff, and A. Mäkitie, "Accuracy of medical models made by additive manufacturing (rapid manufacturing)," *Journal of Cranio-Maxillofacial Surgery*, vol. 41, no. 7, pp. 603–609, 2013.

[17] G. Santler, H. Kärcher, A. Gaggl, and R. Kern, "Stereolithography versus milled three-dimensional models: comparison of production method, indication, and accuracy," *Computer Aided Surgery: Official Journal of the International Society for Computer Aided Surgery*, vol. 3, no. 5, pp. 248–256, 1998.

[18] F. Marinozzi, F. Bini, A. Marinozzi et al., "Technique for bone volume measurement from human femur head samples by classification of micro-CT image histograms," *Annali dell'Istituto Superiore di Sanità*, vol. 49, pp. 300–305, 2013.

[19] F. Marinozzi, A. Marinozzi, F. Bini et al., "Variability of morphometric parameters of human trabecular tissue from coxo-arthritis and osteoporotic samples," *Annali dell'Istituto Superiore di Sanità*, vol. 48, pp. 19–25, 2012.

[20] B. N. Turner, R. Strong, and S. A. Gold, "A review of melt extrusion additive manufacturing processes: I. Process design and modelling," *Rapid Prototyping Journal*, vol. 20, no. 3, pp. 192–204, 2014.

[21] B. N. Turner and S. A. Gold, "A review of melt extrusion additive manufacturing processes: II. Materials, dimensional accuracy, and surface roughness," *Rapid Prototyping Journal*, vol. 21, no. 3, pp. 250–261, 2015.

[22] O. A. Mohamed, S. H. Masood, and J. L. Bhowmik, "Optimization of fused deposition modeling process parameters: a review of current research and future prospects," *Advances in Manufacturing*, vol. 3, no. 1, pp. 42–53, 2015.

[23] W. Oropallo and L. A. Piegl, "Ten challenges in 3D printing," *Engineering with Computers*, vol. 32, no. 1, pp. 135–148, 2016.

[24] G. Graterol Nisi, M. Eugeni, S. Atek et al., "Realization of smart components with embedded electronics by using fused filament fabrication," in *Proceedings of European Conference on Spacecraft Structures, Materials and Environmental Testing*, Noordwijk, Netherlands, May-June 2018.

[25] E. M. Zanetti, V. Crupi, C. Bignardi, and P. M. Calderale, "Radiograph-based femur morphing method," *Medical and Biological Engineering and Computing*, vol. 43, no. 2, pp. 181–188, 2005.

[26] P. Kumar, I. P. Ahuja, and R. Singh, "Application of fusion deposition modelling for rapid investment casting-a review," *International Journal of Materials Engineering Innovation*, vol. 3, no. 3-4, pp. 204–227, 2012.

[27] Stratasys, 2018, http://www.stratasys.com/3d-printers/mojo.

[28] Stratasys, STRATASYS F900, 2018, http://www.stratasys.com/3d-printers/stratasys-f900.

[29] Sharebot, Sharebot 3D Printers, 2018, https://www.sharebot.it/downloads/press/pressENG/flyers/42_EN.pdf.

[30] A. Lalehpour and A. Barari, "Post processing for fused deposition modeling parts with acetone vapour bath," *IFAC-PapersOnLine*, vol. 49, no. 31, pp. 42–48, 2016.

[31] T. Grimm, "Fused deposition modelling: a technology evaluation," *Time-compression technologies*, vol. 11, no. 2, pp. 1–6, 2003.

Research Article

3D Printed Anatomy-Specific Fixture for Consistent Glenoid Cavity Position in Shoulder Simulator

Gabriel Venne [iD],[1] Greg Esau,[2] Ryan T. Bicknell,[2,3] and J. Tim Bryant[3]

[1]*Department of Anatomy and Cell Biology, Faculty of Medicine, McGill University, QC, Canada*
[2]*Department of Surgery, Kingston General Hospital, Queen's University, Kingston, ON, Canada*
[3]*Department of Mechanical and Materials Engineering, Queen's University, Kingston, ON, Canada*

Correspondence should be addressed to Gabriel Venne; gabriel.venne@mcgill.ca

Purpose. Fixation methods for consistent anatomical structure positioning in biomechanical testing can be challenging. Image-based 3D printing is an attractive method for fabrication of biomechanical supports of anatomical structure due to its ability to precisely locate anatomical features with respect to the loading system. *Method*. A case study is presented to provide a design guide for fixation block fabrication. The anatomy of interest was CT scanned and reconstructed in 3D. The model was imported into commercially available CAD software and modified into a solid object and to create the fixture block. The CAD fixture block is standardized such that anatomical features are always in the same position for the testing system by subtracting the anatomy from a base fixture block. *Results*. This method allowed a strong immobilization of anatomical specimens and a controlled and consistent positioning feature with respect to the testing system. Furthermore, the fixture block can be easily modified and adapted to anatomical structures of interest using CAD software. *Conclusion*. This approach allows preservation of the bony anatomy integrity and provides a repeatable and consistent anatomical positioning with respect to the testing system. It can be adapted for other anatomical structures in various other biomechanical settings.

1. Background

The aging population is putting increased demands on health care. Age-related diseases like osteoarthritis are on the rise, underlining the need for increased research in various areas of orthopaedics, including joint biomechanics [1, 2]. This research field encompasses kinematic studies, mechanical testing of implants, and joint simulator development.

In a previous study, we found that additive-manufacturing, also known as fused deposition modeling or 3D printing, could produce bone models derived from CT imaging with an accuracy of less than half a millimeter [3]. This additive-manufacturing technology has also been highly useful in producing bony anatomical structures of complex shapes in preoperative planning [4–6]. It also allows the design and manufacture of complex shapes derived from the patient's anatomy, such as surgical drill-guides that

fit the patient's bony anatomy surface for placing a prosthetic device with respect to the preoperative plan [7]. However, the use of these systems in surgical applications must also account for material properties such as strength and modulus [8, 9].

Anatomical support in biomechanical testing is intended to provide stabilization of the studied anatomy while external loads are applied. Immobilization and mounting techniques include potting with diverse materials, custom-designed fixtures [10], clamping, and direct fixturing using a variety of bearings and fasteners [11]. These methods, although robust, are challenging to apply and to ensure there is no loss of immobilization. Furthermore, the locations of specific anatomical features are challenging to align with respect to the fixture in 3D. As such, the use of custom-designed supports using additive manufacturing is attractive for the fabrication of biomechanical supports following the principles used in machine fixtures used in manufacturing

applications. The purpose of this communication is to describe a standard procedure for 3D printing anatomy-specific support models in a variety of applications and to provide a design guide using a case study for a specific application to a complex fixture for the shoulder.

2. Overview

An anatomy-specific support is a structure in which the 3D-reconstructed anatomy of the region of interest has been subtracted to form a structural negative mold, termed a fixation block. The raw data of the specimen can be provided using medical imaging, 3D scanning, or other systems that can produce a 3D model. A reconstructed model is produced using image segmentation and processing software to isolate the anatomical region of interest. This model is then imported into computer-aided design (CAD) software and subtracted to form the support. Finally, the anatomy-specific support is printed in 3D.

2.1. Image Acquisition. The desired cadaveric anatomy was CT scanned at a high resolution using a 16-slice mobile gantry CT scanner (Lightspeed+XCR, General Electric, Milwaukee, WI, USA) using a slice thickness of 0.625 mm. The datasets were exported in Digital Imaging and Communications in Medicine (DICOM) file format.

2.2. 3D-CT Reconstruction. DICOM files were imported into commercial software (Mimics 15.0, Materialise, Leuven, Belgium) to segment the desired 2D-CT scan anatomy into a 3D-CT reconstructed model. A mask of the target anatomy was created using embedded bone thresholding settings. The mask was inspected in each of the three planes 2D-CT coordinates and edited to ensure accuracy of the anatomy representation. The 3D-CT reconstruction model was then constructed from the 2D-CT mask, and then exported as a stereolithography (∗.stl) file.

2.3. CAD of the Fixation Block. The 3D-CT reconstructed models in ∗.stl format were imported into commercially available software (SolidWorks™, Dassault Systèmes Waltham, MA). This permits the construction of a support by first defining an outer block and then subtracting the 3D-CT reconstructed model from the support.

2.4. Additive Manufacturing of the Fixation Block. The anatomic-specific support CAD model was digitally inspected and exported as a ∗.stl format to be 3D printed using additive manufacturing (Dimension SSt 1200es, Stratasys, Eden Prairie, USA). The anatomic-specific support was printed in Acrylonitrile Butadiene Sytrene (ABS) thermoplastic with a printer resolution of 0.254 mm. The model was finally cleaned of any printing-support material from the printer, inspected for any printing error and finally tested on the studied anatomy.

3. Case Study: Scapular Fixture for Shoulder Simulator

A system was previously designed to study the biomechanics of shoulder arthroplasty [12]. The scapula is fixed to a frame and cables used to represent the anterior, middle, and posterior heads of the deltoid. The cables are attached through ball joints to insertion points on the humerus and routed through pulleys to electric linear actuators. Inline load cells are used to measure force in each cable. Critical to this system is the location of muscle insertion and wrapping points determined from anatomical studies. As such, the use of an image-based reference frame enabled the positioning of the scapula with respect to the cable actuators that has distinct advantages compared to other fixation techniques. Specifically, the method reduces the effect that anatomical variations have on the positioning of deltoid and rotator cuff muscle origins relative to the centroid of the glenoid. By preserving the scapular anatomy, CAD models can be easily modified and reprinted, and the fixture can be removed without altering the anatomical structure.

3.1. Importing Files. Most scanners produce a surface, an infinitesimally thin sheet that covers the entire object. Before any CAD modifications can be done to a model, it must be converted into a solid file, such as a SolidWorks™ part file. This is not always straightforward, and SolidWorks™ has a *KNIT* tool that completes the surface and then attempts to fill it in, but this occasionally requires manual intervention.

3.2. Glenoid Cavity Centroid. When the∗.stl file has been successfully converted to a solid model file, the centroid of the glenoid cavity must be found to define reference planes (Figure 1). First, using CAD software, a face plane is defined that rests on the three most distal vertices of the glenoid cavity and must not intersect any part of the glenoid except those three points. The glenoid cavity is assumed to be a sphere, and its centroid is used in combination with the face plane for reference and measurement.

(a) There is a rim on the glenoid cavity that constrains superior motion of the shoulder. On the face plane, trace a circle that circumscribes the rim, with radius, a.

(b) Find the normal distance between the face plane and the glenoid cavity, b. In SolidWorks™, this can be done using the *MEASURE* tool. It is important to ensure the normal distance from the face plane is measured since the anatomical reference plane is not aligned with the x-y-z axes.

(c) The centroid of the glenoid is located on the normal of the face plane that intersects the centre of the circle. The distance along the normal from the plane is the radius of the traced circle (a) minus the normal distance (b).

3.3. Reference Planes. Although the reference planes are not anatomical planes, per se, they are used to relate the scapula to the biomechanical loading system [13] (Figure 2). These
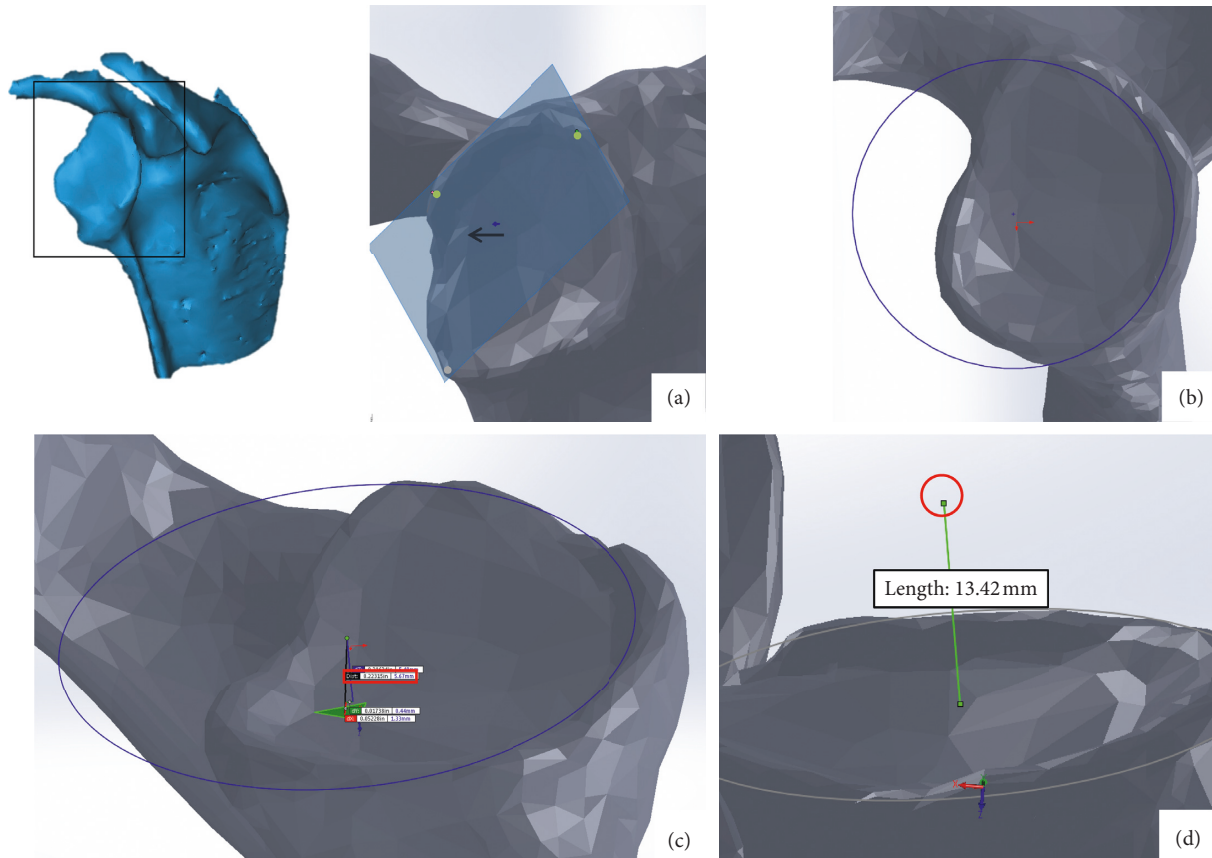
FIGURE 1: Glenoid cavity centroid: (a) the bearing surface is defined by a plane that rests on the three most distal vertices; (b) a circle is fitted to the defined bearing surface; (c) the normal distance is measured from the circle centroid to glenoid cavity surface; (d) the glenoid cavity centroid is then calculated.

can be used to relate to the anatomical planes using digitized measurements, which is the main advantage of using an image-based fixation method.

(a) Coronal plane: the coronal plane consists of the glenoid cavity centroid, the trigonum spinae, and the inferior angle. The centroid of the trigonum spinae and the most inferior part of the inferior angle are selected for this definition.

(b) Transverse plane and mediolateral axis: the mediolateral axis is on the transverse plane and normal to the sagittal plane. The mediolateral axis consists of the line between the centroid of the trigonum spinae and glenoid cavity centroid. These must be the same points as those used to define the coronal plane. The transverse plane is thus defined as containing the mediolateral axis and as perpendicular to the coronal plane.

(c) Sagittal plane: The sagittal plane is perpendicular to the two other planes using the glenoid cavity centroid of the glenoid cavity as the origin.

3.4. Fixation Block Base. Fixation blocks are standardized such that the glenoid cavity centroid is always in the same position relative to the simulator. In general, a fixation block is made by extruding a rectangle of material from the transverse plane in the inferior direction. Guides are then extruded from the inferior surface to align the scapula in the ML and AP directions.

3.5. Parting Line. Once the CAD file for the fixation block has been made, it must be divided into sections so that it can be opened to insert the scapula (Figure 3). This division can be accomplished by creating planes that extrude mediolaterally from the scapula and then by cutting the fixation block with them.

Using two separate 3D sketches, the parting line is traced on the medial and lateral faces of the scapula. Surfaces are then extruded from the sketch. When extruding, the direction is specified from the reference planes. The extrusion should be normal to the sagittal plane. Because the 3D sketch may not consistently intersect the scapula, an extrusion in the opposite direction is specified to ensure that all gaps are closed. The surface must extend above and below the fixation block dimensions; it is much better to have a parting surface that is too large than too small.

3.6. Locating Fins

(a) The transverse profile of the block is sketched on the transverse plane and extruded downwards. It is important to treat the block as a separate body from
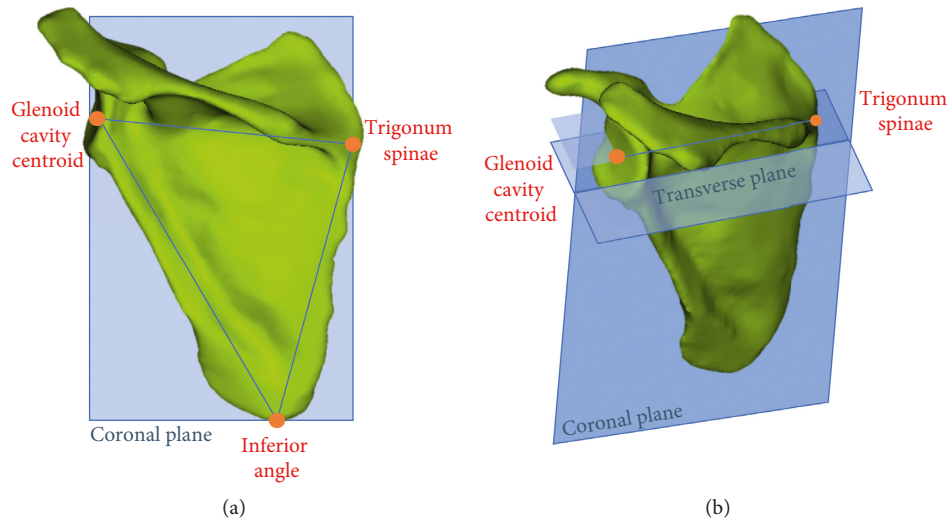
FIGURE 2: Reference planes: (a) coronal plane on scapula model; (b) mediolateral axis used in combination with the coronal plane to find the transverse plane and transverse and coronal plane are used to determine sagittal plane.
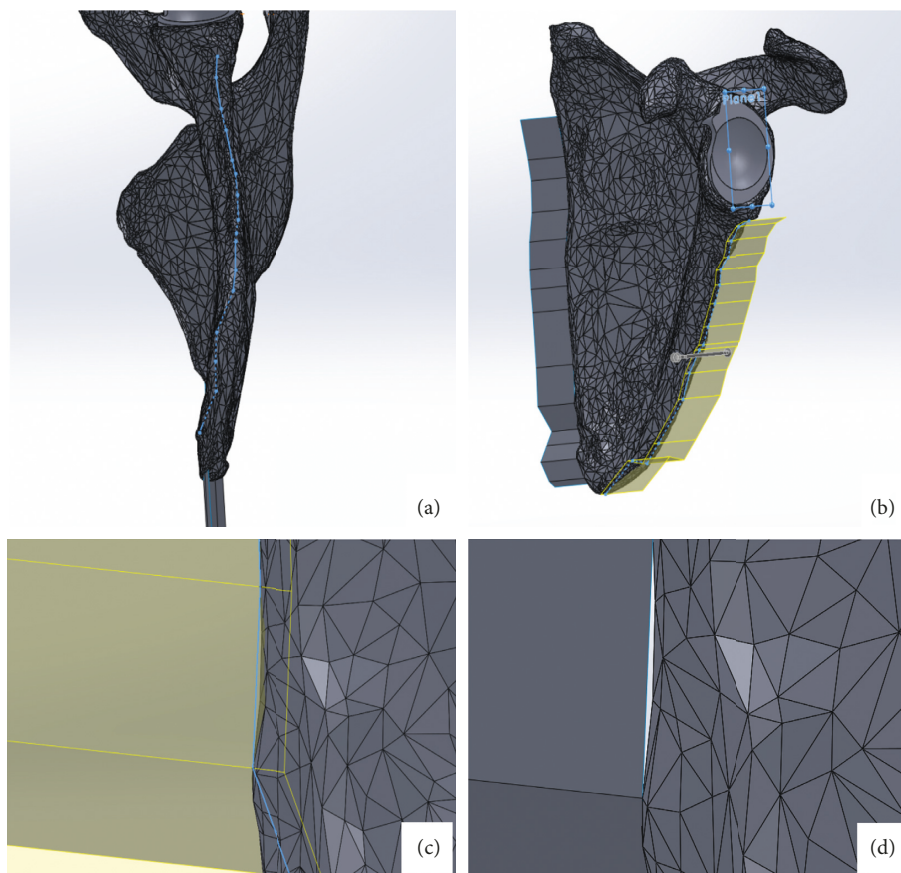
FIGURE 3: Parting line: (a) tracing parting line on lateral side of scapula; (b) extruding a plane from the traced parting line; (c) example of a gap between parting surface and scapula; (d) two-directional extrusion.

the scapula. In SolidWorks™, this is done by unchecking *MERGE RESULT* in the *EXTRUSION FEATURE* window.

(b) Locating fins are extruded downwards from the inferior face of the block. Ensure these features *do* merge with the block.
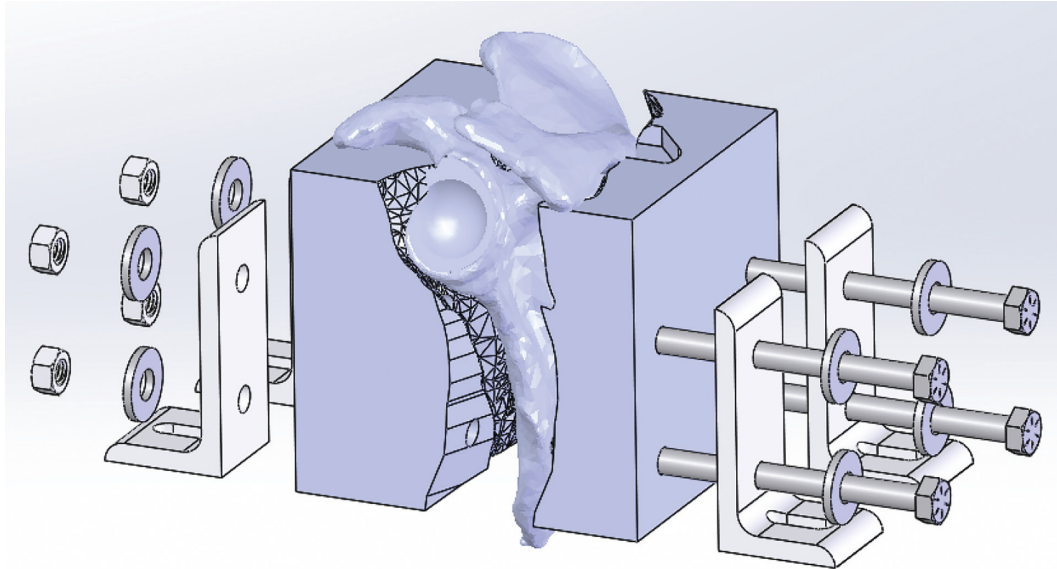
FIGURE 4: Final assembly with locking features shown. Note pocket in right segment.

3.7. Parting Features

(a) The scapula is subtracted from the fixation block, which leaves a cavity in the shape of the scapula (Figure 4). In SolidWorks™, this is done using the *COMBINE* command and selecting *SUBTRACT* rather than *ADD*. Subtracting the scapula from the block leaves the block and parting surfaces intact.

(b) Some CAD packages may be able to perform partial surface cuts; however, SolidWorks™ requires a workaround. This can be done by sketching a slot between the anterior and posterior midpoints with a very tiny radius ($0.00001''$). This slot is then used to create an extruded cut that is $0.00002''$ thick through the entire model, forming two bodies. If prompted, ensure to keep both bodies.

(c) There are now two bodies in the CAD environment—both of which are halved by a parting plane. Use the surfaces to cut both bodies. SolidWorks™ is unable to cut with a surface and keep both sides, so this must be done for each side separately.

(d) When the fixation block has been cut with the surfaces, one half of the block will remain. It will be comprised of two bodies. Select both bodies and save them. SolidWorks™ gives the option of inserting the bodies into a part file in their original orientation.

(e) Before modifying these bodies, ensure that the links to the original model are broken. Select one side of the central cut, and create a sketch on it. Trace the outside perimeter of the face. In SolidWorks™, this can be done quickly by using the CONVERT ENTITIES command.

(f) This traced profile is extruded until it contacts the other body—this can be done by blindly extruding

$0.00002''$ or by specifying the adjacent surface as the limit. Ensure this extrusion merges the two entities.

3.8. Separation Clearance and Locking Features.
For the fixation block to fit the scapula, it must only close on it in one direction (Figure 3). A pocket is used to perform this function by clearing material in the pull direction so that the feature that fits in the inadmissible pocket can be inserted and removed. In addition, features to lock the block to the testing system are added.

(a) When one side of the fixation block is completed, the direction of the surface cuts in the master model is flipped. This is repeated to create a single fixation block section. The fixation block sections may then be saved as ∗.stl files and 3D printed. Typically, the blocks are printed at semisparse infill.

(b) Circular holes are added to align with the locking features of the testing system.

3.9. Application to Testing.
The fixation blocks are on hand, and ready for testing by the time a cadaveric sample is removed from the freezer.

(a) Muscle tissue from the scapula is released to expose the bone and should fit snugly in the fixation block. However, 3D printing tends to produce extra material, so the cavity is undersized. A file, rasp, or sandpaper is used to make modifications to the fixation block parts until the scapula is firmly held. After pilot testing, this rectification step can be reduced if the fixation block is printed to be larger, typically by 2%.

(b) When the scapula is in the fixation blocks, holes are drilled in the scapula to align with the locking features incorporated in the design.

4. Summary and Conclusion

The purpose of this fixture block design method was to create anatomy-specific support for complex anatomical structures allowing a controlled placement and immobilization in a kinematic simulator. This method, using additive-manufacturing, allowed a strong immobilization of cadaveric scapulae and a controlled and consistent positioning of glenoid centroid with respect to the testing system. As well, the CAD of the fixture block can be easily modified and adapted to other anatomical structures of interest. No fixture block failure has been reported during our testing after multiple cycles of use.

The presented method was described for scapulae fixation for a shoulder simulator specifically. However, the same method has been very useful in our laboratory for various other biomechanical testing projects: distal radius and ulna fracture plate mechanical testing, foot prosthetic design and mechanical evaluation, and image-guided surgery platform design for *in vitro* testing [14, 15].

Additive manufacturing provides a good alternative for anatomy fixtures in any situation where biomechanical testing requires repeatable procedures to be applied on bony anatomy. Its integration with image-based solid modeling has advantages in its ability to locate anatomical landmarks precisely with respect to testing systems.

Data Availability

No data were used to support this case study. All the necessary information that might be needed to reproduce the presented method is included within the article.

Disclosure

The authors, their immediate family, and any research foundation to which they might be affiliated to did not receive any financial payment or other benefits from any commercial entity related to the subject of this article.

Conflicts of Interest

The authors declare that they have no conflicts of interest.

Acknowledgments

References

[1] V. L. Johnson and D. J. Hunter, "The epidemiology of osteoarthritis," *Best Practice & Research Clinical Rheumatology*, vol. 28, no. 1, pp. 5–15, 2014.

[2] T. Neogi and Y. Zhang, "Epidemiology of osteoarthritis," *Rheumatic Disease Clinics of North America*, vol. 39, pp. 1–19, 2013.

[3] E. J. Smith, J. A Anstey, G. Venne, and R. E. Ellis, "Using additive manufacturing in accuracy evaluation of reconstructions from computed tomography," *Proceedings of the Institution of Mechanical Engineers, Part H: Journal of Engineering in Medicine*, vol. 227, no. 5, pp. 551–559, 2013.

[4] N. Bizzotto, I. Tami, A. Santucci et al., "3D Printed replica of articular fractures for surgical planning and patient consent: a two years multi-centric experience," *3D Printing in Medicine*, vol. 2, no. 1, p. 2, 2015.

[5] J. G. G. Dobbe, J. C. Vroemen, S. D. Strackee, and G. J. Streekstra, "Patient-tailored plate for bone fixation and accurate 3D positioning in corrective osteotomy," *Medical and Biological Engineering & Computing*, vol. 51, no. 1-2, pp. 19–27, 2013.

[6] A. Sutradhar, J. Park, D. Carrau et al., "Designing patient-specific 3D printed craniofacial implants using a novel topology optimization method," *Medical and Biological Engineering & Computing*, vol. 54, pp. 1123–1135, 2016.

[7] M. Kunz, J. F. Rudan, G. L. Xenoyannis, and R. E. Ellis, "Computer-assisted hip resurfacing using individualized drill templates," *Journal of Arthroplasty*, vol. 25, no. 4, pp. 600–606, 2010.

[8] E. M. Zanetti and C. Bignardi, "Structural analysis of skeletal body elements: numerical and experimental methods," in *Biomechanical Systems Technology*, C. T. Leondes, Ed., vol. 3, pp. 185–225, University of California, Los Angeles, CA, USA, ISBN 978-981-270-983-7, 2009.

[9] E. M. Zanetti, A. Aldieri, M. Terzini, M. Calì, G. Franceschini, and C. Bignardi, "Additively manufactured custom load-bearing implantable devices: grounds for cautions," *Australasian Medical Journal*, vol. 10, no. 8, pp. 694–700, 2017.

[10] E. M. Zanetti, C. Bignardi, and A. L. Audenino, "Human pelvis loading rig for static and dynamic stress analysis," *Acta of Bioengineering and Biomechanics*, vol. 14, no. 2, pp. 61–666, 2012.

[11] E. M. Zanetti and A. L. Audenino, "Differential thermography for experimental, full-field stress analysis of hip arthroplasty," *Journal of Mechanics in Medicine and Biology*, vol. 10, no. 3, pp. 515–529, 2010.

[12] A. L. Clouthier, M. A. Hetzler, G. Fedorak, J. T. Bryant, K. J. Deluzio, and R. T. Bicknell, "Factors affecting the stability of reverse shoulder arthroplasty: a biomechanical study," *Journal of Shoulder and Elbow Surgery*, vol. 22, no. 4, pp. 439–444, 2013.

[13] G. Wu, F. C. T. Van Der Helm, H. E. J. Veeger et al., "ISB recommendation on definitions of joint coordinate systems of various joints for the reporting of human joint motion—part II: shoulder, elbow, wrist and hand," *Journal of Biomechanics*, vol. 38, no. 5, pp. 981–992, 2005.

[14] D. S. Giles, M. P. Kempston, R. W. Sellens et al., "Locked versus non-locked plating for the fixation of radius fractures: a biomechanical comparison," in *Proceedings Computer-Assisted Orthopedic Surgery, Paper #22*, pp. 2–4, Vancouver, BC, Canada, June 2015.

[15] B. J. Rasquinha, A. W. L. Dickinson, G. Venne et al., "Crossing-Lines Registration for Direct Electromagnetic Navigation," *Lect Notes Comput Sci*, vol. 9350, pp. 321–328, 2015.